Diurnal Land Surface Temperature Observation Using Polar Orbit Satellites and an Application to Ecosystem Respiration in Arctic and Pan-arctic Regions

February 2025

ZHIYAN LIU

Graduate School of Science and Engineering

Chiba University, Chiba, Japan

(千葉大学審査学位論文)

Diurnal Land Surface Temperature Observation Using Polar Orbit Satellites and an Application to Ecosystem Respiration in Arctic and Pan-arctic Regions

February 2025

ZHIYAN LIU

Graduate School of Science and Engineering

Chiba University, Chiba, Japan

Abstract

The Arctic and Pan-arctic regions, are currently undergoing unprecedented environmental transformations. The Arctic amplification, as well as the consequent permafrost thawing, and more severe and frequent heatwave and wildfire were changing and threathening the ecosystem of these regions. Thus, temperature monitoring is of great importance to understand the temperature changing and ecosystem response. With the development of satellite observation technology for decades, it provided an effective approach of monitoring land surface temperature (LST) over the Arctic and Pan-arctic regions, for monitoring and understanding these phenomenons continuously over wide area and at fine spatial resolutions. In this study, a novel method that synthesze LSTs from multiple polar orbit satellites was developed for constructing a high temporal resolution LST. To achieve the high observation frequency, Moderate Resolution Imaging Spectroradiometer (MODIS) on Terra and Aqua, and Visible Infrared Imaging Radiometer Suite (VIIRS) on Suomi National Polar-orbiting Partnership (SNPP) with their original swath data were used. Also, the newly launched platform–Medium Resolution Spectral Imager Low-light (MERSI-LL) on Fengyun 3E (FY-3E) that was expected to capture the observations at dawn and dusk time, was included. The combination of MODIS and VIIRS constructed the quasi-hourly LST for regions above 70˚N latitude, and the addition of FY-3E extended coverage down to 60˚N. As the invalid of LST products in 2022 for MERSI-LL FY-3E, a temperature and emissivity separation (TES) approach was applied for retrieving the LST, which was constructed and validated as RMSE at approximately 2 K for vegetated surfaces and 4 K for barren surfaces. Finally, the quasi-hourly LST was integrated as the calculation input of daily mean LST. These developments improved the estimation of ecosystem respiration, where the input of the quasi-hourly based daily mean LST can deal with the ecosystem respiration estimation error caused by instantaneous nighttime LST. As an application indicated in this study that hourly LST data can be used for improving the ecosystem respiration estimation in Arctic and Pan-arctic, it indicates the urgent need for developing satellites and advanced technics for making comprehensive observation for these regions.

Table of Content

List of Figures

List of Tables

Chapter 1 Arctic and Pan-arctic Climate Issues and Brief Review of Land Surface Temperature

1.1 Introduction of Climate Changes in Arctic and Pan-arctic

The Arctic high-latitude regions are currently experiencing unprecedented environmental transformations. These changes are primarily driven by the accelerated pace of global climate change, impacting both oceanic and cryospheric conditions (Bengtsson et al., 2004; Box et al., 2019; Jeong et al., 2018). According to the Intergovernmental Panel on Climate Change (IPCC), the alterations in these areas are especially notable and have significant implications (IPCC, 2022). These transformations are not isolated phenomena but are pivotal in maintaining local ecosystems and exert a considerable influence on broader global environmental dynamics (Box et al., 2019).

One of the most critical aspects of these changes is the phenomenon known as Arctic amplification. This refers to the rapid warming in the Arctic regions, occurring at a rate significantly higher than the global average. The effects of Arctic amplification are extensive, leading to pronounced shifts within these fragile ecosystems. Serreze and Francis (2006) documented that, this warming trend is associated with substantial ecological transformations, including the thawing of permafrost, reduction in sea ice, and changes in terrestrial and marine biodiversity. These shifts pose challenges not only to local wildlife and habitats but also to indigenous communities whose lifestyles and economies are intricately linked with these natural elements (Ahkinga, 2022; Grigorieva, 2024).

Moreover, the consequence of Arctic ice melting is contributing to higher global sea levels, which poses a threat to coastal regions worldwide (Nielsen et al., 2022). Additionally, the loss of ice affects global climate patterns, potentially altering weather conditions across different continents. The warming of the Arctic also has implications for global energy strategies, as the region holds significant untapped oil and gas reserves, making it a focal point for geopolitical interests (Nanni et al., 2024; Zhang et al., 2024).

Overall, the environmental changes occurring in the Arctic and high-latitude regions encapsulate a complex interplay of ecological, social, and economic factors. These

changes are indicative of the broader impacts of global climate change, highlighting the urgent need for comprehensive and sustained international efforts to mitigate these effects and adapt to their consequences. Such efforts must consider the delicate balance of the Arctic ecosystem and the well-being of its indigenous populations, alongside global environmental and economic stability.

1.1.1 Arctic Amplification

Arctic amplification describes the phenomenon where the Arctic region experiences a larger rate of warming. This phenomenon describes the disproportionate increase in near-surface air temperatures in the Arctic compared to lower latitudes and the global average (Figure 1.1). Arctic amplification has been documented across various studies spanning from historical records to present-day observations and future model projections (Hoffert and Covey, 1992; Miller et al., 2010; Serreze et al., 2009). Recent observations have confirmed this trend, which is vividly captured in climate data over recent decades. A detailed examination of temperature records from meteorological stations across Alaska reveals a significant warming trend, with average air temperatures (Ta) rising by approximately 0.19–0.47°C per decade, alongside sustained high temperatures (Sulikowska et al., 2019). These findings at the individual meteorological observation stations are consistent with observations of prolonged periods of elevated temperatures across the region (Box et al., 2019). Additionally, data analysis from reanalysis sources has shown an uptick in the frequency and intensity of heatwave events in Arctic regions such as Greenland and Siberia between 2011 and 2015, further illustrating the acute impacts of this rapid warming (Dobricic et al., 2020). Climate models, particularly those from the sixth Coupled Model Intercomparison Project (CMIP6), have effectively replicated the pattern of polar-amplified warming (Linke et al., 2023). By using the result from ensemble of 20 models in CMIP6, it was found that most Arctic and Pan-arctic terrestrial regions except Greenland showed a 1.5–2.5x much faster temperature rising comparing to the globe temperature rising. Additionally, widespread high increasing trends were observed at Alaska and Eurasia regions (Linke et al., 2023).

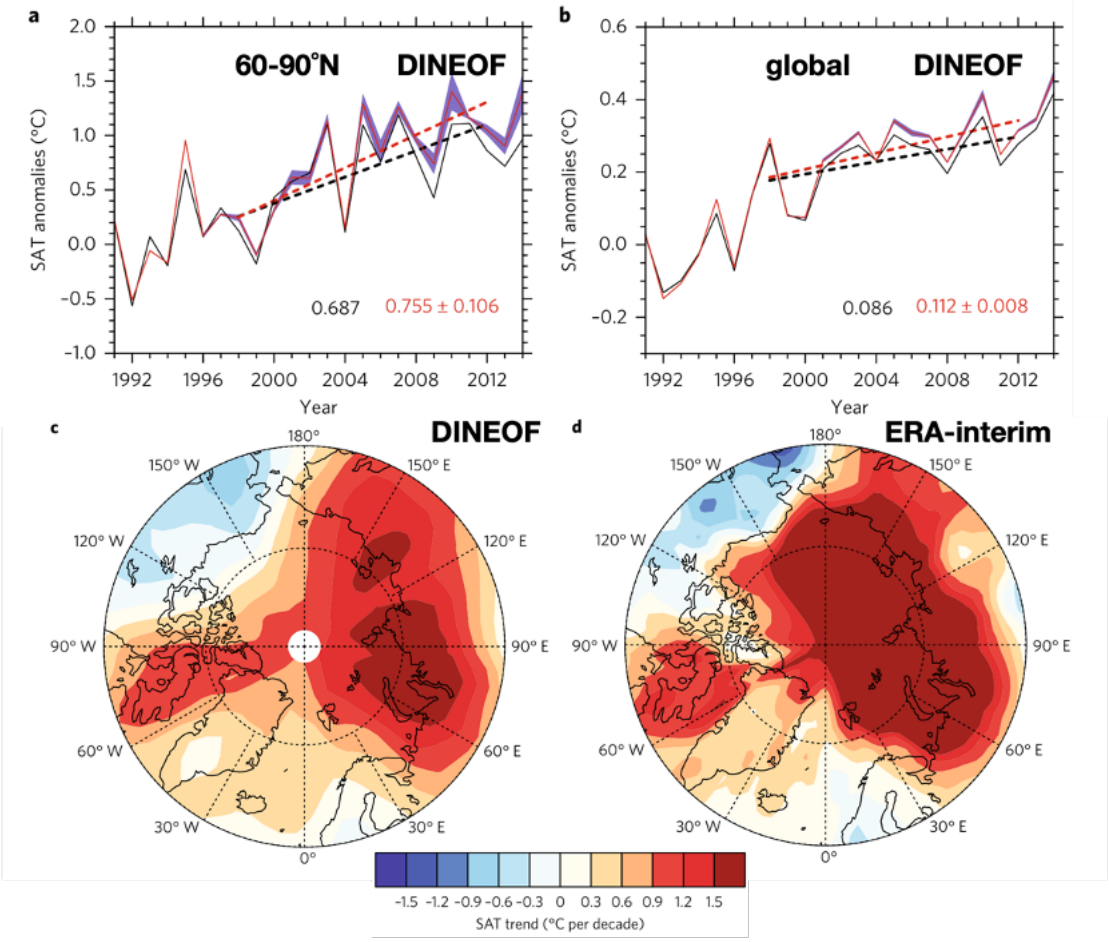

Figure 1.1 Surface air temperature (SAT) anomaly and its trend from 1998 to 2012 for a) Pan-arctic and Arctic regions (60–90˚N) and b) global area relative to 1979-2004. Linear trends of annual mean Arctic SAT using c) DINEOF or d) ERA-interim data over 1998–2012 (Huang et al., 2017).

Arctic amplification, the heightened increase in surface air temperatures in the Arctic, results from multiple interrelated factors. These darker surfaces have a lower albedo, meaning they absorb a higher proportion of solar radiation instead of reflecting it back into the atmosphere. This increased absorption of solar energy accelerates warming in the region (Perovich et al., 2007). Studies indicate that the reduction in albedo from 1982 to 2009 may have contributed to a 30% increase in solar absorption in the Arctic (Hudson, 2011). Also, accompany with the warming temperature, arctic algae become active and furthermore increase the albedo (Hotaling et al., 2021). Furthermore, the interaction between clouds and sea ice significantly related to the Arctic amplification (Linke et al., 2023). Cloud cover in the Arctic can have dual effects; on one hand, clouds can reflect solar radiation, which cools the surface. On the other hand, they can also trap

heat, contributing to warming particularly for lower solar radiation conditions. Cloud radiative effect over the Arctic likely varies seasonally (Shupe and Intrieri, 2004). Most studies agree that clouds have a warming effect during all seasons except summer. The warming is due to emission of longwave radiation by clouds, while cooling in summer is due to scattering of incoming shortwave radiation. Longwave warming dominates throughout the dark months in the Arctic, while shortwave cooling can only take place during summer when the sun is high and the snow has melted, lowering the surface albedo. The increased cloud cover substantially modulates diurnal temperature ranges using air temperatures data from 1951 to 1990 (Przybylak, 1999). This duality adds a layer of complexity to understanding cloud impacts on Arctic temperatures (Shupe and Intrieri, 2004). Moreover, there has been an increase in the northward transport of heat and moisture, further enhancing warming in the region (Rousi et al., 2022). As for the sea ice, the decreasing sea ice accompany with the land ice and snow and the increasing of the vegetation coverage, together changes the albedo of the Arctic regions (Hill et al., 2014).

1.1.2 Sea Ice Declining

Accompany with the ongoing Arctic amplification, the Arctic sea ice is experiencing dramatic declines across all seasons, posing significant implications for global climate and ecosystems (Stroeve and Notz, 2018). The acceleration of ice loss during the winter months is particularly concerning. This period, historically characterized by ice accumulation and stabilization, has seen a shift from a decrease of 2.4% per decade between 1979 and 1999 to a reduction of 3.4% per decade from 2000 onwards. This acceleration can be attributed to several factors, including higher global temperatures and increased CO2 emissions, which exacerbate the natural seasonal fluctuations of the ice cover (Stroeve and Notz, 2018). Meanwhile, summer Arctic ice extent has shown a nearly monotonic decline, losing about 24% per decade over the analyzed 40-year period. This decline in summer ice extent seems to be initiated by atmospheric circulation anomalies over the Arctic in late spring, with the ice-albedo feedback potentially amplifying the summer ice retreat. Arctic Ocean will become ice-free in August and September after an additional 800 ± 300 gigatons of CO2 emissions, using the prediction based on a linear extrapolation method. To see the ice disappear from July to October, an additional 1400 ± 300 gigatons of CO2 would be needed (Stroeve and Notz, 2018). Along with the

shrinking of the sea ice extent, the CMIP5 simulation showed a severer decreasing of sea ice at approximately 30% in the spring and summer seasons of 2100s (Zhang et al., 2020).

1.1.3 Permafrost Thawing

Permafrost refers to the ground that remains completely frozen for two or more consecutive years. It is predominantly found in the Northern Hemisphere, covering vast regions in Russia, Canada, Alaska, and Northern Scandinavia (Obu et al., 2019). As climate change intensifies, permafrost is increasingly at risk of thawing, which could release 1672 Pg of carbon and have profound environmental and economic impacts (Kuhry et al., 2013).

The primary driver of permafrost thaw is global warming, in particular amplified in arctic regions, which leads to increased air temperatures and changes in insulation properties of the ground cover (Torre Jorgenson et al., 2013). Research indicates that for every degree Celsius increase in global temperature, the northern permafrost limit is pushed 80 kilometers south (Biskaborn et al., 2019). This thawing is exacerbated by physical disturbances such as wildfires and infrastructure development, which can significantly alter the thermal balance of permafrost areas (Ueyama et al., 2020). Recent studies project that permafrost areas are at risk of decreasing by up to 35% by the end of the 21st century under a high greenhouse gas emissions scenario (Lawrence et al., 2015).

The thawing of permafrost has several critical environmental implications. Firstly, it leads to the release of greenhouse gases, including carbon dioxide and methane, which are trapped in the frozen soil. Studies estimate that the Northern Hemisphere permafrost contains twice as much carbon as the atmosphere (Schuur et al., 2015). This reduction in permafrost area is expected to contribute up to 1.69 gigatons of carbon annually to the atmosphere, further exacerbating global warming (McGuire et al., 2009). The release of these gases contributes further to global warming, creating a feedback loop that accelerates the thawing process (Zimov et al., 2006). Additionally, permafrost thaw destabilizes land, leading to severe geological disturbances like landslides and sinkholes (Grosse et al., 2013).

The thawing of permafrost poses significant challenges for infrastructure and society, particularly in Arctic regions. Buildings, roads, and pipelines that were constructed on stable, frozen ground are now at risk as the ground thaws and settles. The

cost of maintaining and rebuilding infrastructure in these regions is estimated to run into billions of dollars over the coming decades (Hjort et al., 2018). Furthermore, indigenous communities that rely on the permafrost for their traditional ways of life face disruptions to their habitats and livelihoods (Hassol, 2004). Moreover, permafrost traditionally acts as a barrier reducing radon exposure. However, accompany with the thawing of the permafrost, buildings with basements could experience radon levels over one hundred times the initial levels, exceeding the safe threshold of 200 Bq/m3 for up to seven years (Glover and Blouin, 2022).

1.1.4 Fire and Heatwave

Wildfires, often referred to as forest fires or wildland fires, are uncontrolled fires that occur in natural areas such as forests, grasslands, or prairies. These fires are a critical part of ecosystem dynamics and can be influenced by weather conditions, types of vegetation, and human activities (Chen et al., 2021; Jiao et al., 2021). Historically, wildfires have played a key role in shaping the structure and ecological function of many landscapes, but recent trends indicate a shift in their pattern and intensity due to climate change (Hu et al., 2015).

The Arctic is experiencing a significant increase in fire activity, which poses unique challenges due to the region's sensitivity to temperature and moisture changes (McCarty et al., 2021). Studies have shown that the Arctic tundra and boreal forests are particularly vulnerable, as these areas have historically been protected by their cold, moist climates that inhibit fire ignition and spread (Matt Davies, 2013). Historically, Arctic fires were rare occurrences, but records from the past few decades indicate an alarming increase in their frequency and scale (Box et al., 2019; Kharuk et al., 2022). This shift is largely attributed to rising temperatures and prolonged dry spells, which create conditions more conducive to fire (Hu et al., 2015). The thawing of permafrost, a typical feature in Arctic regions, also contributes to this trend by exposing previously frozen organic fuels to combustion . The current state of Arctic fires has been documented with increasing concern in recent years. For instance, the year 2019 witnessed unprecedented wildfires across the Arctic circle, affecting vast areas of Siberia, Greenland, and Alaska. These fires not only resulted in significant carbon emissions but also led to habitat destruction and adverse air quality impacts (Mack et al., 2011). Remote sensing data and satellite imagery

have been pivotal in tracking these changes, revealing that the area burned in recent years is far greater than historical averages (Figure 1.2) (McCarty et al., 2021). Looking towards the future, projections indicate that Arctic fire regimes may continue to evolve in response to global warming (McCarty et al., 2021), release of stored carbon from burning vegetation and permafrost (Kuhry et al., 2013).

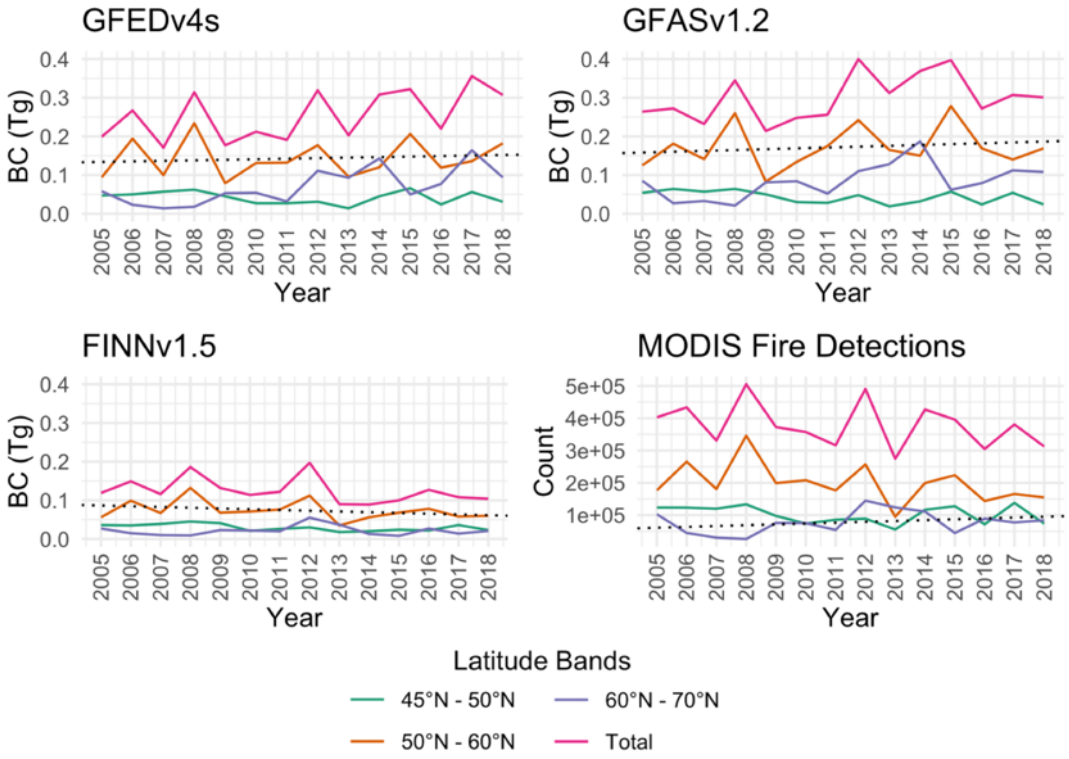

Figure 1.2 Annual black carbon (BC) emissions and annual fire activity from the MODIS Collection 6 active fire product at latitude-bands during 2005–2018. The dotted lines for each product are the positive trend for Pan-arctic and Arctic regions from 60 to 70˚ N (McCarty et al. 2021).

Heatwave is another threaten to the Arctic environment and is characterized by temperatures that are significantly above average for the region and season. Such events are becoming more frequent, intense, and prolonged, contributing to unprecedented changes in the Arctic environment (Johannessen et al., 2004). For example, heatwave duration has expand from part of centeral Siberia regions in 1980s to the high laitutde Eruasia regions, Greenland and high latitude North Ameria in 2010s (Figure 1.3) (Dobricic et al., 2020). Moreover, Arctic heatwaves impact weather patterns beyond the region. They can alter the jet stream, leading to unusual weather conditions in the mid-latitudes, such as prolonged cold spells or intense heatwaves (Zhang et al., 2020). The

more-persistent jet stream was considered to cause the increasing trend of heatwaves across Eurasia regions, especially for regions located in Europe (Rousi et al., 2022), combined the factors of shrinking of sea ice and snow covers (Zhang et al., 2020).

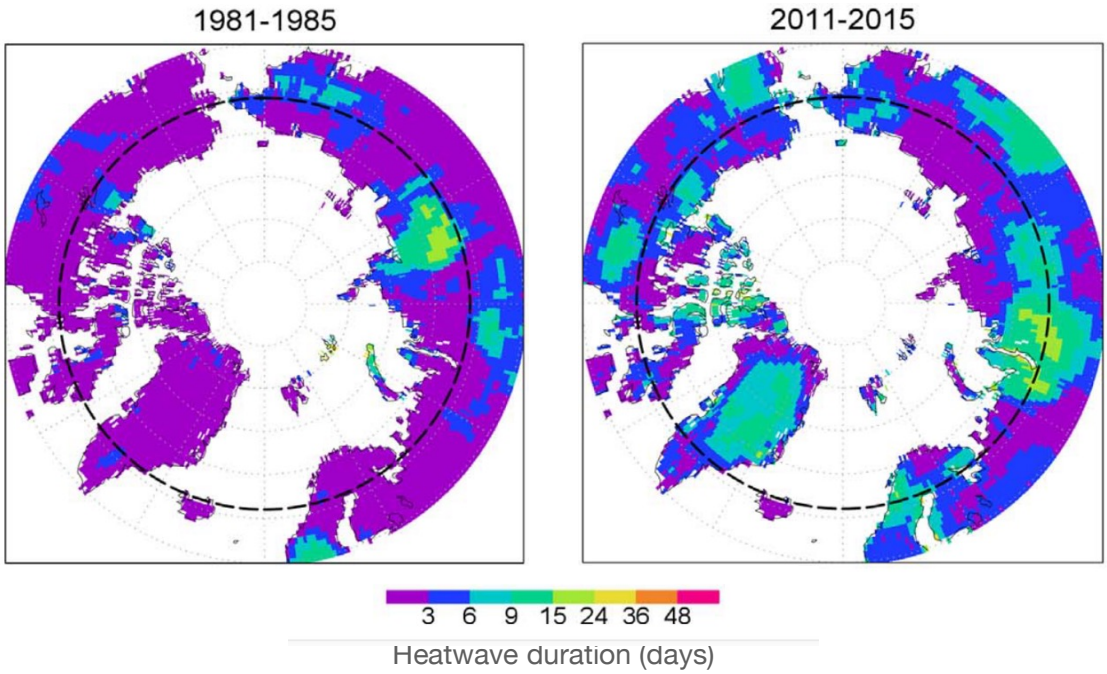

Figure 1.3 Heatwave duration in the high latitude areas using heat wave magnitude index (HWMId) in two pentad years. (Dobricic et al., 2020)

1.1.5 Change of Ecosystem and Carbon Budget

Research indicates that Arctic amplification significantly affects the Arctic ecosystems. Such influence impact the targets like terrestrial vegetation and soil biomes. The increasing of the vegetation photosynthesis that simulated by LPJ-GUESS - a dynamic global vegetation model (DGVM), is align the increasing lead area index (LAI) indicated by MODIS observations (Miller and Smith, 2012). Such increasing of the vegetation that was indicated by increasing of Normalized Differential Vegetation Index (NDVI) or LAI was also reported in various studies (Box et al., 2019). Also, the temporal pattern of the vegetation showed an earlier greening in the early Springs (Miller and Smith, 2012), although improve the annual gross primary production (GPP), however, do not contribute carbon update align to the length of the growing season in heatwave events (Bastos et al., 2020). The change of the vegetation pattern also changed the surface albedo (Miller and Smith, 2012), which can increase the input energy and feedback to the Arctic

amplification (Hill et al., 2014). As a result, leading to severe the global warming. On the other hand, the warmer soils and thawing permafrost leads to increased microbial activity, which accelerates the decomposition of organic matter, releasing more carbon into the atmosphere. It is because that respiration of the soil biome is sensitive to temperature as an exponential relationship to the temperature (Kruse and Adams, 2008). As indicated by (Lee et al., 2024), the respiration will increase accompany with the increasing temperature in Arctic regions at approximately 0.2 $gC/m^2/d$ by 1 ˚C temperature increasing. The ability of terrestrial ecosystems to absorb carbon relies on the balance between GPP and respiration. In scenarios where both GPP and respiration rise due to global warming and Arctic amplification, these ecosystems could shift from being current carbon sinks to future carbon sources if respiration increases more rapidly than GPP. The arctic region under historical estimation is showing an increasing pattern align to the GPP, or for future prediction under different scenarios, showing uncertainty as nonparallel patterns or decreasing trends (Chaudhary et al., 2022). For example, under strong emission of anthropogenic carbon, the arctic will lose its character as carbon sink reservoir and become carbon neutron (Chaudhary et al., 2022).

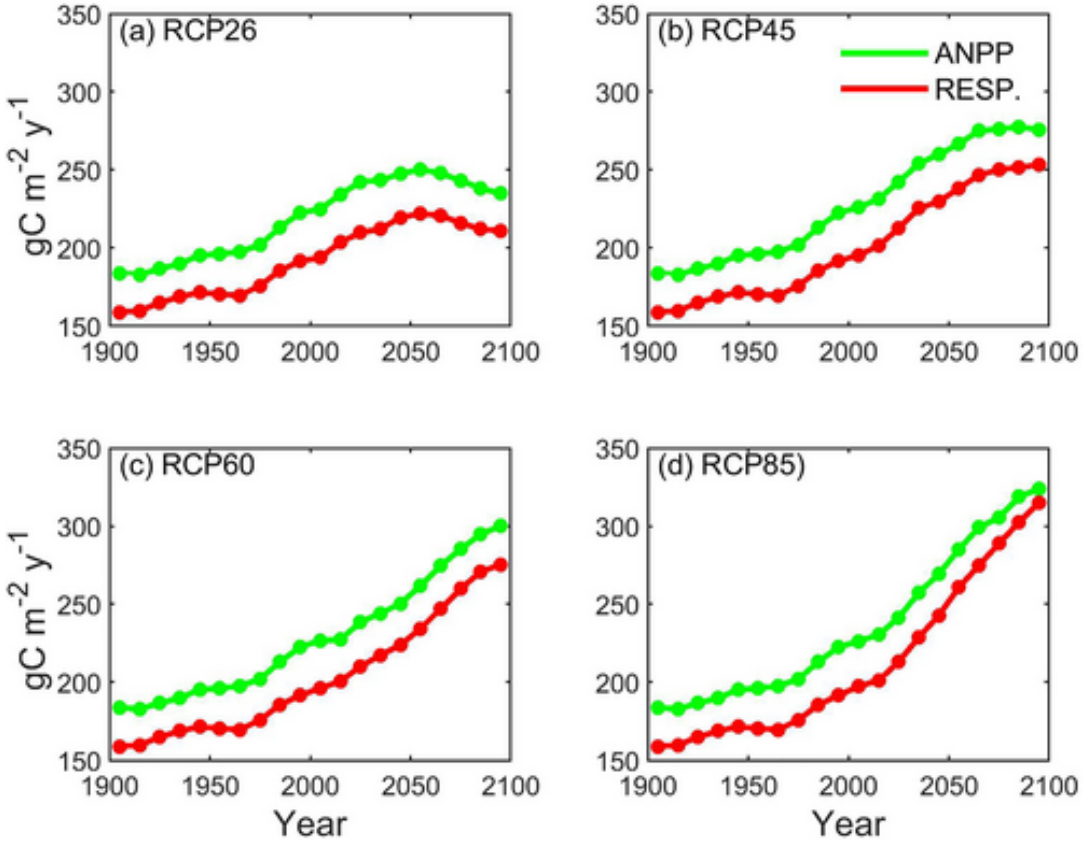

Figure 1.4 Modeled net primary productivity and respiration rates across pan-Arctic (peatland as the case) under different warming scenarios (ANPP—Annual net primary production, the absorption by plants and RESP—Annual heterotrophic respiration, the decomposition by biome). The difference of ANPP and RESP represents the ability of carbon absorption by ecosystem. (Chaudhary et al., 2022).

1.2 Temperature Observations at Arctic and Pan-Arctic Regions: Comparing Air Temperature and Land Surface Temperature

Temperature observations from a range of sources are crucial for tackling the issues and challenges highlighted in section 1.1 concerning the Pan-Arctic and Arctic regions. These observations are essential for gaining a deeper understanding of Arctic amplification and changes in ecosystems. Specifically, these temperature measurements help in comprehending the extent and intensity of changes over time and across different locations. By analyzing how temperature varies over periods and different areas, researchers can better understand the patterns and impacts of environmental changes in these sensitive regions.

1.2.1 Air Temperature Observations

Air temperature (Ta) is the most widely used physical quantity to poses temperature changes or used for processes calculation. It requires the direct measurement by exposing the probe to contact the air using various kinds of thermometers or digital sensors. Such station measurement is limited to its representativeness (Koutroumanou-Kontosi et al., 2022), however, for many analyses, grid data is required to show the spatial distribution (Bounoua et al., 2000). Converting station-measured air temperatures to grid-based datasets typically involves interpolation methods. Temperature values at unsampled locations based on known values from weather stations using spatial interpolation including inverse distance weighting (IDW), kriging, and spline interpolation (Hijmans et al., 2005; Kilibarda et al., 2014), and temporal interpolation into daily, monthly, or even hourly temperature data which support more detailed climate analysis (Haylock et al., 2008)

The method to create grid Ta was influenced by the distribution density of the stations (Hofstra et al., 2010; Njoku et al., 2023). Particularly, station-based observation in arctic region faces more challenges. One of the primary issues in Arctic air temperature observation is the deployment and maintenance of meteorological instruments. Instruments often fail due to extreme cold, icing, and exposure to harsh weather conditions. For example, thermometers and other temperature sensors can give inaccurate readings if ice forms on them or if they are exposed to direct sunlight, on the first case blocking the energy exchange with the environment and latter included extra energy incoming (Teichmann et al., 2024). Additionally, the albedo effect of snow and ice can lead to higher readings under sunny conditions, thereby introducing further biases into temperature records (Musacchio et al., 2021). Secondly, the spatial distribution of temperature monitoring stations in the Arctic is uneven, leading to significant gaps in data, especially in the more remote and inaccessible areas (Rawlins and Willmott, 2003). For instance, the majority of existing stations are located near coastal areas or research facilities, which do not adequately represent the vast interior regions of the Arctic (Buch et al., 2019). Furthermore, temporal coverage issues arise as many stations do not operate

year-round due to the severe winter conditions, thus limiting the continuity of the datasets (Romanovsky et al., 2010).

1.2.2 Land Surface Temperature Observations

Land Surface Temperature (LST) represents the Earth's surface's heat emission and is vital for various scientific and environmental applications (Li et al., 2013). LST is the thermodynamic temperature of a thin layer in the interface between soil, vegetation or other surface components and the atmosphere and in some cases defined as skin temperature (Z. Li et al., 2023). It is an indicator of the energy and water exchange between the land surface and atmosphere, and has been applied in various fields to study various subjects, for example, the surface energy balance (Rocha and Shaver, 2011), the urban heat island effect (Yamamoto and Ishikawa, 2018), surface soil moisture (SM) and evapotranspiration (ET) estimations (Zhan et al., 2014), and permafrost monitoring (Westermann et al., 2011).

Unlike air temperature, LST measures the radiative temperature of the land surface. LST is mainly retrieved from the digital data recorded by thermal infra-red (TIR) sensors or passive microwave sensors (Li et al., 2013). These sensors are onboard the remote sensing platforms including the fixed towers, aerial platforms and satellites (Malbéteau et al., 2018; Westermann et al., 2011). Thermal infrared (TIR) satellite sensors enable cost-effective LST retrieval over large areas with higher spatial and temporal resolutions relative to ground measurements. The satellite-based LST observation has started from 1960s, the first operational steps towards satellite-based environmental monitoring were taken with NASA’s TIROS-1. This satellite was equipped with infrared sensors capable of capturing data on weather patterns and surface temperatures, paving the way for the use of space-based infrared observations in meteorology. The launch of the NOAA satellite series in the 1970s introduced the Advanced Very High Resolution Radiometer (AVHRR), which provided detailed global temperature data crucial for climate studies and vegetation monitoring (Ma et al., 2020; Nemani et al., 2003a). These advancements facilitated widespread scientific research into global environmental phenomena, significantly enhancing our understanding of Earth's atmospheric conditions. The contribution of the AVHRR was it provided continuous LST record from 1970s to 2000s (Ma et al., 2020). On the next stage, the introduction of NASA's Terra and Aqua satellites

in the late 1990s and early 2000s, equipped with the MODIS instruments, marked a significant leap in the quality and utility of LST data (Coll et al., 2005). These instruments offered enhanced temporal resolution, critical for accurate climate monitoring and environmental management. Concurrently, the Landsat program, a collaborative effort by NASA and the USGS, continued to provide invaluable high spatial resolution data, supporting detailed studies of urban heat islands and localized environmental monitoring (Xin et al., 2013). In recent years, initiatives like the ESA's Copernicus program, particularly through its Sentinel satellites, have underscored the importance of integrating LST data with other environmental indicators by SLSTR on Sentinel-3A or Sentinel-3B (Yang et al., 2020). Moreover, scientists have more attention on geostationary Earth orbit (GEO) satellites for LST observations, that were originally designed to meteorological observation purposes. The sensors on these satellites can provide LST at 10–30 min revisit, thus, could depict the LST character that changes at times of the day (Yamamoto and Ishikawa, 2018). These aforementioned sensors have provided the wide observations at 100m to 1000m spatial resolution, higher than gridded Ta data that at tens of kilometers, for example the ERA5 temperature data at 25 km resolution and MERRA-2 temperature data at 0.5˚x0.625˚grids.

In summary, LST data, with its higher spatial resolution and ability to be retrieved remotely, plays a vital role in monitoring and understanding the changing climate of the Arctic and Pan-Arctic regions. It provides valuable information for climate modeling, extreme event analysis, long-term temperature trend quantification, and land cover change detection, complementing the Ta data recorded globally over long periods (Muster et al., 2015; Rocha and Shaver, 2011; Westermann et al., 2011; Williamson et al., 2014; Zhan et al., 2014).

1.3 Introduction of Sub-daily Studies and Related Potential Applications

Sub-daily LST data are pivotal for calculating mean daily LST and understanding processes within hydrological, energy, and carbon cycles at a sub-daily scale (Bodesheim et al., 2018; Q. Wang et al., 2021). A previous study has shown a 2°C discrepancy in daily mean LST calculation employing one daytime and one nighttime LST measurement compared to *in situ* observations. It can be mitigated using sub-daily LST derived from

the combination of the annual temperature cycle (ATC) and diurnal temperature cycle (DTC) models (Hong et al., 2022). Additionally, the diurnal surface temperature of water bodies revealed underground water exchange (Irvine et al., 2017), and hourly LST has been used in evapotranspiration (ET) modeling at hourly or daily temporal scale to understand the local hydrology and droughts (Geng et al., 2022; Young-Robertson et al., 2018). The daily maximum LSTs can be better captured using more observations within a day along with its centroid (X. Li et al., 2023). The extreme high daily maximum LSTs often accompanied by drought, suppress photosynthesis in vegetation and promote ecosystem respiration (Huang et al., 2015; Yamamoto et al., 2023). For example, the photosynthetic response to the DTC behave different heatwave stress during heatwave days and normal days, estimated from the Advanced Himawari Imager onboard Himawari-8, a geostationary earth orbit (GEO) satellite (Xiao et al., 2021) or from Advanced Baseline Imager (ABI) on Geostationary Operational Environmental Satellite (GOES) satellites (X. Li et al., 2023).

Intraday LST data can be valuable for high-latitude regions, though several challenges and opportunities for improvement exist. GEO satellite observations are limited to lower latitudes, typically between 60°S and 60°N, making it challenging to obtain data for high-latitude areas (Figure 4a) (Freitas et al., 2013; Wang et al., 2020). In contrast, polar orbiting satellite on low Earth orbit traverse high-latitude regions in the Arctic or Antarctic regions at approximately 3h intervals (at Polar center 1.5h) or over 20 times per day (with varying intervals) (Chen et al., 2020; Ciappa et al., 2012), enabling high temporal LST observations in the high-latitude regions (Figure 1.4b).

Previous studies have left some issues and unclear aspects regarding the utilization of polar orbiting satellites to achieve sub-daily LST. Firstly, the daily mean LST showed a large bias at high latitude sites using the bidaily LST product from MODIS with DTC and ATC models. This issue was caused by the larger fluctuation of overpassing time in bidaily LSTs at high latitudes (Hong et al., 2022). It can be mitigated using the extra swath LSTs. Secondly, the performance was not discussed between swath LST used to produce bi-daily products (termed as ‘bi-daily LST’) and those that were not (termed as ‘extra LST’) in high latitude regions (Wan, 2014). Finally, the examination of LST observation frequency across different latitudes is lacking, which is crucial for a deeper understanding of original LST data in high latitude regions.

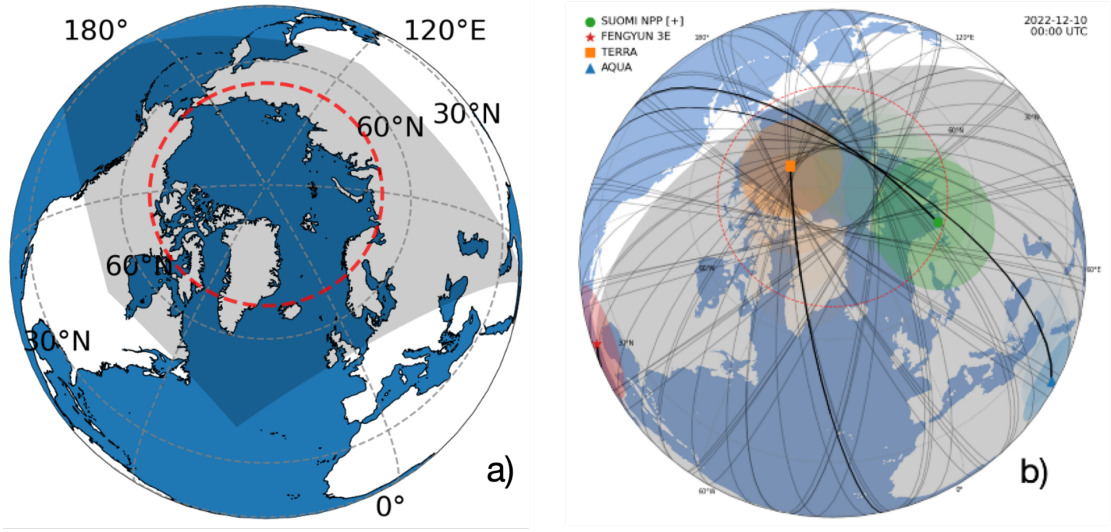

Figure 1.5 a) 3rd GEO satellite coverage where VZA lower than 60˚ using Himawari-8, FY-4A, GOES-16, GOES-17, and Meteosat Third Generation (MTG-I1). The shadowed area represents the high latitude regions cannot be covered by these GEO satellites. b) The orbit track simulation result using two-line element (TLE) for Terra, Aqua, SNPP and FY-3E. The black lines represent the orbit within the example date and the colored markers with the corresponding circles represent the swath size of the thermal band sensors.

1.4 Research Objective and Research Content of This Thesis

In this study, exploring the diurnal pattern and applications of satellite-based quasi-hourly LST monitoring at Arctic and Pan-arctic regions using polar orbiters was the main goal of the thesis. Here, two scientific question was raised and further explored. The first one is, can hourly LST be constructed in high-latitude regions? Particularly, the scope is on using satellite original observation without the integrating models or spatiotemporal interpolation, because the original LST observation provided the basic most information and regulate these advance approaches. On this question, since LST is a time variant variable, two dimensions are important, the first is the time of the observation and another is the corresponding value. For the first issue, if the observation is even distributed at the hours within a day, it can better capture the daily variation well with less losing of the detail, for example, at the early morning that LST climbs fast and the late afternoon that LST starts decreasing with a cooling curve. As for the second issue, the consistency between satellite-based LST and the ground truth. It is necessary to understand the biases and accuracy of these products as providing a quasi-hourly LST at an acceptable

performance. The second question is, how this hourly LST help improving the understanding of Arctic carbon budget? As the carbon budget was regulated by temperature, especially, under the trend of a fast temperature rising, the temperature measured at higher temporal resolution can be integrated and reflect a more reliable estimation. Two main components, except the disturbance, come to the mind, including GPP (Gross Primary Production) and ecosystem respiration. Comparing to the GPP which mainly influenced by solar radiation and aboveground biomass, ecosystem respiration is more sensitive to temperature, is expected to benefit from the hourly LSTs. In this thesis, the improvement to the ecosystem respiration integrating the hourly LST that was constructed and validated in Chapter 2 and 3, was discussed in the Chapter 4.

In the Chapter 2, The observation frequency using swath data and multiple polar orbiting satellites were discussed. The content in Chapter 2 highlighted the comprehensive analysis on observation frequency against latitude which was not well addressed in previous studies. Furthermore, to expand the applicability of hourly LST to entire Arctic and Pan-arctic regions, the new observations at the unique dawn-dusk (early morning) orbit were first integrated. One scenario using MODIS, VIIRS and the other included additional FY-3E showed the viability of constructing quasi-hourly LSTs over the Arctic and Pan-arctic regions. Meanwhile, two scenarios by combining different platforms were given and their limitation were discussed. Application of the hourly LST to the Verkhoyansk 2020 heatwave showed its applicability of monitoring and understanding the diurnal LST changes at this extreme event. Also, applying the hourly LST to Alaska showed the LST spatiotemporal response and influence to other meteorological parameter or ecological parameters at hourly scale. These results provided the applicability of the hourly LST to the research scope and the fundamental information of the dataset in the Chapter 4.

In the Chapter 3, the dataset that introduced in the Chapter 2 were constructed if for achieving its availability, for example, the LST data for FY-3E platform, that works on a unique dawn–dusk orbit, was still a new platform and the data in 2022 was not available. This thesis included the content that first reveals the viability of applying a temperature and emissivity separation (TES) method to the thermal band sensors on FY-3E. Additionally, the performance of FY-3E LST was intercompared with performance of LST from geostationary satellites, and the against performance of LST widely used

MODIS and VIIRS. This thesis synthesis the multiple evaluation approach for understanding the LST of satellite on dawn-dusk orbit. The processes for building the LST was within the discussion under a scientific research framework, for example, the uncertainties analysis when building the LST algorithm. After the construction of the LST algorithm with the new model parameters determined for the new FY-3E platform, the product was comprehensively evaluated using ground-based observations and inter-compared with the LST products from GEO platforms. Meanwhile, the evaluation was conducted to MODIS and VIIRS for understanding their performances against FY-3E, particularly, important when combining these products together to construct the quasi-hourly LSTs. These evaluation results provided the reasonability and the understanding of the uncertainties of using quasi-hourly LSTs which were used in the Chapter 4.

In the Chapter 4, the content can be separated into two steps. First, the estimation of the daily mean LST using quasi-hourly LST constructed in Chapter 2 and Chapter 3. Second, using the estimated daily mean LST to estimate the ecosystem respiration at a daily temporal resolution. For the first part, an ensembled approach was used as the extension of a previous study that only relied 4 observations from MODIS on Terra and Aqua. Also, to achieve a seamless daily LST variation, the LST was linearly interpolated and smoothed. The result showed that adding FY3E LST observations improved estimation for LST before and after interpolation. This emphasis the improvement by adding more observations. For the second part, the daily mean LST replace the nighttime LST which was widely used in the semi-empirical models. As the nighttime LST have risk of drifting at Arctic regions, using the daily mean LST values may help making a better estimation. By using the different model combinations, the best model showed a RMSE approximately 1.29 gC/m2/d over the validation sites while the nighttime LST based estimation showed a worse RMSE at approximately 1.67 gC/m2/d. Additionally, the temporal variation of the ecosystem respiration using daily mean LST as input showed more detail compared to the estimation using nighttime LST. These results suggested the potential for further developing the quasi-hourly LST in case of Arctic environmental monitoring.

The Chapter 5 is the discussion for the whole thesis, including the discussion of the limitation and future perspectives. The final chapter, Chapter 6, gives the summary and conclusion of this thesis.

Chapter 2 Observation Frequency of LST in High Latitude Regions

2.1 High Temporal Frequency Observation using Polar Orbiting Satellites

To achieve the high observation frequency in high latitude regions, w satellites were more suitable than GEO satellites (Figure 1.4) because of the geometry limitation. Another alternative was the satellite in other orbit such as Molniya orbit. For example, using Molniya orbit platforms like Arktika-M series (Frolova et al., 2022), which have longer duration (Around 12 h) over the designed location, could provide continuous hovering over high latitude areas. By using two of the platforms at different crossing time, it enables the all-day observation at high latitude regions. There are two limitations when using this solution: The first one is that we have limited satellites on this orbit and those open to public is still not launched; Another is the Molniya orbit satellite have a higher orbit altitude at the target regions, and as a result have spatial resolution will be limited to several kilometers (e.g. Arktika-M1 TIR have a 4 km NADIR resolution). Thus, to achieve high spatial resolution, polar orbit satellites is the best choice.

There are three key points for achieving high observation frequency observations. The first one is the utilization of swath data. Polar orbiting satellites transvers the polar pole approximately every 90 minutes (Paek et al., 2020), thus, within one day have largest 16 crossing around the pole. This represents the maximum observation frequency of the orbit. When the latitude became smaller, the latitude circle become larger as the swath of the satellite is fixed, thus, result in a decreasing possibility of crossing, which represent the observation frequency. The second point is combination of data from different platforms. It is easy to understand that adding one more satellite will increase the observation frequency. However, simply adding satellites do not make sense because the LEO polar orbiters are commonly with the equatorial crossing time (ECT) at morning or afternoon. In that case, the MODIS and VIIRS, that two most widely used platforms with extensive product line providing the data that relevant to atmosphere, land and ocean. Besides, after the availability of the data from FY-3E, that have a stable and unique ECT at dawn-dusk, that may provide the external data different from MODIS or VIIRS at

afternoon or morning. The final one is that the polar orbit should have ground track over Pan-arctic or arctic regions. An opposite example was the ECOSTRESS on the ISS. Although studies have shown the variation of the changing timing of LSTs on ECOSTRESS can be used to composite the diurnal changes using monthly observations (Figure 2.1) (X. Li et al., 2021), the maximum latitude of the ground track is lower than 60 ˚N, thus not qualified for the application to the desired goal.

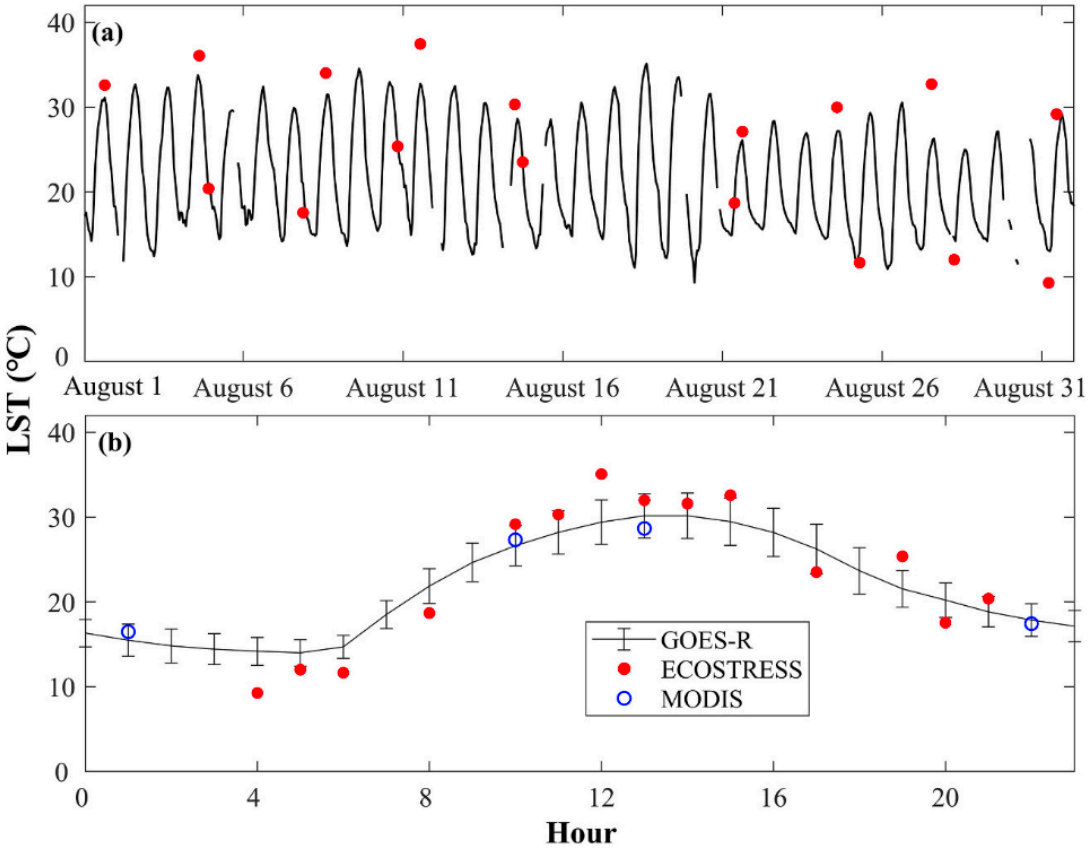

Figure 2.1 Diurnal cycle of LST at an observation site (US-Bi2) during August 2018. (a) shows the LST retrived from GOES-R (GOES-16) and ECOSTRESS from August 1 to August 31 in 2018; (b) shows the hourly averaged LST dirunal cycles during August: GOES-R provides hourly LST; MODIS provides LST at only four times of the day; ECOSTRESS measures LST with 70 m spatial resolution at different hours by stacking observation at different days (X. Li et al., 2021).

2.2 Method for Achieving High Observation Frequency

2.2.1 Basis on Sun-Synchronous Orbit (SSO) Revisit Simulation

The revisit frequency of SSO can be easily simulated under several assumptions. The assumptions were given as following: 1) The ideality of the Earth surface terrain and orbit shape. Earth can be modeled a regular spherical surface and SSOs are regular circles with eccentricity equals zero. 2) The ideality of observation conditions. Gaps in the line scans were not considered and no drift or fluctuation of the orbit. 3) The swath edges are parallel to the center ground track and each other. The projection will look like a belt on the earth surface. The relationship of this belt and pole has general two geometry condition and will result in the different behavior near the polar pole. Since the SSO was central symmetry with the earth's rotation axis and the research interest was in the north hemisphere, the north pole was used for explanation and fit the scope of this study. The two cases include one that the north pole aside the satellite track swath. In this case, the satellite usually has a narrow swath or large inclination that can never capture the observation at the north pole (Figure 2.2a). This condition always occurred when the swath of the sensor on the platform is really small. Another one is that the north pole lies between the tracks of satellite swath (Figure 2.2b). In this case, the satellite swath will certainly cover the pole. And this condition is for most of the satellites for environmental purposes, such as MODIS on Terra and Aqua and VIIRS on SNPP.

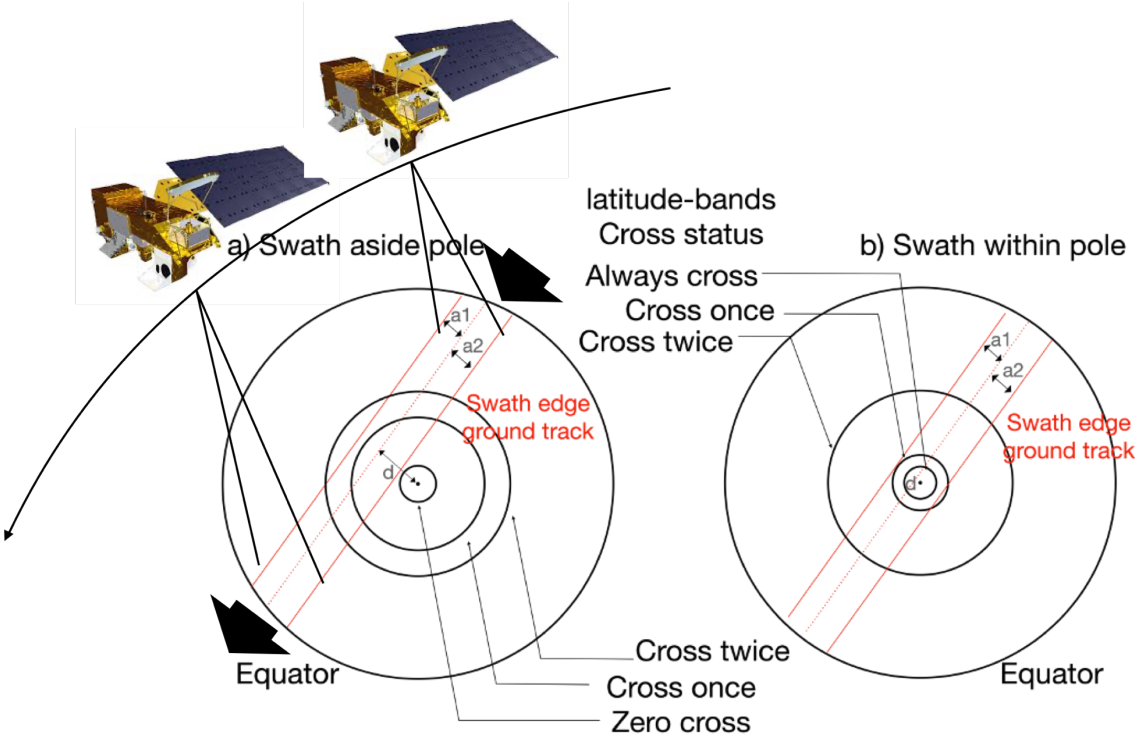

Figure 2.2 Conception of geometry condition of different orbit where a) assumes the north polar pole is always outside the swath; b) the north pole is inside the swath. The circles represent the small circle of the corresponding latitude bands.

Based on the prerequisite assumption and modeling, the revisit frequency can be modeled using math formulas as follows for the two different conditions a) and b) in Figure 2.2. The revisit frequency at the latitude-band was modeled as the expectation of the coverage of the whole latitude circle. Here, the basic geometry calculations and Kepler's law were used for such calculation as following:

General formula:

$$d = R \times \cos(\beta) \tag{2-1}$$

where J is the solution of

$$\begin{cases} J^2 + (H+R)^2 - 2J(H+R)\cos(\alpha) = R^2 \\ (\mathrm{H}+\mathrm{R})^2 > \mathrm{J}^2 + \mathrm{R}^2 \end{cases} \tag{2-2}$$

$$a_1 = H \times \cos(\beta) + J \times \sin(\alpha + \beta - 0.5\pi) \tag{2-3}$$

$$a_2 = d - R \times \cos(\alpha + \beta) \tag{2-4}$$

$$L = R \times cos(\theta) \tag{2-5}$$

a) north pole aside ($\beta + \alpha < \frac{\pi}{2}$):

$$\alpha_1 = \sin^{-1}(\frac{a_1 + d}{L}) \quad (2-6)$$

$$\alpha_2 = \sin^{-1}(\frac{d - a_2}{L}) \quad (2-7)$$

$$cr = \begin{cases} \frac{\alpha_1 - \alpha_2}{2\pi} (L > a_1 + d \; two \; edge \; crossing) \\ 0.5 - \frac{\alpha_2}{\pi} \; (L < a_1 + d \mid L > \; d - a_2 \; one \; short \; edge \; crossing) \\ 0 (L < \; d - a_2 \; complete \; aside) \end{cases} \quad (2-8)$$

b) north pole within ($\beta + \alpha > \frac{\pi}{2}$):

$$\alpha_1 = \cos^{-1}(\frac{a_2 - d}{L}) \quad (2-9)$$

$$\alpha_2 = \cos^{-1}(\frac{a_1 + d}{L}) \quad (2-10)$$

$$cr = \begin{cases} \frac{\pi - \alpha_1 - a_2}{\pi} (L > a_1 + d \; two \; edge \; crossing) \\ 1 - \frac{\alpha_1}{\pi} \; \left(L < a_1 + d \; \middle| \; \& \; L > \; a_2 - d \; one \; long \; edge \; crossing\right) \\ 1 (L < \; a_2 - d \; complete \; wittin) \end{cases} \quad (2-11)$$

For both cr:

$$T = 2\pi \times \left(\left(\frac{\left((R + H) \times 1000\right)^3}{3.986004418 \times 10^{14}} \right)^{0.5} \right) \quad (2-12)$$

$$f_{revisit} = \frac{24 \times 60 \times 60}{T} \times cr \quad (2-13)$$

where α is the maximum field of view (FOV) regarding the angle to the swath; β is the orbit inclination; H is the orbit altitude and the unit is km; R is the radius of Earth and the unit is km; θ is the latitude of the crossing latitude-band for calculating the crossing ratio; cr is the crossing ratio, represent the ratio of crossing length to latitude-band circle, ranging from 0 to 1; cr equals to 0 represents that the ground swath of the satellite can never captured the observation at the given latitude and cr equals 1 represents that ground swath will capture the observation at the latitude given a certain period (the period of the

spacecraft); T is the one round period of the orbit and the unit is second (e.g. MODIS is approximately 90 min=5400 s); $f_{revisit}$ is the revisit time per day as the modeled observation frequency at the given latitude for the specific platform with given characters of the onboarded instrument.

The geolocation data of satellites including MODIS on Terra and Aqua, VIIRS on SNPP and was used as comparison to the simulation which is detailed described in the next chapter. The simulation of FY-3E, Terra, Aqua, and SNPP is using the following information (Table 2.1). The inclination for each platform was calculated using the character of SSO, which is determined by the following equation (Paek et al., 2020):

$$\beta_{SSO} = \cos^{-1}\left(-\left(\frac{H+R}{12352}\right)^{3.5}\right) \qquad (2-14)$$

where H and R are the altitude of the orbit and the radius of the earth given in the unit km, similar to ones in steps for calculating the revisit time.

Table 2.1 Simulation property of each platform (assumes exact SSO without drift)

Platform	Inclination (˚)	Max FOV (˚)	Height (km)
FY-3E	98.7	55.4	836
SNPP	98.79	56.28	834
Terra	98.2098	55	709
Aqua	98.2098	55	709

2.2.2 Observation Frequency Using MODIS and VIIRS (Scenario-1, AM, PM)

The observation frequency attributable to polar orbiting satellites was systematically quantified across specified latitude bands (e.g., 45°N–46°N, 46°N–47°N, ..., 84°N–85°N) and at the locations of the 49 flux towers (Figure 3.38). At the fixed locations of the 49 towers, the maximum observation frequency was calculated under both all-sky (based on geolocation data) and cloud-free conditions (ascertained from LST QA data under cloud-free scenarios) throughout the summer of 2013. Finally, the profiles of observation frequency at individual local solar time and different latitude-bands were retrieved. Furthermore, three sites (RU-Cok, US-Prr, and CA-SCC) at different latitudes were used to demonstrate sub-daily LST variation.

The analysis revealed a clear increasing trend with latitude in daily satellite observation frequency. Specifically, the frequency approximately triples from 8 times daily at 45°N to 23 times at 70°N (Figure 2.3a). The slope is gradually increasing between 45–70°N, with a turning point near 70°N. There's an immediate drop in the slope, followed by a subsequent climb. The observation frequency trends against latitude for individual satellites were the same between MODIS and VIIRS. Additionally, VIIRS SNPP provided a higher observation frequency than either MODIS Terra or MODIS Aqua at each latitude-band.

The observation frequencies under all-sky conditions at specific sites mirrored the observation frequency trend when compared to the average for their respective latitude bands (solid black line, Figure 2.3b). However, the observation frequency under cloud-free conditions did not always align with the potential observation frequencies for the latitude bands, especially for sites such as US-A10, GL-Zaf, and SJ-Adv. For instance, at US-A10 (a coastal site and highlighted as an outlier in Figure 2.3b), the maximum number of cloud-free observations during the study period was roughly 12 times per day, significantly less than the potential maximum of 23 times at its latitude (approximately 70°N).

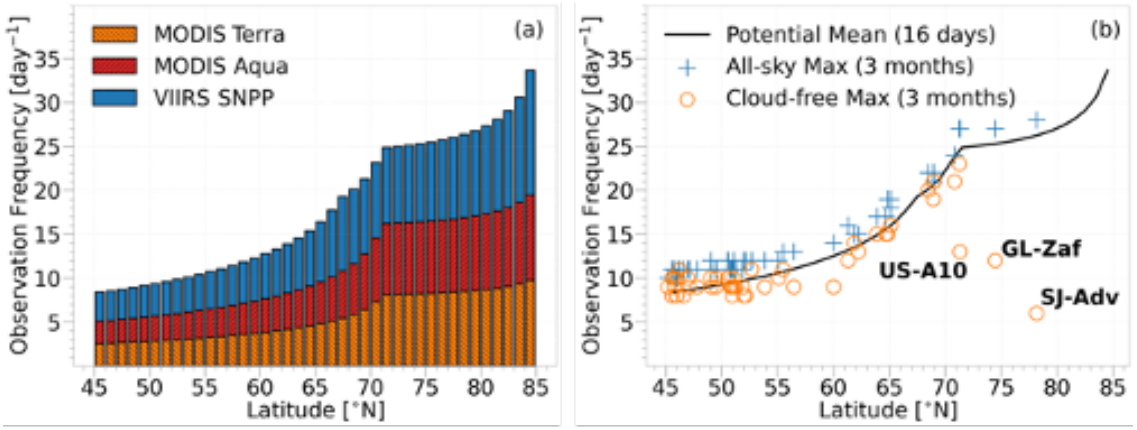

Figure 2.3 (a) Latitude band-averaged distribution of all-sky observation frequencies by each sensor-satellite and (b) observation frequencies for all-sky and cloud-free conditions at the in situ observation sites. In (b), the solid line represents the potential mean observation frequency, with the same data as (a). The markers represent the maximum observation frequency in 3 months at 49 individual sites.

A near-hourly observation frequency for LST was attained at the northerly sites, exemplified by RU-Cok, situated above 70°N (Figure 2.4a). On this site, the intervals

between satellite observations were less than 3 hours, achieving up to 23 observations on August 13th (Figure 2.4d). At lower latitude sites, the observation frequency decreased, and two larger observation gaps occurred. The frequency of observations diminished at US-Prr–a site with lower latitude compared to RU-Cok. On August 25th, US-Prr registered 15 observations, fewer than those recorded at RU-Cok (Figure 2.4d). Particularly, larger gaps between observations were noted during the late afternoon (Figure 2.4e). At a further south site - CA-SCC, 13 observation with two pronounced gaps in observation times were found, mirroring the gaps at US-Prr (Figure 2.4f).

However, the task of amalgamating different LST datasets to reduce biases presents complexities. For example, at 0:00–4:00 and 10:00–14:00, VIIRS over-estimated LST at CA-SCC, whereas it under-estimated LST at RU-Cok (Figure 2.5, Figure 2.6).

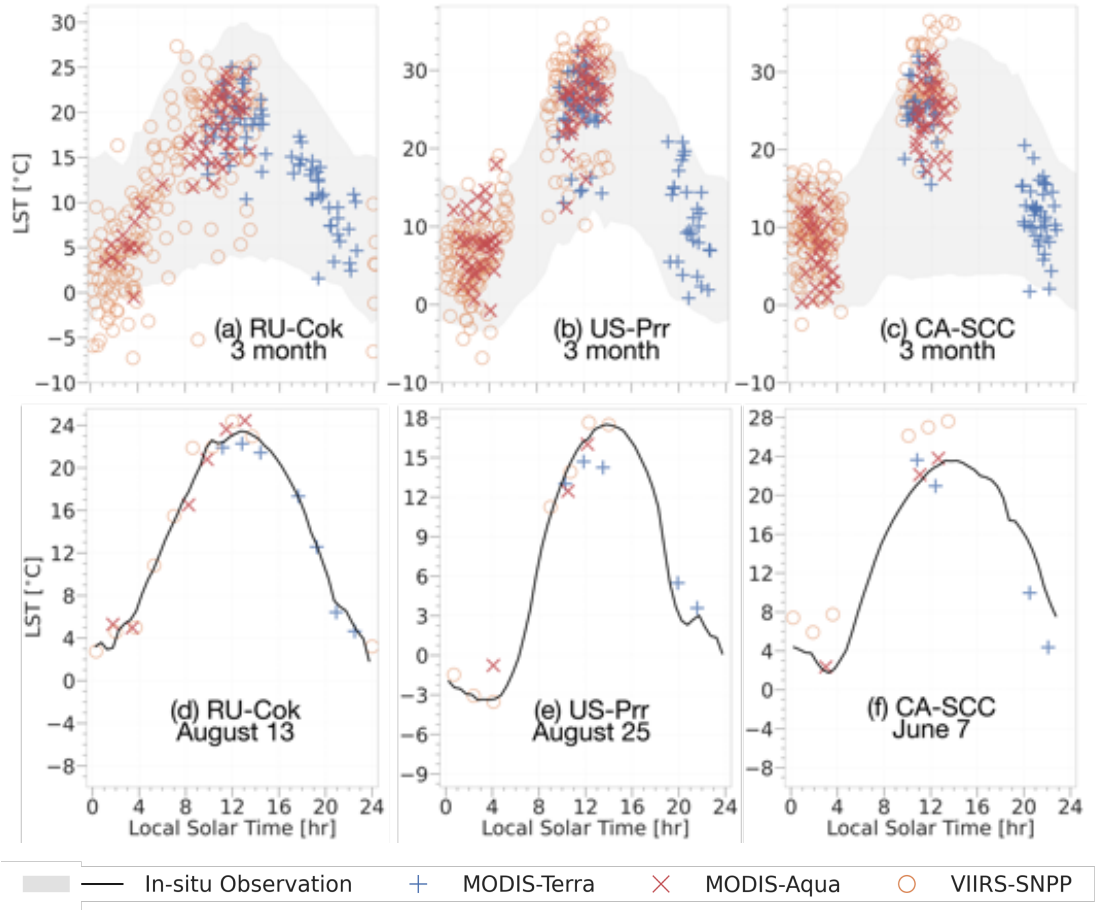

Figure 2.4 (a–c) Diurnal variations in land surface temperature (LST) during June–August 2013 for sample sites. (d–f) LST within a day at each site. Three sites in the typical latitude range: (a,d) larger than 70 °N, RU-Cok (70.83°N); (b,e) 70–65°N, US-Prr (65.12°N); and (c,f) 65–60°N, CA-SCC (61.31°N). The cross, plus sign, and circles represent LST by MODIS-Terra, MODIS-Aqua, and VIIRS-SNPP, respectively. The shadowed areas in (a–c) represent the site LST ranges over

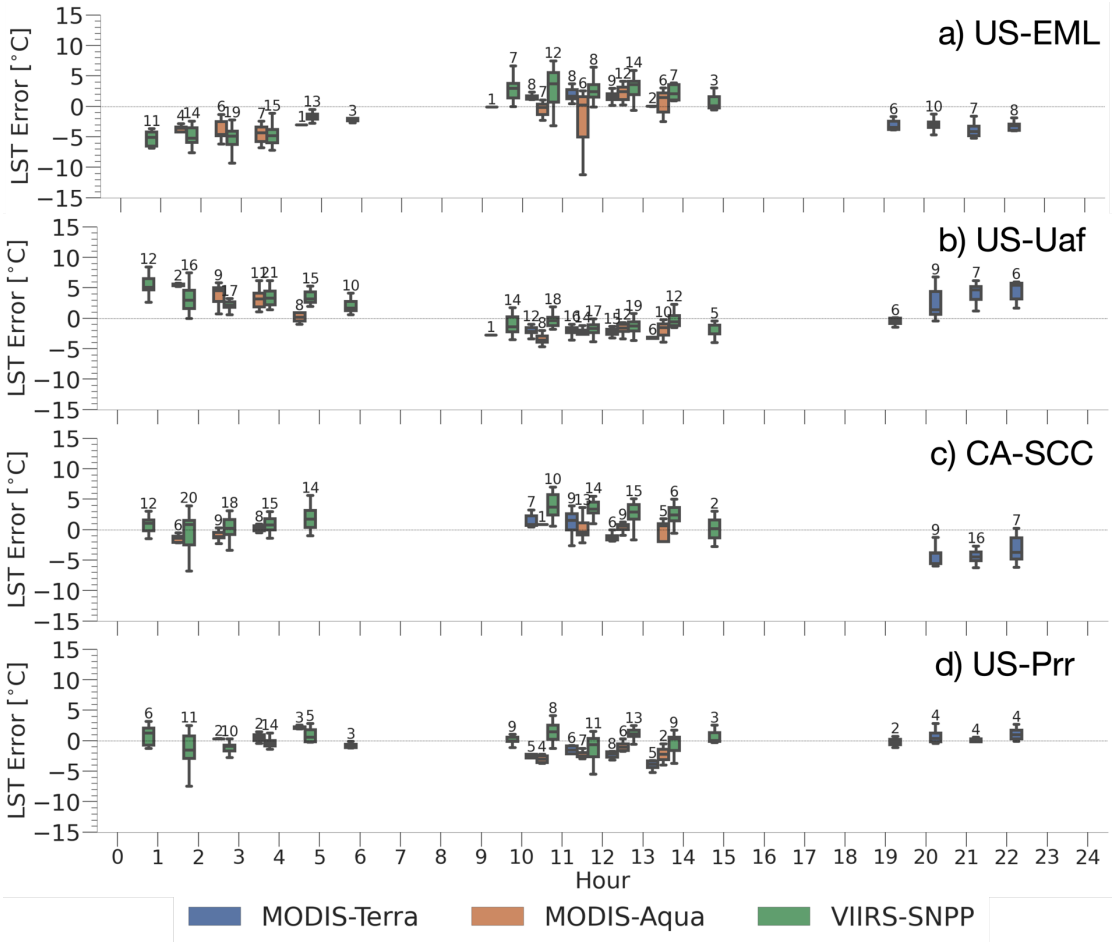

Figure 2.5 The LST error at different hours of the day for MODIS and VIIRS at in situ observations: (a) US-EML, (b) US-Uaf, (c) CA-SCC, (d) US-Prr. The LST error is the difference between the satellite LST and in situ LST, and each color bar represents one platform at the corresponding hour range. The numbers on the cap of the boxplot represent the observation counts over 3 months at the corresponding hour ranges. The different color of the bars represent the data from different satellite.

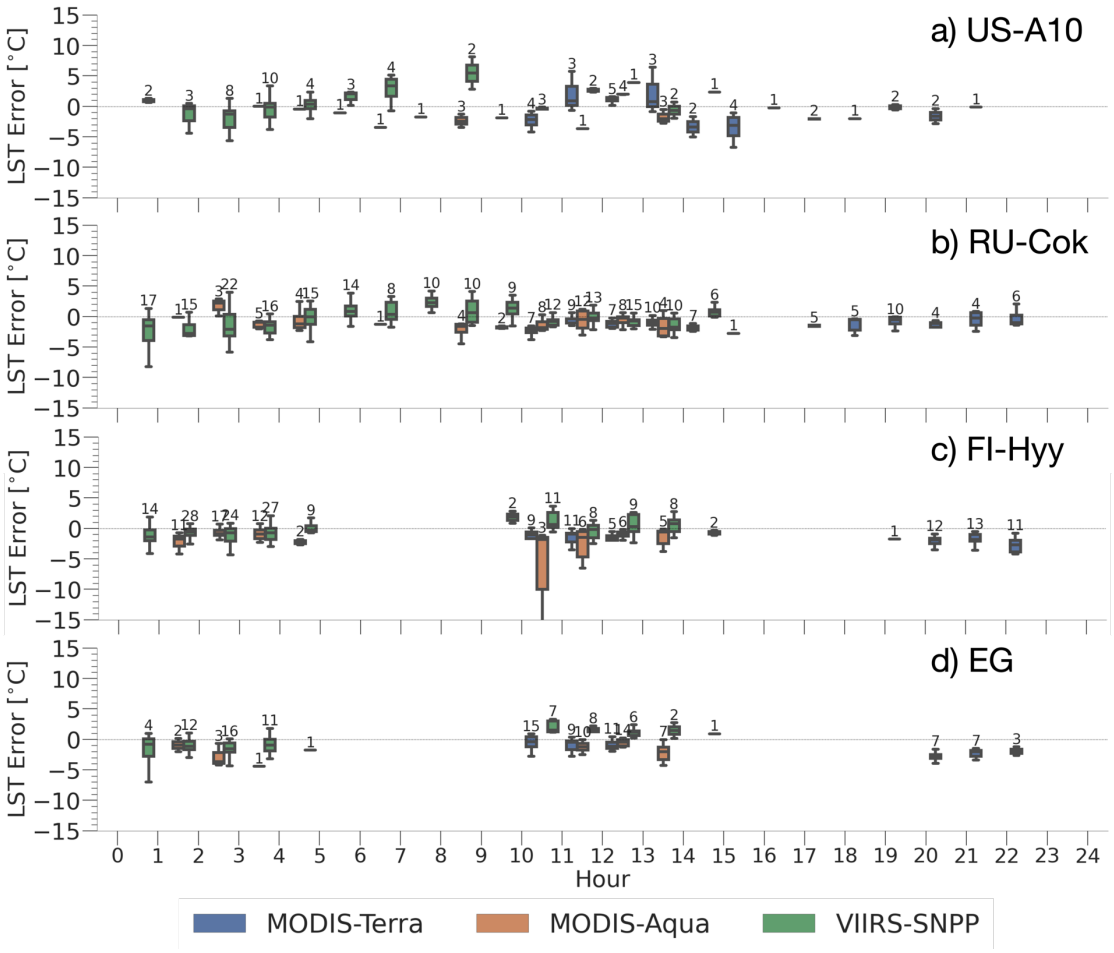

Figure 2.6 The continue of Figure 2.5 but for different sites: a) US-A10, b) RU-Cok, c) FI-Hyy, and d) EG.

2.2.3 Quasi-hourly Observation after Adding FY-3E (Scenario-2, AM, PM, EM)

In previous section 2.2.2, it highlighted the presence of observation gaps in the early morning and late afternoon at latitudes around 60˚N. The introduction of MERSI-LL FY-3E was expected to effectively fill these gaps. The addition of MERSI-LL FY-3E data has resulted in observation frequencies comparable to those of MODIS on Terra or Aqua and VIIRS on SNPP, particularly at latitude bands. The frequencies of observation increase with latitude, as follows: 16 times per day at 60˚N, 20 times at 65˚N, 28 times at 70˚N, and notably higher at 34 times per day at 75˚N, as shown in Figure 2.7a. This pattern of increasing observation frequency with latitude is more pronounced when using swath-dataset-based observations, which are significantly higher at higher latitudes

compared to daily composite data. The latter records observations twice per day, once during the day and once at night, yielding eight products (4 products x 2). The composite observation frequency can be described as a piecewise function against latitude with two segments, with a breakpoint at approximately 72˚N. Below this latitude, the frequency slope increases gradually and resets to nearly zero at 72˚N. Beyond this point, the slope starts from zero and increases at a similar rate.

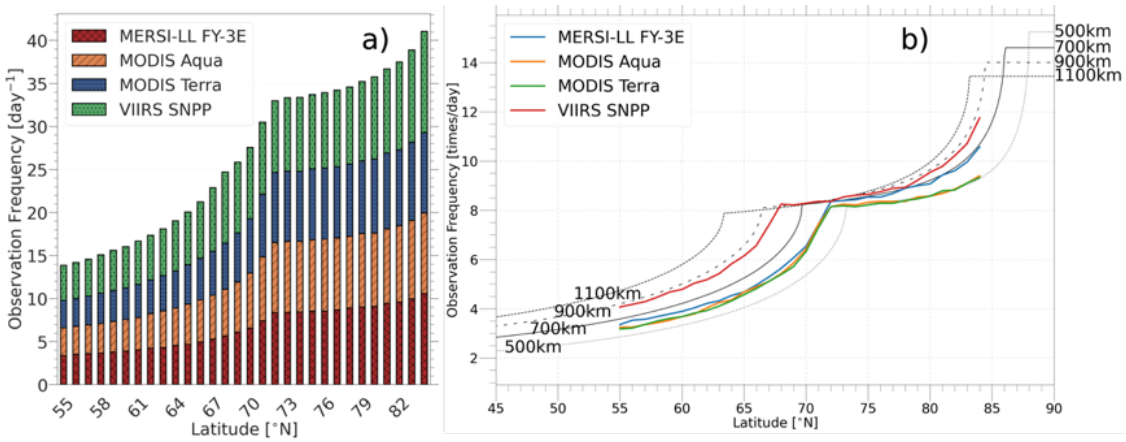

Figure 2.7 a) Latitude-band-averaged distribution of all-sky observation frequencies for each sensor-satellite. The latitudinal band-averaged distribution was obtained by averaging data from June 1 to June 28, 2022. b) Sensor-platform and simulated sun-synchronous orbit (SSO) maximum observation frequency of different latitude-bands. The black lines with different line style represent the simulated observation frequency at different orbit altitude with edge VZA at 70˚. The colored lines represent the observation frequency extracted from the corresponding product data.

In comparison to the simulation results, VIIRS on SNPP demonstrated an actual observation frequency close to the simulated one, with its position between 700 km and 900 km (Figure 2.7b). Meanwhile, MODIS on Terra and Aqua showed frequencies below the 700 km line. FY-3E exhibited a pattern akin to Aqua and Terra for observations below 72˚N and approached the 700km line at latitudes exceeding 72˚N. This is attributed to FY-3E's asymmetric Field of View (FOV) on the two edges, which is smaller on the left and larger on the right sides of the track. Overall, the observed observation frequencies align well with the simulation patterns. It is also noteworthy that VIIRS SNPP exhibits a higher observation frequency than the other platforms across all latitudes.

Satellite based-LST from each product is consistent with in-situ observed LST at most sites in a diurnal variation and adding FY-3E MERSI-LL LST makes diurnal observation complete. For example, at US-Prr from June 6 to June 8, benefit from this continuous cloud free period, satellite captured LST well at all 3 days (Figure 2.8a). The error of LST products were almost at the neglectable level. Firstly, from the beginning (local solar hour 00:00) of June 6, VIIRS SNPP or MODIS Aqua first took charge of the observation just soon after sunrise (very early sunrise because of high latitude). These satellites have very close local crossing time because they are similar ECTs. Secondly, MERSI-LL FY-3E filled the dawn time (although to this location several hours after sunrise) with two successive observations, combined with previous observations, showed linear increasing of LST by time. Thirdly, the slope decreased by time and reached the LST peak of the day. This was observed at the normal and most well-known morning crossing time and afternoon crossing time by MODIS Terra, MODIS Aqua, VIIRS SNPP. Fourthly, accompanied with decreasing of solar radiance from afternoon, MERSI-LL FY-3E well captured the pattern of LST decreasing. Finally, from dusk to evening time, the next observation after FY-3E is twice MODIS Terra observation. Similar pattern was depicted at the cloud free weather on the next new day. Additionally, the most southern site FI-Sii that represents the sites close to 60 ˚N, showed a continuous quasi-hourly LST observation with a slightly loose observation frequency (Figure 2.8d). For example, the observations of MERSI-LL FY-3E can be only captured 4 times per day in FI-Sii while it observed a frequency at 4~5 times per day in other sites, such as US-Prr.

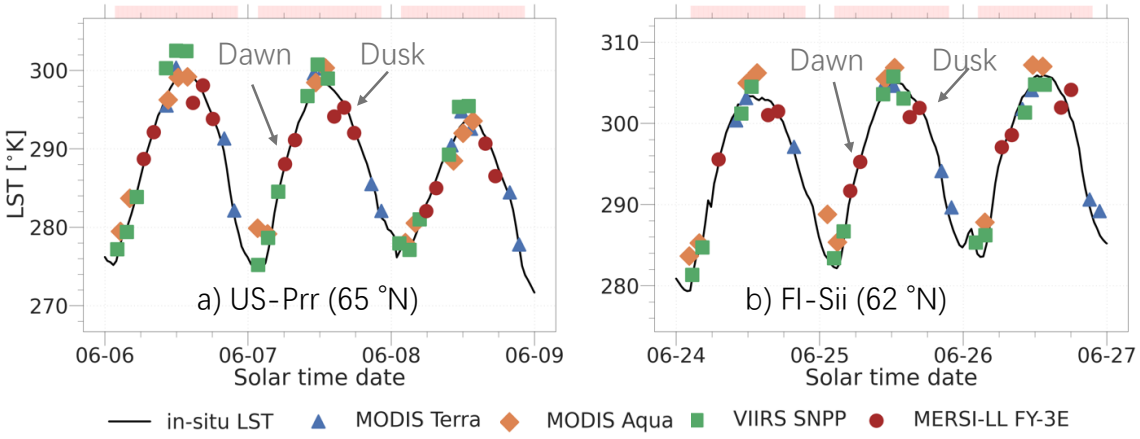

Figure 2.8 Diurnal variation of satellite-based LST and in-situ LST at two sites. The colored markers represent LST observations under cloud-free conditions for different sensors onboard the corresponding satellite. The shaded red area on the top of the margin represents the duration of daytime between one sunrise and the subsequent sunset.

High spatiotemporal variation data around the US-Prr can be constructed (Figure 2.9). Here, a clearer gapless temperature changing was found after adding MERSI-LL FY-3E LST to the series. For example, the LST over the scene is increasing hour by hour at early morning from 02:26 to 07:26. The observation at 07:26 and 08:35 showed small contrast and it indicate the LST is changing slowly in this stepping hour. The continuous 09:08 showed a significant temperature rising and keep stable till 10:00 (09:55 and 10:15). And at the dusk time of 15:10 and 16:50, the LST is observed decreasing compared to 14:08 and much higher than 19:40. Compared to the change in the morning time, it found an asymmetric pattern of the cooling period which takes 3 hours (from 16:50 to 19:40) against the warming period takes less than 2 hours from 08:35 to 10:15.

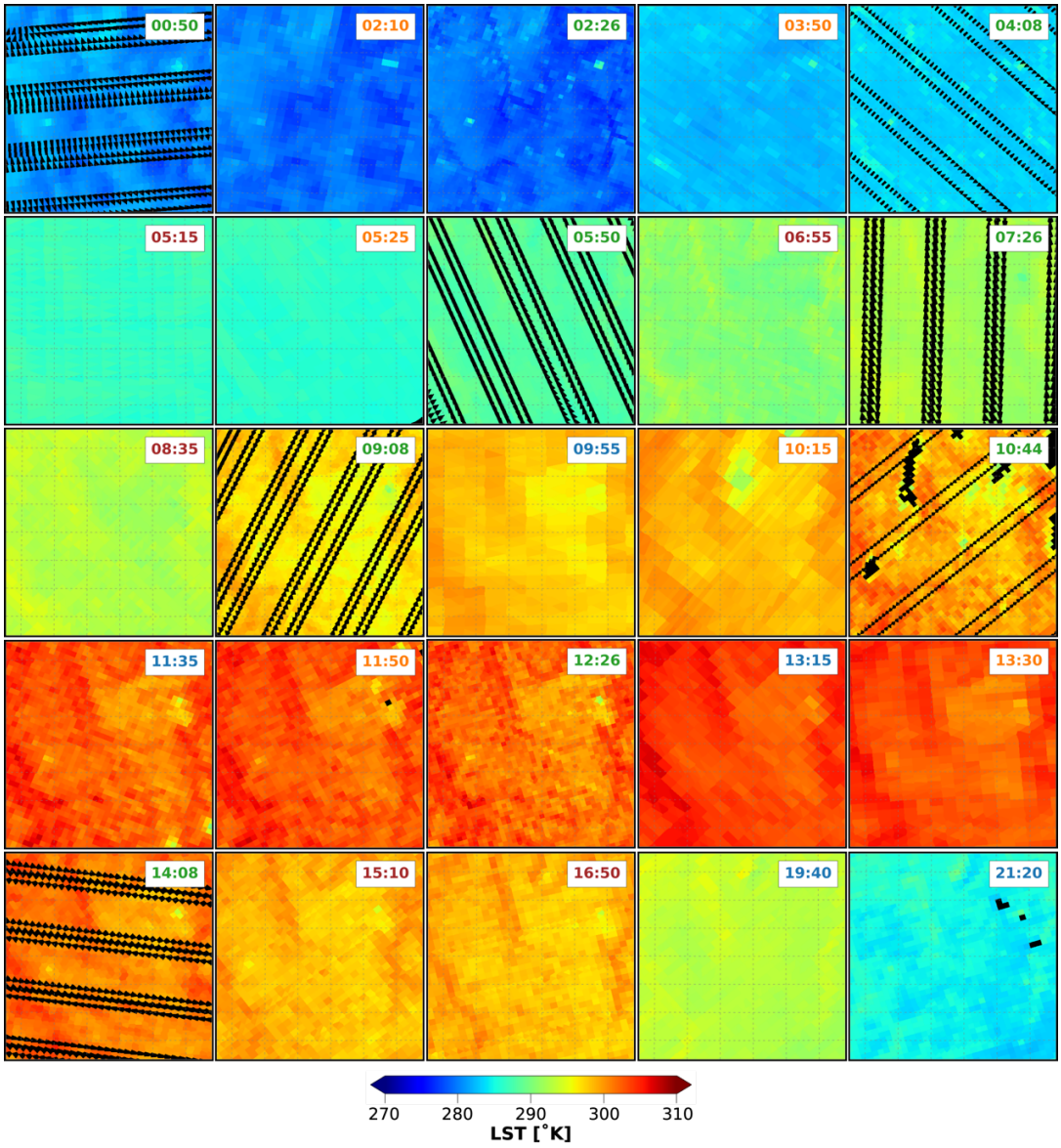

Figure 2.9 LST Spatiotemporal variation around US-Prr on 2022-06-16. The time in each subplot represents the local solar time. The green label color represents observations by VIIRS SNPP, orange represents MODIS Aqua, red represents MERSI-LL FY-3E, and blue represents MODIS Terra

2.2.4 Effective Observations on Different Hour of the Day

The observation frequency of the combined product was analyzed at a sampled longitude of 100˚W and latitudes ranging from 55˚N to 85˚N. This analysis focused solely on the geolocation data without examining the LST product. The relationship between observation frequency and latitude was studied for the observations made from June 1 to June 28 in 2022. Additionally, the observation frequency was counted separately for each

independent local solar hour unit to show the local crossing time pattern of each platform. The hours were divided into intervals such as 0:00-1:00, 1:00-2:00, ..., 23:00-24:00.

Observation frequency sampled at unit hour interval shows similar increasing against latitude, but the patterns are different at different hour of the day (Figure 2.10C-F). Because MODIS Terra, MODIS Aqua and VIIRS SNPP have close ECT around local noon time (10:00 to 14:00 at local solar time), more observation occurs at this period. As for observation at nighttime, Terra MODIS dominates the period before midnight from 20:00 to 23:00 at local time while Aqua MODIS and VIIRS SNPP continues the period after midnight at the new day from 1:00 to 4:00. This made an obvious observation gap at 4:00 to 9:00 and 14:00 to 20:00 without using FY-3E MERSI-LL observation when latitude is smaller than 70˚N (Figure 2.10a). Notably, VIIRS SNPP have possibility to capture the observation during 4:00–8:00 when latitude is higher than 68˚N whereas it was approximately 71˚ for MODIS on Terra or Aqua. However, the terrestrial fraction of the latitude-band between 60–70˚N was between 60% and 80%, was of great significance where diurnal LSTs cannot be captured well by the MODIS and VIIRS. Thus, improving the observation frequency of these regions is important.

After adding FY-3E MERSI-LL, especially, at the regions from 55˚N to 70˚N, it enables the same observation ability at the gaps of MODIS or VIIRS (Figure 2.10B). Also, it increases the observation frequency at the latitude larger than 70˚N.

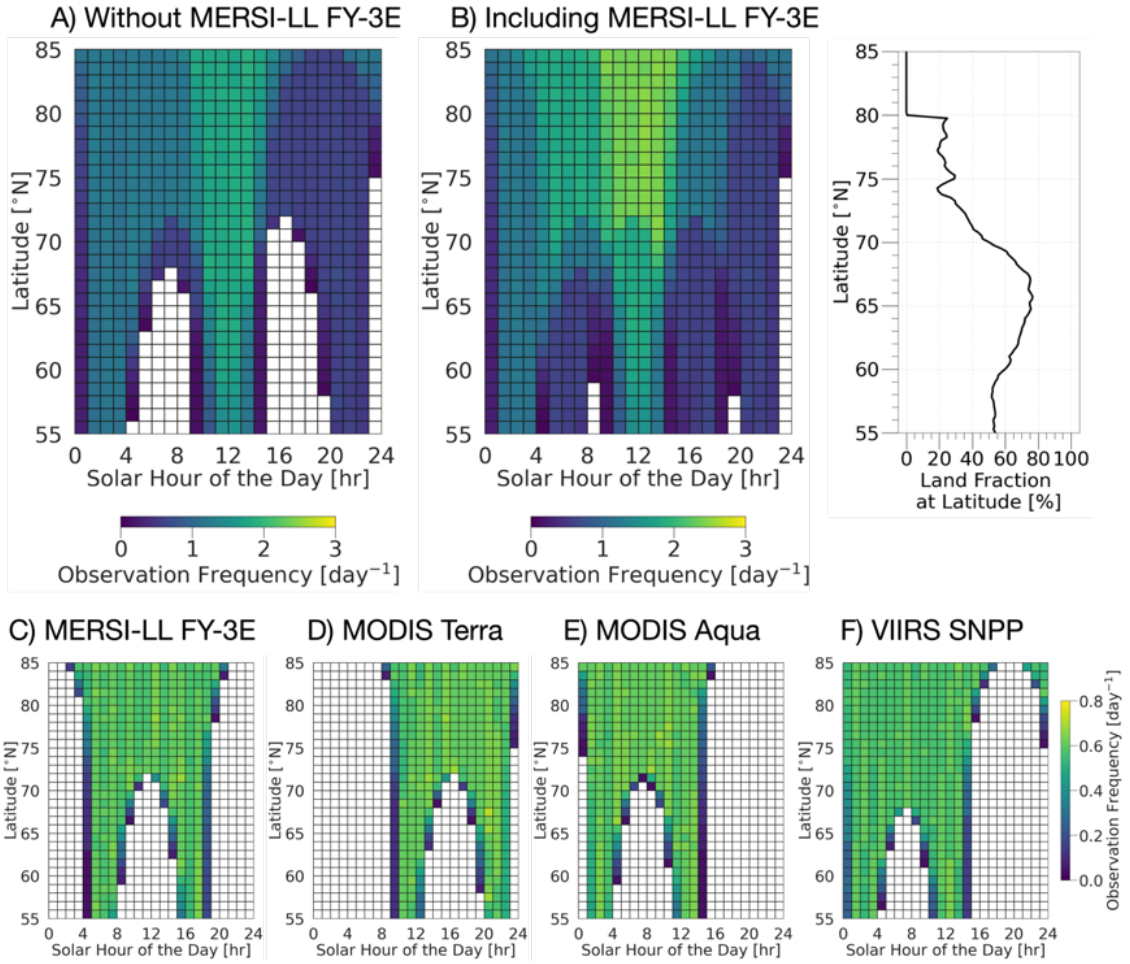

Figure 2.10 Spatiotemporal distribution of latitude-band-averaged all-sky observation frequency. The observation frequency was averaged for each latitude band at individual local hours of the day. The averaging was done over a period of 28 days, from June 1 to June 27, 2022. The X-axis represents the individual local solar hour, and the Y-axis represents the latitude band unit. Each block at (x, y) represents the observation frequency at the local hour x of the day in the latitude band y. A) Observation frequency using MODIS Terra, MODIS Aqua, and VIIRS SNPP. B) Observation frequency including observations from MERSI-LL FY-3E, based on (A). C-F) Individual satellite observation frequency spatiotemporal fingerprints.

2.3 Application for Heatwave Monitoring at Verkhoyansk

2.3.1 Brief Information of Verkhoyansk

Verkhoyansk, a town situated within the Republic of Sakha (Yakutia) in the Russian Federation, is notable for its extreme subarctic climate, which records some of the lowest winter temperatures on Earth. It centered at 67°33′N, 133°23′E (Figure 2.11, Figure 2.12).

The region is characterized by its stark and dramatic landscape, predominantly influenced by its geological and permafrost conditions that shape both its natural environment and human habitation patterns. Verkhoyansk, located within the Arctic Circle, is renowned for experiencing some of the most extreme winter temperatures and significant seasonal temperature variations globally. With average monthly temperatures plummeting to −44.7 °C (−48.5 °F) in January and rising to +16.5 °C (61.7 °F) in July, the region exemplifies an extreme subarctic climate, not a tundra climate. This climatic extreme is largely due to high atmospheric pressure that predominates for most of the year, isolating the region from warmer influences during winter and contributing to substantial heat losses under clear sky conditions. Verkhoyansk is also recognized as one of the northern Poles of Cold, with the record lowest temperature reaching −67.8 °C (−90.0 °F) on multiple occasions in the late 19th century. Temperature inversions are a common winter phenomenon here, with denser cold air pooling in low-lying areas, sometimes causing temperatures to rise with altitude rather than fall. This unique climatic feature is part of ongoing studies to understand the complex interactions of climate and permafrost in the region (Sysolyatin et al., 2023). As a case study, Verkhoyansk was used to illustrate the diurnal changes of LST, where the area experienced a record-breaking heatwave on June 20, 2020, with Ta above 38°C (Ciavarella et al., 2021).

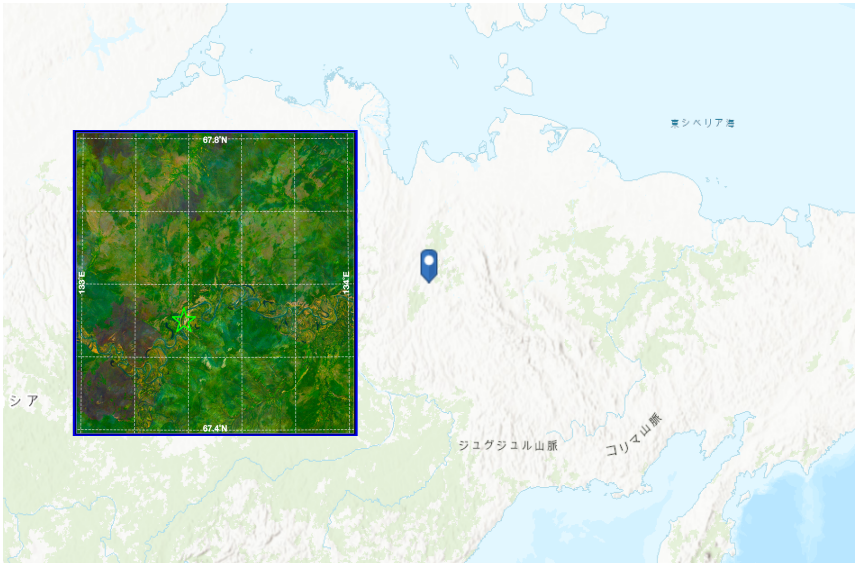

Figure 2.11 The location of Verkhoyansk and RGB image using corresponding reflectance of sentinel-2

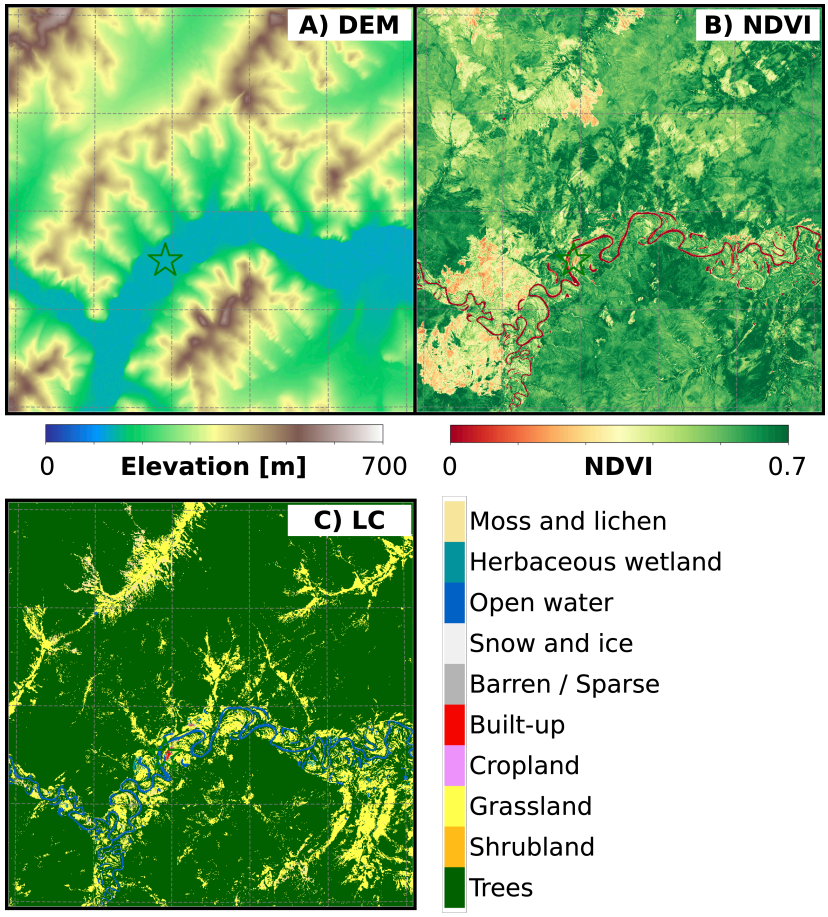

Figure 2.12 (A) Elevation (DEM: Digital Elevation Model), (B) NDVI (Normalized Differential Vegetation Index), and (C) Land cover (LC) around Verkhoyansk during the summer of 2020.

2.3.2 Temporal Variation of Normal Years and the Heatwave Year

Temporal LST variation at Verkhoyansk was captured well during both the heatwave event and normal days (Figure 2.13). Because the month that heatwave happened is almost across the solar day, thus heating and cooling of the LST DTC were assumed symmetrical. For simplicity, the harmonic DTC curves were used to fit the LST diurnal changes as following:

$$LST(t) = a \times \sin(b \times t + c) + d \qquad (2-15)$$

where t is the hour of the day of the local time, a, b, c, d are undetermined coefficient. Levenberg-Marquardt algorithm was used for fitting the curve fitting.

These curves before and during the heatwave peak showed a gradual evolution of the heatwave event in June 2020 (Figure 2.13). In the period before the heatwave peak, diurnal Ta and LST ranged from 10 to 25°C within a day. The fitted LST curve remained

within the Ta range during this period. However, when approaching the heatwave peak day, LST and Ta increased from approximately 12 to 40°C and 15 to 33 °C, respectively. The daily maximum and amplitude of LST exceeded those of Ta, indicating that the surface was extremely heated during the heatwave. Also, from 2018 to 2020, the LST maximum of the day is higher than those the years between 2017 and 2014, indicating that the higher possibility of high temperature occurrence in recent years (Figure 2.13). Also, it is found that only during the 2020 heatwave, the LST raised through the day around the middle of June, indicating the severity of this heatwave comparing to other years at the same period.

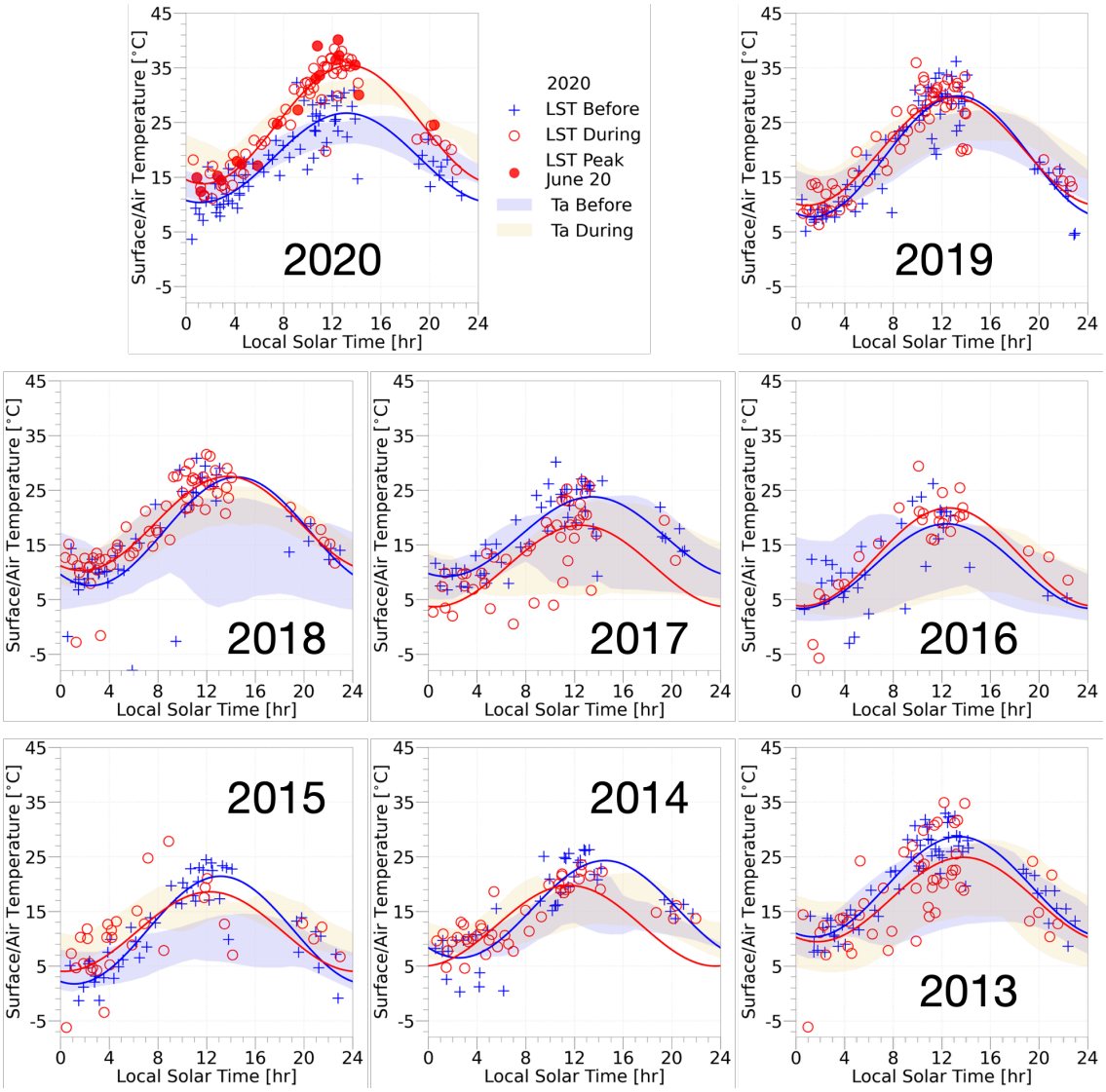

Figure 2.13 Diurnal variations in satellite-based land surface temperature (LST) and surface air temperature (ERA5 Ta) at Verkhoyansk before and during the 2020 heatwave event. Lines indicate the harmonic function-fitted diurnal LST cycle, and shaded areas represent the Ta maximum and minimum during each period. Blue line shaded areas, and markers represent the period before the heatwave peak day (from June 13 to June 17). Red line, shaded areas, and markers represent the period during the heatwave peak (from June 18 to June 22), while filled red circles represent satellite-based LSTs on the heatwave peak day (June 20).

The cloud condition indicated by high observation frequency dataset can explain one factor for causing this extreme event. It was mainly caused by the suddenly increased solar radiation from June 1st, and consequent prolong high solar radiation (Figure 2.14). The cloud condition was defined by cloud flag in the LST dataset. For instance, the clear

condition, thin cirrus, nearby cloud and cloud condition was set as cloud fraction at 0, 0.5, 0.5, and 1. The cloud fraction was nearest neighborhood interpolated and then smoothed. It showed the similar tendency as the variation of the net solar radiation at the surface, for example, the increasing of the net solar radiation and decreasing cloud fraction accompany with the gradually increase temperature from June 1st to June 20th in 2020. This indicating the high frequency observations can also indicate the energy input to the ground surfaces.

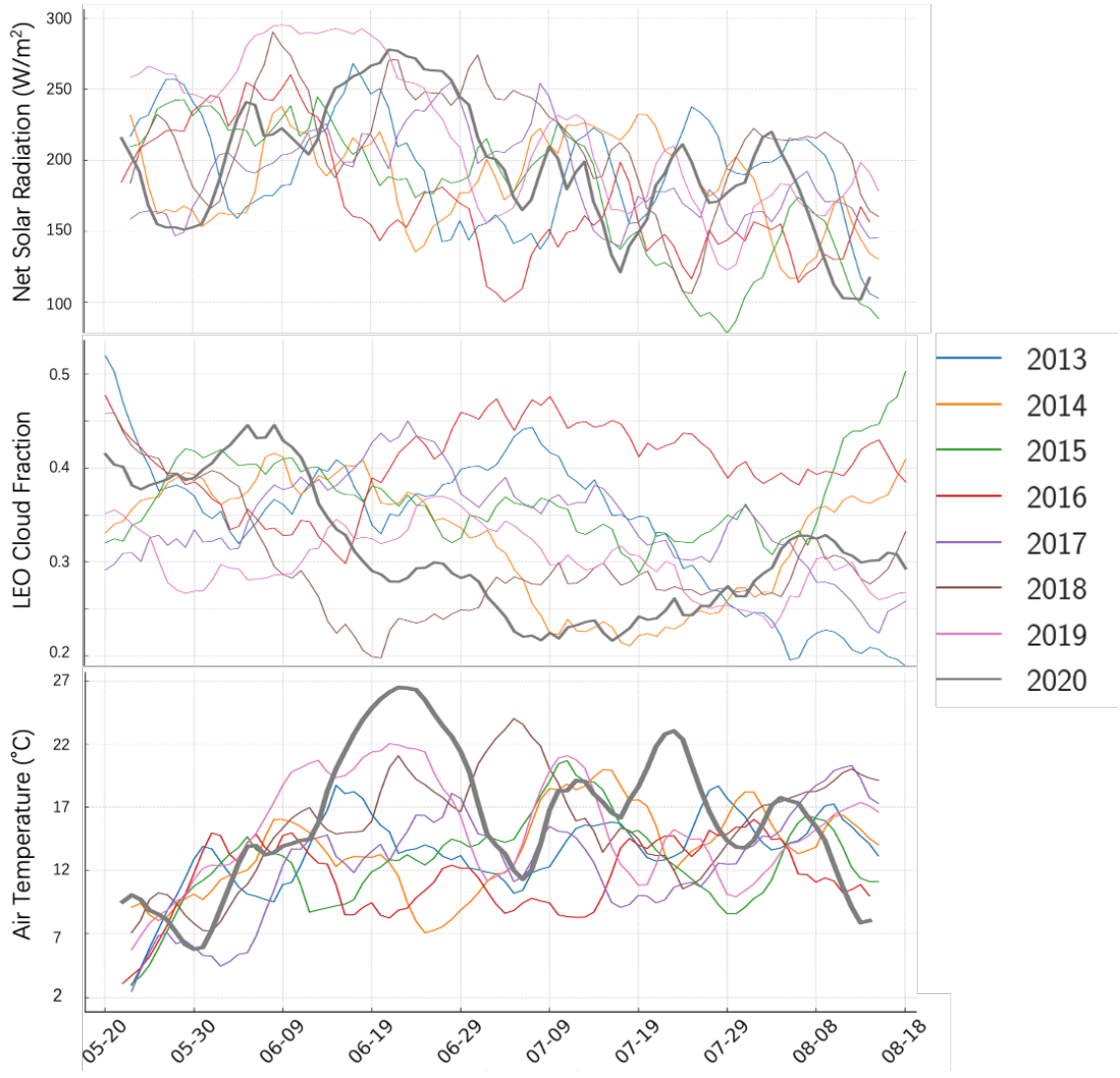

Figure 2.14 Daily variation of the smoothed net solar radiation, cloud fraction indicated using high observation frequency data from satellite, and air temperature from 2013 to 2020.

2.3.3 spatiotemporal changes at the heatwave peak day

The use of high-spatiotemporal-resolution LST data enables the understanding of LST diurnal variation over surfaces with different properties. The LST over regions over Verkhoyansk increased and then decreased with local solar time during the study period (Figure 2.16). At nighttime (low sun elevation), the LST was lower across the whole area, and the topography could be roughly classified (Figure 2.15c–e). Comparing the LST around this time and the elevation map revealed that the LST became larger at higher elevations (Figure 2.15e). This phenomenon can be the local climate because of the weak convection that may occurred in the high latitude valleys (Nill et al., 2019) or the low sun elevation and the consequent low solar radiation in the valleys. Because the positive correlations were found for both days before heatwave and days after heatwave (Figure 2.16b, Figure 2.16d). The consequent inversion layers occurring in the atmospheric temperature profile as its profile temperatures at June 20th had accelerated the local air temperatures and LSTs (Figure 2.17). Also, During the daytime, as the sun elevation increased, the LST exhibited two apparent hotspots in the southwest corner. The hotspots always had a larger LST than the surrounding area, which increased with the surroundings (Figure 2.15j–o). This is considered a vegetation-dominated spatial pattern because the hotspots have less vegetation coverage (Figure 2.12b). To our understand, this phenomenon can be explained by that the vegetation act as a buffer and resists to the rapid rising temperatures (De Frenne et al., 2019). Around the transition times of 07:30 and 09:12, the spatial LST distribution comprised a mixture of terrain- and vegetation-interrelated patterns (Figure 2.15h, i), which cannot be captured if the high observation frequency LST was not used.

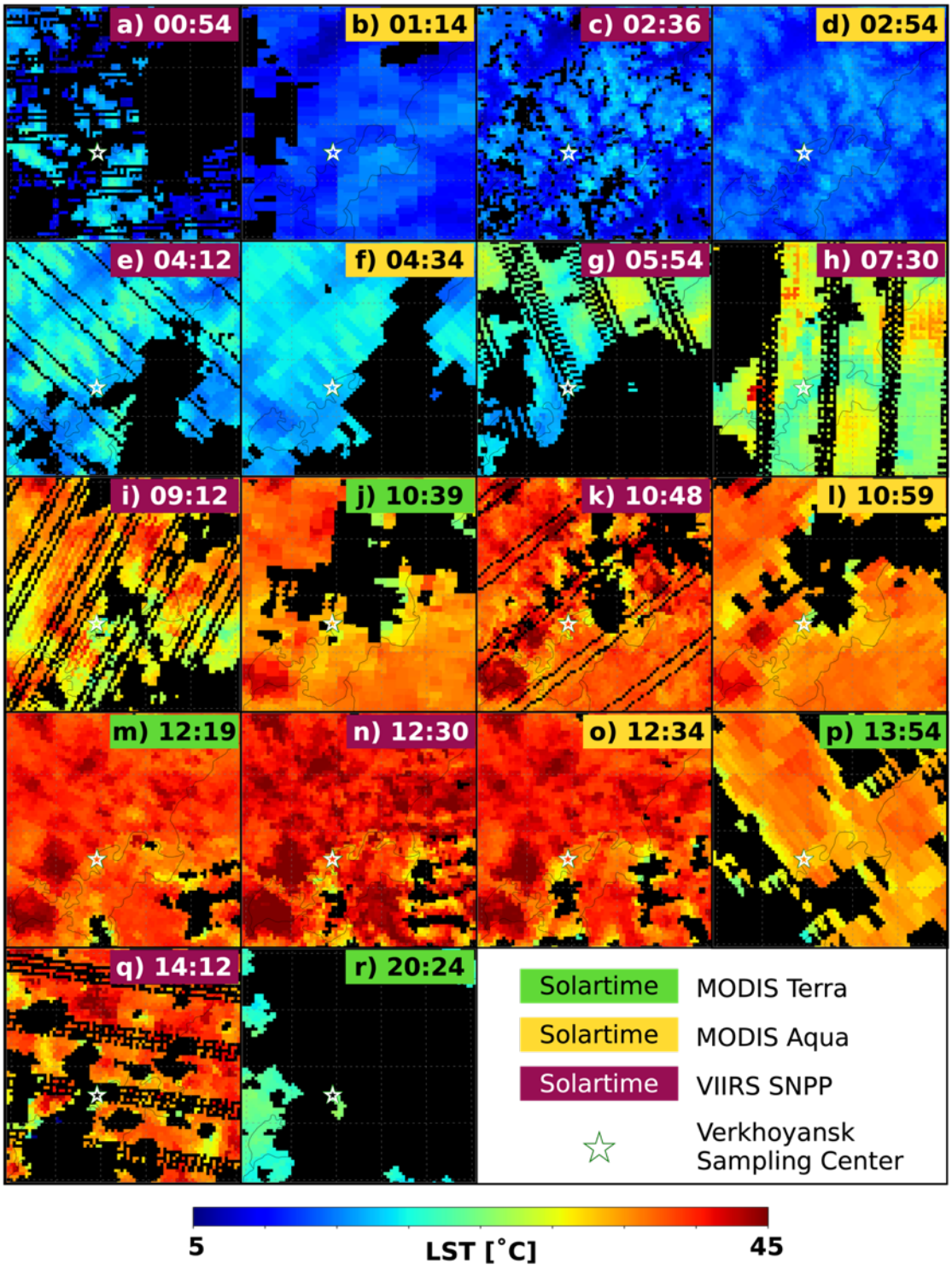

Figure 2.15 Spatiotemporal variation of land surface temperature (LST) around Verkhoyansk during the heatwave event on July 20, 2020. The black area indicates observation failure owing to cloud cover or sensor failure.

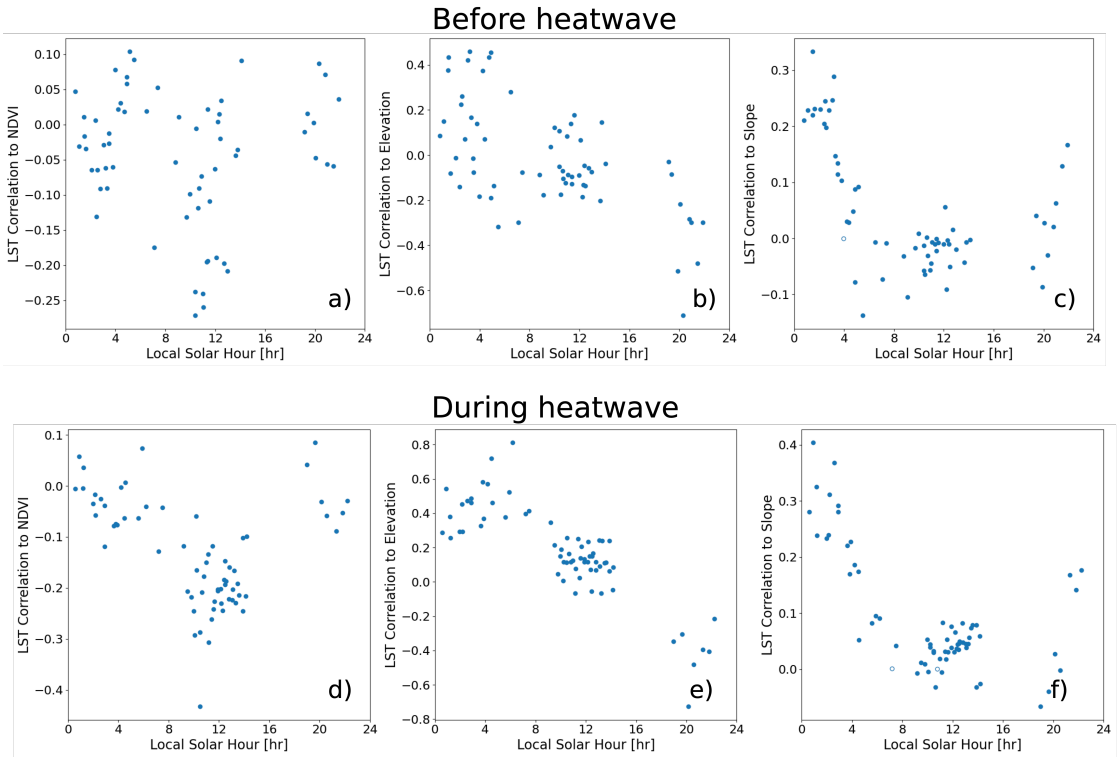

Figure 2.16 Spatial correlation of LST and NDVI (a),(d), elevation (b),(e), and slope (c),(f) by pixels over the Verkhoyansk region (same area as Figure 4.4). (a–c) Correlations before the heatwave. (d–f) Correlations during the heatwave. Positive values represent a positive linear relationship, while negative values represent a negative linear relationship. A value close to zero indicates no clear linear relationship. Filled circles represent $p \leq 0.01$; non-filled markers represent $p > 0.01$ (p value here represent the probability that the slope is 0).

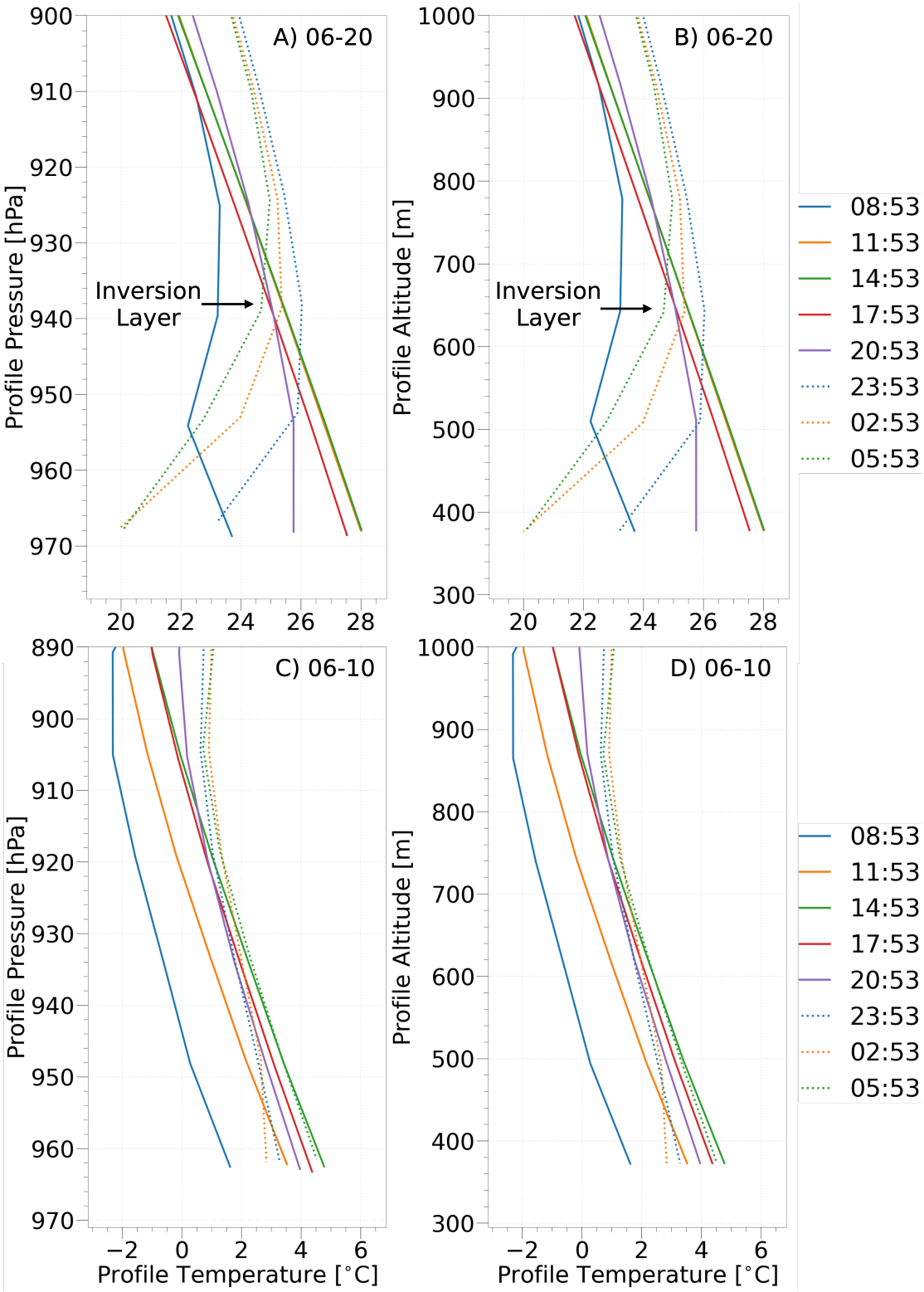

Figure 2.17 MERRA2 atmosphere profile at Verkhoyansk before (June 10th) and during the heatwave (June 20th)

2.4 Application at Alaska

2.4.1 Introduction of Alaska Region

Alaska, the largest state in the United States by area, is situated in the northwest extremity of North America. It is bordered by the Arctic and Pacific Oceans, and Canada to the east. Known for its diverse and extreme climate, Alaska's weather varies dramatically across its vast territory. In the northern regions, Arctic conditions prevail with long, extremely cold winters and short, cool summers, while the coastal areas experience milder temperatures and heavier rainfall. The interior parts of the state see more continental weather, characterized by temperature extremes. Due to its high latitude, Alaska experiences significant seasonal variation in daylight, ranging from 24 hours of daylight in the summer to less than four hours in winter in some areas. This unique phenomenon affects both the climate and the ecosystem. The average temperature in winter can drop below -35˚C while the summer can see temperatures reaching up to 25˚C in some regions (Sulikowska et al., 2019). Alaska faces environmental challenges, including permafrost degradation due to global warming, which threatens infrastructure and traditional ways of life (Romanovsky et al., 2010). Climate change impacts are also evident in the rapidly changing patterns of wildlife populations and plant growth, influencing ecological dynamics (Wolken et al., 2011). In 2022, an extreme severe drought was observed in more than half of the area across Alaska regions during the June and July (https://fire.ak.blm.gov/content/Weather%20Folder/Fire%20Season%20Summaries/2022%20Fire%20Season.pdf). As a result, the wildfire spread fast in early June and had much more occurrence than in normal years. Thus, the analysis of LST in summer 2022 in Alaska was of significance.

2.4.2 Analysis of the Hourly LST and Envinronmental Factors

As the thermal condition of the terrestrial surfaces is changing rapidly in the Arctic and Pan-arctic regions, including minimum temperature (Tmin), maximum temperature (Tmax) and diurnal temperature range (DTR) (Sulikowska et al., 2019), understanding these changes is of importance. In this study, by utilizing the quasi hourly data after including the LST from FY3E, it provided a new inslight for analyzing the LST with other parameter at a hourly scale. This will provide the information how that LST at different hour of the day related to surface vegetation coverage or elevation. The spatial correlation

was calculated using the data within individual weeks using the LST data at each two hour aat the research interest at the region where latitude ranges from 61˚N to 67˚N and longitude ranges from 155˚W to 135˚W. Addtionally, to focus on the ecosphere in the Alaska area, the analysis was only conducted over the vegetation pixels, where NDVI once larger than 0.3 in June, July and August.

The 2-hourly LST correlation to the DEM or NDVI showed a clear diurnal change (Figure 2.18). For example, the LST during the evening time (0:00–6:00 and 18:00–24:00) showed a negative correlation to elevation. As a result, the higher elevation is corresponding to the lower LSTs. This is same to our understanding of the relationship between temperatures and elevations. However, during the daytime especially near noon (12:00), such correlation was close to zero. Instead of elevation, solar radiation (SRAD) had a larger correlation to noon time LST, suggesting the noon time LST is potential for energy balance calculation. The correlation of NDVI and 2-hourly LST is on the opposite to the relationship that against elevation. The correlation of noon time also showed a close to zero pattern but the nighttime, it showed a positive correlation. This indicated that higher nighttime LSTs are corresponding to higher NDVIs. This can be explained in two aspects: 1) the vegetation has the thermal buffering function that reduced the cooling effect in the nighttime (De Frenne et al., 2019); 2) the vegetation prefer higher temperatures (LSTs) and the temperature limits its growth in such sample regions (Nemani et al., 2003b). And this can be found with inspecting 2-hourly LSTs and daily Ta, where higher nighttime LSTs are more related to higher daily Ta, which directly controls and affect the grow of the vegetation.

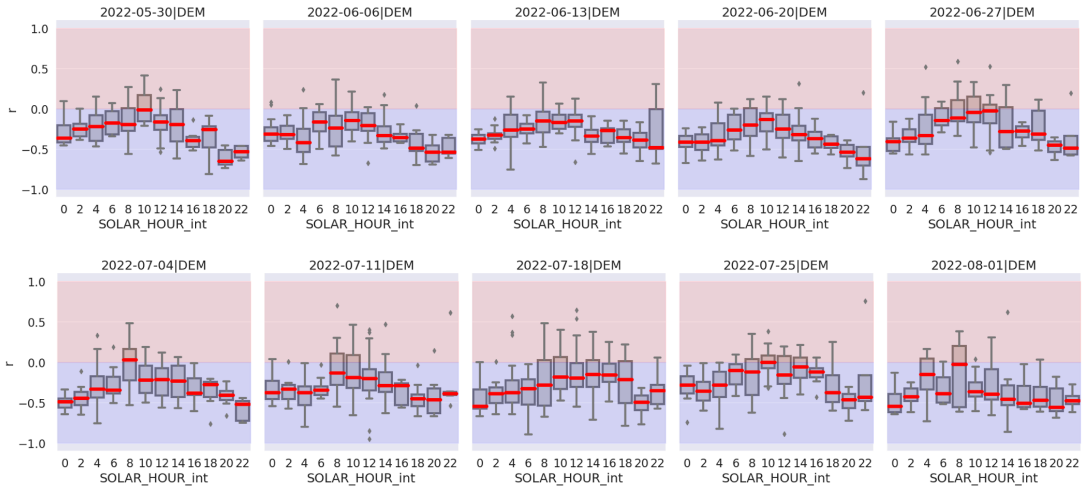

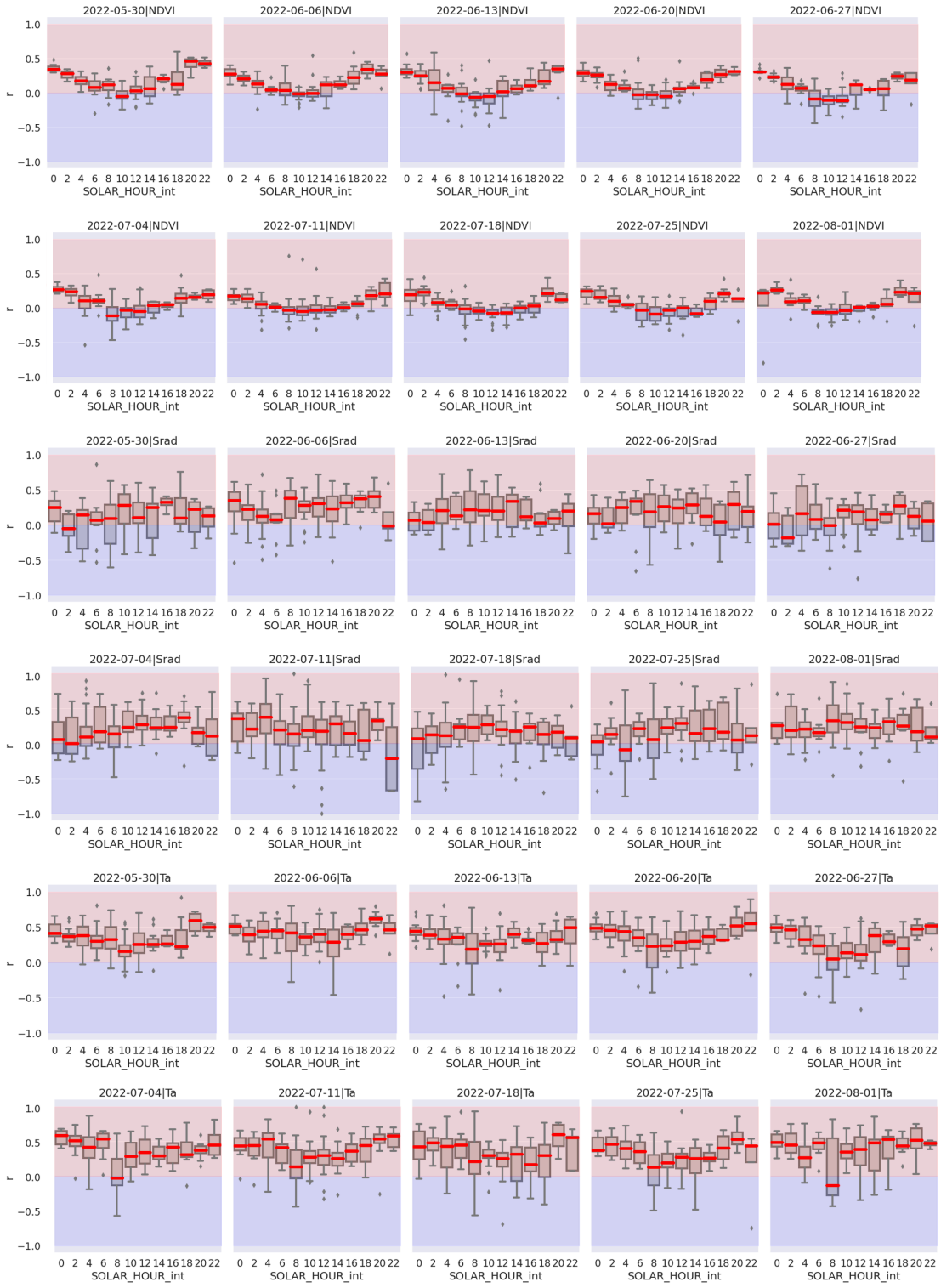

Figure 2.18. Weekly spatial correlation between LST at each two hours and elevation (DEM: Digital Elevation Model), normalized differential vegetation index (NDVI), solar radiation (SRAD) or air temperature (Ta).

2.4.3 Extension of the Hourly Analysis to In Situ Observations

As suggested in 2.4.2, the nighttime LSTs are correlated to NDVI across the Alaska study regions. To address this phenomenon, the analysis of hourly LSTs was conducted at the site to make deeper explanation. The NDVI is an optical parameter that include both structure information and pigment information (Huang et al., 2021). These values represent the biomass content and photosynthesis ability and can be used as the proxy of Light Use Efficiency (LUE) (Gitelson et al., 2012a).Thus, by inspecting the daily LUE of the site data and hourly LST, we can understand if this phenomenon occurred over the sites or not. The calculation of the LUE which is the ratio of the gross primary production (GPP) and the net photosynthesis active radiation (PAR) which represent the efficiency of vegetation transferring solar energy to organic matter in the quantity of fixed carbon matter. This light use efficiency (LUE) is various among different vegetations under different tree ages and environmental conditions such as temperature and water availability condition such as soil moisture and air humidity. In this analysis, LUE was calculated using the GPP and PAR data from in situ observations.

Interestingly, the site hourly-individual LST and site daily LUE also showed the difference at the different time of the day. Similarly, the large correlation of LUE and nighttime LST was observed (Figure 2.19), which is align to the result of larger NDVI and nighttime LSTs. Such result was observed over two individual sites with an ENF and a DBF, indicate this is common phenomenon in the boreal ecosystems. And still the LST is not as high as the level at Verkhoyansk that exceed 310 K, thus not showing the similar response.

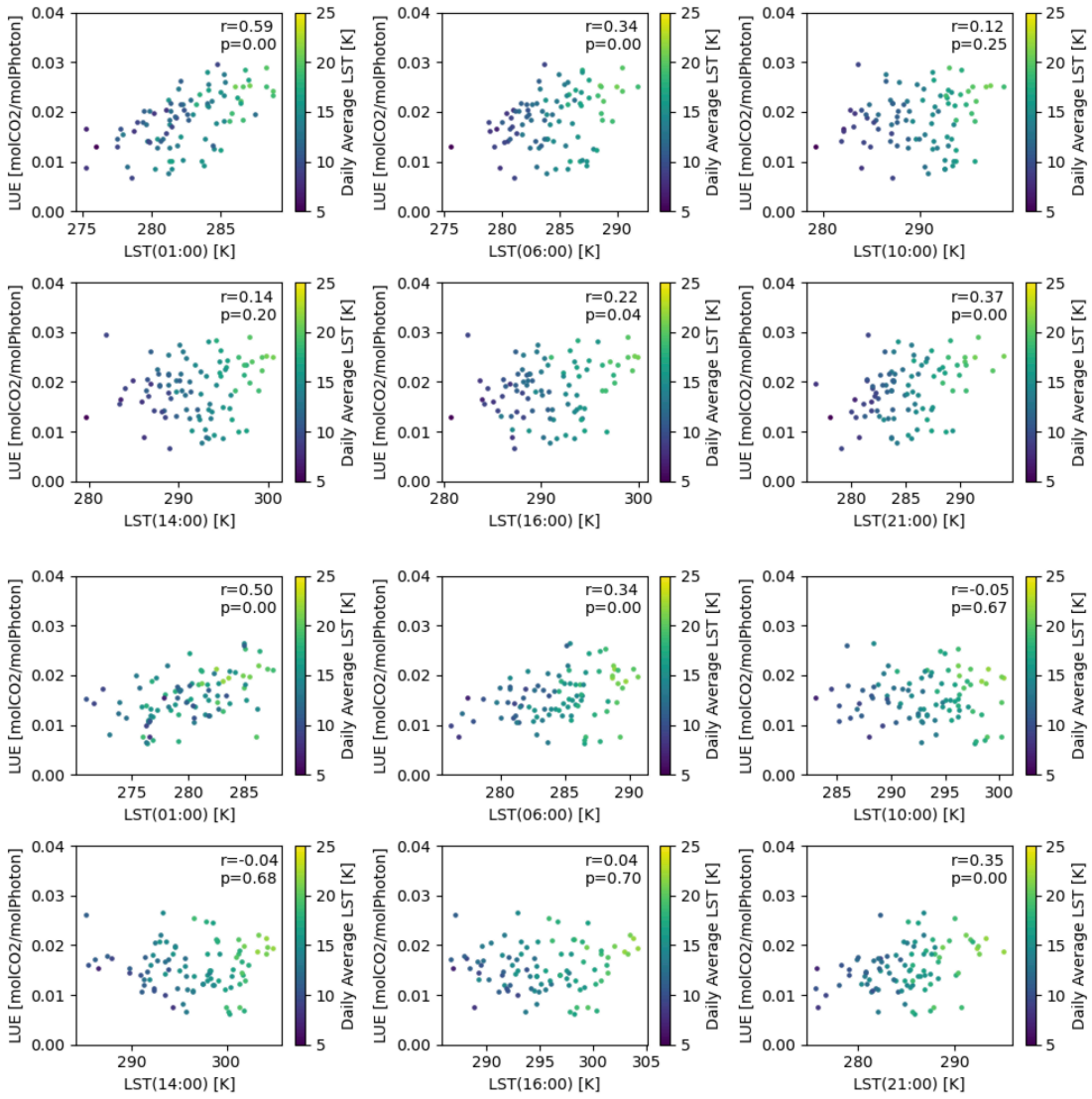

Figure 2.19 The relationship of daily LUE against the LST at the different time of the day over two sample sites (Top: US-Rpf, Bottom: US-Uaf).

2.5 Discussion of Other Polar Orbiting Satellites for Two Scenarios

Satellites used for environmental monitoring were designed for a certain life for a certain scientific mission and provided data from several years to decades. For example, Landsat 8, launched in 2013, has an expected life of about 10 years, while Sentinel-2A, part of the European Space Agency's Copernicus program launched in 2015, has an expected operational life of 7 years, extendable to 12 years. NASA's Aqua and Terra satellites, launched in 2002 and 1999 respectively, were initially designed for 6-year

missions but have continued to operate well beyond their expected lifespans. Similarly, the Suomi NPP satellite, launched in 2011 with a 5-year life expectancy, and the Jason-3 satellite, launched in 2016 with a 5-year life, have also outlasted their planned durations. NOAA's GOES-16, launched in 2016, has a more extended operational life of 15 years. These satellites often surpass their expected lifespans, continuing to provide critical environmental data and contributing significantly to our understanding of Earth's climate and ecosystems. Thus, it is important to expand the understanding of the example satellites used in the scenario-1 and scenario-2 to alternative satellites. In this section, except from MODIS on Terra or Aqua VIIRS on SNPP, MERSI-LL on FY-3E, other candidate satellites were discussed as the source for historical data construction or for future perspective.

2.5.1 Method and Data

The simulation in this section used the orbit two-line element set (TLE) to simulate observation frequency at each individual hour. TLE or three-line element set (3LE) is a standardized data format used to encode the orbital elements of Earth-orbiting objects at a specific time, known as the epoch. Initially, the TLE format was designed for punched cards, encoding orbital elements on two standard 80-column cards. As technology advanced, this format was replaced by text files, with each set of elements written on two 69-column ASCII lines, preceded by an optional title line. The United States Space Force monitors all detectable objects in Earth orbit, creating TLEs for each one. TLEs for many space objects are made publicly available on websites such as Space Track (https://www.space-track.org) and CelesTrak (https://celestrak.org), though data on many military or classified objects may be withheld or obfuscated. The TLE format has become the de facto standard for distributing the orbital elements of Earth-orbiting objects. By applying appropriate predictive models, the position and velocity (state) of the object at any time in the past or future can be estimated with reasonable accuracy. The TLE format is designed specifically for the simplified perturbations models (SGP, SGP4, SDP4, SGP8, and SDP8). Therefore, any algorithm using TLE data must implement one of these SGP models to accurately compute the object's state at a desired time. TLEs are applicable only for objects orbiting Earth and are widely used to project future orbital tracks of space

debris, aiding in risk analysis, close approach assessments, collision avoidance maneuvers, and forensic analysis.

In this study, the SGP4 algorithm was adapted with the python package 'pyorbital', to calculate/predict the location and altitude of the satellite with given TLE data. SGP4 algorithm was reported approximately 1 km error for the epoch of a satellite at a low Earth orbit and grows at approximately 1–3 km per day (error of the simulated position). Thus, all available TLE for the specific satellite were used to calculate the satellite location to avoid the propagation error. Here, these TLE data were acquired from NORAD GP Data Sets Historical Archives maintained by CelesTrak (https://celestrak.org/NORAD/archives/request.php). For simplification, the TLE data was download in May in 2005, 2010, 2015, 2020 for representing the satellite at different era. The TLE data of Metop-B, Metop-C, Fengyun-3D, NOAA-12, NOAA-14, NOAA-15, NOAA-16, NOAA-17, NOAA-18, NOAA-19, and NOAA-20 (JPSS-1) were used in this section to represent the observation frequency pattern from historical satellite records and observation frequency pattern of the new generation satellites.

The corresponding FOV of each sensor was used to simulate the swath tracks as the actual ground coverage. Here, the AVHRR sensors on Metop series or NOAA series used a 55.37˚, MERSI-LL or MERSI-II on Fengyun series used a 55.40˚, VIIRS on SNPP or JPSS-1/2 (NOAA-20/21) used a largest FOV at 56.28˚. The simulation used the sampling points at unit latitude from 55˚ to 85˚N and longitude at 0˚ for easier local time calculation. The sampling points between swath edges was considered as one observation by the satellite.

2.5.2 AM and PM Candidate for Scenario-1

More environmental observation satellites operated or are operating on sun-synchronous morning orbit (AM) or afternoon orbit (PM) to keep the same crossing time by days. Also, this consistency helps in comparing data over time and reduces variability caused by changing illumination angles. Observing at fixed times like morning and afternoon allows for consistent LST comparisons. The temperature differences between these times can help in studying diurnal (daily) temperature variations, which are important for understanding weather patterns, climate change, and surface heating/cooling cycles.

Regarding the long history of LST observation using satellites, Advanced Very High Resolution Radiometer (AVHRR) that works on NOAA series provided the longest records. The first AVHRR on NOAA was launched in late 1970s and now the NOAA-21 represented more than 20 satellites for this mission. As step into 2000s, the MODIS on Terra and Aqua had provided the continuous LST data for more than 20 years at AM and PM orbit. However, the MODIS had much exceeded its original designed life and recent operation reports showed the risk that losing of MODIS observations. Therefore, finding the new candidate at AM or PM orbit to construct scenario-1 is of important for continuous LST observations, especially, at future perspective. As the environmental observation was highlighted and acknowledged among the countries, more new generation satellites were available. For example, as for LST observation by AM orbit satellite, currently, we can use AVHRR-3 on Metop-B and Metop-C or SLSTR (Sea and Land Surface Temperature Radiometer) on Sentinel-3A and Sentinel-3B that maintained by European Space Agency (ESA) of European Organisation for the Exploitation of Meteorological Satellites (EUMETSAT), Second-generation Global Imager (SGLI) on Global Change Observation Mission-Climate 1 (GCOM-C) that maintained by Japan Aerospace Exploration Agency (JAXA), VIIRS on NOAA-20 and NOAA-21 that maintained by National Oceanic and Atmospheric Administration (NOAA) or National Aeronautics and Space Administration (NASA), and Medium Resolution Spectral Imager-II (MERSI-LL) on Fengyun-3D that maintained by National Satellite Meteorological Center (NSMC). Among these candidates, 4 platforms were showed as examples at latitude bands by individual hour with have much larger FOV (Figure 2.20).

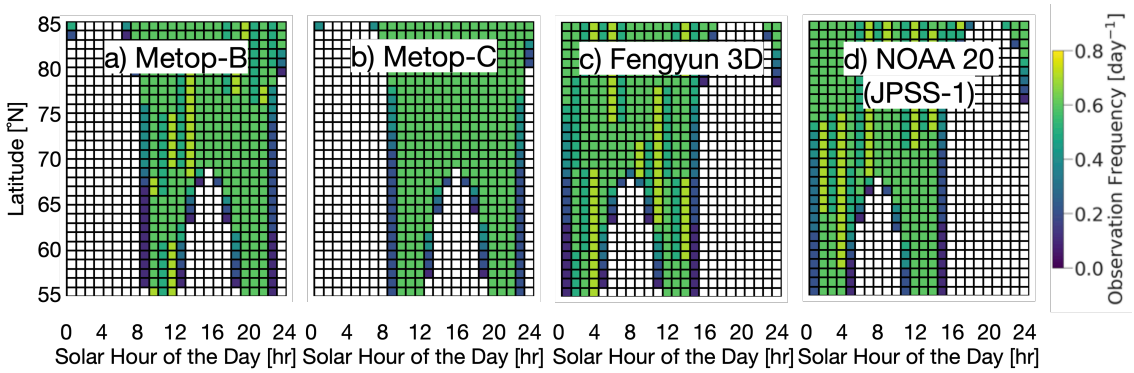

Figure 2.20 Spatiotemporal distribution of latitude-band-averaged all-sky observation frequency for AM and PM new generation satellites including: a) Metop-B (AM), b) Metop-C (AM), c) Fengyun 3D (PM), and d) NOAA 20/JPSS-1 (PM). The observation frequency was averaged for each latitude band at individual local hours of the day. Similar to Figure 2.10

2.5.3 EM Candidate for Scenario-2

There are some potential candidate satellites as MERSI-LL FY-3E that was used in the scenario-2. NOAA series poses the possibility of the observation at early morning or other observation time by its orbit drifting character (Figure 2.21), which was always considered as a big issues for producing the LST map that need normalization, especially, against changing of the crossing time (Ma et al., 2020; Reiners et al., 2021). Although it was a drawback in these studies, on the other hand, it provided the data that at abnormal crossing time, is of different to the standard AM/PM platforms, that have possibility to fill the gaps in the early morning times. Indicating from the figure, such kind of observation at exact early morning time could be achieved in several years in the NOAA series. To discuss the potential of AVHRR on NOAA of getting observations at unique crossing times, in particular, at the years that MODIS is also available for stable data in AM and PM time, AVHRR2 or AVHRR3 on NOAA-12, NOAA-14, NOAA-15, NOAA-16, NOAA-17, NOAA-18, NOAA-19 were included (Table 2.2).

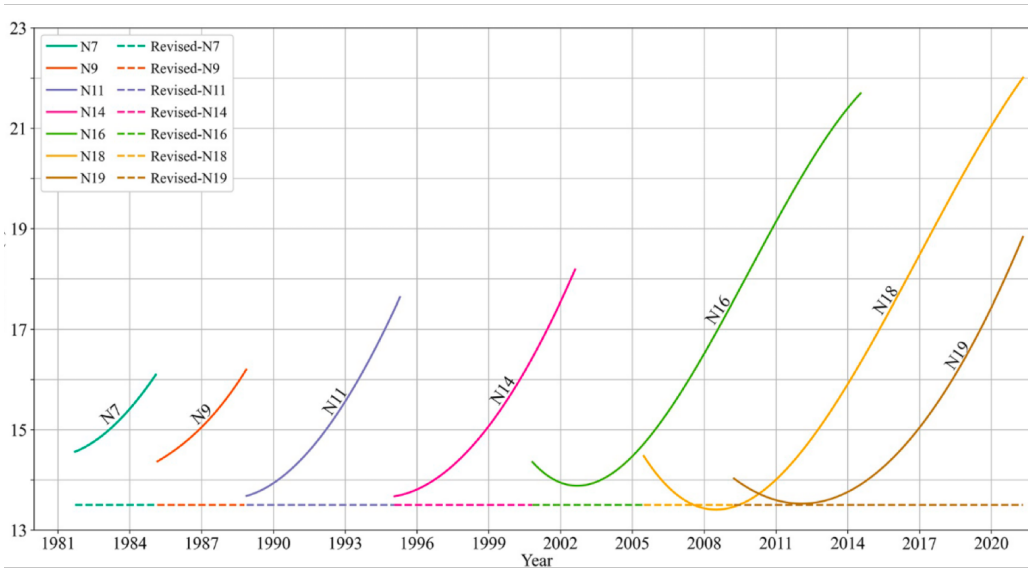

Figure 2.21 Drift of equator crossing times over the life of the NOAA afternoon Satellites (Z. Li et al., 2023).Solid line: real crossing time, dashed line: corrected uniform crossing time (https://www.star.nesdis.noaa.gov/smcd/emb/vci/VH/vh_avhrr_ect.php).

Table 2.2 NOAA satellites as candidate of early morning observations (Green: included in the discussion; Orange: out of the scope of this study or mission failure; *: still operating in 2024)

Generation	Satellite	Launch Year	Decommission Year
4th Gen	NOAA-8	1983	1985
4th Gen	NOAA-9	1984	1998
4th Gen	NOAA-10	1986	2001
4th Gen	NOAA-11	1988	2004
4th Gen	NOAA-12	1991	2007
4th Gen	NOAA-13	1993	1993
4th Gen	NOAA-14	1994	2007
5th Gen	NOAA-15	1998	2024*
5th Gen	NOAA-16	2000	2014
5th Gen	NOAA-17	2002	2013
5th Gen	NOAA-18	2005	2024*
5th Gen	NOAA-19	2009	2024*

First, for the stage during 2000 to 2010, the hourly observation frequency in two typical years: 2005 and 2010, were discussed. In 2005, NOAA-12, NOAA-14, NOAA-15, NOAA-16, NOAA-17 showed observation at three typical categories. The NOAA-12 and NOAA-15 showed an early morning (EM) observation pattern (Figure 2.22a,c). These satellites could capture observations centered at 6:00 and 17:00 for latitude at 60–70˚N and daytime observations throughout the daytime for latitude larger than 70˚N. The NOAA-14 showed a similar pattern as MODIS Terra of AM observations (Figure 2.22b). The NOAA-16 showed a pattern of PM orbit (Figure 2.22d). Interestingly, the NOAA-17 showed a shifted AM orbit that the observation of morning was shifted to afternoon and meanwhile the nighttime observation at around 20:00 was also postponed to around 22:00. In 2010, new member was included such as NOA-18 and NOAA-19, whereas NOAA-12 and NOAA-14 meet end of the life. The new platform did not showed large drift against it initial crossing time because the time did not pass two much since the launch (Figure 2.22i,j). As for NOAA-15 and NOAA-17, their crossing time did not change much comparing to the hourly observation frequency in 2005 (Figure 2.22c,e,f,h). Among these available NOAA series in 2010, the NOAA-16 was shifted from a PM orbit to EM orbit. As consequence, NOAA-12 and NOAA-15 in 2005 could provide the EM observations while in 2010 NOAA-16 can work for this purpose similarly.

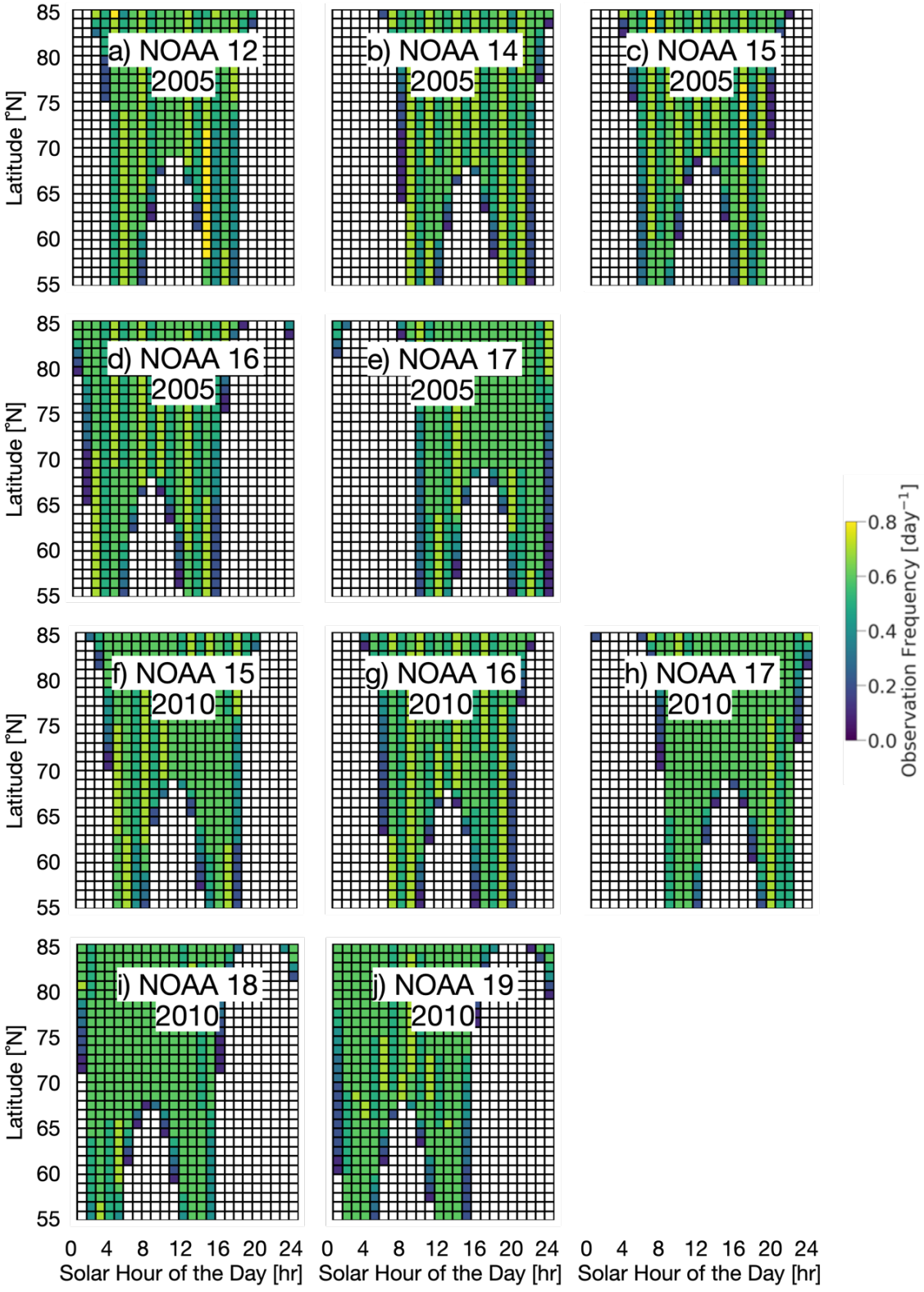
a) NOAA 12
2005
b) NOAA 14
2005
c) NOAA 15
2005
d) NOAA 16
2005
e) NOAA 17
2005
f) NOAA 15
2010
g) NOAA 16
2010
h) NOAA 17
2010
i) NOAA 18
2010
j) NOAA 19
2010
Latitude [°N]
85
80
75
70
65
60
55
0 4 8 12 16 20 24
Solar Hour of the Day [hr]
Observation Frequency [day⁻¹]
0.8
0.6
0.4
0.2
0.0

Figure 2.22 Spatiotemporal distribution of latitude-band-averaged all-sky observation frequency for NOAA satellites in 2005 and 2010. The panels represent: a) NOAA 12 (2005), b) NOAA 14 (2005), c) NOAA 15 (2005), d) NOAA 16 (2005), e) NOAA 17 (2005), f) NOAA 15 (2010), g) NOAA 16 (2010), h) NOAA 17 (2010), i) NOAA 18 (2010), and j) NOAA 19 (2010). The observation frequency was averaged for each latitude band at individual local hours of the day. Similar to Figure 2.10, Figure 2.10

As for the era in 2010s to 2020s, accompany with the era that many new platforms and missions were launched, also, the new launched NOAA series that have serious drift issues are no more presented. For example, the new launched NOAA-20, was designed to work at a stable crossing time and showed a stable PM orbit pattern (Figure 2.20d). In this period, the remaining on operating NOAA15, NOAA18, NOAA19 that had the possibility of the drifting crossing time could be used to capture the early morning observations.

Similar to the discussion in 2000-2010 period, the discussion of the possible candidates used the examples in 2015 and 2020. In 2015, NOAA-15 and NOAA-18 showed the crossing time center at around 6:00 and 5:00, respectively, were the pattern in the early morning orbit (Figure 2.23a,b). As for the NOAA-19, which was the latest launched NOAA series that presented the drift issue (Figure 2.23), showed a typical PM orbit pattern (Figure 2.23c). In 2020, the crossing time of all these platforms exhibited approximately 3–4 hours shift. Both NOAA-15 and NOAA-18 transformed from an EM orbit to an AM orbit pattern. On the other hand, the NOAA-19 exhibited the observations crossing time centered at approximately 7:00, which observed a 1.5 hour lag. As a result, NOAA-15 and NOAA-18 could be used for early morning observations around 2015 and NOAA-19 could fit the invalidity of NOAA-15 and NOAA-18 early morning observations.

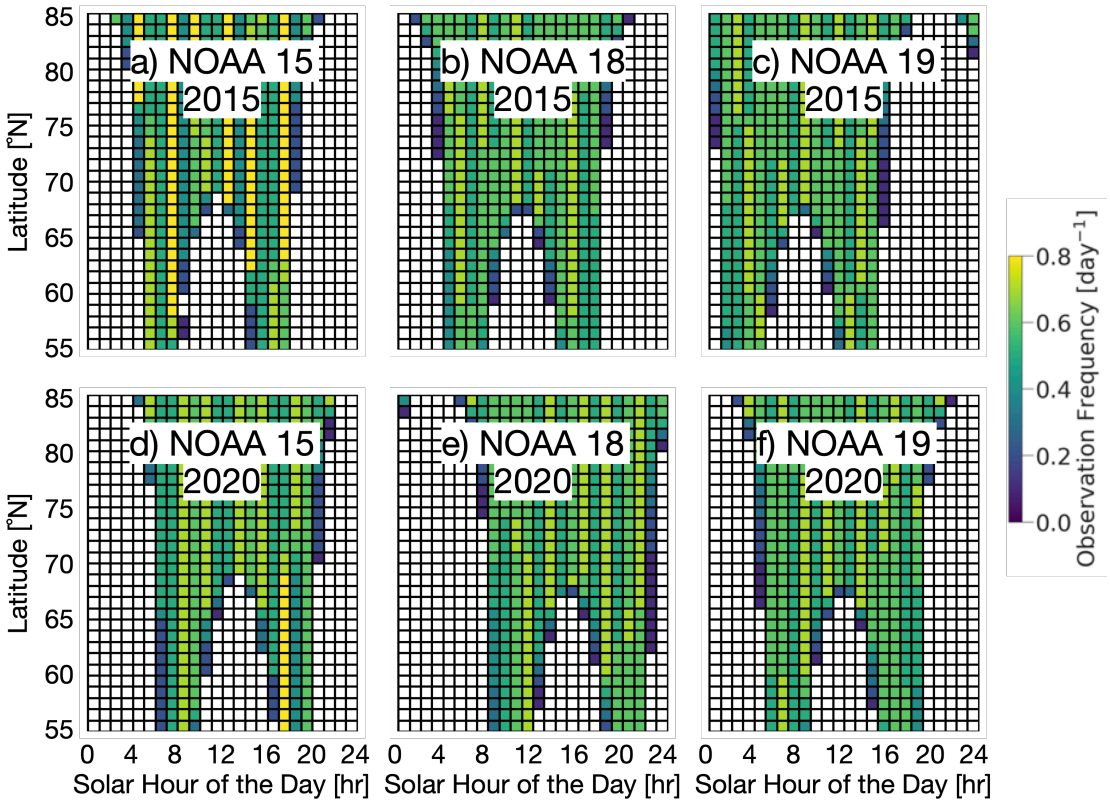

Figure 2.23 Spatiotemporal distribution of latitude-band-averaged all-sky observation frequency for NOAA satellites in 2015 and 2020. The panels represent: a) NOAA 15 (2015), b) NOAA 18 (2015), c) NOAA 19 (2015), d) NOAA 15 (2020), e) NOAA 18 (2020), and f) NOAA 19 (2020). The observation frequency was averaged for each latitude band at individual local hours of the day. Similar to Figure 2.10, Figure 2.10

2.5.4 Combination of Satellites

Reviewing section 2.3 in conjunction with Scenarios 1 and 2 from Sections 2.1 and 2.2 reveals several key points. Despite both scenarios achieving higher observation frequencies at different latitudes, it is crucial to consider alternative satellites to replace MODIS in the AM and PM orbits over the coming years, as MODIS has long exceeded its intended lifespan. Simulations of AVHRR's orbit drift show that this model can provide AM and PM coverage during certain periods. Chronologically, the timeline is divided into three phases: from 2000 to 2010, primarily involving MODIS, supported by NOAA-12, NOAA-15, and NOAA-16, which together enabled hourly LST observations around the clock; from 2010 to 2020, combining MODIS and VIIRS with NOAA-15, NOAA-18, and NOAA-19 satellites; and from 2020 onwards, led by new-generation

satellites, including the AM orbit Metop series, PM orbit SNPP and JPSS series, and the stable dawn-dusk orbit FY-3E satellite (Table 2.3). Furthermore, future orbit drifts of other satellites (for example the altitude changing of Aqua in 2020s) or new satellite missions could also be integrated to achieve new hourly LST observations.

Table 2.3 . Example of satellite candidate for constructing hourly at different era

Era	AM	PM	EM
2000–2010	MODIS Terra	MODIS Aqua	AVHRR NOAA-12 AVHRR NOAA-15 AVHRR NOAA-16
2010–2020	MODIS Terra	MODIS Aqua VIIRS SNPP	AVHRR NOAA-15 AVHRR NOAA-18 AVHRR NOAA-19
2020–	AVHRR Metop-B AVHRR Metop-C	MERSI FY-3D VIIRS SNPP VIIRS JPSS	AVHRR NOAA-19 MERSI FY-3E

2.6 Discussion on Future Satellite Missions

In this study, the high observation frequency was achieved by current available satellites. As the Pan-arctic is under rapid changes and have important influence on global climate, more sensors are expected to be employed for monitoring and understanding the LST in these regions. If assuming the mission for getting higher observation frequencies at high latitude regions, one approach is unique designing of the orbit.

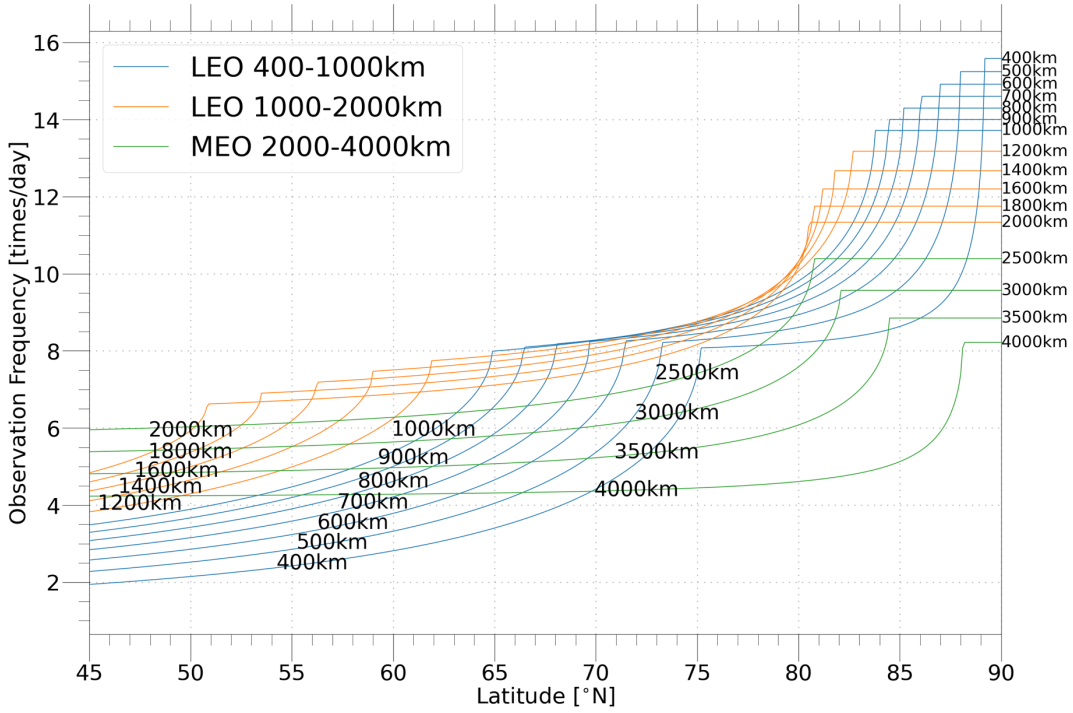

Figure 2.24 Simulated maximum observation frequency against latitude-bands at different altitude, including orbits of low earth orbit (LEO) and middle earth orbit (MEO).

Under the case using SSO as Terra, Aqua, SNPP or FY-3E, observation frequencies at different altitude are very different (Figure 2.7). Higher altitude of the orbit does not always provide more observation frequency at various latitude-bands (Figure 2.24). The observation frequency of orbit altitude from 2500km to 4000 km have smaller differences at different latitude-bands. The observation frequency at lower altitude has a complex order at different latitude-bands. For example, for latitude lower than 50˚N, the observation frequency is increasing to the higher altitude for altitude below 2000 km, however, continuous increasing of the altitude decreased the observation frequency for altitude over 2000 km. As for the latitude at 60˚N, the reverse occurred between 1200 km and 1400 km. As for higher latitude, the observation differences at different altitude of 1000 km ~ 2000 km are small.

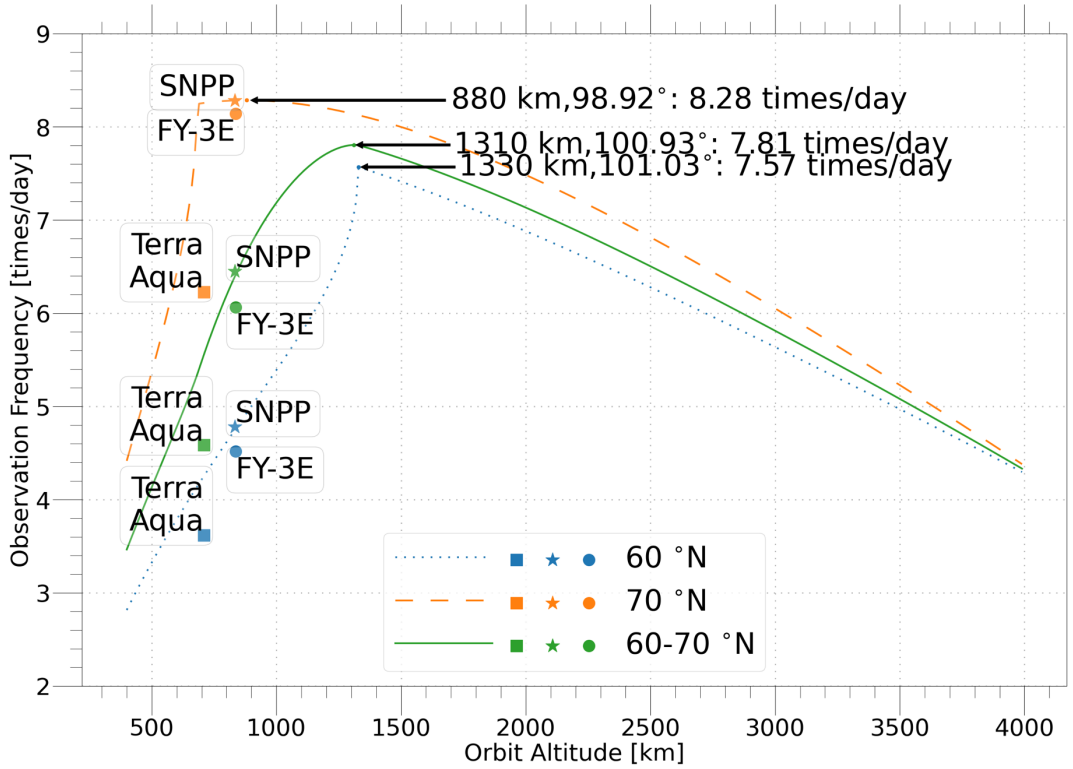

Figure 2.25 Optimized sun synchronous orbit (SSO) observation frequency at 60˚N, 70˚N, and 60-70˚N average. The markers represent the simulated observation frequency different satellites based on the asymmetrical field of view (FOV) at 55˚ (MODIS of Terra and Aqua), 56.28˚ (VIIRS of SNPP), 55.4˚ (MERSI of FY3).

Optimal altitude of SSO is different from the one of current prevailing satellites, if the optimal target are the regions at Pan-arctic regions (60˚N – 70 ˚N). If the optimal regions are the latitude of 70˚N, the optimal altitude is 880 km and simulation of current SNPP and FY-3E have already provided the closest performances, while MODIS of Terra and Aqua have large gaps to optimal observation frequency at the orbit, which is limited by its sensor maximum view angles (Figure 2.25). If the optimal regions are set to 60˚N and the regions of 60˚N – 70˚N, the optimal altitude are 1330 km and 1310 km, respectively. These altitudes are different to most of the satellite-based meteorological observation missions.

Accompany to the changing of the altitude, the shape of ground footprint of the pixels changes as well (Figure 2.26). The first is the changing of the NADIR spatial resolution. After changing altitude to 1300 km, the NADIR of VIIRS changes from 750 m to approximate 1200 m and the representative area increase 40% at both long edge and

short edge. The shape of representative footprint is close to circle for view angles below 40˚ while it is changing to the ellipse which the short edge is horizontal to the track direction.

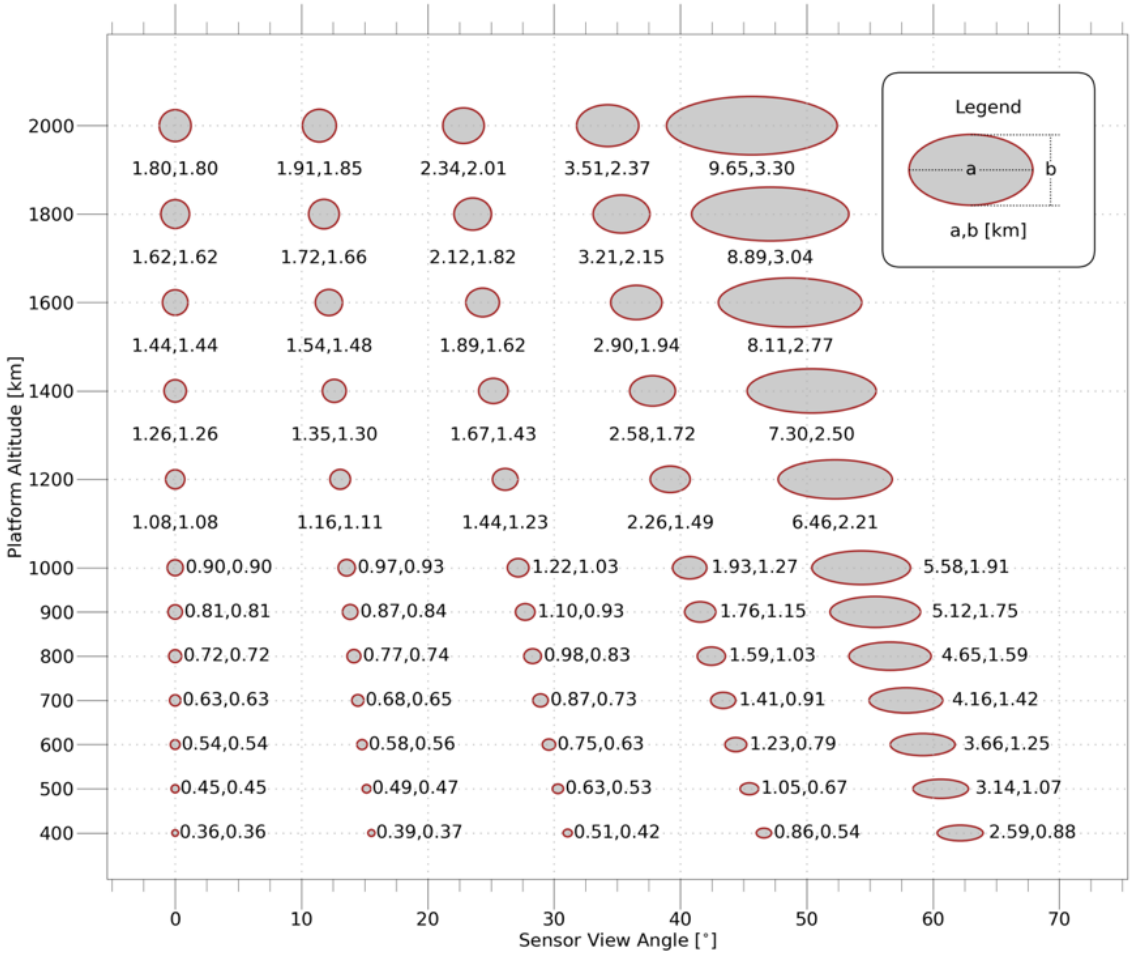

Figure 2.26 Simulated representative footprint of platform at different altitude by sensor view angle at 0, 0.2 FOV_max, 0.4 FOV_max, 0.6 FOV_max, 0.8 FOV_max, and FOV_max. The simulation assumes same sensor IFOV as VIIRS (NADIR resolution 0.75km). Maximum field of view (FOV_max) represents the sensor view angle when the edge view zenith angle (VZA) is 70˚.

Changing the inclination at the same orbit altitude can result in changing observation frequencies (Figure 2.27). Changing the inclinations breaks the stable ECT, which is similar to ISS, but have possibility to gain larger observation frequency at Pan-arctic regions. Adding a ±10˚ changing of the inclination leads to 3 more observation frequency at 70˚N and 1 more observation frequency at the regions ranging from 60˚N to 70˚N.

However, it has a slight influence to regions at 60˚N. This is because the inclination changing of only 10˚ is not large enough.

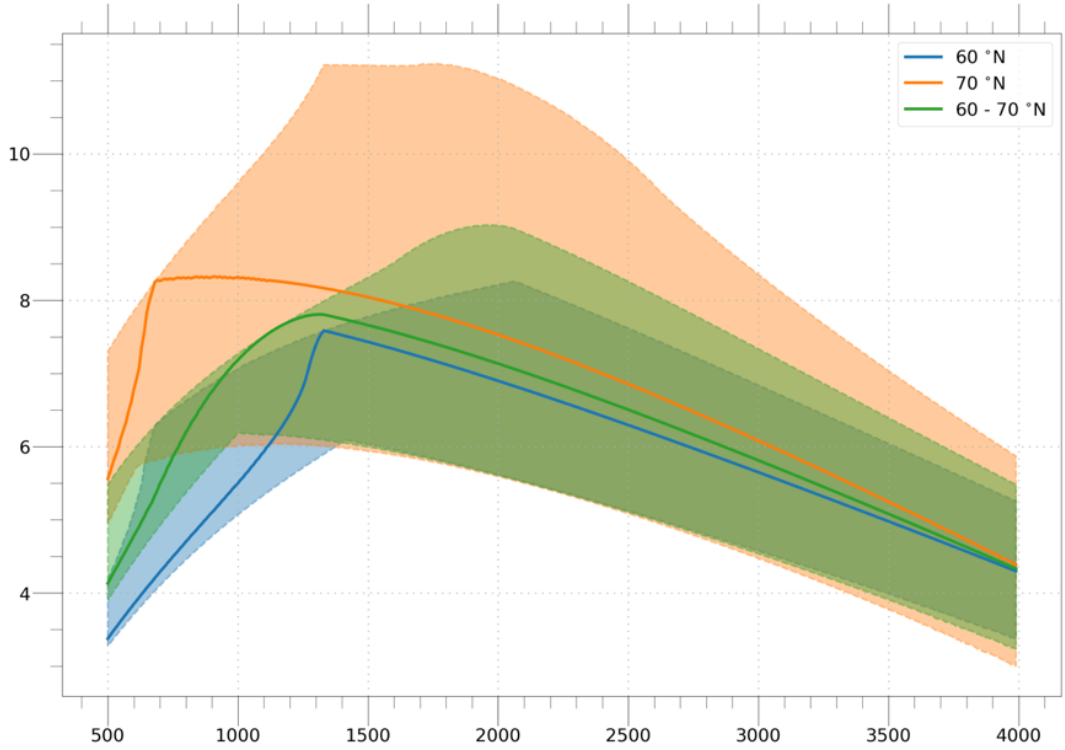

Figure 2.27 Optimal observation frequency ranges at different orbit altitude with a 10˚ title of the original SSO.

2.7 Conclusion of the Chapter

In this chapter, Sub-daily LST at high-latitude areas was achieved by compositing overlapping swath observations using different polar orbiting satellites. The observation frequency showed an increasing against latitude, and these counts are larger than 2 time per day, which refer to daytime observation and nighttime observation in our understanding. Besides, the observation frequency profiles were quantified for different latitudes, under both all-sky and cloud-free conditions, revealing that up to 23 observations per day could be achieved at 70°N, quadrupling the frequency offered by bi-daily products. Furthermore, the newly included observations using the approach filled the observation gap that was not recorded in the bi-daily LST product, particularly, in the early morning and late afternoon for the regions at latitude close to 70 ˚N.

After adding the observation of FY-3E, the gaps in the early morning and late afternoon were more effective filled. Notably, this approach can cover to regions southern

to 60˚N which was of great importance to application such as the Arctic and Pan-arctic environment monitoring and understanding the LST responses at an hourly scale.

Chapter 3 Construction of FY-3E LST and Validation of LST from Polar Orbiting Satellites

3.1 Introduction of Polar Orbiting Satellites

Low Earth Orbit (LEO) satellites operate within altitudes typically ranging from 200 kilometers to 2,000 kilometers above Earth's surface. These satellites complete orbits in approximately 90 to 120 minutes, leveraging their proximity for a range of applications including communication, Earth observation, and scientific research (Lalbakhsh et al., 2022). The strategic positioning of LEO satellites enables them to offer significant advantages in data transfer speeds and sensor accuracy. For instance, when equipped with sensors of the same Instantaneous Field of View (IFOV), LEO satellites can achieve superior spatial resolution compared to their counterparts in Medium Earth Orbit (MEO) or GEO (Lalbakhsh et al., 2022).

The exceptional capability of LEO satellites for precise and consistent Earth monitoring is particularly evident in their use of sun-synchronous polar orbits. These orbits are designed to synchronize with the Sun, ensuring that each orbital pass over a particular area of Earth occurs at the same local solar time. This consistency is crucial for environmental and scientific observations, as it maintains stable lighting conditions, facilitating comparable data collection across different times and dates. For example, studies have shown that (sun-synchronous) polar orbiting satellites are instrumental in observing climate phenomena, monitoring ecosystem changes, and managing natural disturbances at short time span or over long term (Chandrasekar et al., 2010; Gitelson et al., 2012b; X. Li et al., 2021; Nemani et al., 2003a; Sims et al., 2006; X. Wang et al., 2021). Furthermore, the research indicates that the repeated coverage provided by these orbits allows for the collection of a series of temporally consistent images, which are vital for tracking changes over time (X. Li et al., 2021). The ability of polar orbiting satellites to frequently revisit the same area enhances the temporal resolution of observations, making them particularly useful for time-sensitive applications such as real-time meterological/environmental monitoring and tracking rapid response activities (Waigl et al., 2017).

In this study, the sun-synchronous satellites were mainly used and discussed. Thus, LEO in this chapter hereafter refers to polar orbiters with sun-synchronous properties in most of the cases. The reason for using polar orbiting satellites was described in **section 1.3 in Chapter 1** for its advantage in high latitude Pan-arctic and Arctic regions. In this chapter, the LST construction of LST for a new sensor on a new platform – FY-3E was introduced first in detail. Then, the constructed product was conducted with cloud mask checking, uncertainty analysis, and was validated at the in situ observations or compared to the LST from other satellite-based products to ensure its performance. At the remaining pages, the validation of LST products from other polar orbiting satellites for extra-LST and swath LST make sure the same performance of the LST that were used for producing bi-daily products or not. This will support that the approach was reasonable when utilizing all the swath data.

3.2 Introduction of MERSI-LL FY-3E and Related Data

The FY-3 series of satellites represent a significant advancement in China's meteorological monitoring capabilities, enhancing both national and global weather forecasting and environmental monitoring (Tang, Zhang, & Wang, 2014). Launched by the China Meteorological Administration (CMA), the FY-3 series includes multiple polar-orbiting satellites equipped with sophisticated sensors designed to collect a variety of meteorological data. Each FY-3 satellite carries multiple payloads, including visible and infrared radiometers, microwave sensors, and other instruments that significantly enhance observational capabilities. These satellites are crucial for observing atmospheric and environmental changes, collecting data on cloud properties, ocean color, and sea surface temperatures, among others (Cheng et al., 2023; Zeng et al., 2021; Zou, 2021).

The Fengyun-3E (FY-3E) satellite, launched on July 5, 2021, marked a significant advancement in meteorological observation as the world's first early-morning-orbit meteorological satellite for civilian use (P. Zhang et al., 2022). Launched from the Jiuquan Satellite Launch Center. The satellite's data are received and processed through a network of ground stations located globally, including both domestic (Beijing, Guangzhou, Urumqi, Jiamusi, and Kashi) and international stations (Kiruna and Troll). These stations facilitate the rapid processing and dissemination of satellite data, essential

for real-time weather forecasting and climate monitoring. The ground system's design ensures data is received and processed with minimal latency, supporting the global meteorological community (P. Zhang et al., 2022). FY-3E fills a crucial gap in global early-morning-orbit satellite observations. It works in conjunction with the FY-3F and FY-3D satellites to provide comprehensive data coverage across early morning, morning, and afternoon orbits towards the nights. This trio of satellites enhances the accuracy and efficiency of global numerical weather prediction (NWP) by offering data at 6-hour intervals, thereby significantly improving the global earth observing system (WMO, 2013).

FY-3E operates on a sun-synchronous orbit at the height approximately 836 km with an inclination at approximately 98.75˚. It has a unique equatorial crossing time (ECT) at approximately 5:30 under the descending node and another ECT at approximately 16:30 for another typical bi-daily revisit. FY-3E is equipped with 11 onboard instruments designed to capture a wide range of atmospheric data (Figure 3.1) (P. Zhang et al., 2022). These instruments include one imager–medium resolution spectral imager with low-light capability (MERSI-LL), the Microwave Humidity Sounder-II (MWHS-II), which is also on the FY-3D satellite, and new devices such as the dual-frequency wind radar (WindRad), the solar spectral irradiance monitor (SSIM), and the solar X-ray and extreme ultraviolet imager (X-EUVI). This diverse suite of tools allows for comprehensive monitoring of meteorological, oceanographic, and solar-terrestrial parameters.

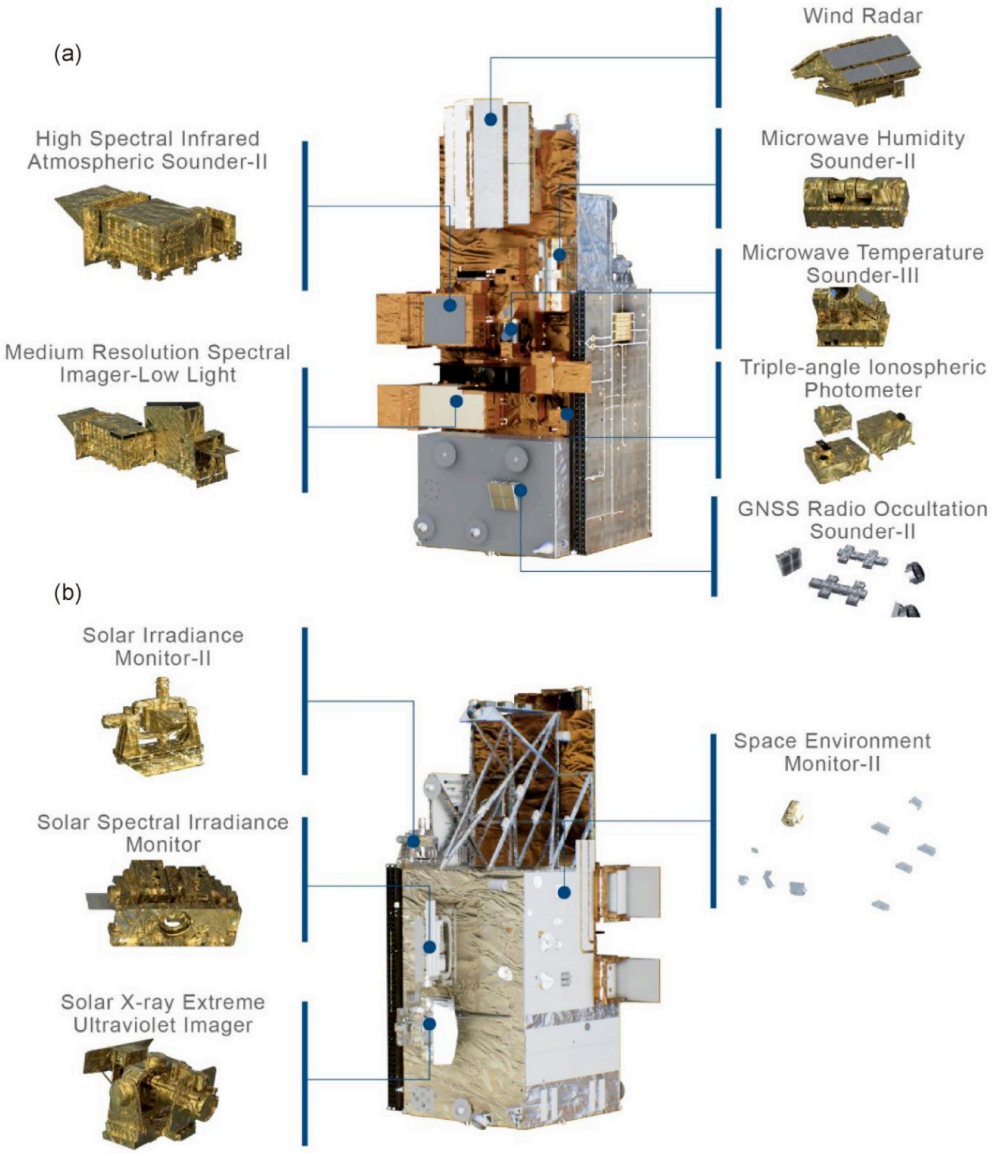

Figure 3.1 The FY-3E spacecraft model and onboarding payload instruments (P. Zhang et al., 2022)

FY-3E is expected to make LST observation at its unique ECT approximately 5:30 local standard time by utilizing the onboarded MERSI-LL. MERSI-LL consists of one panchromatic visible channel operable with low-level illumination (band 1) and 6 thermal infrared channels (band 2-7,Figure 3.2). The panchromatic visible channel can work with changing illumination under different gain at visible ranges but not suitable for LST retrieval. The center wavelengths for TIR bands from band 2 to 7 are 3.90um, 4.05 um, 7.20um, 8.55um, 10.8 um, and 12.0 um, respectively (Figure 3.2). Not all the bands were

eligible for LST retrieval and only band 5-7 was used. Band 2 and 3 fall within 3-5um atmospheric window, with acceptable sensitivity to CO2 and water vapor content. Although some studies are adapting TIR band around this band width, it was not a common way in the community (Zeng et al., 2021). Additionally, due to their proximity to the shortwave infrared range, these bands are more susceptible to solar irradiation noise during the daytime (Sun, 2003). Band 4 is characterized by very low atmospheric transmittance and is typically used for top layer water vapor retrieval, making it unsuitable for land observation missions (Sun, 2003). Remaining Band 5-7 located within the 8-14 um atmospheric window, are good candidate for land observation missions. Band 5 (8.55 um) has a center wavelength similar to MODIS band 29 (8.55 um) and VIIRS band M14 (8.55 um). Band 6 (10.8 um) has a close center wavelength to MODIS band 31 (11.03 um) and is similar to VIIRS band M15 (10.76 um). Band 7 (12.0 um) has a center wavelength similar to MODIS band 32 (12.02 um) and VIIRS band M16 (12.02 um). These aforementioned typical wavelengths of the bands were used to LST retrievals in previous studies and confirmed the performances and robustness. For, example, MODIS or VIIRS bands were used in each TES method-based product (Figure 3.2) or in dual-channel method-based product using the 11 um and 12um bands only. Therefore, band 5-7 were deemed suitable for triple-channel method (TES: Temperature and Emissivity Separation) and were selected as the satellite data input for FY-3E LST production. Groups of similar MERSI-LL, MODIS, and VIIRS channels are hereafter referred to as TES bands, namely, TES B1, TES B2, and TES B3, respectively (corresponding to the official band ID 5, 6, and 7 for MERSI-LL FY-3E).

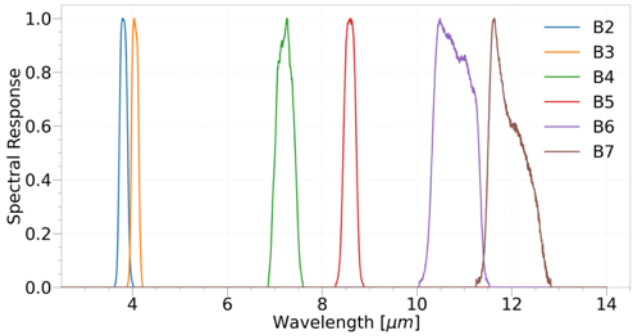

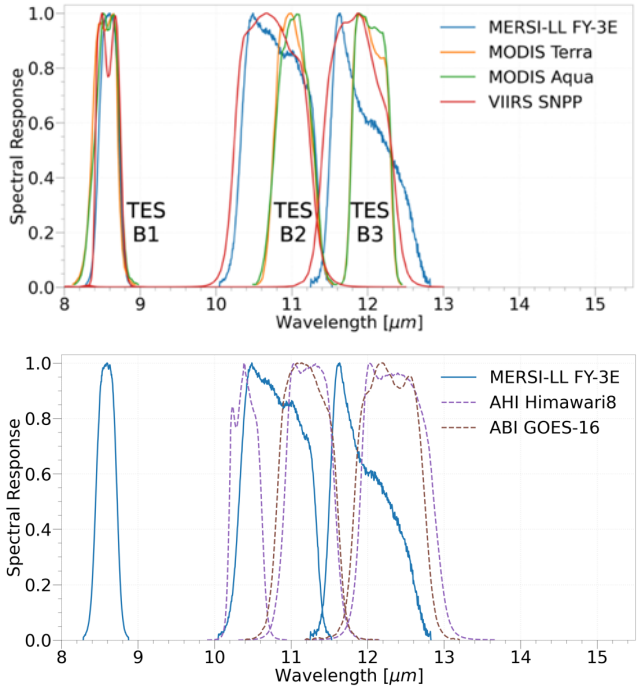

Figure 3.2 Spectral response function (SRF) of polar orbiting platforms and GEO platforms. a) SRF of MERSI-LL FY-3E. b) SRF of three temperature and emissivity separation (TES) channels on each polar orbiting satellite, including MERSII-LL FY-3E, MODIS Terra, MODIS Aqua, and VIIRS SNPP. c) SRF of the TIR bands on two GEO satellite AHI on Himawari-8 and ABI on GOES16. Different colors represent the SRF of different sensor-platforms. For each sensor-platform in b) , TES B1 with a central wavelength of approximately 8.6 μm, TES B2 at approximately 11 μm, and TES B3 at approximately 12 μm, were individually plotted with the same color.

The L1 Radiance data (FY3E_MERSI_GRAN_L1) of band 5, band 6, and band 7 were used for MERSI-LL FY-3E LST retrieval. The original data was given with unit $\mathrm{mW/(m^2 \cdot cm^{-1} \cdot sr)}$ which can be converted from the digital number (DN) with the scaling factor 0.01. Specifically, band 5 possesses a nadir spatial resolution of approximately 1 km, whereas bands 6 and 7 both have a nadir spatial resolution of 250 m. Notably, a 1 km rescaled resolution versions for both bands 6 and 7 was used to generate 1 km MERSI-LL FY-3E LST. Such resolution converting was bundled with the original dataset. Additionally, an extra 1 km geolocation data product associated with MERSI-LL FY-3E L1 radiance data was applied for locating pixels at site coordinates, reprojecting the LST outputs and indicating water-land mask. These datasets were

provided by the data portal of National Satellite Meteorological Center (NSMC, url: http://www.nsmc.org.cn/nsmc/en/home/index.html).

The following data were included in the LST retrieval procedure: 1. MERSI-LL FY-3E L1 radiance, which was used as an input to solve the TIR radiative formulas in sections II-B and II-D; 2. Modern-Era Retrospective analysis for Research and Applications version 2 (MERRA-2) atmospheric profiles and surface conditions were used to estimate other remaining atmospheric components of the radiative formulas; 3. MODIS Nadir Bidirectional Reflectance Distribution Function Adjusted Reflectance (NBAR) product (MCD43A4) was used to calculate the vegetation and water indices to determine gray body pixels, which was used to refine the atmospheric terms obtained in step 2.

3.3 Overview of the LST Retrieval Algorithm

3.3.1 Basis of TIR Remote Sensing

A satellite equipped with an infrared sensor monitors Earth's surface by measuring the radiation emitted by the Earth and its atmosphere. This measurement relies on the Radiative Transfer Equation (RTE) and assumes a clear atmosphere in thermal equilibrium, as depicted in Figure 3.3. At the top of the atmosphere (TOA), the infrared radiance, designated as I_i, is captured by the sensor. The satellite-measured radiance is comprised of two main components: the land surface radiance as perceived at the sensor, and the atmospheric upwelling term. These are calculated using specific equations incorporating zenithal and azimuthal viewing angles, θ and φ. For simplicity, these angles are omitted in subsequent formulas. Furthermore, for ease of calculation, the emission and scattering terms, typically derived from Radiative Transfer Model (RTM) output, are treated as a single, uniform element. Additionally, in accordance with Wien's Law and due to their relatively small magnitude compared to Earth's surface emission, solar beam-related reflected terms are disregarded, particularly in the 8-14 μm wavelength range (Coley, P., & Jonas, P. 1999). Based on this assumption, it will eliminate the component 3, 6 and 7.

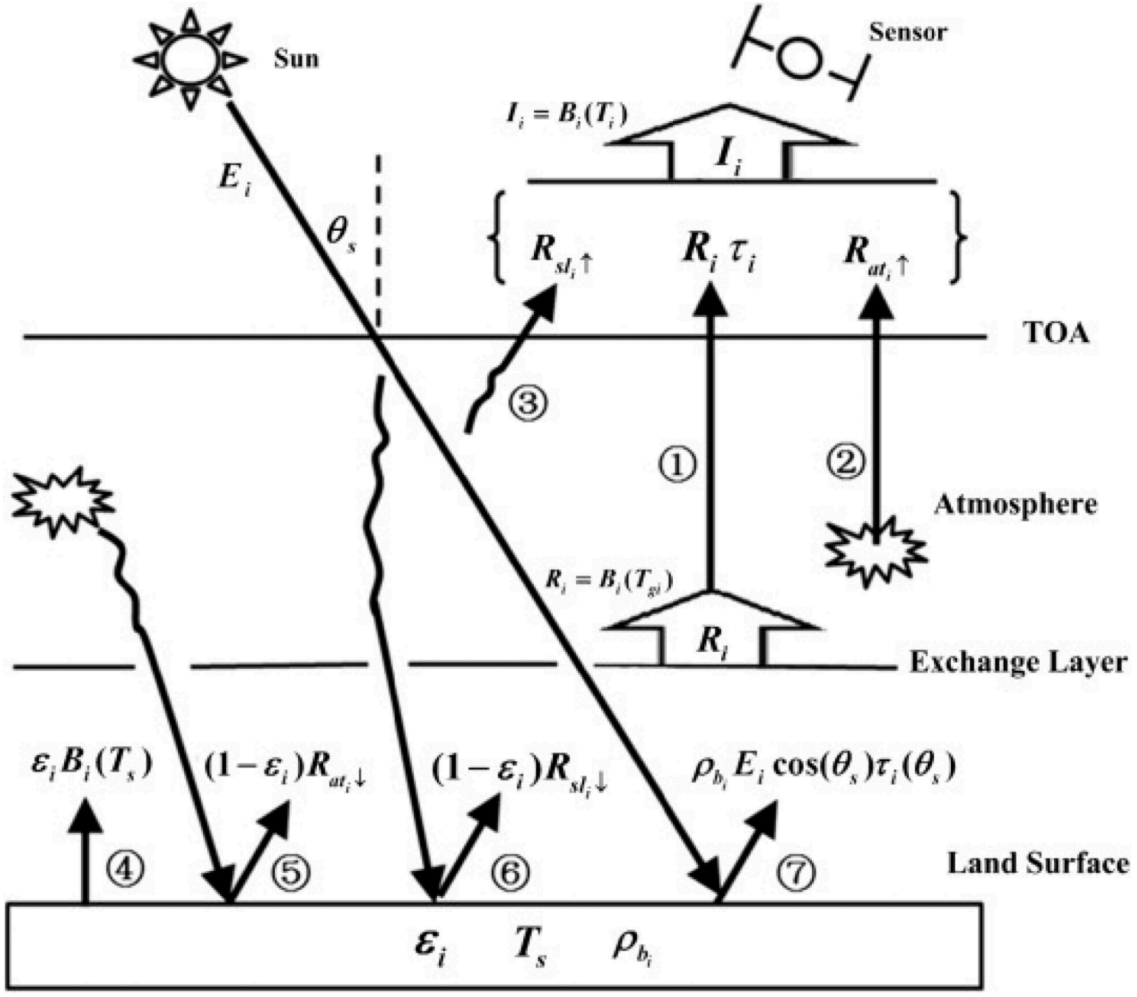

$$I_i(\theta,\varphi) = \underbrace{R_i(\theta,\varphi)\tau_i(\theta,\varphi)}_{\substack{\text{Surface outgoing radiation term}\\ \text{attenuated by the atmosphere}}} + \underbrace{R_{at_i}\uparrow(\theta,\varphi)}_{\text{Atmospheric emission term}} + \underbrace{R_{sl_i}\uparrow(\theta,\varphi)}_{\text{Atmospheric scattering term}},$$

$$R_i(\theta,\varphi) = \underbrace{\varepsilon_i(\theta,\varphi)B_i(T_s)}_{\text{Surface emission term}} + \underbrace{\left[1-\varepsilon_i(\theta,\varphi)\right]R_{at_i}\downarrow}_{\substack{\text{Surface reflected downwelling}\\ \text{atmospheric emission term}}}$$

$$+ \underbrace{\left[1-\varepsilon_i(\theta,\varphi)\right]R_{sl_i}\downarrow}_{\substack{\text{Surface reflected downwelling}\\ \text{atmospheric scattering term}}} + \underbrace{\rho_{b_i}(\theta,\varphi,\theta_s,\varphi_s)E_i\cos(\theta_s)\tau_i(\theta_s,\varphi_s)}_{\substack{\text{Surface reflected downwelling}\\ \text{solar beam term}}},$$

Figure 3.3 Conception of the radiative transfer model and equations in infrared wavelengths. Here, I_i is the radiance detected by channel i of satellite platform. ①-⑦ represent the compoents in the model corresponding to the equation in the bottom fomula. (Li et al., 2013)

Under the simplification and assumption that the land surface acts as a Lambertian reflector, the land-leaving radiance can be succinctly described following by equations:

$$I_i = \tau_i L_{g,i} + L^{\uparrow}_{a,i} \quad (3\text{-}1)$$

$$L_{g,i} = \left[\varepsilon_i B_i(T_s) + (1-\varepsilon_i) L^{\downarrow}_{a,i}\right] \quad (3\text{-}2)$$

where, i is the MERSI-LL FY-3E TIR band number, L_i is the at-sensor radiance, $L_{g,i}$ is the at-surface land leaving radiance, $L^{\uparrow}_{a,i}$ is the atmospheric upwelling radiance, $L^{\downarrow}_{a,i}$ is the atmospheric downward radiance, τ_i is atmospheric transmittance, ε_i is the surface emissivity, T_s is the LST, and $B_i(T_s)$ is the Planck function of the specific band i as follows:

$$B(\lambda, T) = \frac{2hc^2}{\lambda^5} \frac{1}{e^{\frac{hc}{\lambda k T}} - 1} \quad (3\text{-}3)$$

$$B_i(T_s) = \frac{\int B(\lambda, T) \times \alpha_i(\lambda) d\lambda}{\int \alpha_i(\lambda)\, d\lambda} \quad (3\text{-}4)$$

where, B(λ,T) $[W \cdot m^{-2} \cdot sr^{-1} \cdot m^{-1}]$ is the spectral radiance of the blackbody, which represents the amount of energy it emits at a certain temperature T [K] and wavelength λ [m], and it is same to $B_i(T_s)$ for band with id I at wavelength λ. *h* is Planck's constant, approximately 6.626×10^{-34} [J·s]. *c* is the speed of light in a vacuum, approximately 2.998×10^{8} [m/s]. k is the Boltzmann constant, which relates the average kinetic energy of particles in a gas with the temperature of the gas. Its value is approximately 1.381×10^{-23} [J/K]. $\alpha_i(\lambda)$ is the spectrum response function of band i for MERSI-LL FY-3E. This simplification facilitates a more streamlined approach to interpreting satellite data, while maintaining a focus on the most significant radiative components for Earth observation. Based on these equations, there are 3 unknown components for each band: the radiance from atmosphere, the land surface emissivity (LSE) of band i and the kinetic surface temperature. Only the kinetic surface temperature is same among different bands. Thus, most of the LST retrieval methods were trying to determine the individual band LSE or atmospheric radiations for individual bands to solve the LST in the equation.

3.3.2Introduction of LST Retrieval Method

Approaches for LST retrieval include methods such as Single Channel Algorithm (SC), Generalized Split Window (GSW),and Temperature and Emissivity Separation (TES) (Z. Li et al., 2023). The SC requires both atmospheric information and land surface

emissivity (LSE) information, whereas multi-channel algorithms such as GSW or TES requires LSE information or atmospheric information under the assumption that LSE can be retrieved from land surface types or that the relationship between the minimum LSE and spectral contrast remains consistent across the full spectrum of surface materials. The GSW is widely used on sun-synchronous platforms, such as the Moderate Resolution Imaging Spectroradiometer (MODIS) on Terra and Aqua or the Visible Infrared Imaging Radiometer Suite (VIIRS) on the Suomi National Polar-orbiting Partnership (SNPP) (Guillevic et al., 2014). The method is also used on geostationary platforms, such as the Advanced Himawari Imager (AHI) on Himawari-8 and the Advanced Baseline Imager (ABI) on GOES-16 (Chang et al., 2021; Yamamoto et al., 2022). The LSE atlas was mainly estimated using vegetation fractions and the existing spectrum of samples that represent the vegetation and the underlying surfaces (Cheng et al., 2023). TES algorithms have been developed since the 1990s to simultaneously retrieve LST and LSE, and initial attempts have been successful for the Advanced Spaceborne Thermal Emission and Reflection Radiometer (ASTER) (Gillespie et al., 1998), which inspired the development of TES-based products for MODIS and VIIRS (Islam et al., 2017; Malakar and Hulley, 2016). TES algorithm does not require the LSE but need the accurate atmospheric radiation retrieval. Recently, a SW-TES method have be developed that combines the idea of GSW and TES (Zheng et al., 2022, 2019). It used a GSW method at the specific band wavelength to determine the approximate $L_{g,i}$ in the formula and then used the TES method to separate the LSE and LSE.

3.3.3 TES overview

TES was used in this study for several reasons. First, TES is thought to achieve better performance over barren regions because it can retrieve the changing LSEs over soil and rock surfaces. A GSW-based LST product for MERSI-LL FY-3E is associated with large uncertainties over barren regions, and the number of available validation sites is limited (Cheng et al., 2023). Examination of LSTs obtained for barren sites in China using MODIS TES and MODIS GSW showed that the TES method produced better daytime LST results (H. Li et al., 2021). Second, fewer LST differences among products were observed when combining TES LST products than when combining GSW LST products; for example, a bias reduction of approximately 1 K was observed when MODIS was

combined with VIIRS (Hulley et al., 2018). Similarly, biases should also be reduced when early morning LST is combined with LST measured by other satellite products, which should also aid in constructing diurnal LST cycles. Third, TES can simultaneously retrieve the LSE, which is helpful for understanding how emissivity changes over long time span (Hulley et al., 2018). Finally, to the best of our knowledge, this is the first study to explore the use of the TES method for LST products from the MERSI-LL FY-3E at dawn and dusk.

Solving the LST using TES method mainly relies on the following processes: 1) Determine the atmospheric components; 2) The refinement of the atmospheric components by scaling method and interpolation; 3) Using constrain of minimum LSE and the emissivity contrast to solve the LST.

The surface leaving radiance (L_{gi}) can be corrected from at sensor radiance while atmospheric path radiance ($L_{ai}^{\uparrow}$) and atmospheric transmittance (τ_i) are properly estimated. These atmospheric parameters are typically estimated using a physical radiative transfer model (RTM) with atmospheric profile input. Two widely used RTMs for estimating atmospheric parameters in land surface temperature (LST) retrieval tasks are Radiative Transfer for (A)TOVS (RTTOV) and MODerate resolution atmospheric TRANsmission (MODTRAN) (Berk et al., 2014; Saunders et al., 2018; Zeng et al., 2021; Zhou and Cheng, 2020). To achieve efficient processing and good consistency, this research adopted RTTOV (version 13) in both the model building procedures and LST production processes.

The RTTOV model is an essential tool in meteorology, particularly in the realms of satellite data assimilation and numerical weather prediction (NWP). RTTOV was initially developed for the TIROS Operational Vertical Sounder (TOVS) radiometers by EUMETSAT-funded Numerical Weather Prediction Satellite Application Facility (NWP SAF) (Matricardi et al., 2004). It plays a crucial role in interpreting satellite observations of radiation, particularly in the microwave and sub-millimeter spectral regions, which range broadly from 1 to 1000 GHz. With officially provided sensor coefficient settings, RTTOV can now be applied to different satellite sensors with measuring spectra ranging from microwave (MW) and infrared (IR) to visible (VIS).

Temperature and water vapor atmospheric profile are necessary for spinning up RTTOV. Such data is available from radiosonde observations at fixed locations but

cannot be directly used at large scales. Therefore, a common approach is to apply a re-analyzed meteorological profile during the production stage of satellite LST retrieval tasks (Gillespie et al., 1998). In this study, the atmospheric profile from the Modern-Era Retrospective analysis for Research and Applications version 2 (MERRA-2) was utilized, which was widely used for LST retrieval with various sensors/platforms, including VIIRS and Himawari-8 (Islam et al., 2017; Zhou and Cheng, 2020). A MERRA2 instantaneous 3-dimensional 3-hourly data collection (M2I3NVASM or inst3_3d_asm_Nv, V5.12.4) consists of assimilations of meteorological parameters at 72 model layers was selected (Global Modeling And Assimilation Office and Pawson, Steven, 2015a). This data collection provided the profiles of temperature, water vapor content, ozone, and pressure layers within 1000 hPa with a 0.5˚ x 0.625˚ (latitude x longitude) spatial resolution. Additional surface data at same spatial resolution, a MERRA2 hourly time-averaged 2-dimensional data collection (M2T1NXSLV or tavg1_2d_slv_Nx, V5.12.4), was employed to provide near-surface meteorological parameters in order to meet the input requirement of RTTOV, for example, near surface 2m air temperature, near surface 2m atmosphere pressure and near surface 2m water vapor content (Global Modeling And Assimilation Office and Pawson, Steven, 2015b).

The preliminary atmospheric terms using RTTOV and MERRA-2 still have some degree of uncertainty. Therefore, additional steps are required to producing a more accurate ones before moving to the final TES algorithm solving step (Tonooka, 2001). Firstly, at gray body pixels, MERSI-LL FY-3E land leaving term at each band was estimated using an empirical relationship based on at-sensor BT and total precipitable water (TPW). Secondly, a water vapor scaling (WVS) method is applied using land leaving terms calculated in previous step, to refine atmospheric terms at gray pixels (mainly judging from MCD43A4 reflectance-based indices). Thirdly, the WVS-corrected atmospheric transmittance and atmospheric path radiance at gray pixels were horizontally interpolated to none gray pixels and then smoothed across the whole image. Simultaneously, the downward atmospheric radiances were estimated from nadir-corrected atmospheric path radiances using a quadratic polynomial regression. Finally, the TES algorithm was applied to solve LST and band emissivity using the atmospheric components obtained and refined in the previous steps (Gillespie et al., 1998).

3.4 Sub-process in FY-3E LST Retrieval

3.4.1 Cloud Mask Construction and Validation

A machine learning approach - Gradient Boosted Decision Tree (GBDT) (Ke et al., 2017), which was optimized for large dataset, was utilized to predict the cloud mask based on the MERSI-LL FY-3E brightness temperature (BT) and view zenith angle (VZA) as input variables. GBDT is a popular machine learning algorithm used for both regression and classification tasks. It is an ensemble technique that builds the model in a stage-wise fashion. It constructs the model by sequentially adding predictors, where each one corrects its predecessor, hence the term "boosting". The "gradient" part comes from the use of gradient descent algorithm to minimize the loss when adding new models. One of its implements - LightGBM, offers efficient memory usage. LightGBM is an open-source gradient boosting framework developed by Microsoft and is widely used for a variety of tasks, including classification, regression, and ranking problems. In our study, binary log loss was selected as the loss function for the LightGBM GBDT classification task during training and validation.

The RTM - RTTOV was applied with various sample atmospheric profiles (Figure 3.4, Figure 3.5), cloud scenarios, VZAs, and LST-air temperature differences to generate the simulated at-sensor radiance and associated inputs. The sample profiles were obtained from the SeeBor database (Version 5.0) (Borbas, E. E. et al., 2005) and filtered for land areas. The profiles with relative humidity below 90% for all layers were used as clear condition profiles (Figure 3.5a), whereas profiles with the relative humidity greater than 95% for any layer were used as cloud condition profiles. Clouds were generated at 80 hPa, 180 hPa, 310 hPa, 440 hPa, 560 hPa, 680 hPa, and 800 hPa to represent different cloud types (Figure 3.5b), with assigned cloud fractions of 0 and 0.1 denoted "cloud-free" with clear condition profiles, and cloud fractions of 0.7 and 0.9 denoted "cloud" with cloud condition profiles. VZAs between 0° and 70° were randomly selected to simulate the actual satellite viewing geometry. The LST values were set according to variable offsets from the surface air temperature (–10 K, –5 K, 0 K, 5 K, 10 K, or 15 K), and only profiles with LST values between 220 K and 340 K were retained (Zhou and Cheng, 2020). Finally, the simulated radiances and generated ancillary inputs were used to construct a dataset containing 14,417,480 instances, and it was utilized to train the cloud classification model.

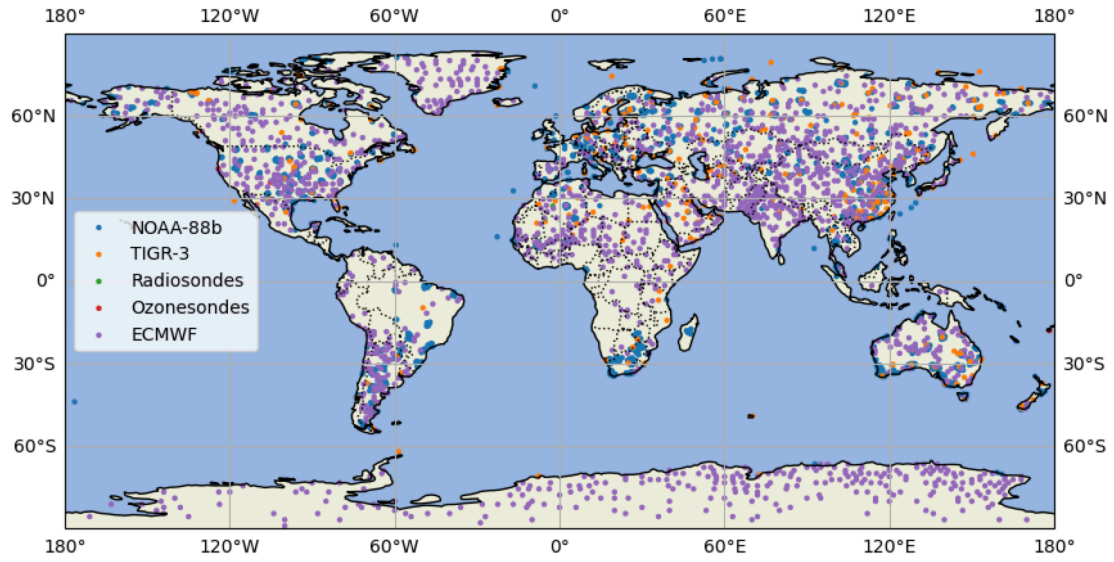

Figure 3.4 Global distribution atmospheric profile data points at clear sky conditions collected from various sources for the SeeBor V5.0 database. This map illustrates the geographic spread of temperature, moisture, and ozone profiles collected by NOAA-88b, TIGR-3, radiosondes, ozonesondes, and ECMWF, represented by different colors.

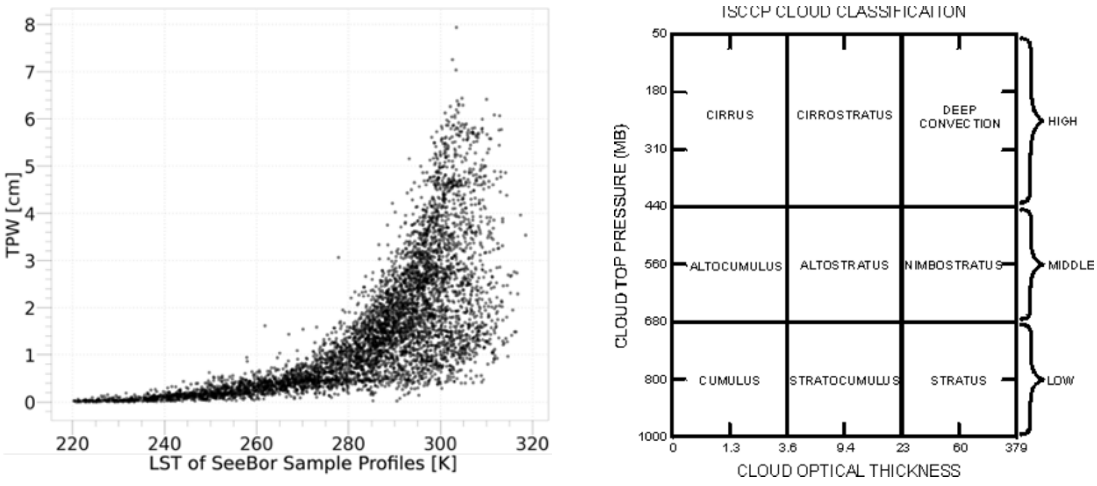

Figure 3.5 a) Total Precipitable Water (TPW) and simulated land surface temperature (LST) of the SeeBor profile used in this study. b) Cloud scenario using the cloud definition of ISCCP for cloud at High, Middle and Low altitude.

The performance of the trained cloud mask product was evaluated on a random held-out test set comprising 10% of the simulated data. The 10% validation showed a binary log loss of 0.071 and confusion matrix metrics as follows: true positives (TP) of 0.620, false positives (FP) of 0.016, false negatives (FN) of 0.011, and true negatives (TN) of

0.353. The corresponding recall, precision, accuracy, and F-score were 0.983, 0.975, 0.973, and 0.979, respectively. Based on this accuracy assessment, the model was retrained using the combined training and validation subsets to generate the final cloud-masking algorithm employed in the subsequent LST retrieval procedures.

To ensure the performances of cloud mask, the cloud mask was intercompared to the one from other satellites. To overcome the ECT differences of polar orbiting satellites, the intercomparison target were the cloud mask from geostationary satellites. In this study we adopted the cloud mask of two most widely used sensor platform: AHI on Himawari-8 and ABI on GOES16. The cloud mask product of AHI Himawari has two categories: cloud and clear, while the cloud mask product of ABI GOES16 has four levels as following: clear, probably clear, probably cloud and cloud. Here the clear is regarded as clear while other flags were considered as cloud.

The FY-3E cloud mask constructed in this study had good consistency with the cloud mask product of AHI on Himawari-8 and ABI on GOES-16 (Figure 3.6) during the entire validation period. The overall accuracy of the cloud mask was approximately 0.8 against both GEO cloud masks. At different surface conditions, including barren (NDVI < 0.3), and vegetation (NDVI ≥ 0.3), and pixels at elevations lower than 1000m (DEM $\leq$ 1000m), the MERSI-LL FY-3E cloud mask exhibited similar accuracies. However, uncertainty became slightly larger when compared to the ABI GOES-16 cloud mask for pixels at elevations higher than 1000 m (DEM > 1000 m). Comparing between the cloud mask in summertime and wintertime, largest difference was observed against AHI Himawari-8 cloud mask, whereas less variation of it in ABI GOES16 cloud mask products, particularly, over the barren surfaces (Figure 3.6b, Figure 3.6c).

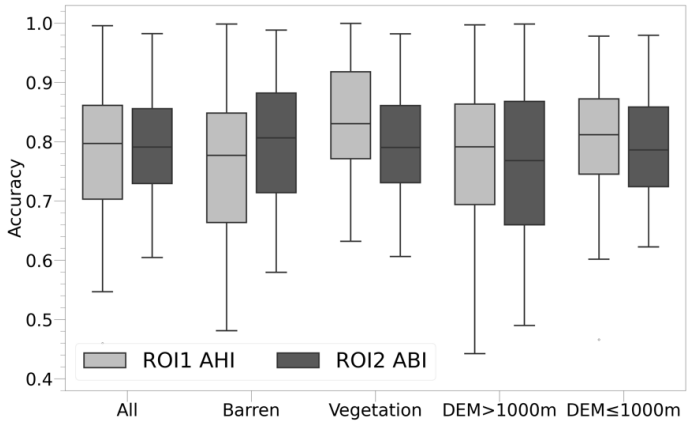

a) summer+winter

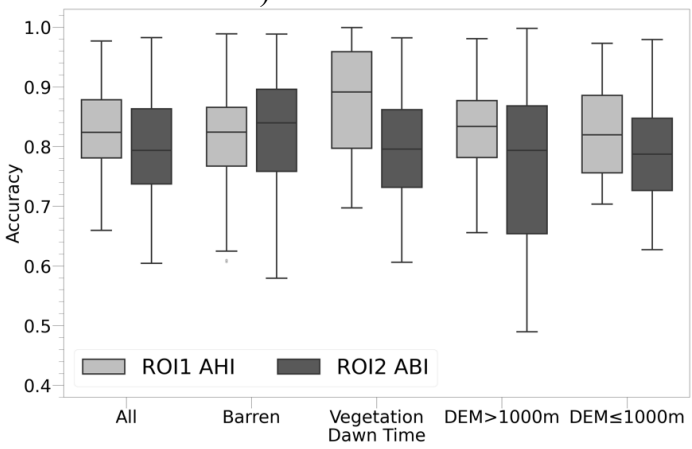

b) summer

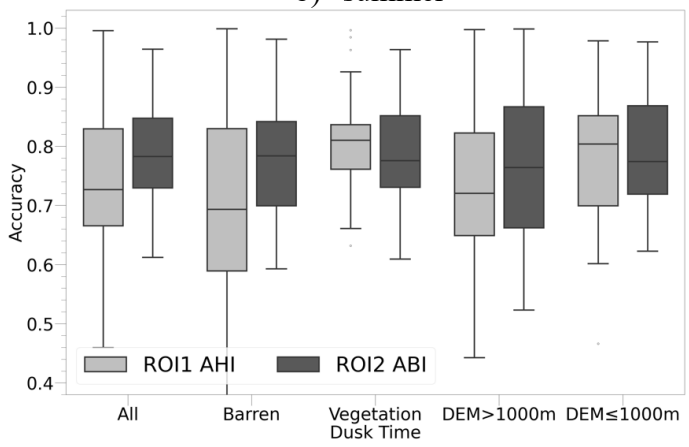

c) winter

Figure 3.6 Intercomparison of the MERSI-LL FY-3E cloud mask with the AHI Himawari-8 (ROI1) and ABI GOES-16 (ROI2) cloud masks under different surface conditions and at different seasons. The a,b,c represent the results in summer+winter, summer, winter respectively. The y-axis represents the classification accuracy, which is the ratio between the number of correct predictions and the total number of predictions.

3.4.2 Refining of Atmospheric Components

Coarse spatial resolution and incomplete atmospheric terms estimated using RTTOV and MERRA-2 usually still remaining large errors (Hulley et al., 2012). A water vapor scaling (WVS) model was implemented as a refining step. The WVS approach was originally proposed by Tonooka (Tonooka, 2005, 2001) and has been extensively utilized as a standard procedure in various TES-based LST products, including those from MODIS, VIIRS, and Himawari-8 (Islam et al., 2017; Malakar and Hulley, 2016; Zhou and Cheng, 2020).

The WVS algorithm depends on an extension of the multichannel water vapor dependent (EMC/WVD) algorithm (Tonooka, 2000). The EMC/WVD method was initially developed to estimate ocean surface temperatures under various atmospheric moist conditions (Sobrino et al., 1993), and extend to estimating the equivalent at-surface BT other gray bodies, such as vegetation, water, ice, or snow in later study(Tonooka, 2001). The determination of gray bodies depends on land-water mask data, and vegetation indices (Normalized Differential Vegetation Index – NDVI), and snow indices (Normalized Differential Snow Index–NDSI). In this study, the land-water mask bundled with the MERSI-LL FY-3E geolocation product and the MODIS reflectance (Collection 6 MCD43A4) (Wang et al., 2018) were used, meeting at least one of: 1) NDVI > 0.3; 2) NDSI > 0; and 3) classified as a water body. The EMC/WVD algorithm modeled the at-surface BT using at-sensor BT and TPW, and the equation is given as follows:

$$T_{g,i} = \alpha_{i,0} + \sum_{k=5}^{n} \alpha_{i,k} T_k \qquad (3\text{-}5)$$

$$\alpha_{i,k} = p_{i,k} + q_{i,k} W + r_{i,k} W^2, (k = 5, 6, 7) \qquad (3\text{-}6)$$

where W is the TPW; i or k is the band number; $T_{g,i}$ is the ground leaving equivalent BT for band i; $\alpha_{i,k}$, $\alpha_{i,0}$, $p_{i,k}$, $q_{i,k}$ and $r_{i,k}$ are the coefficients of combination for band i and band k (Table 3.1, Figure 3.7, Figure 3.8, Figure 3.9). The accuracy of this algorithm has an around 0.2 K improvement than EMC algorithm (that do not include the water vapor parameter) for ASTER/TIR at the TPW ≤ 1g/cm^2.

The EMC/WVD coefficients were determined using RTTOV and atmospheric profiles from the SeeBor (V5.0) dataset (Table 3.1, Figure 3.7, Figure 3.8, Figure 3.9). In this study, we calculated the coefficients for different VZAs and several gray body materials

with a minimum emissivity greater than 0.95 from the ECOSTRESS Spectral Library (Baldridge et al., 2009; Meerdink et al., 2019). VZAs were set at 0.00˚, 36.87˚, 48.19˚, 55.15˚, 60.00˚, 63.61˚, 66.42˚, and 68.68˚. The differences between the LST and surface air temperature were set to -10, -5, 0, 5, 10, and 15. Also, to avoid the discrete $T_{g,i}$ that calculated for individual VZAs, the coefficients were interpolated as a function of third order polynomial as the following figures (Figure 3.7, Figure 3.8, Figure 3.9). Notably, only materials with emissivity between 0.95-0.99 were used, since it was a procedure for grey bodies. In the figures, it was indicated as orange lines.

Table 3.1 Root Mean Square Error (RMSE, unit: Kelvin) and coefficients of estimated MERSI-LL FY-3E ground leaving equivalent brightness temperature (BT(TG,I)) using the EMC/WVD method (Equation 3 in the main text) at different viewing zenith angles (VZAs) and different bands. Here, $p_{I,J}$, $q_{I,J}$, and $r_{I,J}$ represent the simulated coefficients.

VZA	Band	RMSE	$p_{i,0}$	$q_{i,0}$	$r_{i,0}$	$p_{i,5}$	$q_{i,5}$	$r_{i,5}$	$p_{i,6}$	$q_{i,6}$	$r_{i,6}$	$p_{i,7}$	$q_{i,7}$	$r_{i,7}$
	5	0.191	-2.3439	0.3153	2.5702	-1.8741	0.1874	-0.2274	2.1857	-0.9583	0.8351	-0.3080	2.1821	-0.8773
0.00	6	0.164	1.2136	0.3806	-0.1941	-0.1882	1.0315	0.3039	0.3299	-0.6363	0.0278	0.3925	0.2731	-0.6633
	7	0.185	-1.5724	-0.0052	-0.0027	0.0131	-1.3917	0.0386	-0.0983	0.0647	-1.2246	0.0293	-0.0934	0.0684
	5	0.229	-2.4264	0.1893	2.5817	-1.7592	0.1864	-0.2671	2.2809	-1.0139	0.8360	-0.3372	2.2700	-0.9363
36.87	6	0.210	1.9004	0.3824	-0.0756	-0.3110	1.4968	0.3327	0.3630	-0.6996	0.5941	0.3988	0.3259	-0.7242
	7	0.226	-2.2318	0.0174	-0.0365	0.0267	-2.0435	0.0529	-0.1203	0.0747	-1.8709	0.0463	-0.1177	0.0780
	5	0.273	-2.3752	0.0835	2.6004	-1.6721	0.2325	-0.3029	2.3575	-1.0549	0.8814	-0.3649	2.3424	-0.9812
48.19	6	0.260	2.5080	0.3939	0.0239	-0.4240	1.9392	0.3603	0.3973	-0.7628	1.1149	0.4120	0.3730	-0.7862
	7	0.274	-2.9792	0.0394	-0.0697	0.0406	-2.7835	0.0689	-0.1437	0.0849	-2.6096	0.0639	-0.1427	0.0881
	5	0.322	-2.2605	-0.0036	2.6211	-1.6061	0.3006	-0.3345	2.4199	-1.0861	0.9482	-0.3899	2.4023	-1.0164
55.15	6	0.314	3.0907	0.4072	0.1118	-0.5270	2.3999	0.3840	0.4346	-0.8250	1.6362	0.4261	0.4188	-0.8477
	7	0.326	-3.8177	0.0619	-0.1027	0.0543	-3.6161	0.0868	-0.1688	0.0952	-3.4426	0.0829	-0.1688	0.0983
	5	0.376	-2.1206	-0.0752	2.6412	-1.5552	0.3748	-0.3618	2.4709	-1.1103	1.0217	-0.4121	2.4521	-1.0445
60.00	6	0.372	3.7251	0.4178	0.1941	-0.6220	2.9410	0.4018	0.4768	-0.8867	2.2231	0.4373	0.4668	-0.9086
	7	0.382	-4.7586	0.0857	-0.1363	0.0676	-4.5517	0.1070	-0.1959	0.1055	-4.3787	0.1038	-0.1966	0.1087
	5	0.435	-1.9857	-0.1339	2.6590	-1.5149	0.4375	-0.3851	2.5124	-1.1288	1.0844	-0.4312	2.4930	-1.0667
63.61	6	0.434	4.4572	0.4241	0.2746	-0.7112	3.5987	0.4136	0.5247	-0.9484	2.9150	0.4444	0.5185	-0.9695
	7	0.443	-5.8069	0.1113	-0.1712	0.0808	-5.5945	0.1297	-0.2252	0.1161	-5.4218	0.1269	-0.2264	0.1193
	5	0.606	-1.7373	-0.2222	2.6032	-1.3719	0.5262	-0.4268	2.4868	-1.0619	1.1615	-0.4668	2.4676	-1.0062
66.42	6	0.607	5.3635	0.3849	0.4797	-0.8805	4.3609	0.3833	0.6829	-1.0790	3.7120	0.4094	0.6791	-1.0980
	7	0.613	-6.8123	0.1506	-0.2225	0.0968	-6.5754	0.1645	-0.2680	0.1278	-6.4017	0.1620	-0.2693	0.1309

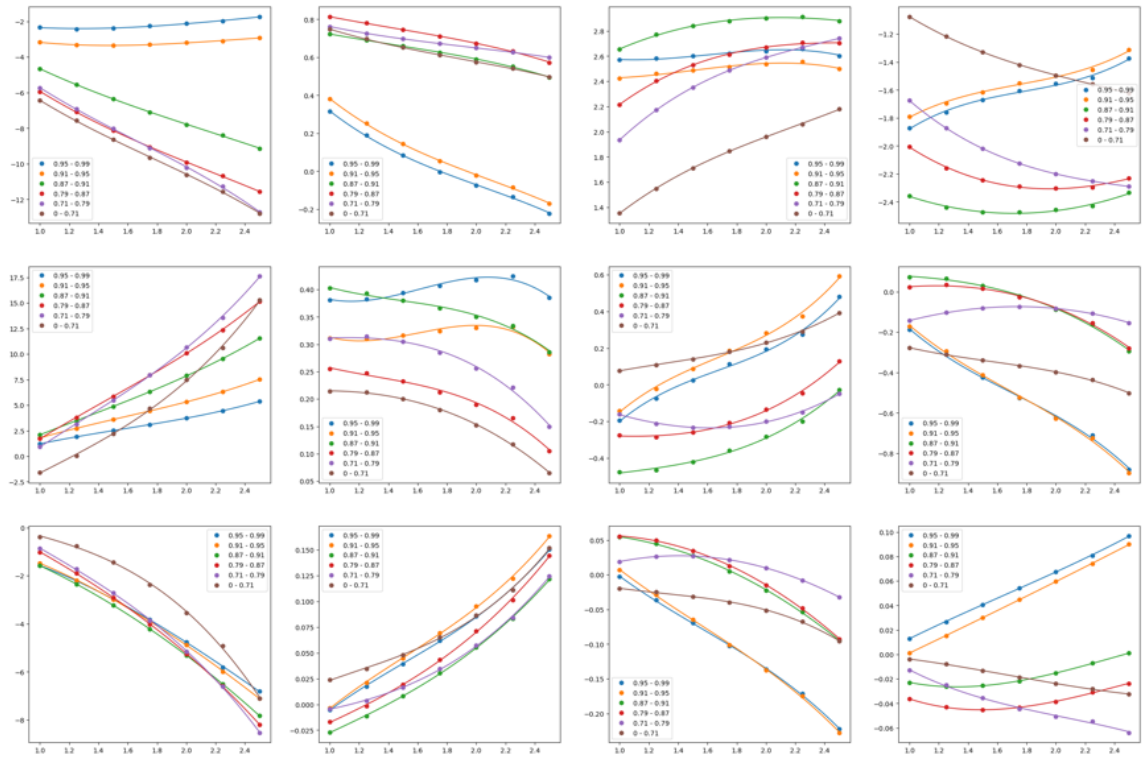

Figure 3.7 Ground-Leaving Equivalent Brightness Temperature (Tgi) Coefficient (y-axis) versus Cosine of Viewing Zenith Angle (VZA, x-axis). Fitting Curve for FY-3E Band 5 at Different Surface Emissivities, as shown in Table 3.1. The different color represents the simulation material with different emissivity ranges.

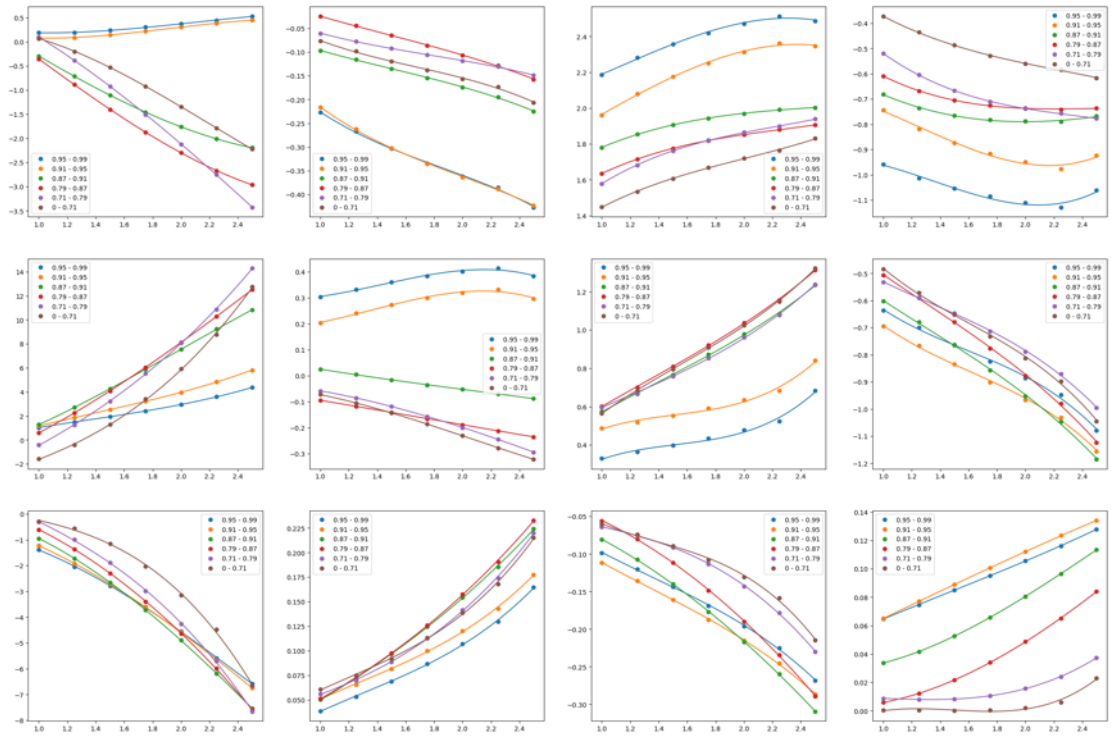

Figure 3.8 Similar to Figure 3.7 for band 6

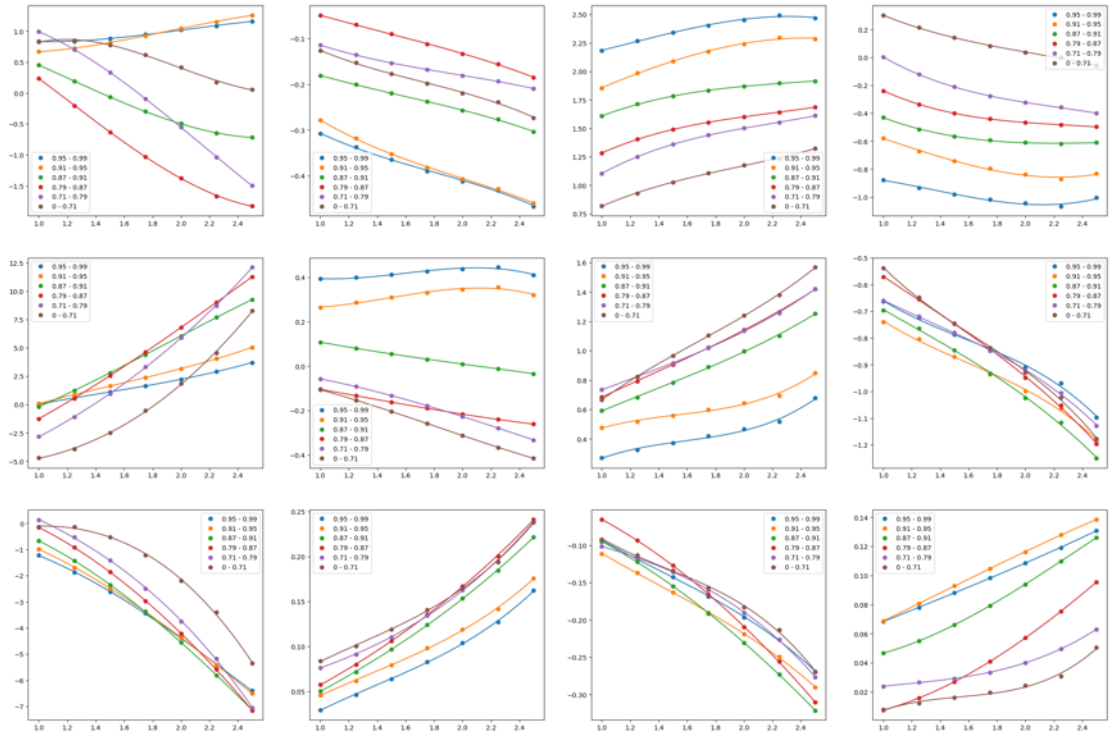

Figure 3.9 Similar to Figure 3.7 for band 7

Next, the water vapor profile scaling factor (γ_i) was computed for each band using the approximated land leaving radiance to the observed at-sensor radiance, under the assumption of the Pierluissi double exponential band model and the assumption that upward longwave band radiation is proportional to the sum of absorptivity and reflectivity that at different water vapor scaling factor, given as following:

$$L^{\uparrow}(\gamma) = L^{\uparrow}(\gamma_1) \cdot \frac{1-\tau(\gamma)}{1-\tau(\gamma_1)} \qquad (\ 3\text{-}7\ )$$

$$\tau_i(\theta,\gamma) \ = \ \tau_i(\theta,\gamma_1)^{\frac{\gamma^{a_i}-\gamma_2{}^{a_i}}{\gamma_1{}^{a_i}-\gamma_2{}^{a_i}}} \cdot \tau_i(\theta,\gamma_2)^{\frac{\gamma_1{}^{a_i}-\gamma^{a_i}}{\gamma_1{}^{a_i}-\gamma_2{}^{a_i}}} \qquad (\ 3\text{-}8\ )$$

and combining these formular, the γ_i was given as following:

$$\gamma_i = \left(\frac{\ln\left(\frac{\tau_i(\theta,\gamma_2)^{\gamma_1{}^{a_i}}}{\tau_i(\theta,\gamma_1)^{\gamma_2{}^{a_i}}} \cdot \frac{B(T_{g,i}) - \frac{L_i^{\uparrow}(\theta,\gamma_1)}{1-\tau_i(\theta,\gamma_1)}}{L_i - \frac{L_i^{\uparrow}(\theta,\gamma_1)}{1-\tau_i(\theta,\gamma_1)}} \right)}{\ln\left(\frac{\tau_i(\theta,\gamma_2)}{\tau_i(\theta,\gamma_1)}\right)} \right)^{\frac{1}{a_i}} \qquad (\ 3\text{-}9\ )$$

where a_i is the WVS model parameter for band i (estimated from the atmospheric components using profile, RTM under constrain of 3-8, as Table 3.2); γ_1 and γ_2 are two scaling level and were assigned as 1.0 and 0.7, based on previous studies; $\tau_i(\theta,\gamma)$, $\tau_i(\theta,\gamma_1)$ or $\tau_i(\theta,\gamma_2)$ is the atmospheric transmittance scaled by γ, γ_1 or γ_2 at the view angle θ; $B(T_{g,i})$ is the at-surface land surface leaving radiance; L_i is the at-sensor radiance measured by satellite at band i; $L_i^{\uparrow}(\theta,\gamma_1)$ is the atmospheric upward path radiance of band i at view angle θ and scaled by γ_1. $\gamma_i > 1$ means MERRA2 atmospheric profile is drier, while $\gamma_i < 1$ means it contains more moisture. As for atmospheric condition with transmittance close to unit, scaling is not required here and the γ_i was set to 1.0. On the contrary, if $\tau_i(\theta,\gamma_1)$ and $\tau_i(\theta,\gamma_2)$ are small and is close to each other, it represents atmospheric terms are not sensitive to water vapor content at this condition and γ_i calculation fails at these pixels. The pixels where γ_i calculation failed, or at not none-gray body were interpolated using the inverse distance weighting

(IDW) and then spatially smoothed using median filtering. The atmospheric terms in (3-1, 3-2) were refined using the interpolated and smoothed.

Table 3.2 Simulated Water Vapor Scaling (WVS) Coefficients (a_i) for MERSI-LL FY-3E Channels. The Root Mean Square Error (RMSE, unitless) was calculated using a WVS factor (γ) of 0.9, $\gamma 1$ of 1.0, and $\gamma 2$ of 0.7.

Band No. (i)	Band5	Band6	Band7
Coefficient (a_i)	1.453	1.841	1.783
RMSE of γ	2.752×10^{-3}	1.324×10^{-3}	1.614×10^{-3}

WVS factor γ_i, which was calculated using (3-9). The atmospheric upwelling path radiance $L_i^{\uparrow}(\theta, \gamma)$ and atmospheric transmittance were first scaled using (3-8) and (3-10). Assuming a plain-layered atmosphere, the nadir atmospheric upwelling radiance was inverted from the scaled atmospheric upwelling radiance and the scaled atmospheric transmittance at a VZA of θ, as in (3-11). The equivalent downwelling atmospheric radiance was estimated as a quadratic function of the nadir upwelling radiance term with the trained coefficient, as (3-12) and Figure 3.10. The mentioned equations used are:

$$L_i^{\uparrow}(\theta, \gamma) = L_i^{\uparrow}(\theta, \gamma_1) \frac{1 - \tau_i(\theta, \gamma)}{1 - \tau_i(\theta, \gamma_1)} \quad (3\text{-}10)$$

$$L_i^{\uparrow}(0, \gamma) = L_i^{\uparrow}(\theta, \gamma) \frac{1 - \tau_i(\theta, \gamma)^{\cos\theta}}{1 - \tau_i(\theta, \gamma)} \quad (3\text{-}11)$$

$$L_i^{\downarrow}(\gamma) = b_i L_i^{\uparrow}(0, \gamma)^2 + c_i L_i^{\uparrow}(0, \gamma) + d_i \quad (3\text{-}12)$$

where $L_i^{\uparrow}(\theta, \gamma)$ is the atmospheric upward path radiance of band i at view angle θ scaled by γ. $L_i^{\downarrow}(\gamma)$ is the scaled atmospheric downward radiance for band i. b_i, c_i, and d_i are the trained coefficient parameters for band i (Figure 3.10).

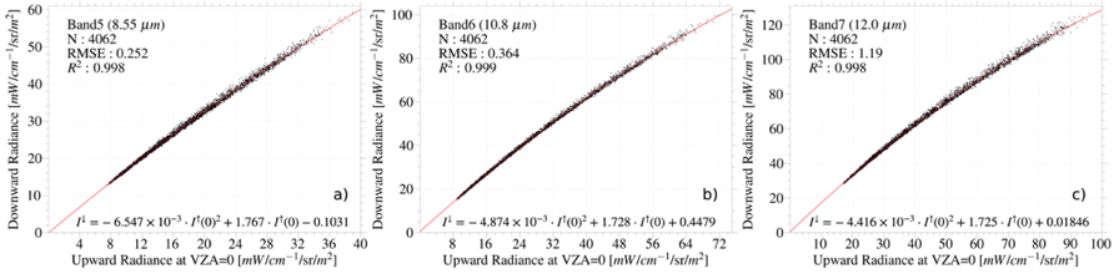

Figure 3.10 Atmospheric downward radiance estimated from the atmospheric upward radiance of (a) band 5, (b) band 6, and (c) band 7 of the MERSI-LL FY-3E. Black dots represent simulated downwelling radiance values obtained using the nadir upwelling radiance. The red line represents the fitted curve.

3.4.3 Retrieval of LST and LSEs

The normalized emissivity method (NEM) is used to constrain the emissivity contrast (minimum-maximum emissivity difference: MMD, described as 3-13, 3-14) versus the minimum emissivity (ε_{min}) for different natural surface materials and was applied to reduce the unknowns in the radiative formulas (Gillespie et al., 1998). The correlation between the minimum emissivity value and the emissivity contrast range across different wavelengths for a given material is characterized using laboratory-measured emissivity spectra. The relationship is given as:

$$\beta_i = \frac{\varepsilon_i}{\underset{i=5,6,7}{\text{mean}}(\varepsilon_i)} \qquad (3\text{-}13)$$

$$MMD = \max(\beta_i) - \min(\beta_i) \qquad (3\text{-}14)$$

where β_i relative emissivity calculated from the individual band emissivity ε_i for band i; mean, max and min represent the calculation of the mean function, maximum function and minimum function.

In this study, a dataset consisting of 91 emissivity spectra from diverse surface types was compiled with data from the ECOSTRESS spectral library and used to calculate the MERSI-LL FY-3E band emissivities and the associated NEM relationships (Baldridge et al., 2009; Meerdink et al., 2019). Five manmade materials, 17 vegetation samples, 29 soil signatures, 31 rocks, and nine water, snow, ice spectra were included as surface categories, representing a broad sample of natural land covers (Figure 3.11a). Manmade materials include asphalt and concrete. The materials of soil, rock or vegetation were selected from

corresponding materials in the library using a k-means cluster algorithm. Also, a manual check of the category was conducted to ensure the surface sample types included in each category. The rock category included igneous rocks, sedimentary rocks and metamorphic rocks. The soil category included alfisol, entisol, inceptisol, aridsoil and mollisol. And these soil types cover most of the areas of the global surfaces as indicated by the soil map of FAO (https://data.apps.fao.org/map/catalog/srv/eng/catalog.search#/metadata/cc45a270-88fd-11da-a88f-000d939bc5d8). The vegetation included various shrubs, trees and grass corresponding to different ecosystems. Using the selected materials, the estimated results for MMD against ε_min are shown in Figure 3.11b.

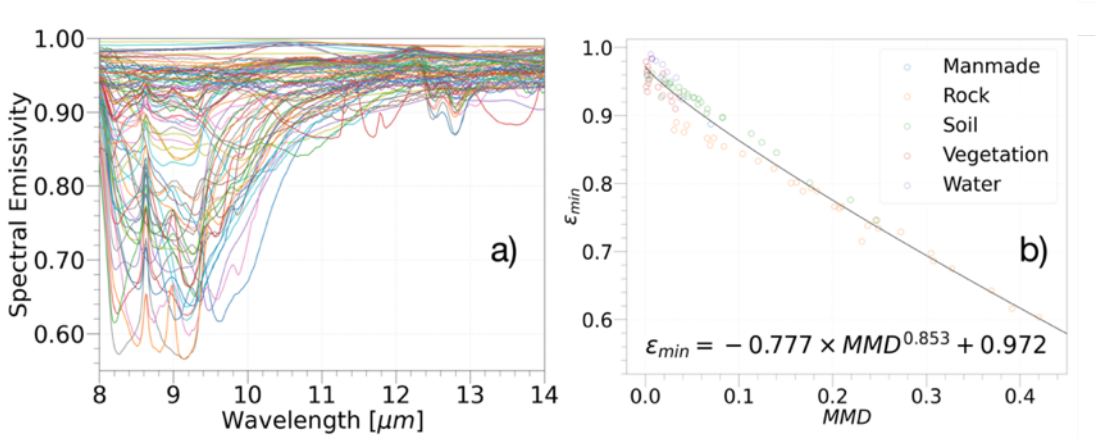

Figure 3.11 a) Emissivity spectra of sample materials used for training the normalized emissivity method (NEM) module. Lines represent the emissivity spectra of sample materials. b) Minimum emissivity (ε_{min}) for TES channels estimated from the minimum-maximum emissivity difference (MMD) in the MERSI-LL FY-3E normalized emissivity method (NEM) module. Colored dots represent the minimum emissivity and MMD values for sample materials in the database. The black solid line represents the fitted line, with the ε_{min} using MMD as a variable.

A global search approach was implemented to retrieve the LST and band emissivity values by applying constraints from the derived NEM correlation. The allowable emissivity range for each MERSI-LL band was discretized from 0.70 to 0.99 in 0.02 steps, resulting in an initial 15 × 15 × 15 emissivity vector solution space. Vectors in which the NEM contrast exceeded the interval (in this iteration, 0.02) were discarded and the remaining candidate emissivity combinations were used as input into the radiative transfer equations and the Planck function to estimate the LST for each band. The vector

that produced the minimum variance in the multiband LST was selected as the optimal solution within each iteration. Additional iterative searches were then conducted using successively narrowing emissivity ranges (including first iteration 0.02, and next iteration at 0.005, and 0.001) that were centered on the prior optimal result, and the mean LST and associated emissivity vectors output after three iterations were retained as the final retrieved values. Such approach will boost the processing speed when accomplished using python because for loop is much slower in python.

3.5 Evaluation of the FY-3E LST

3.5.1 Uncertainty Analysis of the TES Method

The simulation of the TES method was initially conducted to identify systematic errors within the method, to broaden the scope of validation to encompass diverse conditions not addressed by existing validation sites and periods. The figures provide a comprehensive validation of the Temperature Emissivity Separation (TES) method across various conditions and materials, demonstrating its robustness particularly in environments with high-emissivity surfaces like vegetation and water (Figure 3.12). The data used for simulation was the same combination of VZAs, surfaces materials, and the offset between LST and Ta that were used when retrieving coefficients. The true LST values were used as inputs, and the results were generated by applying these true values to simulate radiance data. The estimated LST from the radiances were the validation target in this task. The data reveals that the RMSE increases with higher Viewing Zenith Angles (VZA) and is generally lower in summer conditions, suggesting better performance due to seasonal factors. Surfaces with higher emissivity showed consistently low RMSEs for both LST and band LSEs, particularly within 1 K for LST and about 0.02 for LSE. Conversely, manmade materials, rocks, and soils displayed higher RMSEs, showed worse RMSEs though still within acceptable limits (Figure 3.13). Additionally, RMSE for LSE tends to decrease as LST increases, indicating more accurate measurements at higher temperatures. The data underscores the efficacy of the TES method, while also highlighting potential areas for refinement, especially in observations at large VZAs and on low-emissivity surfaces.

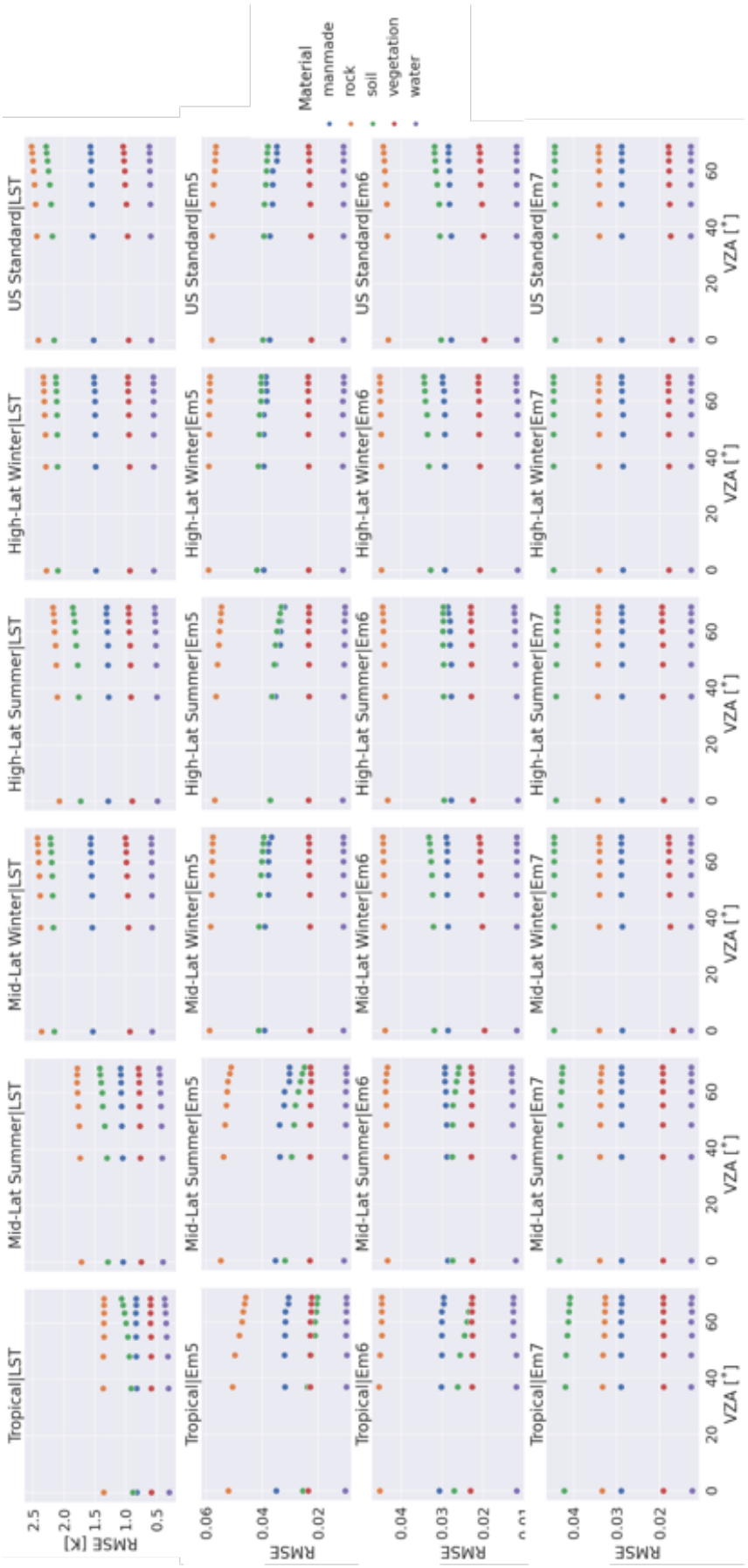

Figure 3.12 The RMSE of the TES method for LST (Unit: Kelvin) and LSE (Unitless) at band 5 (Em5), band 6 (Em6), band 7 (Em7) in this study using simulation dataset at different sample surface materials and different VZAs. Different columns represent the simulation with different atmospheric profiles including 5 types representing different seasons and latitudes, and one type of US standard. Different color of the scatter represents the different types of the simulation materials.

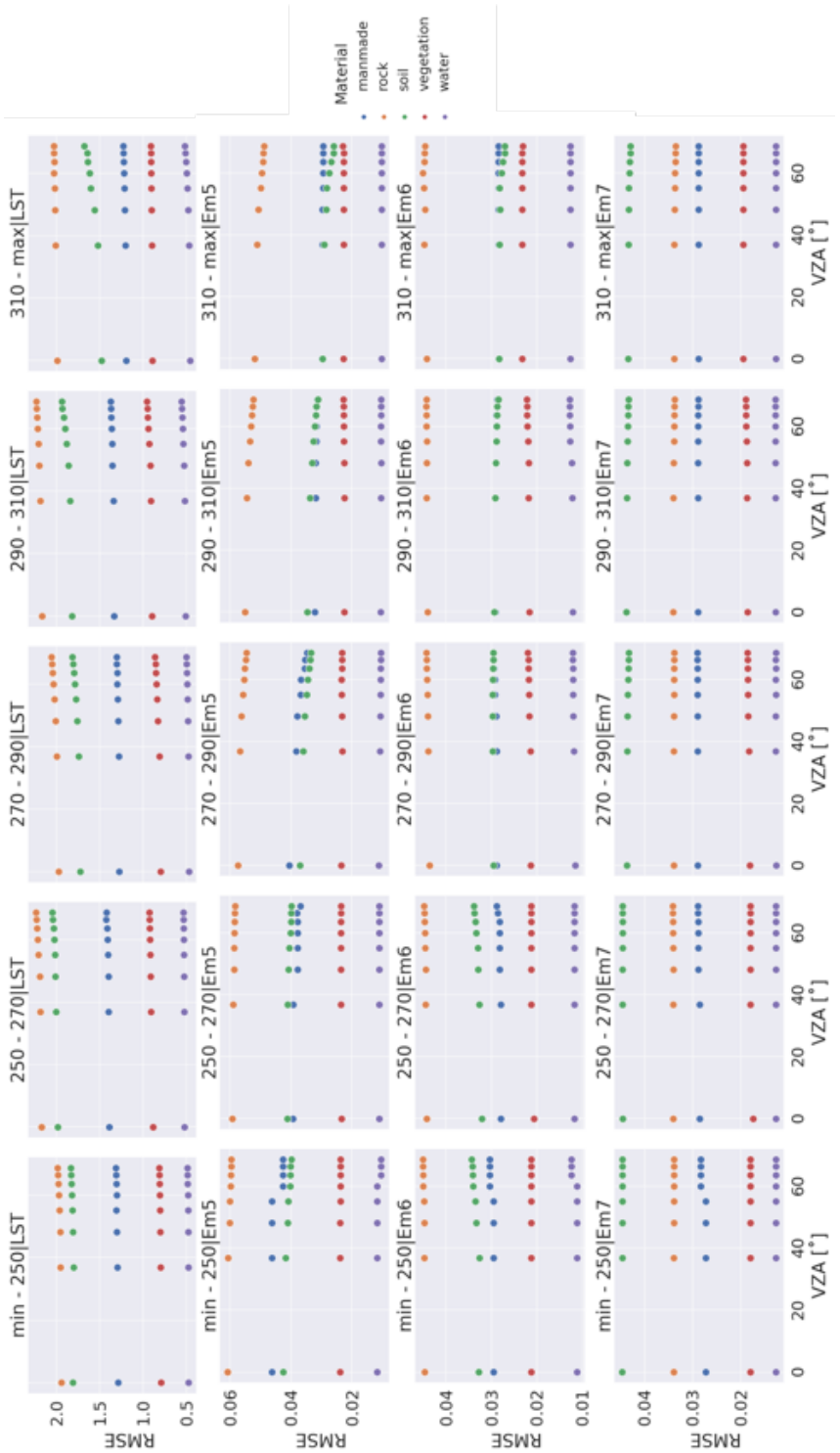

Figure 3.13 The figure similar to Figure 3.12 Different columns represent the simulation under different surface LST ranges.

3.5.2 Sensitive Analysis of the TES Method

The atmospheric terms retrieved by RTM models and even after refinement using WVS method still cannot the absolute accuracy. Thus, it is important to understand the errors that caused by these uncertainties in the atmospheric components. To test the sensitivity against the error from the atmospheric component, -5%–5% random noises were added to the column water content to understand the uncertainty caused by water content profiles. Similarly, noises randomly from 0–1 K were added to layer temperatures in atmospheric profiles. Each of these experiments included 100 cases with different noises. The data and method were same as previous analysis, and the evaluation was conducted for the retrieved LST or LSEs (Em5, Em6, and Em7 for band 5, 6, and 7).

The sensitivity of the FY-3E TES method to column water content is notably high, particularly at larger VZAs (Figure 3.14). This sensitivity is evidenced by the behavior of both the LSE and LST RMSEs across different environmental conditions and surface types. Specifically, under a tropical atmospheric profile and over water surfaces, the RMSE for band 5 LSE escalates significantly from around 0.005 to 0.03 as the VZA increases from 0 to approximately 68 degrees. Concurrently, the LST RMSE rises from about 0.3 K to 1.5 K over the same VZA range, with a notable doubling of the RMSE when VZA is around 55 degrees. This increase highlights a critical range of 55–68 degrees VZA where the method shows heightened sensitivity and leads to larger uncertainties. When comparing different surface materials under these conditions, it's observed that vegetation and water surfaces exhibit less sensitivity to measurement noise. This reduced sensitivity is attributed to their larger band LSEs, which are less influenced by atmospheric variations due to a smaller multiplication factor with atmospheric terms. Moreover, other atmospheric profiles with lesser water content exhibit considerably less uncertainty compared to the tropical profile. The greater uncertainty associated with the summer profile is also linked to its higher column water content, emphasizing the influence of atmospheric conditions on the accuracy of TES measurements.

The impact of incorporating a 1 K temperature noise into atmospheric profiles significantly exceeds the effects of introducing a 5% column water noise, particularly affecting the accuracy of remote sensing measurements (Figure 3.15). This is exemplified in the increase of root mean square error (RMSE) for band 5 land surface emissivity (LSE),

which escalates to 0.12 when the viewing zenith angle (VZA) reaches approximately 68 degrees. The influence of temperature noise is more pronounced at higher VZAs, similar to the effects observed with column water noise. At these larger angles, the retrieval of both land surface temperature (LST) and LSE becomes increasingly susceptible to errors. The larger VZA not only intensifies the direct impact of atmospheric interferences but also amplifies the retrieval uncertainties, underlining the challenges in accurately capturing surface characteristics from remote sensors under varying atmospheric conditions and viewing angles.

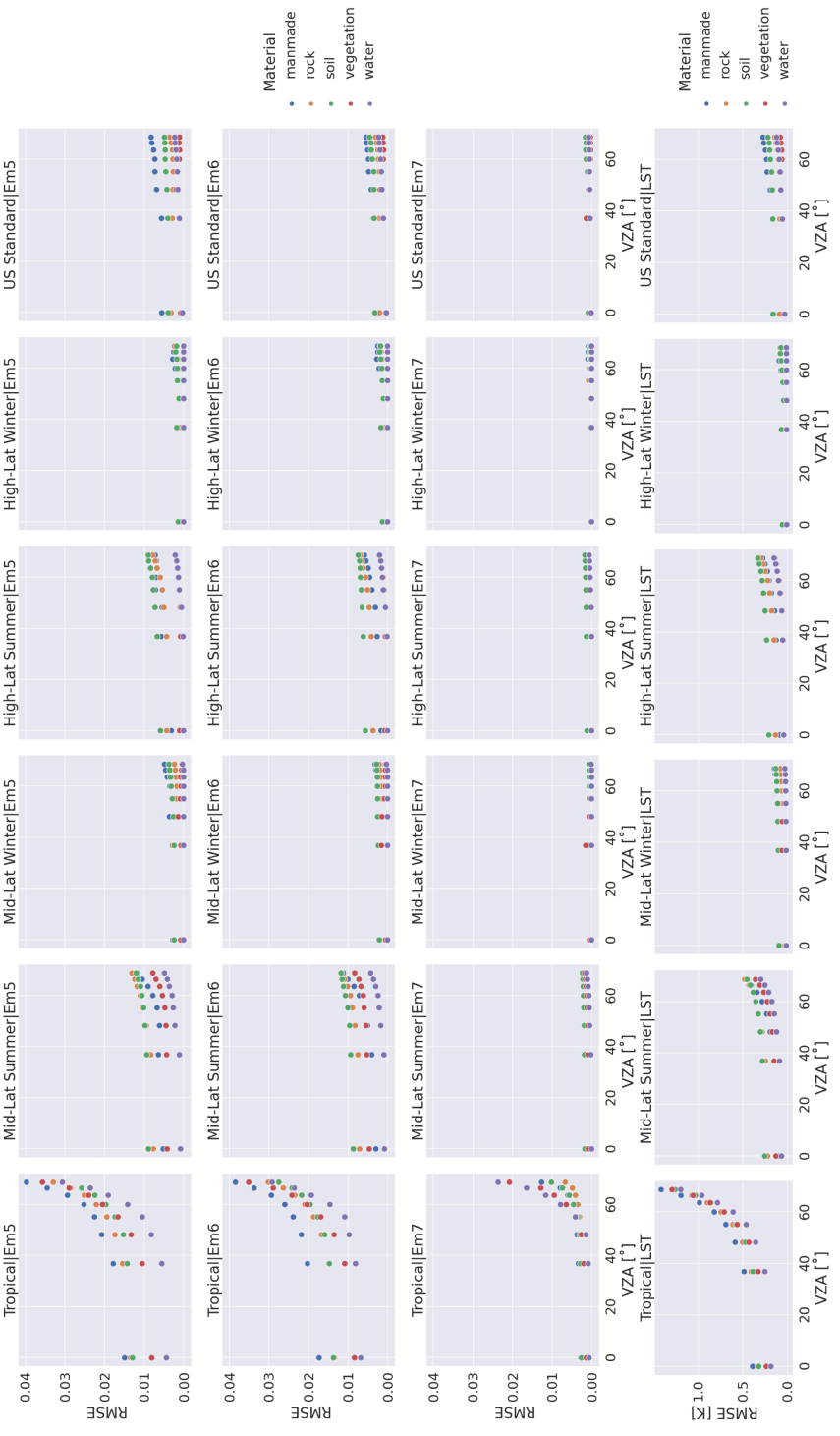

Figure 3.14 The RMSE of the column water sensitivity analysis for LST and LSE at band 5 (Em5), band 6 (Em6), band 7 (Em7) in this study using simulation dataset at different sample surface materials and different VZAs. Different columns represent the simulation with different atmospheric profiles including 5 types representing different seasons and latitudes, and one type of US standard. Different color of the scatter represents the different types of the simulation materials.

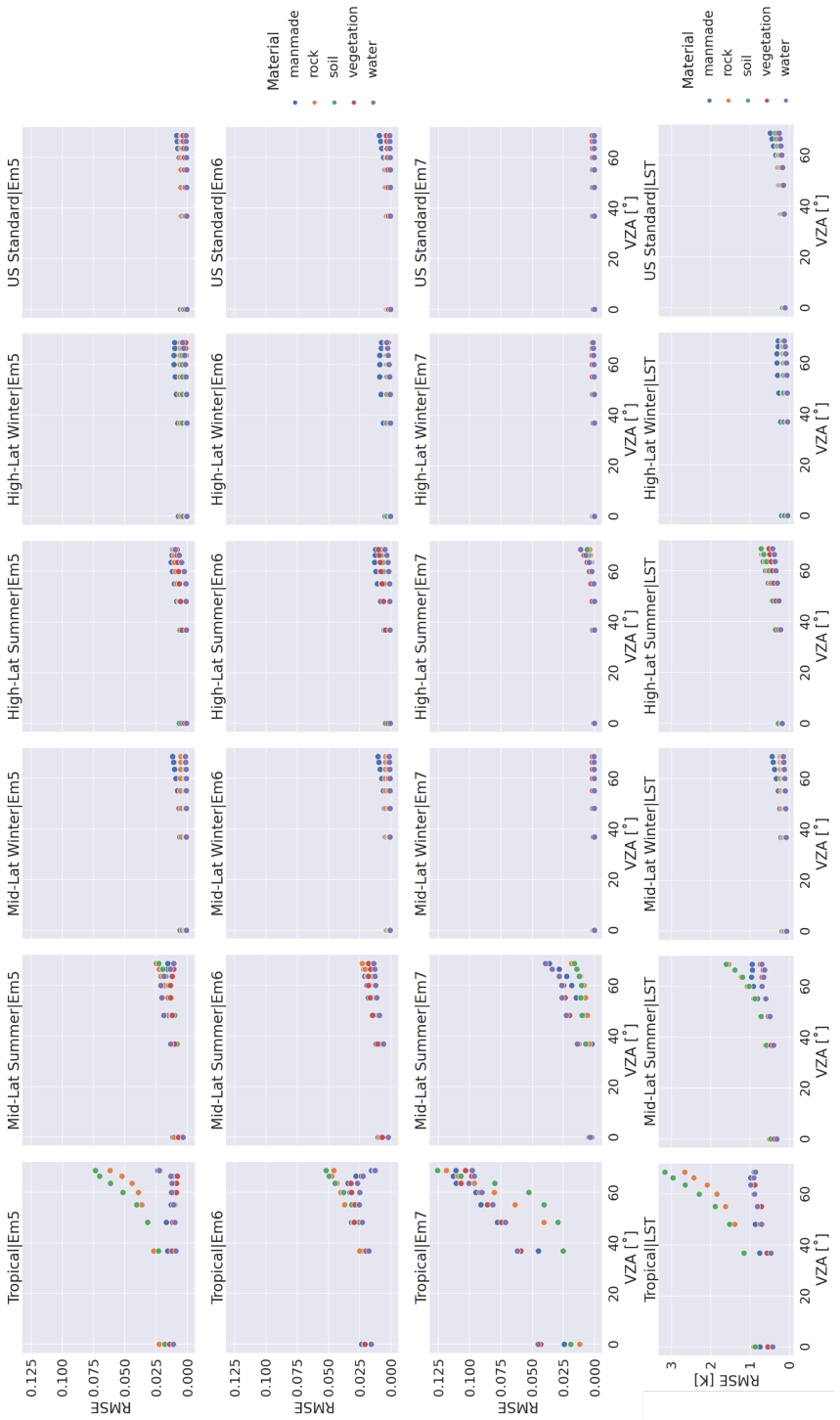

Figure 3.15 Sensitivity analysis similar to Figure 3.14 but was the profile temperature sensitivity analysis.

3.5.3 LST Ground Observation Data and T-based Validation

Ground-based measurements collected during June 2022 were leveraged to validate the FY-3E LST product developed in this study. The in-situ datasets were obtained from network stations in the AmeriFlux, Integrated Carbon Observation System (ICOS), and Surface Radiation Budget Network (SURFRAD) collaborative observation networks (Table 3.3, Figure 3.18) (Augustine et al., 2000; Chu et al., 2021; Rebmann et al., 2018).

These sites are instrumental in providing continuous, long-term data essential for modeling and understanding ecosystem function, carbon sequestration, feedback mechanisms to the climate system and validating satellite measurements of surface radiation. AmeriFlux is a network primarily based in the Americas, including both North and South America, dedicated to measuring carbon dioxide, water vapor, and energy fluxes from a variety of ecosystems. Established in the mid-1990s, AmeriFlux has grown significantly over the years. As of my last update, it consists of over 110 active sites spanning forests, grasslands, agricultural lands, and urban areas. The Integrated Carbon Observation System, ICOS provides standardized and open data from more than 170 measurement stations across 16 European countries from 2010s. The Surface Radiation Budget Network (SURFRAD) was established in 1993 by the National Oceanic and Atmospheric Administration's (NOAA) Global Monitoring Laboratory. Currently seven SURFRAD stations are operating in climatologically diverse regions: Montana, Colorado, Illinois, Mississippi, Pennsylvania, Nevada and South Dakota.

Table 3.3 A List of 46 Observation Sites Used for Validating Satellite-Based Land Surface Temperature in This Study.

ID	Network	Latitude	Longitude	Altitude	LC
US-ARM	AmeriFlux	36.6058 ˚N	97.4888 ˚W	314 m	low_vegetation
US-Bi1	AmeriFlux	38.0992 ˚N	121.4993 ˚W	-2.7 m	low_vegetation
US-Bi2	AmeriFlux	38.1091 ˚N	121.5351 ˚W	-5 m	low_vegetation
US-Prr	AmeriFlux	65.1237 ˚N	147.4876 ˚W	210 m	tree
US-RGB	AmeriFlux	39.5782 ˚N	121.8579 ˚W	33 m	low_vegetation
US-Rms	AmeriFlux	43.0645 ˚N	116.7486 ˚W	2111 m	low_vegetation
US-Rpf	AmeriFlux	65.1198 ˚N	147.4290 ˚W	497 m	tree
US-Uaf	AmeriFlux	64.8663 ˚N	147.8555 ˚W	155 m	tree

US-xAB	AmeriFlux	45.7624 ˚N	122.3303 ˚W	363 m	tree
US-xAE	AmeriFlux	35.4106 ˚N	99.0588 ˚W	516 m	low_vegetation
US-xBN	AmeriFlux	65.1540 ˚N	147.5026 ˚W	263 m	tree
US-xDJ	AmeriFlux	63.8811 ˚N	145.7514 ˚W	529 m	tree
US-xKZ	AmeriFlux	39.1008 ˚N	96.5631 ˚W	381 m	low_vegetation
US-xMB	AmeriFlux	38.2483 ˚N	109.3883 ˚W	1767 m	low_vegetation
US-xNG	AmeriFlux	46.7697 ˚N	100.9154 ˚W	578 m	low_vegetation
US-xNQ	AmeriFlux	40.1776 ˚N	112.4524 ˚W	1685 m	low_vegetation
US-xRN	AmeriFlux	35.9641 ˚N	84.2826 ˚W	334 m	tree
US-xSE	AmeriFlux	38.8901 ˚N	76.5600 ˚W	15 m	tree
US-xST	AmeriFlux	45.5089 ˚N	89.5864 ˚W	481 m	tree
US-xTR	AmeriFlux	45.4937 ˚N	89.5857 ˚W	472 m	tree
US-xUK	AmeriFlux	39.0404 ˚N	95.1921 ˚W	335 m	tree
US-xUN	AmeriFlux	46.2339 ˚N	89.5373 ˚W	518 m	tree
US-xWD	AmeriFlux	47.1282 ˚N	99.2414 ˚W	579 m	low_vegetation
US-xWR	AmeriFlux	45.8205 ˚N	121.9519 ˚W	407 m	tree
BE-Bra	ICOS	51.3076 ˚N	4.5198 ˚E	16 m	tree
BE-Lon	ICOS	50.5516 ˚N	4.7462 ˚E	170 m	low_vegetation
BE-Maa	ICOS	50.9799 ˚N	5.6319 ˚E	87 m	tree
CZ-Lnz	ICOS	48.6816 ˚N	16.9463 ˚E	150 m	tree
DE-Geb	ICOS	51.0997 ˚N	10.9146 ˚E	161.5 m	low_vegetation
DE-HoH	ICOS	52.0866 ˚N	11.2224 ˚E	193 m	tree
DE-Tha	ICOS	50.9626 ˚N	13.5652 ˚E	380 m	tree
DK-Sor	ICOS	55.4859 ˚N	11.6446 ˚E	40 m	tree
FI-Hyy	ICOS	61.8474 ˚N	24.2948 ˚E	181 m	tree
FR-Fon	ICOS	48.4764 ˚N	2.7801 ˚E	103 m	tree
FR-Hes	ICOS	48.6741 ˚N	7.0647 ˚E	310 m	tree
FR-Pue	ICOS	43.7413 ˚N	3.5957 ˚E	271 m	tree
IT-Cp2	ICOS	41.7043 ˚N	12.3573 ˚E	19 m	tree
IT-Ren	ICOS	46.5869 ˚N	11.4337 ˚E	1735.6 m	tree
IT-SR2	ICOS	43.7320 ˚N	10.2909 ˚E	4 m	tree
SE-Htm	ICOS	56.0976 ˚N	13.4190 ˚E	115 m	tree
SE-Nor	ICOS	60.0865 ˚N	17.4795 ˚E	45 m	tree

SE-Svb	ICOS	64.2561 ˚N	19.7745 ˚E	267 m	tree
bon	SURFRAD	40.0500 ˚N	88.3700 ˚W	213 m	low_vegetation
dra	SURFRAD	36.6240 ˚N	116.0190 ˚W	1007 m	solid (barren)
fpk	SURFRAD	48.3100 ˚N	105.1000 ˚W	634 m	low_vegetation
sxf	SURFRAD	43.7300 ˚N	96.6200 ˚W	473 m	low_vegetation

The in situ LST were involved with several processes. SURFRAD data obtained at 1-min intervals were converted to a 30-min average to match site data from AmeriFlux and ICOS, which were obtained at a 30 min average. The 30-mins data points were linearly interpolated using a 1-min interval and converted to local solar time. The satellite-based LST data nearest to each target site were then matched to the corresponding site data. Cloud contaminated observations were excluded in this validation. The in-situ LST data were calculated using the Stefan-Boltzmann law, with the measured upward longwave radiation, downward longwave radiation, and satellite-estimated surface broadband emissivity (BBE) input into the equation, as follows:

$$LST_{site} = \left[\frac{LW^{\uparrow} - (1 - \varepsilon_{site})LW^{\downarrow}}{\varepsilon_{site}\,\sigma}\right]^{\frac{1}{4}} \qquad (3\text{-}15)$$

where $LW^{\uparrow}$ is the upwelling longwave radiance emitted to the atmosphere from the land surface; $LW^{\downarrow}$ is the downwelling longwave radiance received from the atmosphere; σ is the Stefan–Boltzmann constant ($5.67 \times 10^{-8}\ \mathrm{W \cdot m^{-2} \cdot K^{-4}}$); The calculation of BEE was described as Figure 3.16 and ε_{site} is the BBE estimated using a linear combination of the emissivity at three TES bands (Figure 3.17a) and compared to a previous study (Figure 3.17b) (Wang et al., 2005). The coefficients in linear formula were determined by BBE aggregated within 8-13.5 μm (as target) which was suggested by (Cheng et al., 2013), and the simulated TES band emissivity (based on response coefficient function, as variable). The approach used the materials from the ECOSTRESS Spectral Library and separated into 20 cross-validation (CV) split to test the performances and robustness of the approach. Finally, the estimated BBEs at individual observation time collected from Terra MODIS, Aqua MODIS, and VIIRS SNPP were smoothed over a 15-day window as the in situ BBE and used for in-situ LST calculation (Figure 3.16).

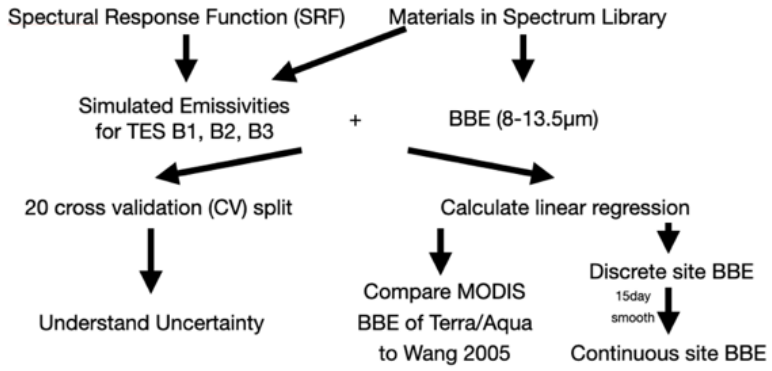

Figure 3.16 The flowchart for the calculation of the broadband emissivity (BBE) of the sites using the linear regression and three TES band emissivities.

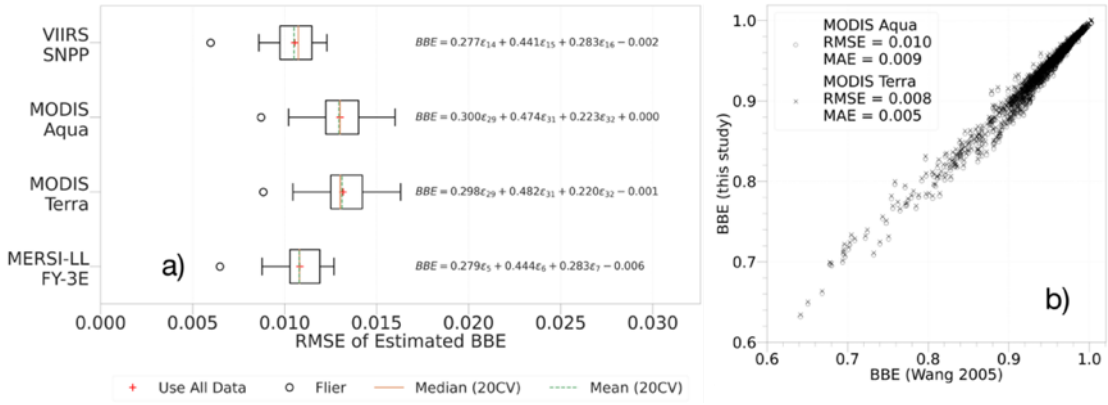

Figure 3.17 a) Root Mean Square Error (RMSE) of Estimated Broadband Emissivity (BBE) using linear regression for each sensor-platform. The box plot represents the group RMSE of the estimated BBE in a 20-fold cross-validation. Red cross markers indicate training using all emissivity spectra and validation with the same data. Orange lines represent the median RMSE in the cross-validation groups, while green lines represent the average RMSE. b) Estimated BBE in this study comparing to previous study (Wang et al., 2005).

Data from a total of 46 stations were used for the T-based validation, with 29 forest sites, 16 low vegetation sites (including cropland, grassland, shrubland) and one barren site after screening using the heterogeneity information (Table 3.3, Figure 3.18). One of the most important criteria for screening the site is the spatial heterogeneity around a site, which was determined using the dataset named Dynamic World, a dynamic land cover dataset developed by Google and the World Resources Institute (Brown et al., 2022). A

high temporal resolution and a spatial resolution of 10 m were achieved over a window of a few days; thus, any changes in the land cover heterogeneity could be captured over shorter time periods such as months or seasons. Only spatiotemporally homogeneous sites were retained (46 sites); homogeneity was assumed when no change was observed in a major land type from May to July (temporal homogeneity: the major land cover type remained unchanged) and the percentage covered by that land type surpassed that of other categories (spatial homogeneity: major category occupies over 90 % of the total area with a 1km window size). Examples of heterogeneity calculation over 4 sites were given in Figure 3.19. Here, 3 sites showed typical heterogeneity issues using surrounding land cover and one site is suitable for homogenous criteria.

Besides, a widely used statistical method based on the '3σ -edit rule' was applied to remove abnormal data that caused by noise such as cloud contamination (Duan et al., 2019; Göttsche et al., 2013; Pearson, 2002). It is under the assumption that error is normally distributed. As suggested by previous studies, standard deviation (Std) of error is calculated by the median instead of mean to accomplish a more robust outlier removal, and known as '3σ -Hampel identifier' (Chiang et al., 2003). The Std was given as:

$$Std = 1.4826 \times median(|x_i - median(x_i)|) \quad (3\text{-}16)$$

$$x_i = LST_i - LST_{site_i} \quad (3\text{-}17)$$

where, x_i is the median error sequence which was calculated using the LST_i for satellite LST sequence and LST_site_i for site observed LST sequence. Finally, theLST_i and LST_site_i corresponding to x_i that within ±3× Std was used for data validation.

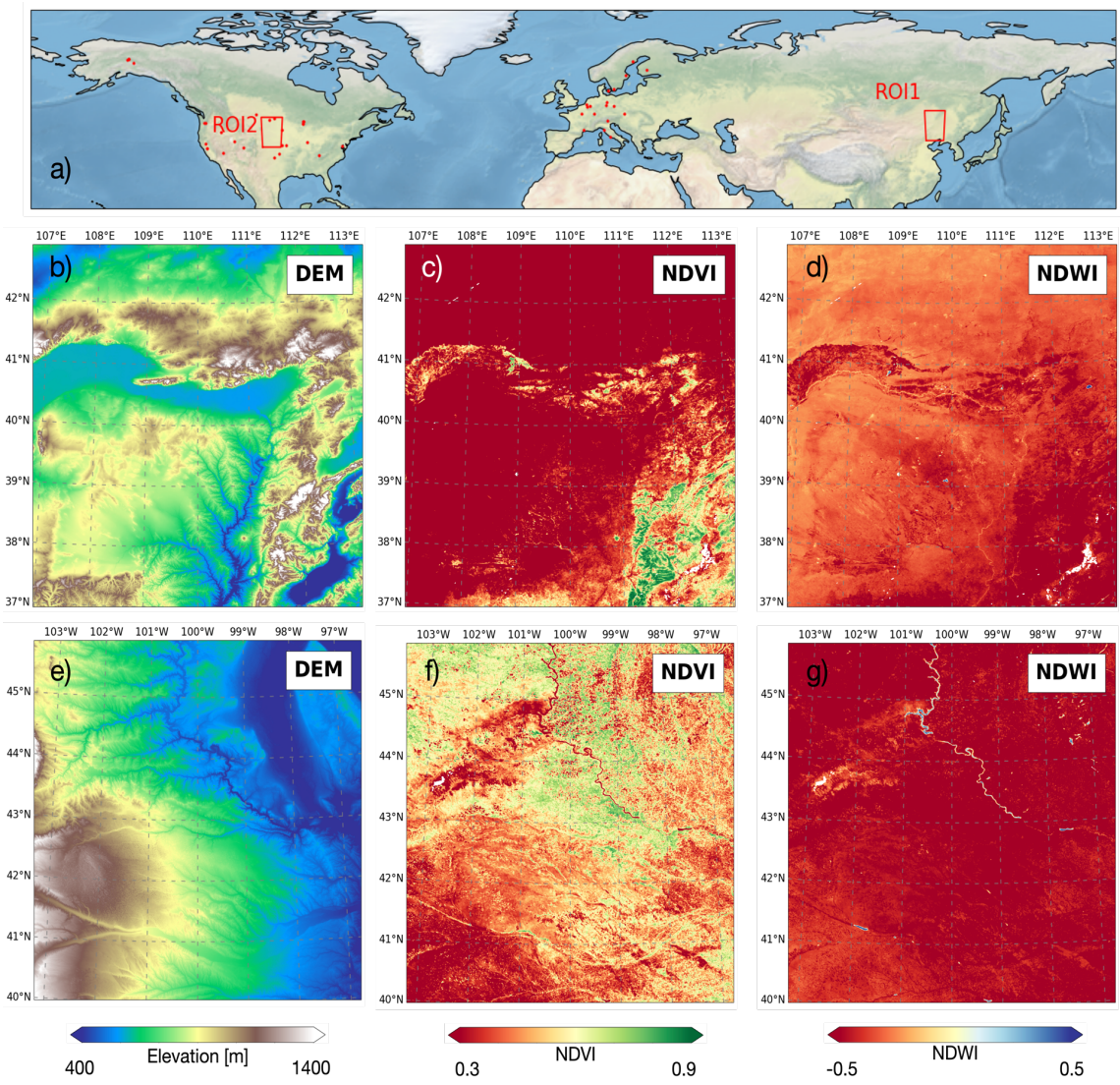

Figure 3.18 a) Validation sites and region of interest (ROI) margins. Red dots represent site locations and red polygons intercomparison ROIs. b-g) Auxiliary information for area surrounding ROI 1 (b,c,d) and ROI 2 (e,f,g) ROI 2, including elevation (DEM, digital elevation model), NDVI, and normalized differential water index (NDWI) in June, 2022.

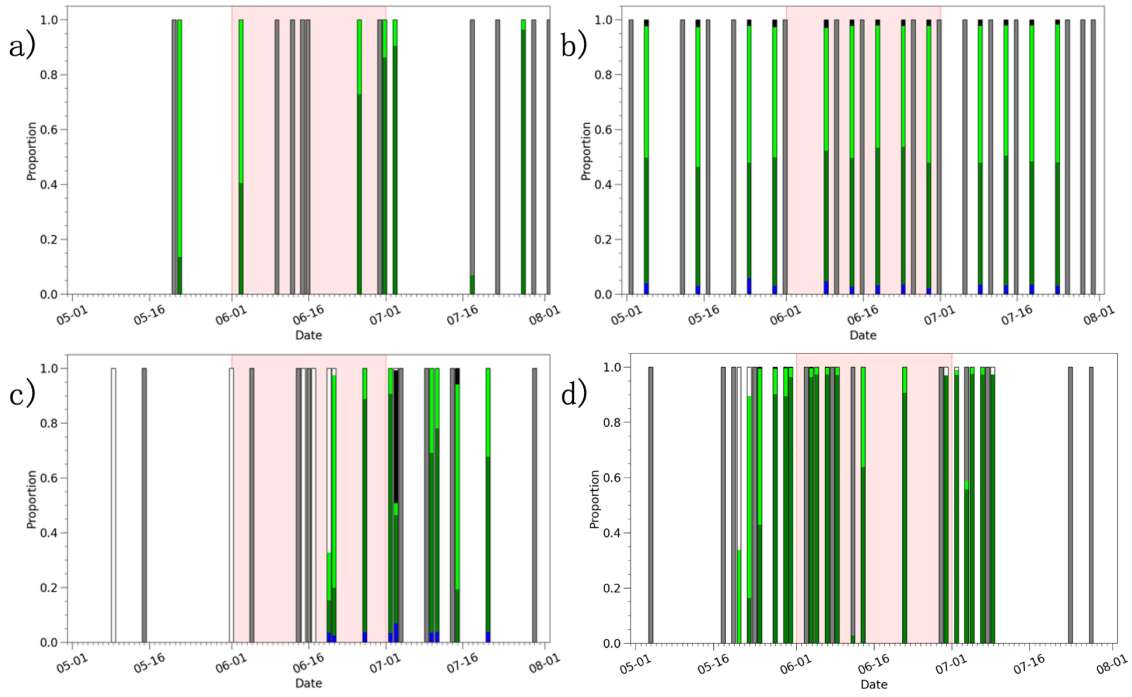

Figure 3.19 Example of changing majority LC using Google Dynamic World dataset over 3 months at CA-LP1 (a) and mixing of different Land cover types at US-Dmg (b). Example of contamination of snow in the research period at US-xBA (c) and good homogenous site–US-Rpf (d). The shadowed area was the validation period.

Among 46 sites, US-Rpf (Ueyama et al., 2019), US-RGB (Schuppenhauer and Biraud, 2022) and SURFRAD dra were used as the validation example of forest, low vegetation and barren, respectively (Figure 3.20). US-Rpf located at Poker Flat Research Range of the University of Alaska Fairbanks for 65°07′11″N, 147°25′44″W, with an altitude at 491 m. In 2017, the dominant overstory was reported as paper birch. US-RGB located at Butte County Rice Farm for 39° 34' 42" N, 121° 51' 28 " W, with an altitude at 33 m. It was a farmed area, with mid-grain japonica rice variety. SURFRAD dra located at Desert Rock, Nevada for 36° 37' 25 " N, 116° 1' 10" W, with an altitude around 1007 m. It has a texture mixed by shallow shrubs and barren surfaces.

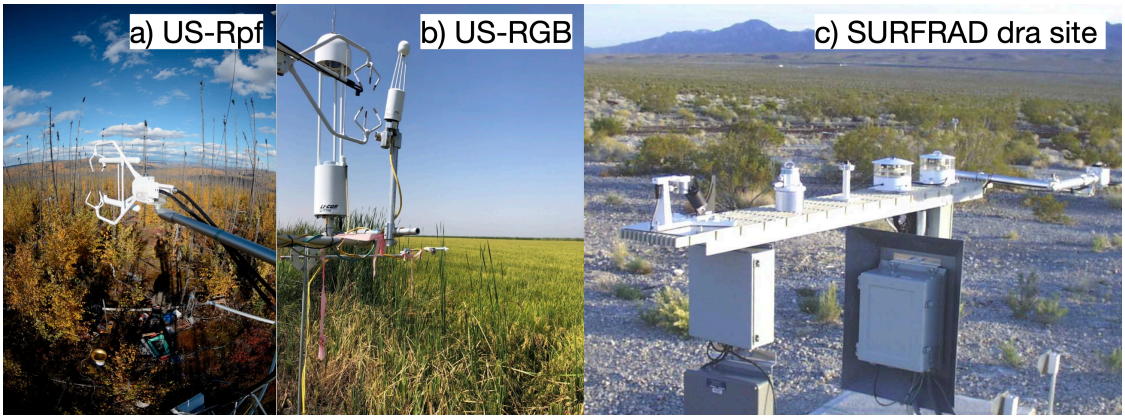

Figure 3.20 The gallery of the instrument and surrounding environment of ground targets for the example sites, including a) US-Rpf, b) US-RGB, c) site dra

3.5.4 Result of T-based Validation

The MERSI-LL FY-3E LST showed good consistency with ground observations at vegetated surfaces. The LST was ranging from 270 to 320 K with a RMSE of 2.07 K using the validation dataset (Figure 3.21a). Most points were aligned along the 1:1 line, with a small positive bias of only 0.85 K observed, and no obvious over- or underestimation was obtained across the entire LST range.

Separating the vegetation into forest and low-vegetation resulted in only minor differences between the MERSI-LL FY-3E LST and in situ LST. Both categories displayed comparable LST ranges and positive biases; however, a slightly lower RMSE of 1.87 K and reduced bias were obtained for forest sites (Figure 3.21b, Figure 3.21c). The bias for forests remained stable over the whole LST range, whereas overestimation was exhibited for low vegetation sites for lower LSTs.

Similar performance was obtained for two example sites with cloud free observations: US-Rpf (forest) and US-RGB (low vegetation), both of which produced a RMSE of approximately 2 K and a positive bias over the entire LST range. However, a higher bias (1.50 K) was obtained for the US-Rpf forest compared to the low vegetation US-RGB site (1.11 K) (Figure 3.21d, Figure 3.21e), where an underestimation of LST occurred for surfaces with LST larger than 300 K.

The MERSI-LL FY-3E LST showed a different performance for the only barren site, the dra site (Figure 3.21f). The LST at this site exhibited a larger RMSE of 4.09 K, as compared to the vegetated sites. LST Underestimations were observed across the LST

ranging from 285 K to 325 K and larger LST underestimations occurred at higher LSTs. For example, an underestimation of approximately 1 K was observed for a LST of approximately 280 K, and even larger underestimations of over 5 K were observed for LSTs exceeding 320 K.

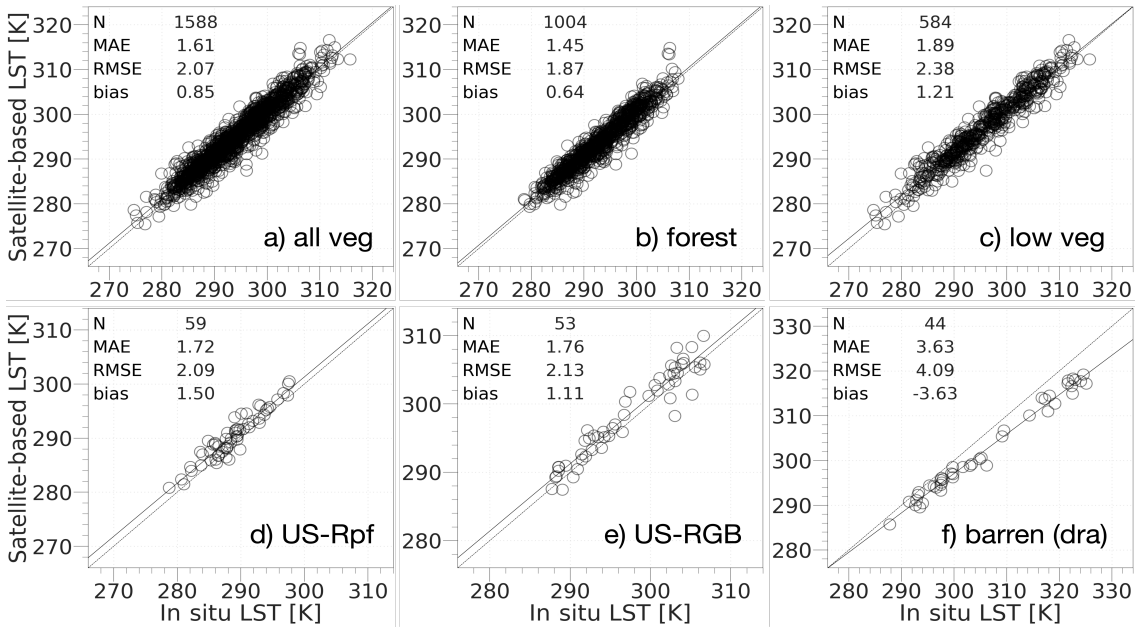

Figure 3.21 MERSI-LL FY-3E LST validation against in-situ LST at a) all vegetated sites; b) forest sites; c) low-vegetation sites; d) US- Rpf; e) US-RGB; f) the only barren site (dra). N is the count for the match of one satellite pixel and corresponding in situ observation. Dash line is the 1:1 line while solid line is the linear regression line of satellite - site LST.

The MERSI-LL FY-3E LST exhibited significant sensitivity to atmospheric moisture and medium sensitivity to view angle; however, it was minimally influenced by LST magnitude and altitude (Figure 3.22). Larger differences were observed in the satellite-observed LSTs compared with the ground observations at higher atmospheric humidity (Figure 3.22a), especially when the total precipitable water (TPW) was larger than 4 cm. The median difference increased from 1.223 K at TPW of 0–2 cm and 1.407 K at TPW of 2–4 cm to 2.283 K at TPW larger than 4 cm. The various VZAs resulted in smaller changes in the LST differences compared to TPW (Figure 3.22b), with the median difference increasing from 1.2 K at 0–25° to 1.326 K at 25–50° and 1.402 K at 50–75°, with large differences more frequent at higher angles. Surfaces at 290–310 K were associated with a difference of 1.343 K, which was slightly higher than that obtained for

the other LST ranges and had more outliers (Figure 3.22c). Notably, surfaces with higher LST have a larger risk of producing larger errors. The LST distribution was minimally associated with site altitude, with median differences of 1.317 K and 1.239 K observed for altitudes below 1000 m and higher than 1000 m, respectively (Figure 3.22d).

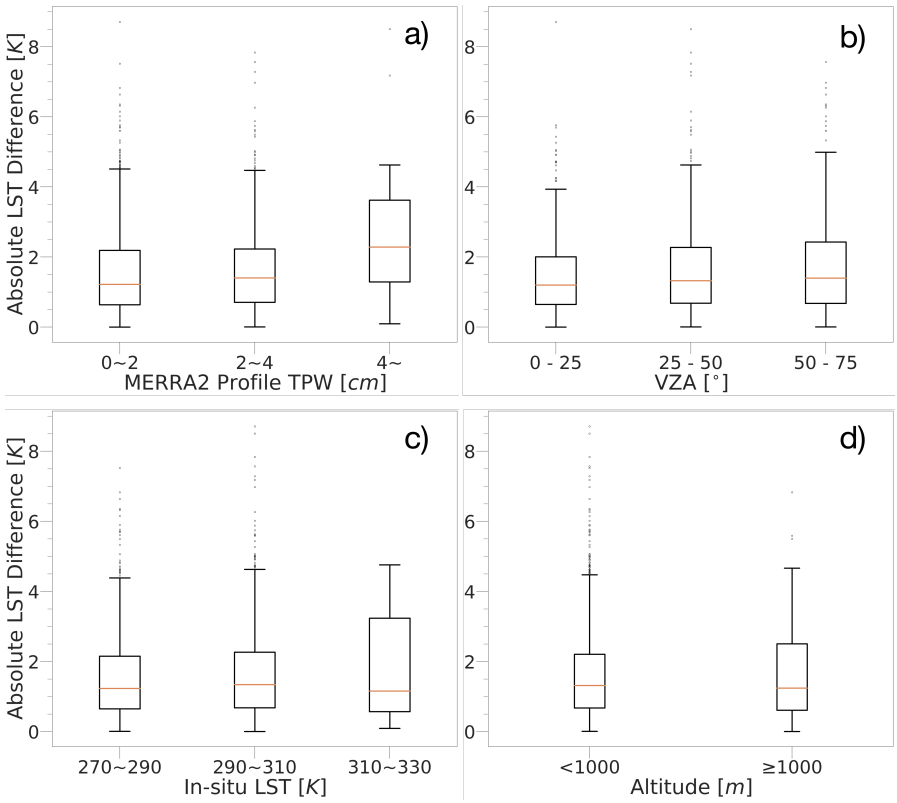

Figure 3.22 Sensitivity analysis of absolute difference (MERSI-LL FY-3E LST and in situ LST) under different conditions: a) different atmospheric total precipitable water (TPW); b) different observation VZAs; c) different in situ LST ranges; and d) low (below 1000 m) and high (over 1000 m) altitude.

3.5.5 Polar Orbiter-based LST and Emissivity Products

The LST&E (LST and Emissivity) products of MODIS onboard Terra and Aqua and VIIRS onboard SNPP were used for inter-comparison with the emissivity obtained by MERSI-LL FY-3E or as a reference to indicate the performance of FY-3E LST. MODIS is an optical scanner that measures Earth radiance in 36 bands, ranging from 0.4 to 14 μm. It has been in operation aboard the Terra and Aqua satellites since the late 1990s and early 2000s, central to NASA's Earth observation program. VIIRS, on the other hand, was designed to continue and enhance the data records initiated by MODIS deployed on SNPP satellite in 2011 (Xiong and Butler, 2020). MODIS TES-based LST data with a 5-min-

per-scene interval and an approximately 1 km resolution at nadir were extracted from Collection 6 MOD21 or MYD21 (Malakar and Hulley, 2016), and VIIRS TES-based LST data with a 6-min-per-scene interval at an approximately 750 m resolution at nadir were obtained from version 001 VNP21 (Islam et al., 2017). A quality control (QC) flag was used to filter the observation conditions. A strict cloud criterion (cloud, thin cirrus, and nearby cloud pixels were excluded) was used for in situ validation and spatial intercomparisons. The geolocation data extracted from MODIS product MOD03/MYD03 collection 6 or VNP21 were used for map reprojection and elucidation of which observations were spatially closest to the in situ study locations. Intercomparison of the emissivity was conducted in June 2022, for the validation sites. The emissivity of different bands and broadband was extracted at a single pixel and intercompared.

The TES band LSE and broadband emissivity for MERSI-LL FY-3E were reasonable compared to those obtained by other sensors on polar orbiting satellite across all sites (Figure 3.23a). The median of LSE showed the diffrence within 0.01. It was except for the TES B1 obtained using MERSI-LL as compared to VIIRS, which was higher than most of the cases. The MERSI-LL FY-3E occasionally produced LSE values lower than 0.9 for the TES bands, and MODIS was observed to produce emissivities below 0.93. These results were confirmed over both forests and sites with low-growing vegetation, although larger uncertainties were associated with the latter (Figure 3.23b, Figure 3.23c). The emissivities obtained using MERSI-LL FY-3E was more stable at the two example sites: US-Rpf, a forest site, and US-RGB, a low-vegetation site (Figure 3.23d, Figure 3.23e). Large uncertainties in the MERSI-LL FY-3E TES emissivities and larger intra-satellite differences were observed over barren land cover (Figure 3.23f). In particular, compared to the TES B2 and TES B3 obtained using MERSI-LL FY-3E, TES B1 was associated with a much larger uncertainty.

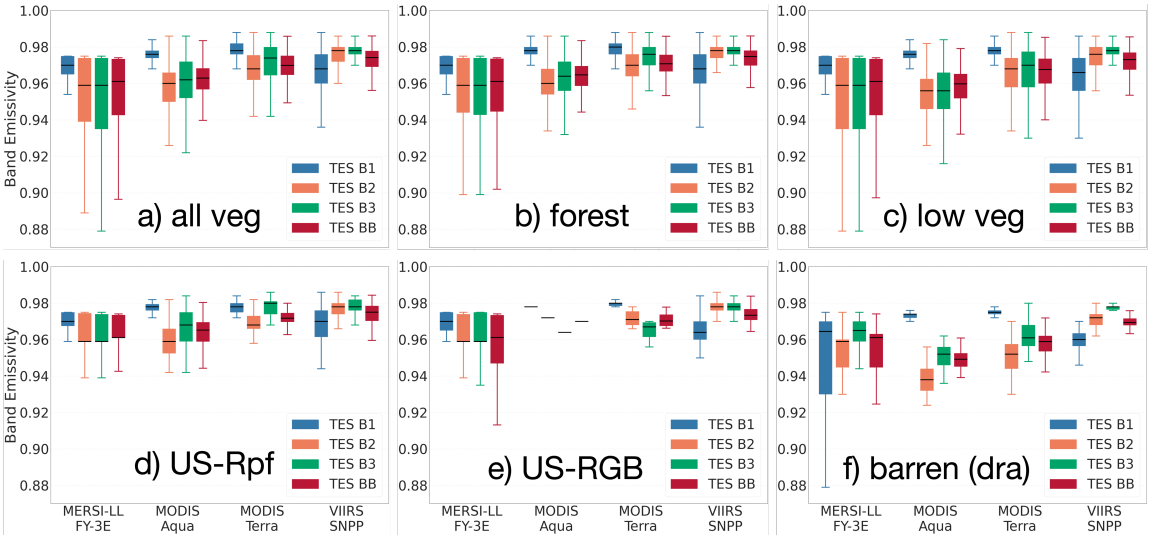

Figure 3.23 Emissivity obtained using each TES band in the polar orbiters for a) all vegetated sites; b) forest sites; c) low-vegetation sites; d) US-Rpf; e) US-RGB; and f) barren site (dra). TES B1, TES B2, and TES B3 indicate the emissivity of the corresponding bands in the TES algorithm, while TES BB denotes the estimated BBE that depends on the linear combination of all three bands. Emissivity data were collected in June 2022. In the boxplots, black lines represent the median value and fliers exceeding the range 25%–1.5IQR and 1.5IQR+75% are not shown (IQR: interquartile range, the difference of value at 75th percentile and 25th percentile, 75% and 25% represent the value at 75th percentile and 25th percentile).

3.5.6 Intercomparison with the GEO Satellites

Intercomparisons with other LST products facilitates the evaluation of LST consistency across different land surfaces (Duan and Li, 2015). However, temporal normalization is required to standardize differences between the LSTs for polar orbiters with different ECTs (Reiners et al., 2021). GEO satellites provide more direct LST comparison because of their higher temporal resolution, and most 3rd generation GEOs revisit a site every 10–30 min, reducing the LST changes caused by ECT differences between the sensors for intercomparison (Wang et al., 2020).

In this study, the LST products from the ABI on GOES-16 (Beale et al., 2020) and AHI on Himawari-8 (Yamamoto et al., 2022) were used as a reference for evaluating the LST product from polar orbiting satellites (mainly MERSI-LL FY-3E). GOES-16, developed by the National Oceanic and Atmospheric Administration (NOAA) in collaboration with NASA, was launched on November 19, 2016. It is the first spacecraft

in the GOES-R series and is located at 75.2˚E, providing coverage of the contiguous United States (CONUS) and the Atlantic Ocean in the northern hemisphere. Himawari-8, operated by the Japan Meteorological Agency (JMA), was launched on October 7, 2014, and is located at 140.7˚W, covering Southeast Asia and the Pacific area. Both satellites used a GSW approach to develop their LST products, with an approximate nadir resolution of 2km. The validation was conducted over two ROIs with a margin of approximately $10° \times 10°$ (Figure 3.18b-g). The first ROI (ROI 1), centered at 110°E, 40°N in Asia, is covered by Himawari-8 AHI, with well-developed LST products. Another ROI (ROI 2) was used to reduce the uncertainties and differences associated with the different GEO LST products, centered at 100°W, 43°N in North America (ROI 2) that is covered by ABI GOES-16. In addition, a cloud mask intercomparison was conducted at two ROIs.

LST products from GEO or polar orbiter over the two ROIs were first processed using cloud masks. Intercomparisons were then performed for the resampled LST products from GEO or polar orbiter at the two most common local crossing times for each intercomparison pair. To reduce the VZA effect produced by different platforms, the MERSI-LL VZA at the scene center was limited to 50°–60° to match up the GEO VZAs at the two ROIs (55.998° for ROI1 center and 55.561° for ROI2 center). At each ROI, the available pixels in the scene were grouped into four categories: barren (NDVI < 0.3), sparse vegetation ($0.3 \leq$ NDVI < 0.6), dense vegetation (NDVI ≥ 0.6), and the total of the three. It is important to understand the LST performances over different land covers with different spectra; for example, vegetated surfaces have larger LSEs than bare soil or rocks based on spectrum library. Moreover, it will extend the understanding from sites to larger areas (Jacob et al., 2017).

The MERSI-LL FY-3E LST showed similar differences against AHI Himawari-8 and ABI GOES-16 (Figure 3.24) at dawn and dusk. At dawn (Figure 3.24a, Figure 3.24c), the MERSI-LL FY-3E showed larger LSTs than GEO satellite-based LSTs across both ROIs and an overall good consistency. The median difference was around 0.7 K and most of the error lies within 0–4 K. Additionally, it did not show bias differences over the three types of vegetation density. At dusk, the MERSI-LL FY-3E LST exhibited an approximately 1 K negative bias against GEO LSTs and showed larger differences ranging between –5 K and 5 K compared to dawn time (Figure 3.24b, Figure 3.24d). For

different vegetation densities, the densely vegetated pixels tended to produce smaller biases, whereas for more sparsely vegetated pixels, the MERSI-LL FY-3E LST obtained lower LSTs, especially at the ROI2.

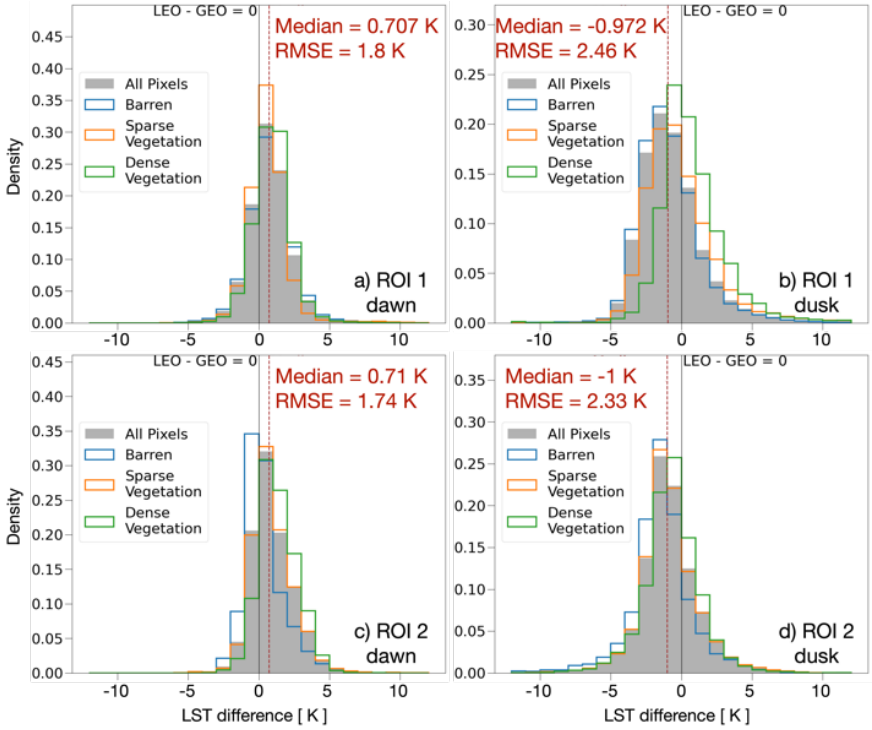

Figure 3.24 LEO-GEO LST differences (LEO here represent polar orbiters) obtained using MERSI-LL FY-3E at dawn and dusk over two regions of interest (ROIs). a,b) ROI 1 (110 ˚E, 40 ˚N) at 05:20 (local time) on June 16, 2022, and 17:55(local time) on June 7, 2022 as compared to AHI; c,d) ROI 2 (100 ˚W, 43˚N), at 05:20 (local time) on June 4, 2022, and 17:50 (local time) on June 11, 2022 as compared to ABI. Each bar represents the density of the difference between the satellite-obtained and in situ obtained LSTs over all pixels. Shadowed bars represent the difference distribution of all categories of NDVI ranges, while colored lines represent different vegetation densities: barren (blue), sparse vegetation (orange), and dense vegetation (green).

FY-3E showed a totally lower LST when comparing to GOES-16 LST in the example region (Figure 3.25). The bias mainly lies within the range of -2 K – -1 K and sometimes have a -3 K – -2 K bias. This can be connected to the following possibility: 1. FY-3E is really underestimated the LST; 2. GOES-16 is overestimated and; 3. Either underestimated or overestimated, and the bias was caused by the magnitude of error. Therefore, an additional in-situ validation was conducted to reveal the reason which relies on the sites surround the ROI2 (Figure 3.26a, comparison to GOES-16 LST). The both

LST error median of FY-3E and GOES-16 showed a positive bias, that represents both have a tendency of overestimation of the LST. Moreover, GOES-16 LST showed a higher overestimation, at approximately 0.6 K than FY3E LST (Figure 3.26b). This is consistent to the lower LST observed in the ROI2 when doing the spatial intercomparison.

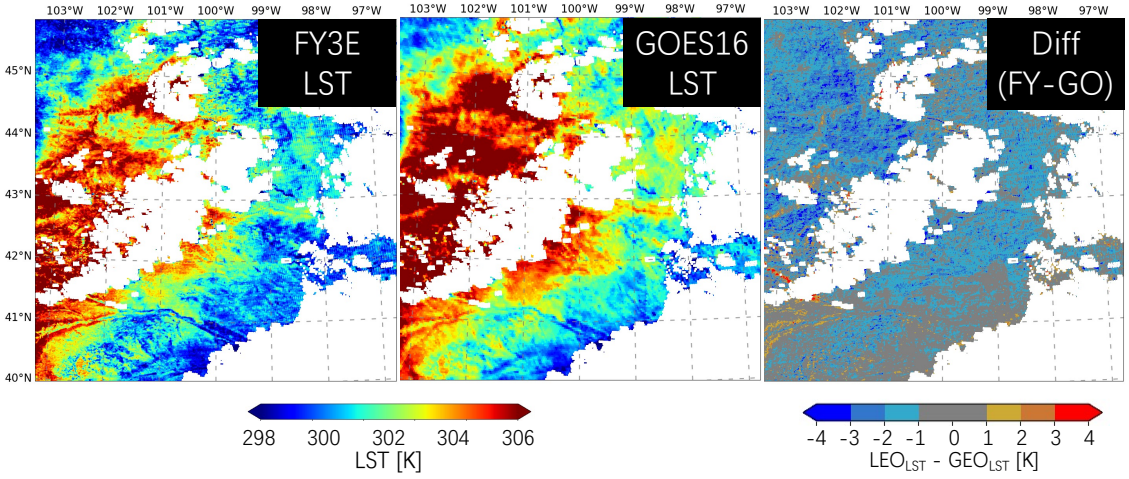

Figure 3.25 Spatial comparison of the FY-3E LST and GOES-16 LST.

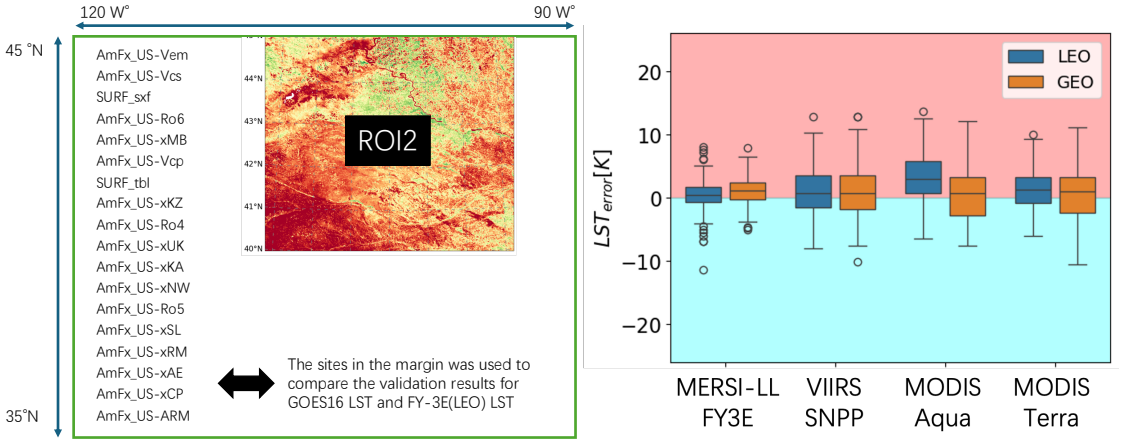

Figure 3.26 (a) Margin of the spatial comparison and border of validation sites, and (b) LST errors of LEO polar orbiting satellites comparing to GEO satellites (GOES16) in June 2022. The comparison was only counted of the observation at the same hour of utc time.

3.5.7 Limitations and Issues Associated with MERSI-LL FY-3E LST and LSE

Among the 46 validation sites, the results at the dra site showed larger underestimates (Figure 3.21f). The surrounding terrain character and vegetation

distribution were checked first, but the heterogeneity is rather small within the MERRA2 grid (Figure 3.27). Both elevation and vegetation index showed a rather homogenous surfaces for the area surrounding of the SURFRAD dra site. Furthermore, the inspection of the data showed that underestimation is less directly related to large VZA, tpw of MERRA2, and the retrieved LSE but with large errors associated with greater downward longwave radiations (Figure 3.28). The large atmospheric component in the atmospheric correction procedures potentially caused an underestimation in the LST at the dra site. Moreover, under some larger VZA conditions, the MERSI-LL FY-3E LST produced larger errors. This finding is consistent with the large error at larger VZA conditions as shown in Figure Figure 3.22b. In addition, a systematic underestimation was pointed out by previous studies based on MODIS LST at the dra site, and an approximate 4 K underestimation was observed at nighttime compared to an approximately 2 K underestimation at daytime (Duan et al., 2019; Guillevic et al., 2014). Indicating the issues in dra is complex and not only the reason of the performance of MERSI-LL FY-3E LST at barren surfaces.

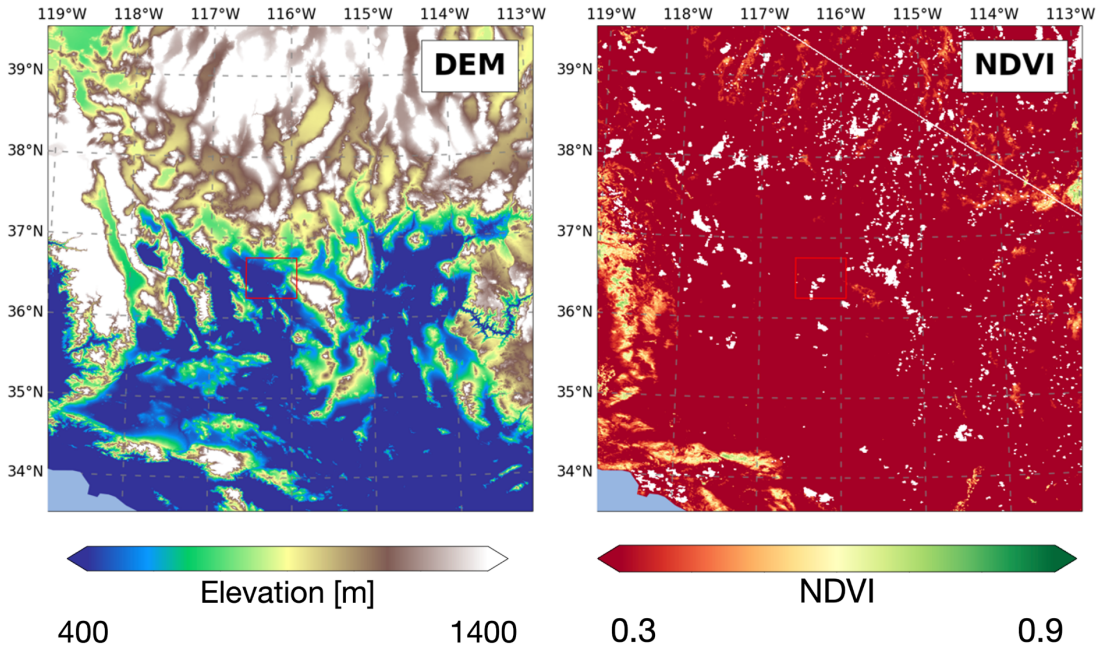

Figure 3.27 The surrounding terrain character (DEM: Digital Elevation Model) and vegetation distribution (NDVI: Normalized Differential Vegetation Index) around the dra site.

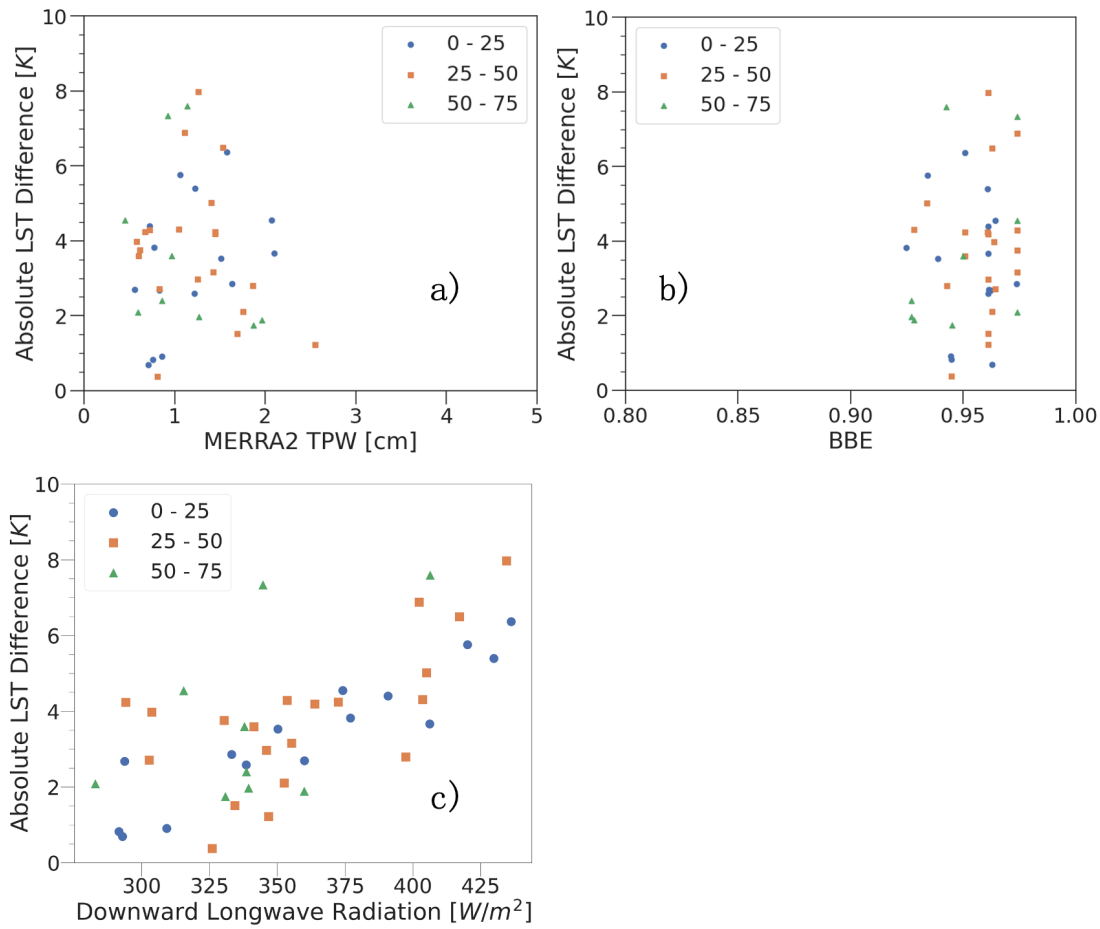

Figure 3.28 Absolute error at the dra site at different a) total precipitable water (TPW); b) estimated (broadband emissivity) BBE, and c) downward longwave radiation. The markers represent the observation at different VZA ranges: blue dots represent VZAs ranging from 0 to 25˚, orange squares represent VZAs ranging from 25 to 50˚; and green triangles represent VZAs ranging from 50 to 75˚.

Another possibility was the unique crossing time of FY-3E that may have different meterological condition or ground character. To reduce the error among the sensors (MODIS, VIIRS, MERSI-LL), GOES-16 LST was used to test if the different hour of the day will cause the large underestimation of FY-3E at dra site. Overall, GOES-16 indicates the underestimation over all of the hours Figure 3.29. The LST error showed largest underestimation at 6:00–8:00 am at approximately -6 K and smallest underestimation at 0:00–4:00 am at approximately -3 K. However, the larger underestimation of FY-3E LST occurred when LST is high is corresponding to LST at 16:00 pm with a medium underestimation. This indicates that FY-3E LST underestimation is not due to its unique timing of the day.

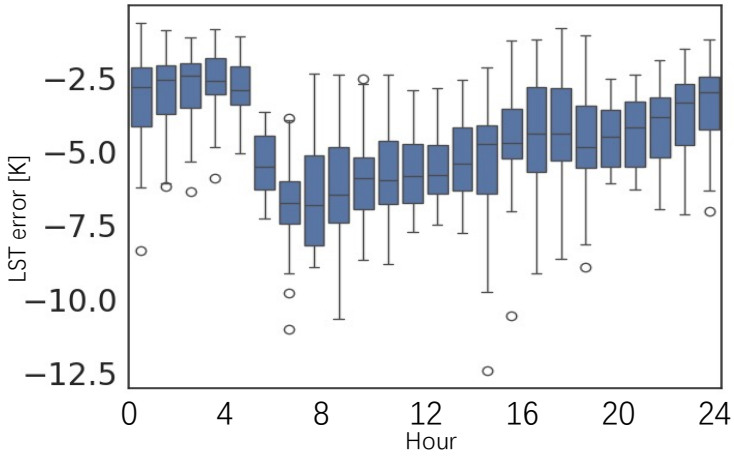

Figure 3.29 GOES-16 LST error at dra site in June 2022

Finally, it was found that one step in TES method, the WVS approach, caused the large underestimation at higher LSTs (Figure 3.30). Dra site was surronded by a very large area of barren landscape (Figure 3.27), but WVS included the atmospheric refinement that relies on the grey pixels, and usually vegetated surfaces. Thus, it has large uncertainty at landscape of dra site. Then, the WVS was removed to test if WVS procedures influence the final LST result. It was found that without WVS procedures, the RMSE and bias are both improved (Figure 3.30) and become comparable to MODIS LST and better than VIIRS LST (Figure 3.31). Besides, by removeing the WVS procedure and use atmospheric component directly, LSE retrival becomes stable and indicate it also influencing the LSE retrival (Figure 3.32).

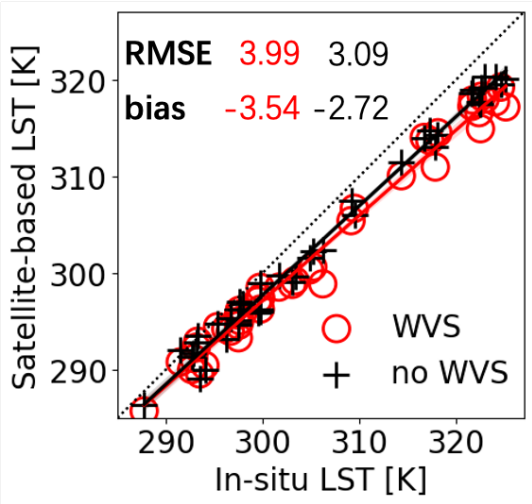

Figure 3.30 Comparison of the LST retrieved at dra site with and without the WVS (Water Vapor Scaling) process

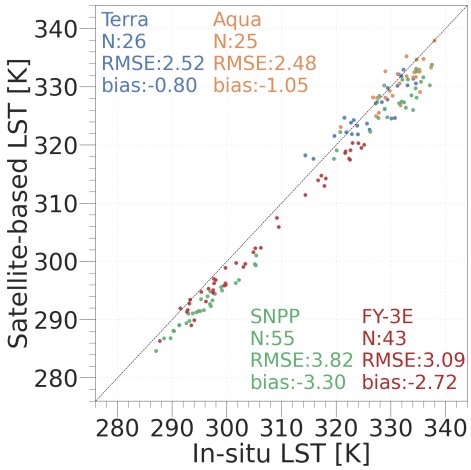

Figure 3.31 FY3E LST validation comparison among the LST products from polar orbiters after applying the correction of WVS.

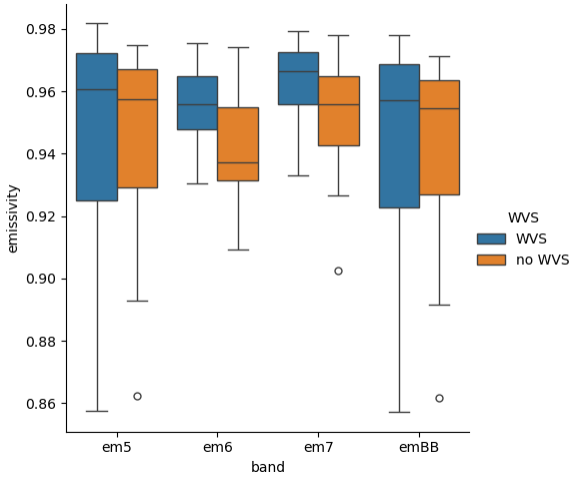

Figure 3.32 Comparison of the LSE (including emissivity of individual channels - em5,6,7 and the estimated broadband emissivity - emBB) retrieved at dra site with and without the WVS (Water Vapor Scaling) process

Small fluctuations are common for TES-based LST&E products, because components used in the equation solving steps always include noise (Yamamoto et al., 2022). However, considerable emissivity variation was observed from the MERSI-LL FY-3E LST in this study, especially for TES B2 and TES B3 (Figure 3.23). One possible reason is the occurrence of stripes between the scan lines. The TES method attempted to compensate for the stripes from the emissivity components of TES B2 and B3 (Figure 3.33), especially over low NDVI regions. As a result, it led to the uncertainty of emissivities (Figure 3.23f), causing a large error at the dra site (Figure 3.21f). Moreover, TES B2 and TES B3 are aggregated from the original 250 m radiance product, and the

noise associated with conversion may have been transferred to the 1 km resampled dataset. These issues can be resolved if a de-stripe algorithm is applied or if stripes are cut off as a VIIRS product. Furthermore, the constant part of the MMD formula in this study is around 0.972, which limits the final retrieved emissivity below this value; therefore, for LSE larger than this value, the components contributed by atmosphere were becoming larger in the equation than expected and resulted in errors. In further studies, refining the MMD relationship based on models that consider the cavity effect for vegetation surfaces is expected to improve this issue (Jacob et al., 2017; Zhou and Cheng, 2020).

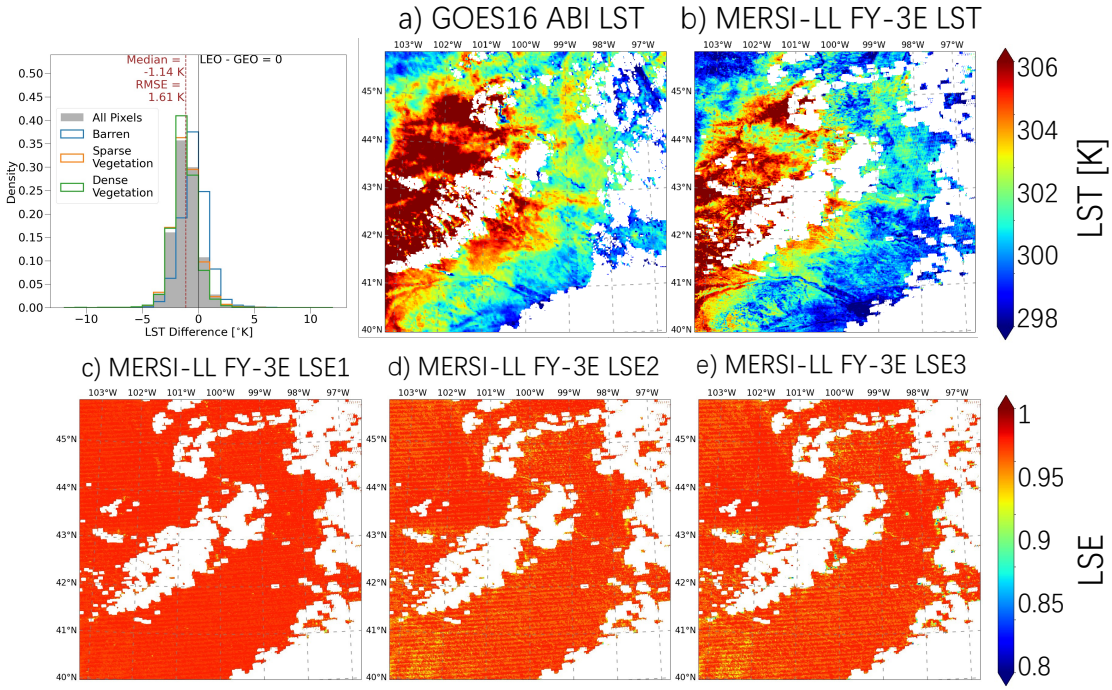

Figure 3.33 Spatial patterns of land surface temperature (LST) estimated by (a) ABI GOES-16, and (b) MERSI-LL FY-3E, and MERSI-LL FY-3E channel emissivities (c-e) estimated in this study. The observation time is 17:50 (local time) on June 28, 2022 for ROI2.

3.6 Performance of LST Products from Other Polar Orbiters

Understanding the performance of MERSI-LL FY-3E LST in comparison with LST products from other polar orbiters is important for promoting its further application, such as utilizing LST from different products. Regarding the LST ranges retrieved among the sites,

the LST range for MERSI-LL FY-3E falls within that observed by MODIS and VIIRS, as expected given its crossing time (Figure 3.34). This is because the minimum and maximum diurnal LSTs were obtained when crossing a ROI at night and noon, whereas MERSI-LL FY-3E LSTs were recorded at the early morning or late afternoon. At these times, the LSTs usually fall within the maximum-minimum range. In terms of accuracy, an RMSE of approximately 2 K for MERSI-LL FY-3E LST indicates a slightly better accuracy than that obtained by the LST products on other polar orbiter sensors (Figure 3.34a). The low biases and RMSEs obtained indicate accurate LST retrieval for both MERSI-LL FY-3E and VIIRS SNPP. These results demonstrate that the MERSI-LL FY-3E LST can achieve comparable results to widely used LST products from other platforms over vegetated surfaces. The validation was extended to three months from June only to the combination June, July and August at the same site using the same approach. The RMSE and bias did not see large differences. Additionally, the good performance of MERSI-LL FY-3E was not because of its narrower LST ranges because of its special crossing time. In Figure 3.35, the performance the RMSE of each LST product do not change larger than 0.2K and as a result not changing the ranking of the performances compared to the result showed in Figure 3.34a.

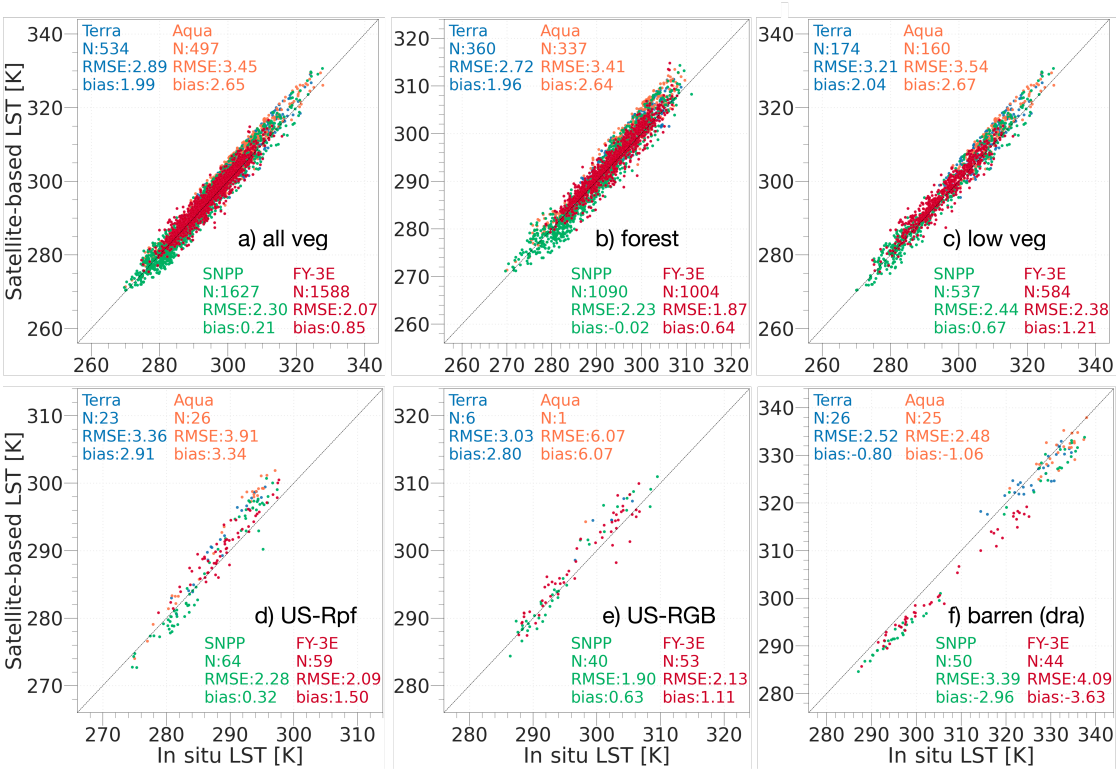

Figure 3.34 Validation of LST from polar orbiters (Terra, Aqua, SNPP, FY-3E) using in situ LST under clear conditions for a) vegetated sites; b) forest sites; c) low-vegetation sites; d) US- Rpf; e) US-RGB; and f) barren site (dra). And similar validation under clear or thin cirrus conditions for: g) all vegetated sites and h) barren site (dra). N indicates the number of satellite-site pairs. The dashed line indicates 1:1.

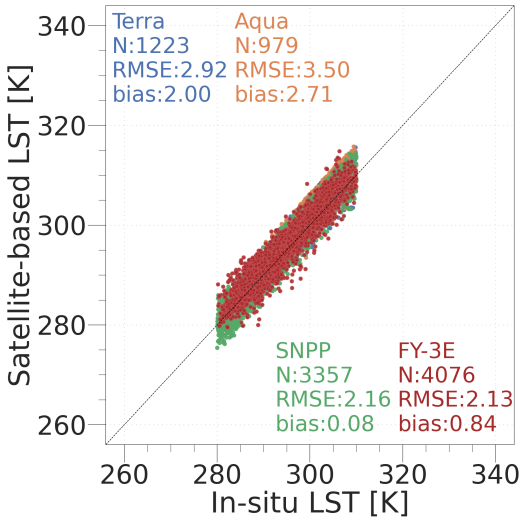

Figure 3.35 Validation of LST from polar orbiters (Terra, Aqua, SNPP, FY-3E) using in situ LST under clear conditions as Figure 3.34 but only for in situ observations within 280 K–310K.

The LSTs obtained for forest, low-vegetation, and two individual example sites were stable for both MERSI-LL FY-3E and VIIRS SNPP in terms of RMSEs (Figure 3.34b-e). MODIS LSTs presented similar RMSEs and biases between the forest and low-vegetation categories. At US-Rpf, the LSTs for MERSI-LL FY-3E and VIIRS SNPP showed similar RMSE and bias as the category for all vegetation, whereas the MODIS LST products showed worse estimations. At US-RGB, the LSTs for MERSI-LL FY-3E and VIIRS SNPP showed good RMSE and bias, but MODIS LST products suffered from issues with the fewer count of cloud-free observation. MODIS is thought to obtain the near-maximum and near-minimum LST values throughout the day; however, only high LST values were observed, which affected both the quality and quantity of LST observations.

The MERSI-LL FY-3E LSTs showed worse retrieval at the barren site (the dra site) compared with the MODIS LST. Except for the MERSI-LL FY-3E LST, the VIIRS SNPP LST product showed a similar large RMSE and a large negative bias, whereas the MODIS LSTs showing the best RMSEs and biases compared to the MERSI-LL FY-3E and VIIRS SNPP LSTs (Figure 3.34f). All LST products showed a negative bias for this land type, while MERSI-LL FY-3E and VIIRS SNPP showing large biases. Notably, LST underestimations were associated with low LST observations for both MERSI-LL FY-3E and VIIRS SNPP. Similar issue was found at dra site as the issue at US-RGB, in which missing observations with MODIS products occurred for low LST ranges. This has an influence on the different LST RMSEs and biases among MERSI-LL FY-3E, MODIS Terra, MODIS Aqua, and VIIRS SNPP. This is related to the spectral characteristics for detecting cirrus are different between MODIS and VIIRS (Frey et al., 2020; Xia et al., 2018). And if the thin cirrus was added to the validation results, these lower LSTs become available and the valid LST doubles for MODIS LST products (Figure 3.36).

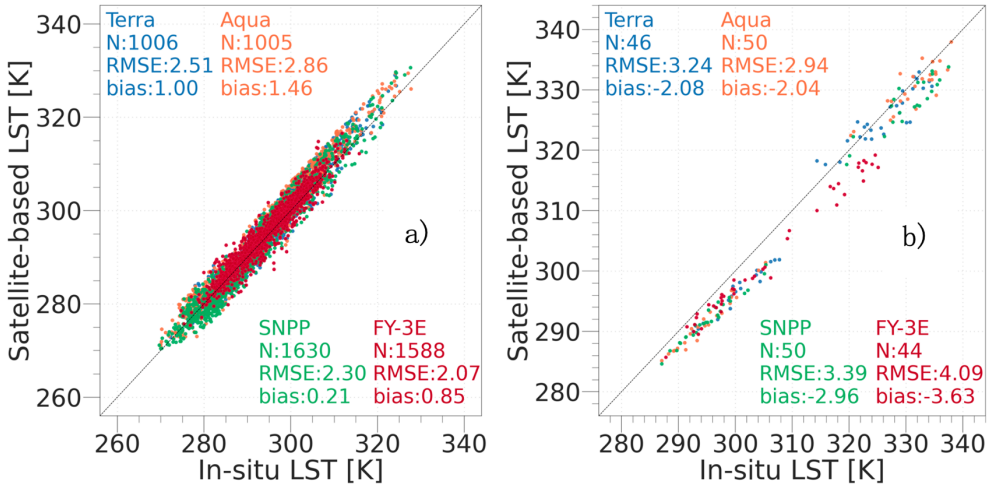

Figure 3.36 Validation of LST from polar orbiters (Terra, Aqua, SNPP, FY-3E) using in situ LST under clear and thin cirrus conditions for a) vegetated sites and b) barren site (dra).

To ensure the performance of the LST products over different seasons, especially the highest temperatures in summer and lowest temperatures in winter, the validation was extended from June to June, July, August, and December. As for the extended result in three months during summer in 2022, more LSTs at approximate 320 K were observed, however, the RMSE and bias did not show large difference against the result derived only using June data. Notably, MERSI-LL FY-3E collected more observations than VIIRS SNPP, which was related to the missing observations caused by system failures of the SNPP spacecraft (https://ladsweb.modaps.eosdis.nasa.gov/alerts-and-issues/138072). As for the validation result in winter, the LSTs were observed in the range from 230 K to 300 K. In this lower LST range, the LSTs from the VIIRS SNPP and the MERSI-LL FY-3E observed worse RMSEs than the results in summer. For instance, the RMSE changed from 2.25 K to 2.87 K on the VIIRS SNPP, smaller than the change from 2.15 K to 3.48 K on the MERSI-LL FY-3E. As for MODIS on the Terra or Aqua, the RMSE exhibited a better result but the available observation counts were much more reduced than summer (Figure 3.37). For example, the valid observation was approximately 1:3 between MODIS and VIIRS in summer but this ratio was 1:10 in winter. Such difference is related to the cloud detection and snow-cloud misclassification in the winter of the north hemisphere (Frey et al., 2020; Østby et al., 2014; Xia et al., 2018). These result at various seasons combined with sensitivity analysis and simulation result will ensure the applicability of MERSI-LL FY-3E.

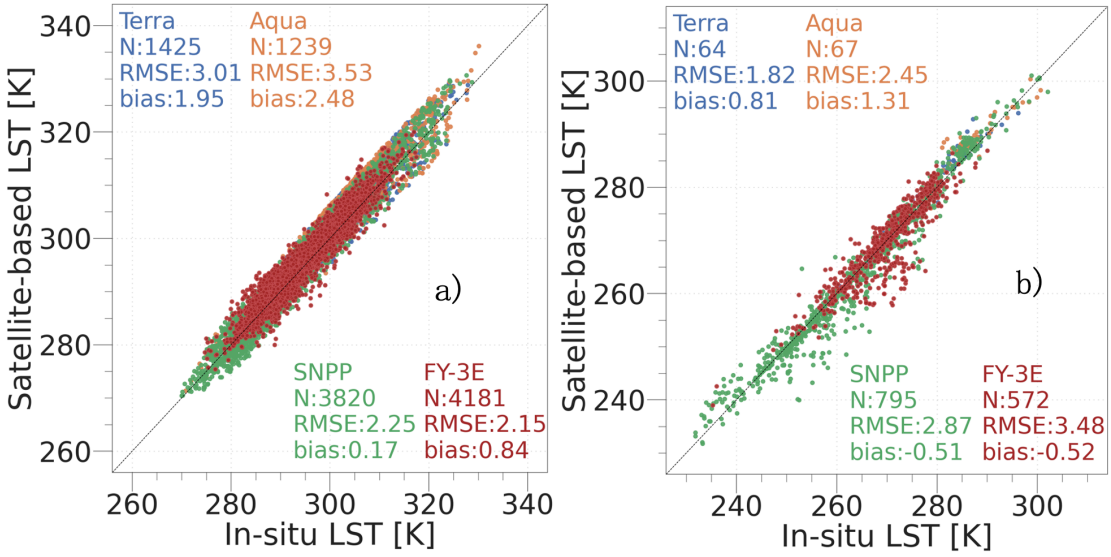

Figure 3.37 Validation results over the all-vegetation categories as figure which was extended to longer period. a) The validation results with 3 months data including June, July, August. b) The validation result using data in December.

Additionally, to address the sensor degradation issue of MODIS on Terra or Aqua and VIIRS on SNPP comparing to the newly launched FY-3E, the validation for MODIS and VIIRS was validated in 2013. Also, to answer the question that the swath data that was not used in producing bi-daily data is at the same performance as swath data that was used in producing the bi-daily data, the comparison of the validation was conducted on the separation of the swath data. Due to this reason, only sites at high latitude have many unused swath LST data. As a result, from 49 site in the Figure 3.38, 8 sites as following were selected as the candidate validation sites.

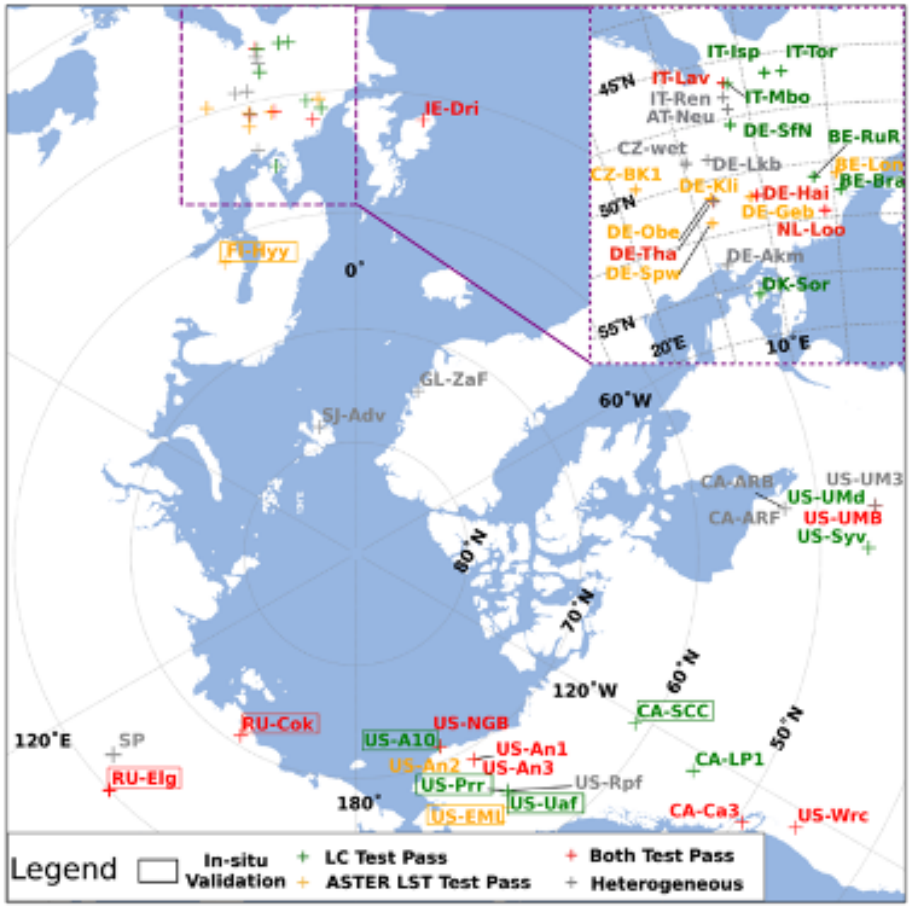

Figure 3.38 Eddy Covariance tower location, and heterogeneity test information based on Land Cover (LC) and ASTER surrounding LSTs. The site ID with rectangular was used for validation.

Table 3.4 Validation Sites For Comparison in 2013 Summer

SITE ID	LC	Latitude	Longitude	ε_b
CA-SCC	ENF	61.31 °N	121.30 °W	0.974
RU-Elg	DNF	60.02 °N	133.82 °E	0.975
FI-Hyy	ENF	61.85 °N	24.29°E	0.976
RU-Cok	OSH	70.83 °N	147.49 °E	0.971
US-A10	BSV	71.32 °N	156.61 °W	0.970
US-EML	OSH	63.88 °N	149.25 °W	0.973
US-Prr	ENF	65.12 °N	147.49 °W	0.973
US-Uaf	ENF	64.87 °N	147.86 °W	0.974

*ENF: Evergreen Needleleaf Forest; DNF: Deciduous Needleleaf Forest; OSH: Open Shrubland; BSV: Barren Sparse Vegetation; LC: land cover; ε_b: surface broadband emissivity

In situ LSTs were calculated using the Stefan–Boltzmann law as follows:

$$\varepsilon_b = 0.197 + 0.025\epsilon_{10} + 0.057\epsilon_{11} + 0.237\epsilon_{12} + 0.333\epsilon_{13} + 0.146\epsilon_{14} \quad (3\text{-}16)$$

$$\mathrm{LST} = \left(\frac{\mathrm{LW_{OUT}} - (1-\varepsilon_b)\mathrm{LW_{IN}}}{\sigma\varepsilon_b}\right)^{1/4} \quad (3\text{-}17)$$

where ε_b is the surface broadband emissivity estimated from the ASTER-GED dataset and ϵ_{10-14} are the ASTER-GED band emissivities (Cheng et al., 2013). $\mathrm{LW_{OUT}}$ is the site upward longwave radiation ($\mathrm{W \cdot m^{-2}}$), $\mathrm{LW_{IN}}$ is the site downward longwave radiation ($\mathrm{W \cdot m^{-2}}$), and σ is the Stefan–Boltzmann's constant ($5.67 \times 10^{-8}\ \mathrm{W \cdot m^{-2} \cdot K^{-4}}$).

Eight sites from the original 49 was chosen for satellite LST validation based on criteria such as spatial heterogeneity, latitude, and several specific considerations (Figure 3.38, Table 3.4) (Hiyama et al., 2021; Ikawa et al., 2015; Nakai et al., 2013; Sullivan et al., 1997; Ueyama et al., 2014). Spatial heterogeneity tests were conducted within a 1 km × 1 km window, excluding sites failing both the LST and land cover (LC) tests. The annual mean LST from ASTER-GED-100m (Hulley et al., 2015), where 25th and 75th percentile data with a difference larger than 3°C, was regarded as LST heterogeneity. Sites with a Shannon Diversity Index larger than 0.5 were deemed LC heterogeneous using the ESA-WorldCover-10m-v100 (Zanaga et al., 2021). In addition, sites below 60°N were excluded to focus the analysis on higher latitude locations. Besides the common rules, the US-NGB was removed because of the large standard deviation band emissivities extracted from MODIS and VIIRS products. These values were at approximately 0.015 for channels at 11 μm or 12 μm. It indicated the changing surface characters in the research period. The US-An1, US-An2, and US-An3 were removed because of the prior burn event in 2007, and the possibility of different emissivities between the one from the ASTER GED dataset during 2000-2008 and ground truth one in 2013 (Thunberg et al., 2021).

The LSTs derived from satellites within this research demonstrated consistency with *in situ* observed LSTs under cloud-free conditions. Notably, the swath LST categorized as extra LST showed similar performance against the one categorized as bi-daily LST (Figure 3.39). Notably, the extra LST exhibited comparable Root Mean Square Errors (RMSEs) and biases to those of the bi-daily LST. Both the extra LST and the bi-daily LST presented an RMSE below 3°C and biases approximately -0.6°C when integrating satellite LST data (Figure 3.39d). These LSTs from the MODIS sensors show a negative bias (Figure 3.39b), while the VIIRS SNPP LSTs exhibits a negligible bias (Figure 3.39c).

Upon examining the performance metrics of the extra and bi-daily LST, MODIS Terra and VIIRS SNPP both demonstrated consistent RMSEs and biases (Figure 3.39a, Figure 3.39c). However, there is a notable discrepancy between the extra LST and bi-daily LST from MODIS Aqua, attributed to the occurrence of a significantly underestimated LST observation (Figure 3.39b).

Regarding observation availability, the extra LST yielded comparable counts as bi-daily LST for MODIS Terra and MODIS Aqua at each latitude (Figure 3.39a). Moreover, the count of extra LST from VIIRS SNPP significantly exceeded more than twice the count of bi-daily LST, thereby markedly improving observation frequency (Figure 3.39c).

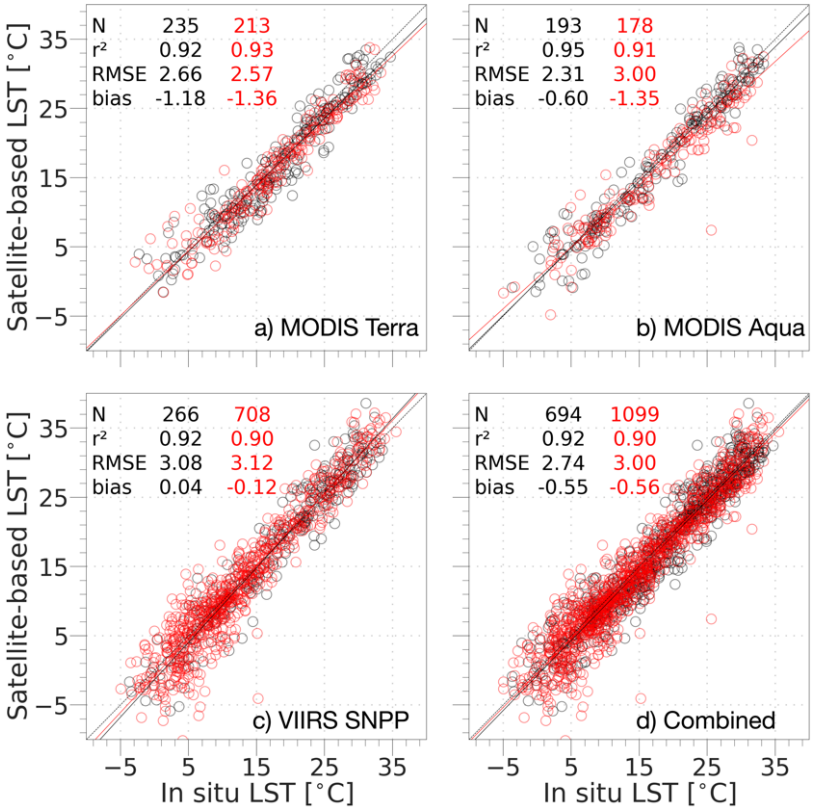

Figure 3.39 LST obtained from *in situ* (abscissa) and satellite-based (ordinate) measurements by (a) MODIS Terra, (b) MODIS Aqua, (c) VIIRS SNPP, and (d) the three satellites combined at all eight validation sites in the summer of 2013. The red markers represent the extra LST, while the black markers represent the bi-daily LST. Thin dotted lines are 1 to 1 lines, while solid lines are regression lines of satellite-based LST against *in situ* LST.

3.7 Conclusion of the Chapter

A TES-based MERSI-LL FY-3E LST was successfully constructed and validated. The subprocess including cloud mask, refining of the atmospheric component was under comprehensively validated. Validation using situ observations confirmed the robustness of the retrieved LST over vegetated surfaces and the issues at the barren surfaces, with further analysis revealing larger uncertainties in the obtained LST under large atmospheric components and larger viewing angles. Validations and comparisons were expanded to include regions, thereby extending the results of the pinpoint observations and supporting the reasonableness of the MERSI-LL FY-3E LST. Emissivity intercomparisons over in situ observations indirectly guaranteed the TES algorithm built in this study.

The intercomparison of the validation with LST from other polar orbiting satellites showed the LST build in this study is acceptable to terrestrial LST monitoring throughout the seasons. Also, the usage of swath data that not used for building the bi-daily product have same performances as those used for building bi-daily products. These results will allow for the combination of the MERSI-LL FY-3E LST with LST products from other polar orbiting satellites, the using of all available swath LST data, and as a consequence provide sufficient LST observations for rapid changes to be observed.

Chapter 4 Improvement of the Ecosystem Respiration Estimation Using Quasi-hourly LSTs in Arctic and Pan-arctic Regions

4.1 Introduction

Ecosystem respiration (Reco) refers to the component of carbon dioxide production in an ecosystem's carbon flux, whereas photosynthesis generally represents the largest part of carbon consumption within the ecosystem. It contains the component from aboveground respiration (mainly from leaves and woody tissues), and belowground respiration (derived from soil respiration, Rsoil, the sum of both autotrophic and heterotrophic processes, including root and soil biomes), and other minor components (carbonate weathering, subterranean ventilation, photo-degradation) (Barba et al., 2018). Its difference to the gross primary productivity (GPP) that mainly from plant photosynthesis represents the carbon budget between the ecosystem and atmosphere (NEE: net ecosystem exchange). As we known, the carbon will be released into atmosphere as carbon dioxide if the uptake is smaller than emission. Moreover, The Arctic region is undergoing rapid and profound changes due to climate warming, with temperatures rising at a rate much faster than the global average (Huang et al., 2017). This accelerated warming has significant implications for the carbon dynamics of the region, particularly concerning the abundant soil organic carbon (SOC) stored in permafrost (Biskaborn et al., 2019). Permafrost soils, which contain over 50% of the global SOC pool, are vulnerable to thawing as temperatures rise, potentially releasing substantial quantities of carbon dioxide (CO_2) and methane (CH_4) into the atmosphere through the ecosystem activities (Kuhry et al., 2013). Recent studies using eddy covariance (EC) flux observations in northern Alaska and Canada have shown that enhanced soil respiration during anomalously warm winters can offset carbon gains from GPP (Liu et al., 2020). For instance, during the warm winter of 2015–2016, increased soil respiration in these regions counterbalanced any carbon sequestration provided by plant growth (Liu et al., 2020). Similar trends have been observed in boreal forests in Finland and Sweden, where soil respiration has transitioned these ecosystems from carbon sinks to sources (Pumpanen et al., 2015). For example, in northern Sweden, a steady increase

in soil respiration, coupled with no change in forest GPP, resulted in a net annual CO_2 source. These releases could further accelerate global warming, creating a feedback loop with critical implications for the global climate system. This process is particularly concerning in boreal forests and tundra ecosystems, where soil respiration is a major component of the ecosystem's annual CO_2 emissions in most of the ecosystems.

Soil respiration was approximately 50% of the GPP in Alaska regions and such ratio have an uneven spatial distribution (Figure 4.1). And the ecosystem that include the soil respiration and aboveground respiration is general larger than this value, indicating a larger ratio. Soil respiration in boreal forests accounts for 48% to 68% of total respiration, while in tundra ecosystems, it is the primary source of CO2 efflux, with summer emissions alone constituting 60% to 90% of annual respiration (Figure 4.2) (Watts et al., 2021). Thus, the accurate estimation of the ecosystem respiration in the summertime is critical to understand the carbon budget of the Arctic and Pan-arctic regions.

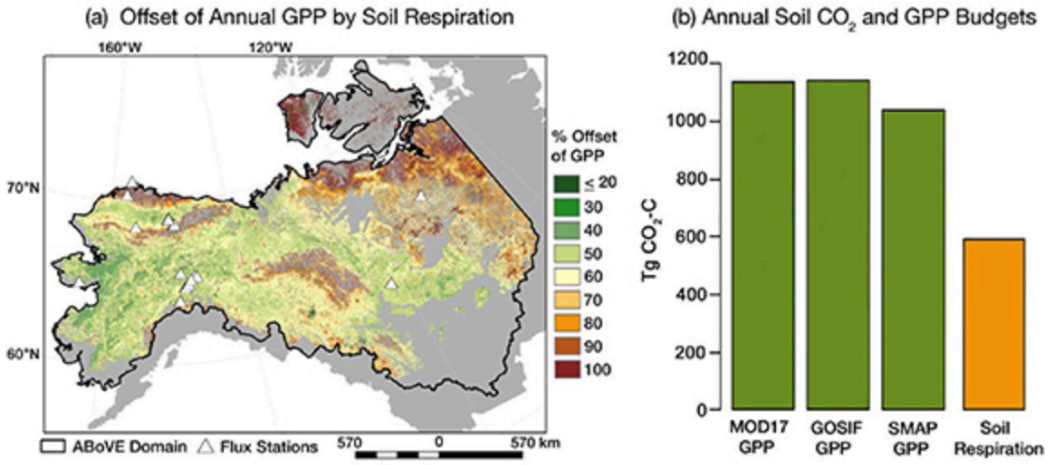

Figure 4.1 (a) Distribution of ratio between Reco and GPP in Alaska region. A 100% ratio indicates that soil respiration equaled or exceeded GPP. (b) Annual soil respiration and GPP totals (Tg CO_2) for the research area. GPP is from MODIS (MOD17), GOSIF, and SMAP L4_C products (Watts et al., 2021).

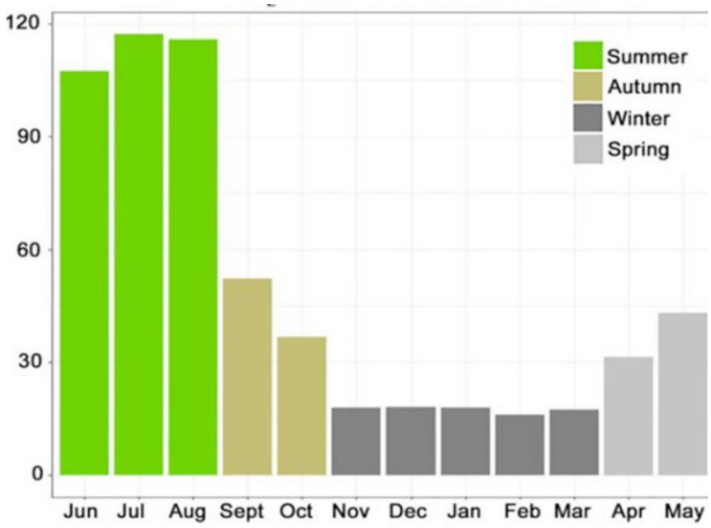

Figure 4.2 Monthly random forest-derived soil respiration (Tg CO2–C) for the region in Figure 4.1 (unit: Ton Carbon) (Watts et al., 2021).

Several issues exist for the estimation of ecosystem respiration. The first issue was remaining large uncertainties of the respiration derived from different process-based models (Figure 4.3). Respirations estimated from process-based models range from a 0.5 PgC to 2.0 PgC, which the maximum is 4 time of the minimum, comparing to the 1.1 PgC GPP indicated by (Watts et al., 2021), without the autotrophic respiration, it would identify the area as a carbon sink at 0.5 PgC respiration and as a carbon source at 2.0 PgC. Ecosystem respiration is notably sensitive to shifts in environmental conditions and varies widely across different biomes and regions. Understanding the dynamics of ecosystem respiration (Reco) is challenging due to the intricate interplay of physical, chemical, and biological factors involved in respiration processes. To enhance our grasp of ecosystem respiration dynamics and its implications for climate, respiration-temperature (R-T) models are good diagnostic model for achieving this (Cramer et al., 2001). The second issue was caused by the usage of the remote sensing based approaches. Most of the studies were using an annual indicator such as the mean of EVI or mean of NDVI, as well as the minimum LST to estimate a reference respiration (Rref) at a reference temperature (Tref) (Ai et al., 2018; Azevedo et al., 2021; Jägermeyr et al., 2014; Mahadevan et al., 2008; Rahman et al., 2005). However, the result at high latitude showed the large fluctuation of ecosystem respiration and it might be caused by the wrong estimated Tref and Rref. Also, considered the much shorter growing season in high latitude area, adopting same mean

values as other regions in the globe may produce a calculation bias due to longer cold seasons. As for the third issue, most of these remote sensing based estimation strongly relies the instantaneous nighttime LST at a certain overpassing time (MODIS Terra, approximately 21:00 at local time), and if such time cannot represent the mean status of the day, in particular, at the day that LST changes dramatically, such bias will be directly input to the calculation of R-T curve and make an error for ecosystem respiration that is exponential related to the temperature error (Figure 4.4, Figure 4.5).

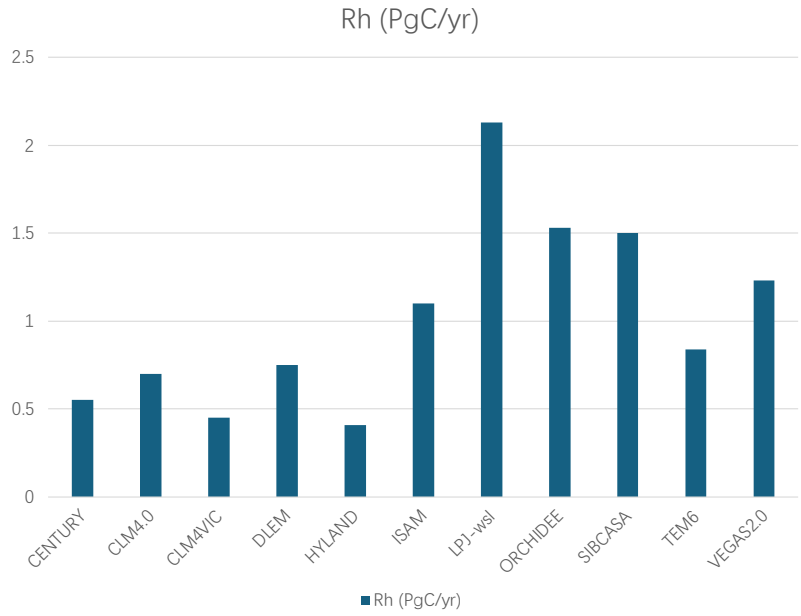

Figure 4.3 Heterotrophic respiration (Rh) for whole Arctic-Boreal Vulnerability Experiment (AboVE) region using the simulation output of process-based models during 2000-2010. The figure is reorganized from previous study Table1 (Huntzinger et al., 2020).

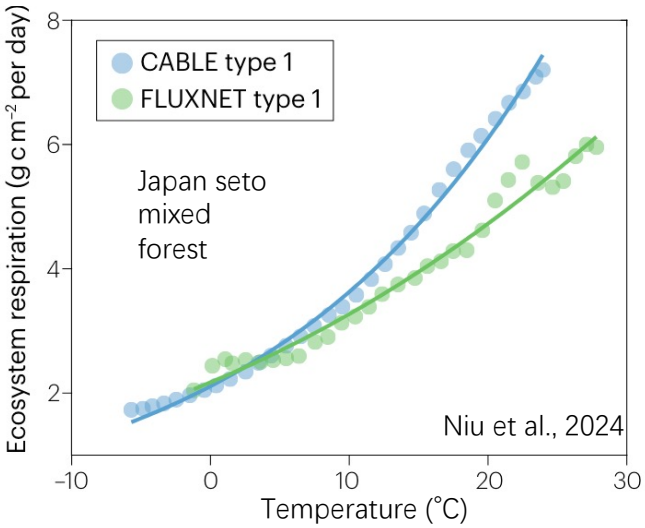

Figure 4.4 Ecosystem Respiration response to the temperature (Niu et al., 2024)

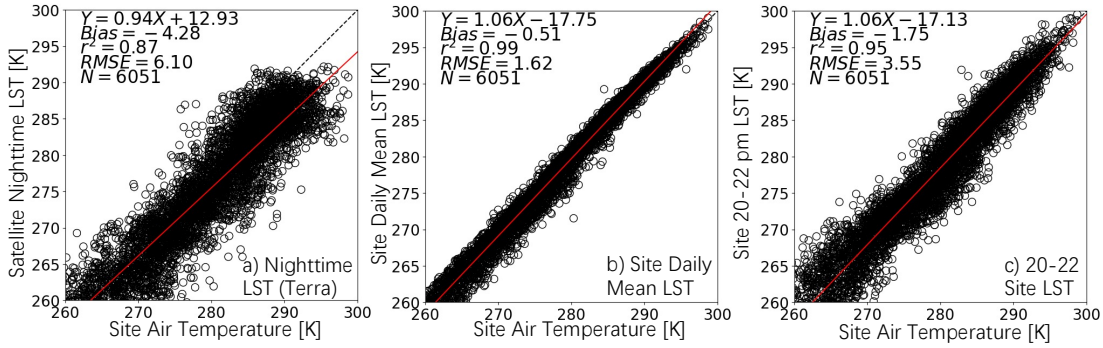

Figure 4.5 Comparison of nighttime LST and site daily mean LST alignment to the daily mean air temperature at 11 sites during 2010-2022 (section 4.2.1)

To address these issues, the following effort was examined. First, the approach with data-driven model using remote sensing as input is adopted to avoid the uncertainty that exist in the process-based models. Second, a growing season filter was applied to determine the Tref and Rref in Arctic and Pan-arctic regions. Meanwhile, the pair of Tref and Rref were optimized. Third, the daily mean LST estimated from sub-daily LST in Chapter 2 and Chapter 3 was used to drive the ecosystem respiration models, to avoid the error that caused by the usage of the instantaneous nighttime LST from MODIS Terra. In this study, the refining procedures were mainly for estimating the ecosystem respiration from April to October, because of its large contribution to the annual total comparing to

spring, autumn and winter, as well as the EVI inavaliablity in the polar nights. Additionally, the estimation was conducted at a daily scale, because ecosystem respiration response to temperatures which changes among the days and the daily mean LST data could provide the dynamic temperature changes.

4.2 Method

4.2.1 Site Observation Data

In situ observation data for ecosystem respiration was consist of 11 sites with observation period from 2010 to 2022 (Table 4.1). The sites located in Alaska, USA or the northern region in the Canada (Figure 4.6). The data was under the screening rules with the year that summertime have more than 60% data availability as well as the Q10 values through the season was below 4 [$gC/m^2/day/10^{\circ}C$]. Except from soil respiration data, other parameters were extracted or processed to make related analysis. The upward and downward longwave radiation with a fixed broadband emissivity at 0.97 was used for calculating the site LST. Same to the calculaFigure 4.6tion mentioned in the Chapter 3, the Stefan–Boltzmann law was used. Meanwhile, other parameters were extracted, for instance, the air temperature (Ta) and soil moisture of the site. Ultimately, the data was aligned with the remote sensing data mentioned in section 4.2.2 and those hourly LST constructed in Chapter 2 and Chapter 3. The finalized dataset was then split into 2 groups: 1) for those observation in 2010–2021, the data was used as training dataset for determination of parameters in daily mean LST estimation algorithm, also for optimizing the coefficients in ecosystem respiration estimation; 2) for those observation in 2022, as the avaliability of FY-3E data, the data in this year including 5 site years were used for testing the estimation for both daily mean LST and ecosystem respiration.

Table 4.1 In situ observations used for ecosystem respiration

Site Code	IGBP	lon	lat	Years Active (40% good data)
CA-HPC	ENF	-133.5188	68.3203	2018 (1)
CA-SCB	WET	-121.2984	61.3089	2014, 2016–2019 (5)
CA-SCC	ENF	-121.2992	61.3079	2014–2016 (3)
CA-SMC	ENF	-123.2522	63.1534	2018 (1)
CA-TVC	OSH	-133.5017	68.7462	2017 (1)
US-EML	OSH	-149.2536	63.8784	2011–2014, 2016–2020 (9)
US-Prr	ENF	-147.4876	65.1237	2011–2015, 2017-2021 (10), **2022**
US-Rpf	DBF	-147.4290	65.1198	2013–2017, 2020 (8), **2022**
US-Uaf	ENF	-147.8555	64.8663	2010–2021 (12), **2022**
US-YK1	WET	-163.2228	61.2723	2021 (1), **2022**
US-YK2	WET	-163.2590	61.2548	2020 (1), **2022**

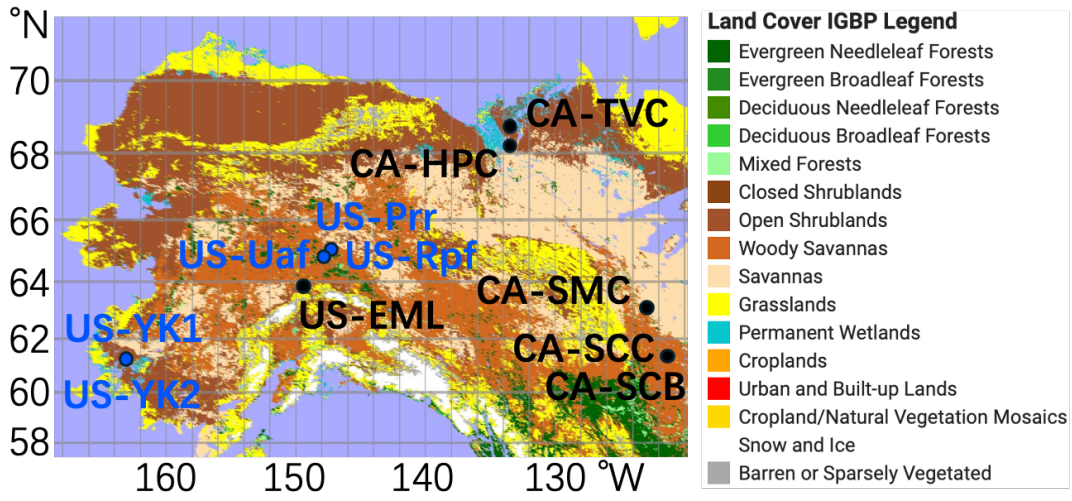

Figure 4.6 Location of gound observation sites in Alaska and Canada

The ecosystem respiration data was mainly calculated using the nighttime partitioning method. This method used the net ecosystem exchange (NEE) in the night as the completely respiration cases (Lasslop et al., 2010). Additionally, it assumes the ecosystem respiration throughout the day was regulated by the exponential relationship to the temperature at the site and known as Q10 method. Combining the nighttime data and the Q10 assumption, the Reco was calculated, quality controlled and interpolated by the site PI. The limitation included: 1) The respiration model is only driven by

temperature the sensitivity to the temperature is different among ecosystems (Richardson et al., 2006). 2) Soil respiration can be sensitive to soil moisture content that can be dynamic to meteorological conditions or to the soil properties including the nutrient and pH that have spatial differences (Ai et al., 2023; Maes et al., 2024). 3) Diurnal lag effect can exist between the respiration and temperature that mainly happened to deep soil (Bahn et al., 2008).

4.2.2 Remote Sensing Data

Three categories of the remote sensing data were used in this chapter: the LST data that represent the temperature, the EVI (Enhanced Vegetation Index) data that represent the biomass quantity and moisture content, and the LC (land cover) data that discriminate different ecosystem types to separate the group, especially that related to the nutrient avaliability and substrade supply, which lacks of the temporal dynamics or has difficulties to retrive from remote sensing technic. As for LST data, the 8 days LST from MODIS Terra (MOD11A2) was used to drive the R-T curve was used as a comparison as well as the daytime LST to drive the Tref estimation approach in the ecosystem respiration estimation. The sub-daily (hourly) LST that composed and validated in the Chapter 2–3 was used to estimate the daily mean LST and expect a better reproducing of the daily LST dynamic and as a consequence for a better estimated ecosystem respiration. Additionally, 16-days EVI from MODIS Terra (MOD13A2) was used to control the EVI fraction module in the ecosystem respiration. Because the EVI data was provided at a 250 m resolution, it was aggregated to 1 km as LST data for same spatial coverage. Both EVI data and LST data were filtered at good quality and then linear interpolated to daily scale and meanwhile filled the gaps for missing data. As for the LC data, the IGBP provided by site PI were used for site level analysis as well as the data from MCD12Q1 that used IGBP classification was used for spatial upscaling. The remote sensing data at the observation site was retrieved using the data from tool that provided the MODIS collection 6 observation at fixed location. This fixed sites subsets tool was provided by Terrestrial Ecology Subsetting & Visualization Services under the maintained by Oak Ridge National Laboratory (ORNL).

4.2.3 Daily Mean LST Estimation

As introduced in Chapter 1, the satellite-based LST have been collected for decades across globe for various applications. Most previous studies employed temporally aggregated results (8 days or monthly mean) of instantaneous cloud-free LSTs for long-term LST time-series analysis (Wongsai et al., 2017). As the ECT of the most polar orbiting satellites are the morning time or afternoon time, some studies use the LST at the exact time directly (daytime LST or nighttime LST). However, the time drift will cause the change of LST especially at the Arctic region or Pan-arctic region (Hong et al., 2022). This will add the external uncertainty or bias when making analysis of long-term trend. By utilizing the high observation frequency at high latitude regions, the LST diurnal changes can be represented by more samples. Thus, it was expected to be used for retrieving, improving, or simplifying the development of daily mean LSTs.

Many methods were used for retrieving the daily mean LSTs and the simplest approach was taking the average (AVE) of the LST. This will cause some issues if the sample is not sufficient especially the DTC curve is a convex function during the morning increasing. By adding more observations in the sample by using the approach in this study, such effect is expected to be reduced. Another way is the usage of the nearest neighborhood (NN) method. It assumes the LST around the sample time can be represented by the sample LST. It can be regarded as the weight based on the sample density. Thus, it can also benefit from high observation frequency LSTs. The empirical weight for LST at exact ECT can also be used retrieving more accurate daily mean using limited observations (Xing et al., 2021). Although method that combines annual temperature cycle (ATC) and DTC models (Hong et al., 2022), using spatiotemporal interpolation method (T. Zhang et al., 2022), or using surface energy balance models (SEB) (Jia et al., 2022) can be used to filling gaps in the LST DTCs or constructing gapless daily, these models require much more input data and assumptions to get daily mean, thus not meet the simplicity of the method.

To address the advantage in applying high observation frequency LSTs to retrieving the daily mean LST, the following three approaches were conducted: 1) The daily mean LST calculated from the NN interpolated; 2) The daily mean LST calculated from the all the sampled LSTs within the day without the consideration of observation time (AVE); 3) The daily mean LST that use the average of a fitted a 2-degree polynomial function

(Fit) that depicted the diurnal LST changes. 4) Ensembled daily mean LST estimation using linear regression and ensembled estimation.

The calculation of these method can be simple or rather complex based on their initial assumptions. The AVE method and NN method are the two most traditional methods for signal processing without relying on certain parameters. The Fit method assumes the LST is changing as a parabola opens downwards. And this approach used flexible 2 parameters and an empirical climax of the curve with a given tmax. The tmax was assumed stable for days in the whole season and was determined using the median of the tmax over the months from April to October.-Additionally, those day with diurnal temperature range (DTR) smaller than 5 ˚C as well as the DTR that much larger than the maximum DTR of the summer was regarded as the bad data.

In this study, the method proposed by Xing et al., 2021 was used and extended to individual hours as the fourth algorithm to estimate the daily mean LST which was mentioned in the previous paragraph. In the previous study (Xing et al., 2021), the daily mean LSTs were estimated using the LST at 2, 3, or 4 observation timing as the combination of day/night by Terra/Aqua. Validation at the same site data showed a decreasing of RMSE from 1.60 K to 0.80 K and the RMSE from approximatelly 2.20 K to 0.40 K depending the land cover type or climate type (Figure 4.7). However, the external validation at 6 SURFRAD sites (BND, TBL, DRA, FPK, PSU, SXF) showed the RMSE between 1.99 K and 2.52 K and the combination with more input do not always improve the estimation.

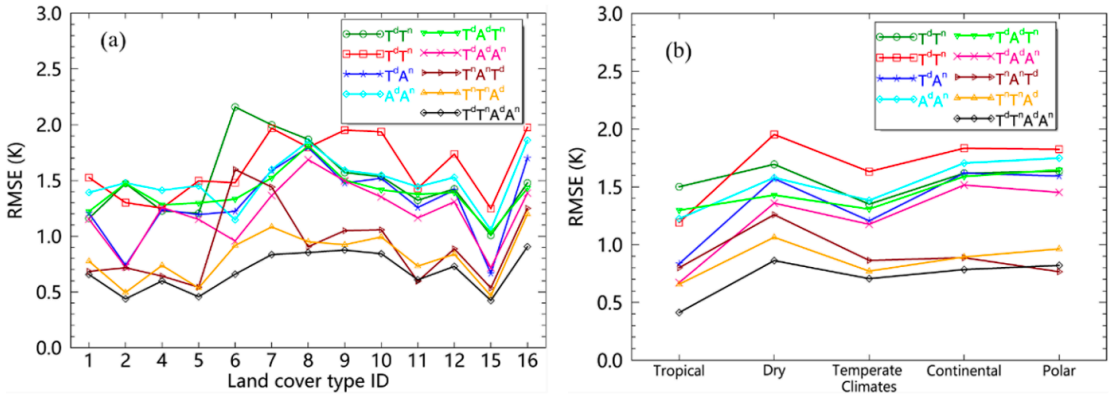

Figure 4.7 Estimation of daily mean LST using day or night observation from Terra or Aqua satellite at different land cover types and different climate types (Xing et al., 2021)

Based on these foundings, we can recogonized that the avalibility of the input LST is perferred but not the critical issue. Addtionally, making all the combination of LST at 24 individual hours made it very complex and abundant of parameters in the analysis. Thus, the input only include one or two LST input for a candidate daily mean LST estimation to reduce the complexity. Also, inspired by the ensembled (vote) idea such as algorithm like random forest, the final result included and balanced the values from these candidate LSTs, through taking average or median of the candidate LSTs.

The daily mean LST comeup with these ideas and previous studies and include the following procedures as Figure 4.8. First, screen and find out the avaliable LST at individual hours based on the data quality flag. If two or more observation was captured by satellites (Here, MODIS-Terra, MODIS-Aqua, VIIRS-SNPP, MERSI-LL-FY3E), the average value was applied for the corresponding hour. After collecting the LST data and their corresponding hour, the pair of LST was produced. For example, LST_{1-5} at t_{1-5}, we can get the pair (t_1, t_2), (t_1, t_3), (t_1, t_4), (t_1, t_5), (t_2, t_3)…(t_4, t_5), and these pairs included 2 inputs that $t_i \neq t_j$. Addtionally, since it was an ensemble approach, it is also important to test the criteria that allows $t_i = t_j$. Then, candidate daily mean LSTs from each pair (LST_i, LST_j at t_i, t_j) with a set of corresponding linear coefficient ($a_{i,j}$,$b_{i,j}$,$c_{i,j}$) can be estimated individually. These coefficients were optimzied using site observed LST in the training dataset in 2010-2021. After the estimation of LST candidates, the median calculation was applied to aggregate the candidate daily mean LSTs to avoid the influence of outliers. These estimation produced the representative daily mean LST estimation at corresponding date as an intermediate output. Finally, to achieve a seamless time series of the daily mean LST, a linear interpolation was applied to fill the gaps between the estimation. Then, an average smooth with a 3-days window size was applied to remove the spikes in the time series of the daily mean LST.

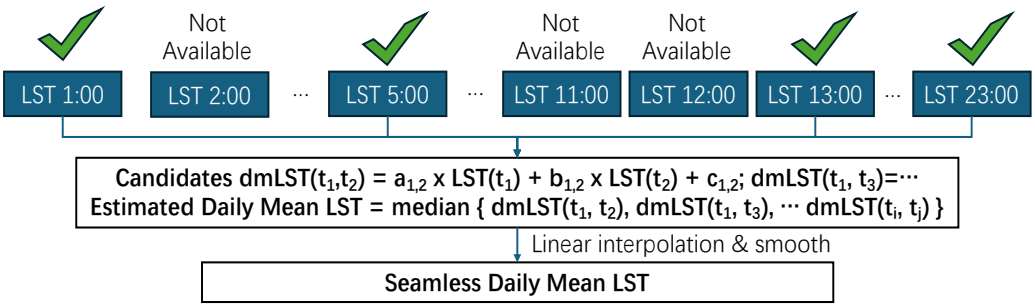

Figure 4.8 Flowchart and conception of daily mean LST estimation

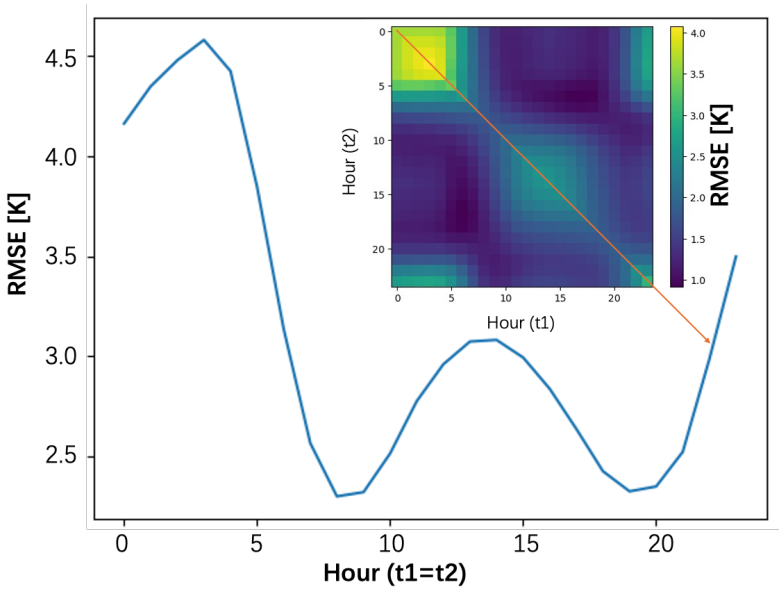

Figure 4.9 RMSE of estimated daily mean LST using site LSTs with the two time LST (at t1 and t2) linear combination

4.2.4 Ecosystem Respiration Estimation Approach

Ecosystem respiration is the carbon flux as the result of the complex interactions among physical, chemical, and biological processes. Studies have revealed the soil respiration response to parameters that influence the processes in the ecosystem respiration. For example, the ambient temperature (usually air temperature) is controling the activation of the enzeme and its related biochemical processes. Especially, in Arctic areas, low temperatures limited the growth of the vegetation during long winter and snow coverage period, and is one of the key factor that influence the ecosystem respiration. Additionally, as the ecosystem respiration consist of those respiration from heterotrophic respiration and autotrophic respiration, and the biomass is correlated to the autotrophic respiration and also vegetation that provided the avaliability of the organic carbon for the whole ecosystem thus linked to the heterotrophic respiration. Except for these factors, the soil moisture and nutrient (Carbon content, Nitrogen content) that involved in the metabolism also controls the ecosystem respiraion.

Remote sensing observations can provide product that indicates the factors that related to ecosystem respiration. 1) Thermal infrared remote sensing provided temperature information with LST products, also, extremely high LST indicates the drought disturbances and related to the soil moisture condition. 2) Vegetation indices that

calculated from reflectance at shortwave bands, especially with the combination of NIR (near infrared) bands and visible bands, can reflect the biomass of the vegetation. Meanwhile, EVI that represents the greeness of the the vegetation also indicate the water content in the vegetation and the ceosystem water avaliability. 3) Nutrient and soil property can also influecne the autotrophic or heterotropheic respiration thus related to ecosystem respiration. For example, studies find that low nitrogen concentration limited the respiration rate in the leaves and stems in plants. Additionally, soil oraganic carbon is the source for heterotropheic resperation and regulates it. Beucase most of these soil parameters were difficult directly meansured or estimated from remote sensing appraoches, here, these properties are assumed land cover dependent and the land cover classification was from satellite-based land cover map.

Table 4.2 Factors considered in the ecosysem respiration modeling

Temperature	**LST**	**Niu et al., 2024**
GPP (growing season)	**VI (EVI)**	**Zhang et al., 2024**
Moisture Content	**EVI**	**Shan et al., 2013**
Soil organic/nutrient	**Assume LC constant**	**Nissan et al., 2023**

Existing studies had shown the success of applying remote sensing data to estimate the ecosystem respiration. Those studies separate the ecosystem respiration into a temporal static parameter reference reapiration (Rref) and the fraction function. The Rref was defined as the ecosystem respiration at a fixed temperaure (or LST) and assummed location dependent, and varies by site and year, reflecting spatial differences in climate and vegetation. Generally, the pairs of Tref and Rref go through the Reco-T fitted curve and can control the position of the curve after a slected Tref and an estimated Rref. The determination of Rref and Tref will be introduced in the next paragraph. As for the fraction function, that controls the temporal changes, in this study, such as daily changes of the tmepratures and seasonal changes of the vegetation index were included in the model.

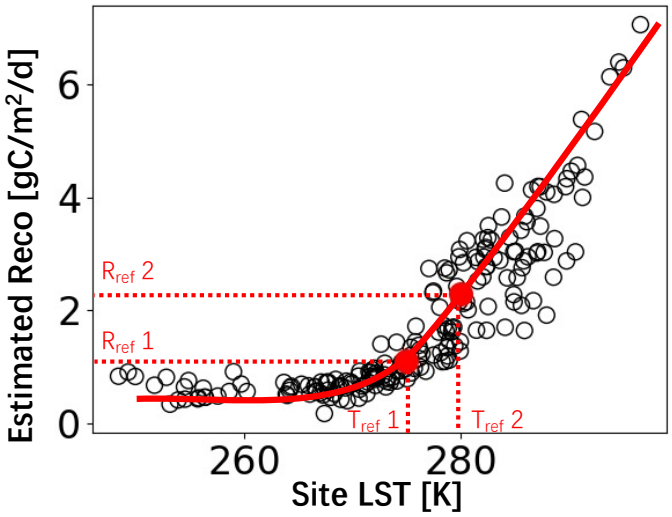

Figure 4.10 Example of the Tref and Rref pairs at the site CA-HPC in 2018 at a daily resolution.

Some rules were used to determined the Tref and as consequence estimate the corresponding Rref. Empirical Tref that based on the nighttime instantaous was set according to climate types in the study (Jägermeyr et al., 2014). For example, 0˚C for low temperature high latitude regions, 12˚C for higher temperate and tropical regions, and 13˚C for arid regions. Also, Ge et al., 2018 used the annual mean LST as Tref for two different climate regions (alpine grassland and temperate grassl and). Besides, some study also determined Tref completely empirically, for example 15 ˚C (Ai et al., 2018). Either of these effort was to select a Tref and Rref that lies in the curve that Rref started increasing obviously, as too much low Rref and high Rref makes the model unstable. Thus, in this study, the Tref was slected based on the performance of the estimated Rref (at the individual corresponding Tref), also, the reasonability of the value was considered. As for Rref estimation, using annual statistical information (including mean, maximum) of temperature and EVI was proofed working across the sites in different regions (Figure 4.11). In this study, 4 compoents were included to model for estimating the Rrefs at individual Trefs: including the annual average of the daytime LST (based on Terra daytime LST), the annual average of the daily mean LST (based on daily mean LST estimated using the approach in section 4.2.3), and the annual average and maximum of EVI (based on Terra EVI). Additionally, the annual statistical values were filtered to rather higher temperature seasons, similar to the strategy that applied in a study with rather cold and long snow season (Ge et al., 2018). Instead of using the doy for

determining the window of data, in this study, only when the daytime LST (Terra daytime observed LST) larger than 0 ˚C (273.15 K), the data was used to calculate the annual representative values to avoid long snow season effects in the Arctic region. Finally, as evergreen forest showed different biomass aginst other land cover in the arctic region (Alaska), thus, the estimation was separated into two category: ENF and none ENF. Also, this separation was applied to other parameter determination and further analysis in this chapter. The Tref was finally determined as 282 K for ENF sites and 280 K for None ENF sites (Figure 4.12).

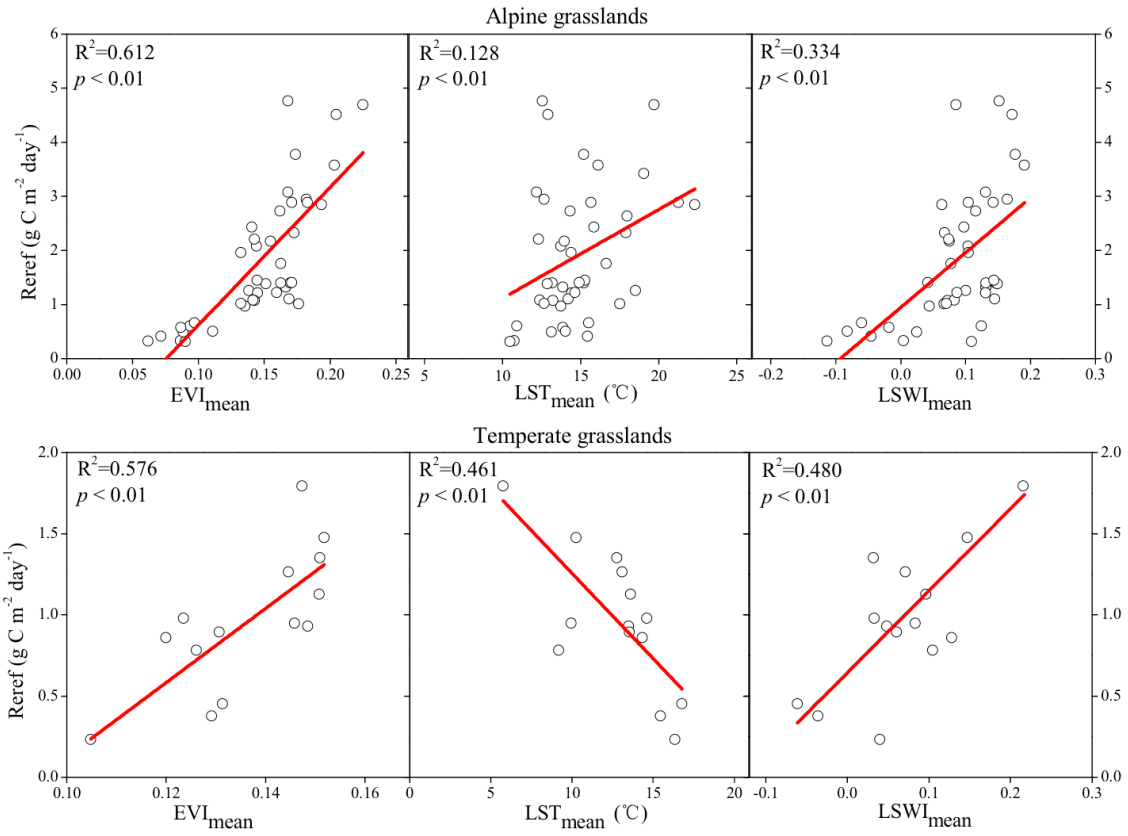

Figure 4.11 Correlation of between Rref and EVI or LST values in glassland sites (Ge et al., 2018).

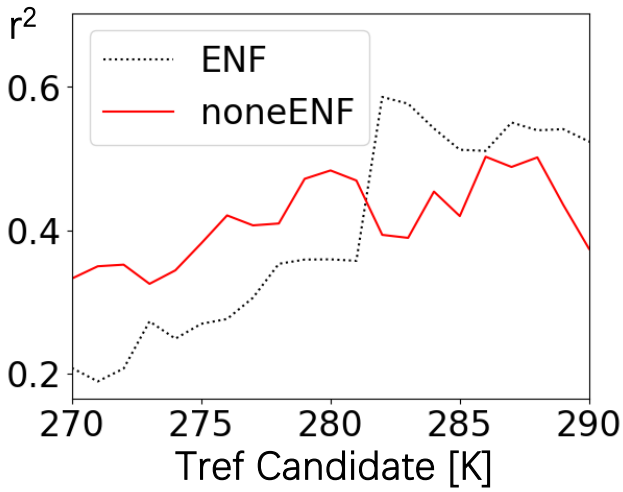

Figure 4.12 r^2 of Rrefs estimated at different Trefs in ENF sites or None ENF sites.

$$Reco = R_{ref} \times \begin{cases} (e^{f(T)} + a \times g(EVI) + b) \\ (e^{f(T)} \times a' \times g(EVI) + b') \end{cases} \quad (4-1)$$

$$\begin{aligned} Rref = {} & c1 \times LST(daytime\ annual\ average) \\ & + c2 \times LST(daily\ mean\ annual\ average) \\ & + c3 \times EVI(annual\ average) \\ & + c4 \times EVI(annual\ max) + c5 \end{aligned} \quad (4-2)$$

f(T): Q10, ARR, LT, ETA (Table 4.3) ***g(EVI)***: EVI, EVI_{std}(EVI/EVI_{mean})

Table 4.3 Description of candidate temperature moudles

Q10	ARR	LT	ETA
$p1(T - Tref)$	$p2(T^{-1} - Tref^{-1})$	$p3((T - T_0)^{-1} - (Tref - T_0)^{-1})$	$p4 \times \left(\frac{T - T_{ref}}{T \times T_{ref}}\right) + p5 \times \left(\frac{T - T_{ref}}{T \times T_{ref}}\right)^2$
Constant increasement of respiration by 10 ˚C	The incensement was proportional to 1/T in a chemistry reaction	Add an offset to ARR	Add a squared component to ARR model, reflect the Reco decrease at high temperature
Van't Hoff, 1884	Arrhenius, 1889	Lloyd&Taylor, 1994	Kruse & Adams, 2008

*a, b, c_{1-5}, p_{1-5} are the flexible parameters and determined by training data, T0 = 227 K, Tref was 282 K for ENF and 280 K for none ENF.

The fraction module including various settings. The general formular have 2 patterns: one is the biased of the EVI to the temperature sensitive component and another is the scaled EVI to the temperature sensitive compoent. As for the temperature sensitive component, 4 kernels f(T) was selected and compared in this study, including 3 most

popular: Q10, ARR (Arrhenius), LT (Lloyd&Taylor) and one newer model – ETA (Exteral ARR) that can reflect a Reco drop at higher temperature conditions. In these models, Q10 assumes a constant increasement of respiration by 10 ˚C, ARR was based on the effective collision in chemstry field that describes the incensement was proportional to 1/T, LT was the ARR with a offeset to avoid rapid change of dReco/dT in a natural temperature. Additionally, ETA was the ARR including a 2-powered compoent, considered alternative oxidase (AOX) and Cytochrome oxidase (COX) pathway comparing to traditional model that only use Q10 value to describe the relationship between respiration rate and temperature (Kruse & Adams, 2008; Ai et al., 2018).

4.3 Result of Estimated Daily Mean LST

4.3.1 Comparison of daily mean retrival approaches

Because of utilizing the high observation frequency, the validation was conducted over high latitude sites where the latitude is larger than 60˚N. The ground truth was calculated using the average of hourly or 30 minutes in situ LSTs using the same method for satellite LST validation as Chapter 2. The error was defined as the difference between the estimated daily mean and the ground truth. Also, to emphasis the advantage of adding FY-3E LSTs, the results were compared between the ones used FY-3E and the ones that not.

AVE and NN approach cannot achieve an applicable RMSE comparing to the Fit appraoch or the Ensembled approach described in the section 4.2.3 (Figure 4.13). The RMSE of the daily mean LST estimation ranges 4.66–6.75 K at the estimations where the day that satellite LST data is avaliable. Even after adding the FY-3E LST observations, through which AVE and NN method can benefit from more observations, the RMSE was improved to the range at 3.93–6.05 K, but still not a large gap to an application. On the contary, the Fit and Emsembled approaches exhibited the RMSE of the estimated daily mean LST at approximately 2 K, although slightly higher than the 1.5 K standard, which still produced an applicable the performance for applications.

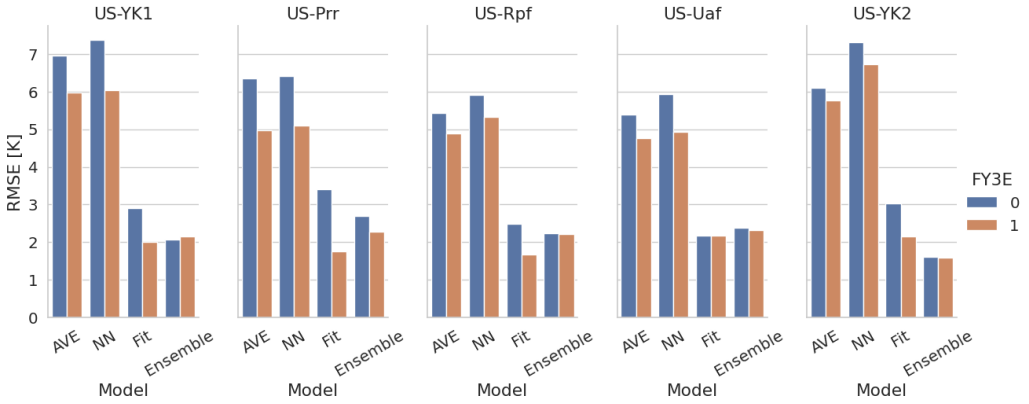

Figure 4.13 The RMSE of estimated daily mean LST using different approachs (AVE, NN, Fit, Ensemble) at 5 validation sites

The large errors produced by AVE or NN approach was considered as the limitation of the avaliable observation. First, comparing to Fit and Ensemble method in Figure 4.13, adding the FY-3E observation imrpoved the RMSE approximately 1 K in most of the sites in the estimation at the days. Second, with the analysis between the error and daily LST avaliability, it was found a clear decreasing of the daily mean LST error as the more satellite LST observations becomes avaliable (Figure 4.14). Additionally, adding FY3E observations can help the error become moderate with same observation avalibility when the avalibility is smaller than 8 times per day.

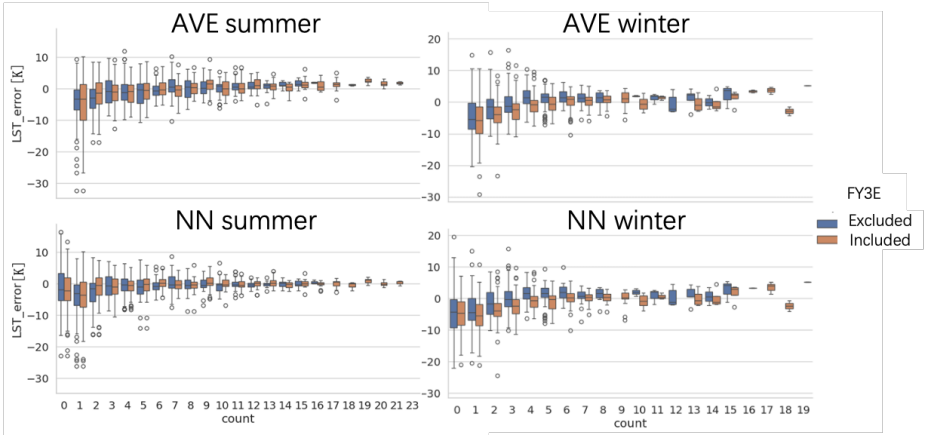

Figure 4.14 Comparison of the daily mean LST error against the valid observation using nearest neighborhood (NN) method or average (AVE) method with the site data in the 2022 summer. The boxplot distributions representing errors in land surface temperature measurements for two methodologies, 'AVE' and 'NN'. The FY3E True represent the data that included the FY3E LST in the calculation whereas the FY3E False represent the FY3E was not included in the calculation.

The RMSE of the estimated daily mean LST after interpolation and smoothing shows small difference among 4 models (Figure 4.15). Especially, at most sites, without including the LST observations of FY3E, the RMSE differences are smaller than 0.5 K. This is much smaller than the large model differences in the original daily mean LST estimations (Figure 4.13). The result changes after including FY3E LST observations. Firstly, including the FY3E observations improved the RMSE in all models. Second, Fit and Ensemble approach can benefit more then AVE and NN approaches.

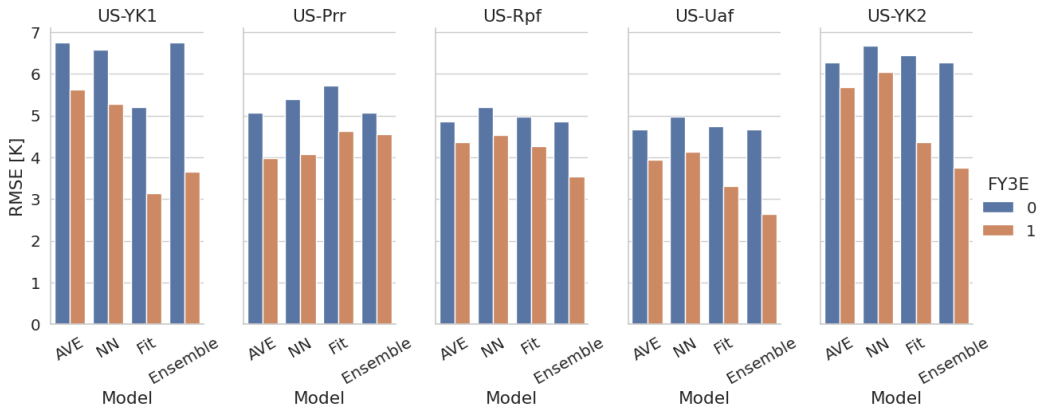

Figure 4.15 RMSE of the temporal interpolated and smoothed for the daily mean LST estimated in the Figure 4.13.

Fit and Ensemble approaches are good candidate than AVE and NN approaches as indicated in the discussion above. The Fit approach with FY3E LSTs input produces best RMSE and r^2 than other settings (Figure 4.16). However, without FY3E LST inputs, the performance of Fit approach decreased, for example, the RMSE decreased 1 K, also, the avaliable output decreased 95 observations, which was only approximately 60% when including the FY3E. The RMSE from Ensemble approach was 0.2 K higher when FY3E included.

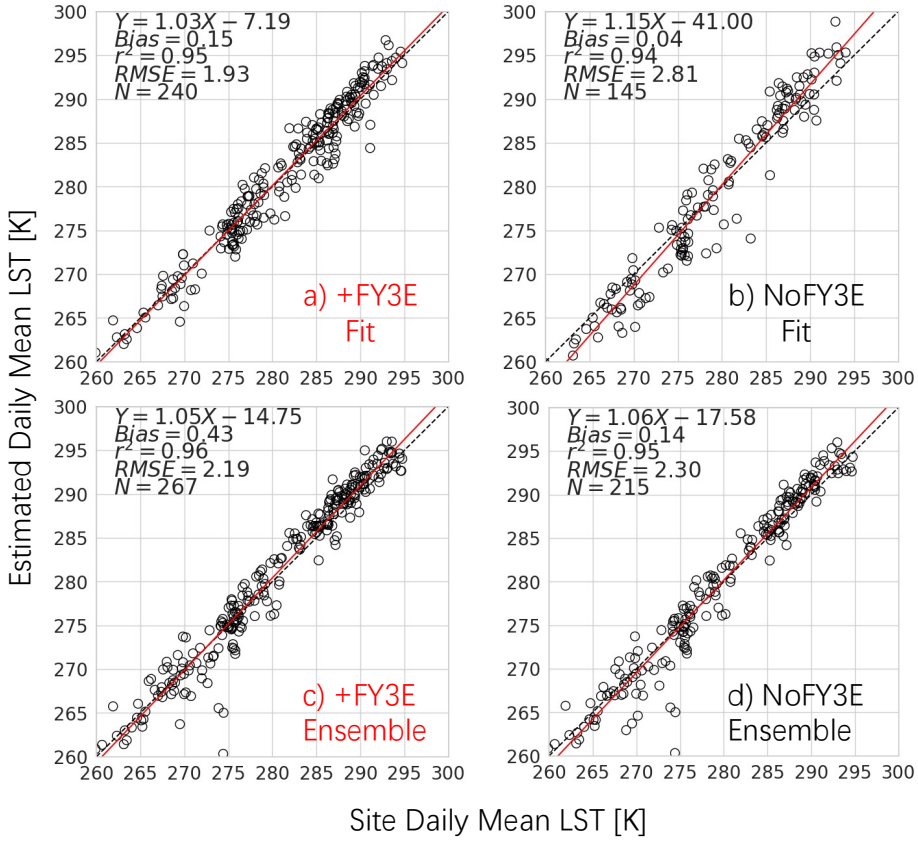

Figure 4.16 Estimated Daily Mean LST based on different settings (existence of FY3E and different Models) without interpolation and smoothing.

Ensemble approach showed better performance than Fit approach after the interpolation and smoothing with or without FY3E LST inputs (Figure 4.17). Notability, comparing the estimated daily mean LST form two models for the LST lower than 275 K, underestimation larger than 10 K almost corrected in Ensemble approach. Also, fewer overestimation was observed in theEnsembled approach. As for the comparsion of input with and without FY3E, the Fit approach showed much larger difference, this is related to the large difference of control points of the interpolation when using the Fit approach.

Thus, if the target was to get a seamless daily mean LST, Ensembled approach was a better approch than Fit approach.

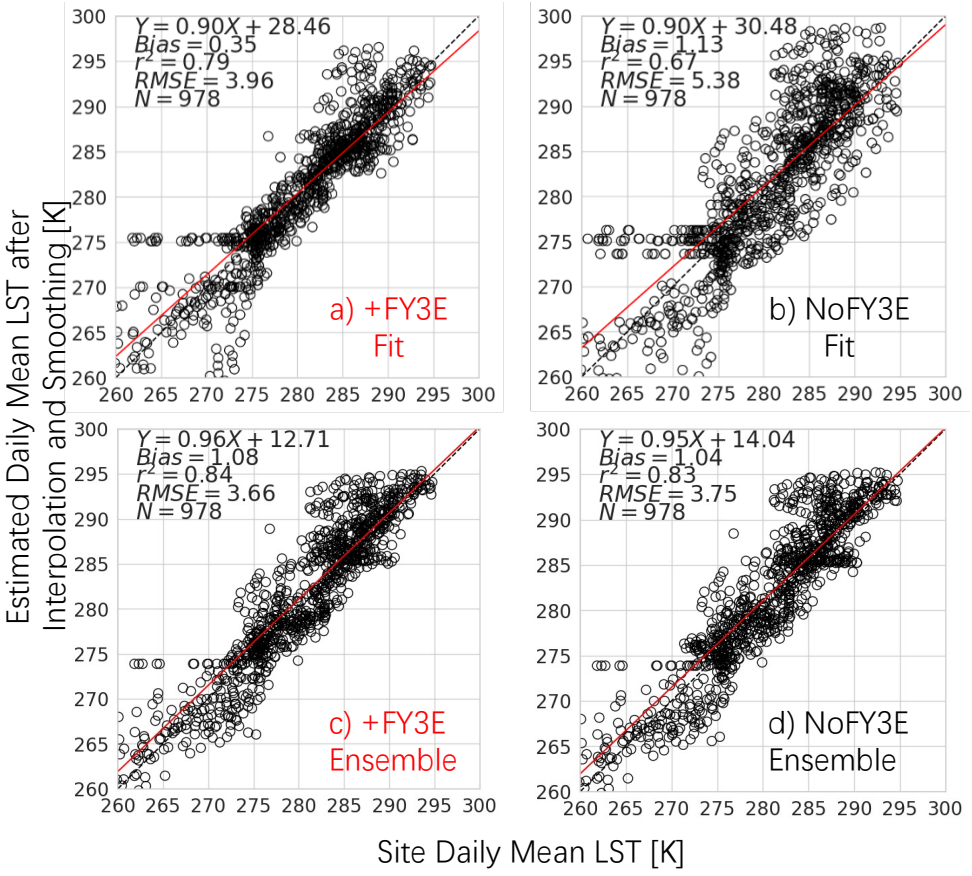

Figure 4.17 Estimated Daily Mean LST based on different settings (existence of FY3E and different Models) with interpolation and smoothing.

4.3.2 Influence of Observation Availability on the Ensemble Approach for Daily Mean LST

More LST input tends to produce better performance aforementioned, thus, increasing or decreasing of the input LST needs further discussion for the most potential Ensemble approach. Here, three aspects were considered: 1) With or without the input of FY3E; 2) Including the daily mean LST estimation using single time LST; 3) The avalibility of the estimated daily mean LST within a day.

Adding the FY3E LST input slightly improved the performance regarding the r^2 and RMSE (Figure 4.16, Figure 4.17). This imrpovement is almost same to orginal estimations and interpoalted results, as a 0.2 K RMSE difference. Considering the data avalibility boosting to the LST performance indicated by NN and AVE method (Figure 4.14), the data avalibility within a day may influence the performance of the result before and after the interpolation and smoothing procedure. The data avaliability defined here is the avalibility of candidate daily mean LST, which is different from NN and AVE. For exmaple, 1 means at least 1 daily mean LST estimation exist with the corresponding LST pair at t1 and t2; 2 means at least 2 daily mean LST estimations exist with the corresponding LST pair, and those days with only 1 daily mean LST estimation was regarded as a failure. Also, as the importance of the data avalibility in the interpolation/smoothing procedure, the single time LST based estimation was allowed as comparison.

The orginal estimation becomes better with more candidate within a day (Figure 4.18). For exmaple, the estimaition can achieve the RMSE smaller than 2 K when the avalible pairs more than 4 within a day. Allowing the single LST estimated daily mean LST slightly decreases the performance regarding the RMSE decreasing approximately 0.1K. As for the output of the intermediate daily mean LST, the limitation on the pair avalibility can reduced more than half of the intermediate LST that only used two different temporal LSTs. Furthermore, the reduce was much more under the setting that allows daily mean LST estimation with single LSTs.

The interpolated result was oppsite while estimation becomes better with less candidate within a day (Figure 4.18). For example, the RMSE of the final interpolated daily mean LST increased from approximately 4 K to 8 K using the two-time based daily mean LST estimations by limitingthe daily candaidate from 1 to 5. Similar change can be found on differenrt settings for both the existence of FY3E LST, the single LST based candidate included. As a result, including single time based daily mean LST, including the FY3E LSTs, and use all possible candidate without limiting the data avaliability showed the best performance of all. The combined result of Figure 4.18 can be used to explain the performance. FY3E could slightly improve the daily mean LSTs and could propagate to final estimaition (Figure 4.19). On the other hand, the increasing of input avaliability is more important since it provided more control points in the interpolation.

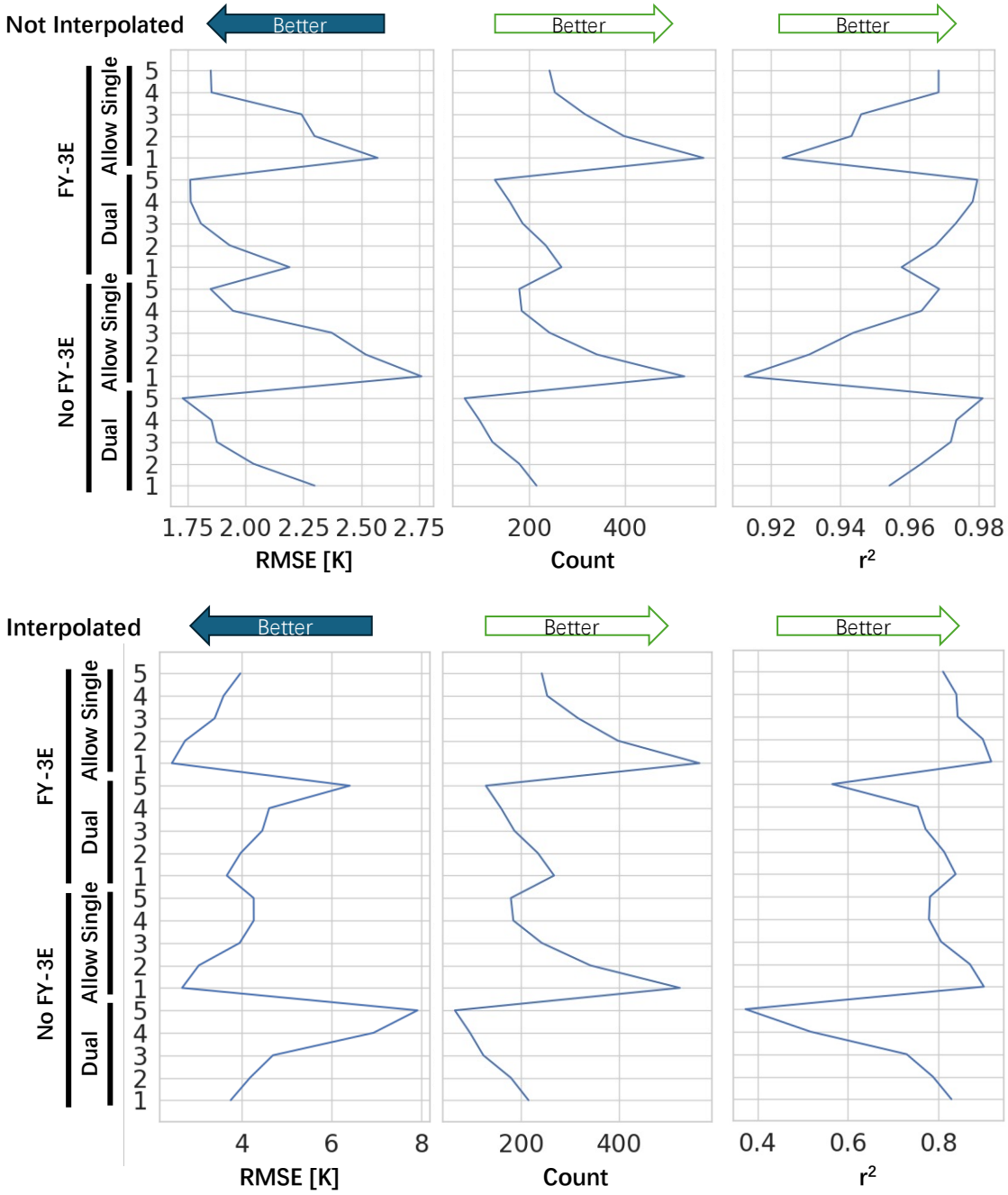

Figure 4.18 Performance of the estimated daily mean LST with different data avalibility conditions. The settings include the differnece of allowing single LSTs and including of the FY3E.

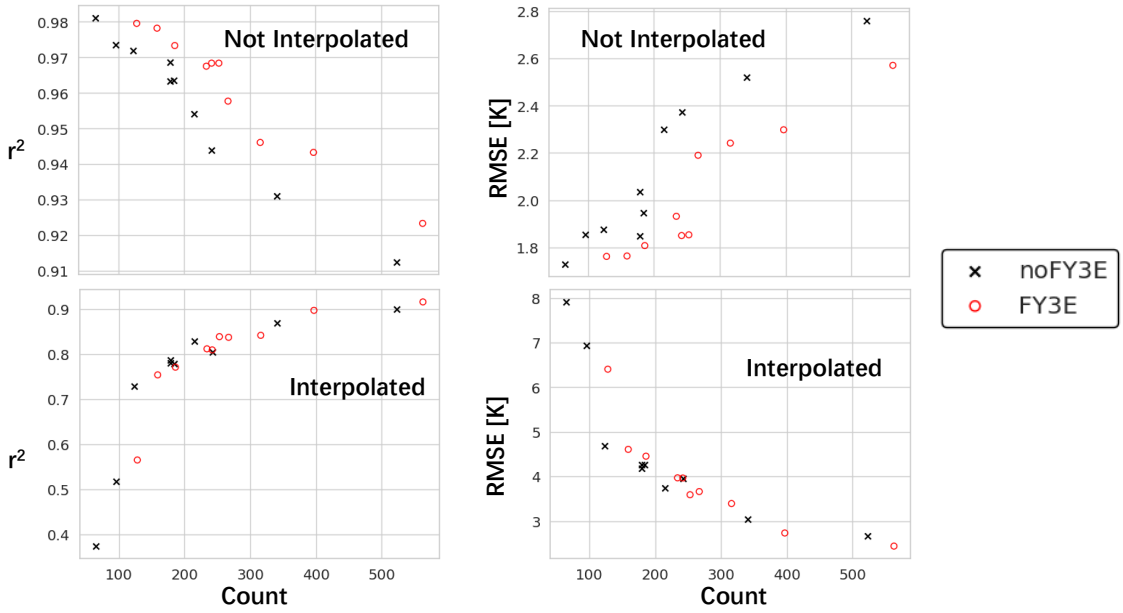

Figure 4.19 The ensemble result indicated in Figure 4.18.

4.3.3 Evaluation of Daily Mean LST using the Ensemble method

The ensembled approach adding FY3E input and allowing single time estimated LSTs can produce good original estimation and interpolation results (Figure 4.20). The uncertainty analysis that replacing the satellites with the ground truth showed an approximately 1.6 K RMSE, indicating the error caused by the linear interpolation and smoothing procedure. The gap between this 1.6 K value to 2.44 K when FY3E included and 2.67 K when FY3E was not included (Figure 4.20d, e), indicate the uncertainty that was caused by the satellite LST error.

FY3E can provided the extra estimation and as a result improve the interpolated estimations (Figure 4.21). For example, at US-YK1 in the first half of the August, one extra estimation that occurred after including the FY3E LST observations provided a critical control point that correct the interpolated values and avoid the overestimation approximately 10 K. Similar correction can be found in September and confirmed that including FY3E observations could provide a more robust seamless daily mean LST. Finally, if only considered using nighttime LST to represent daily changes, many gaps were observed and lead to underestimation. Thus, the daily mean LSTs estimation proposed in this study can better represent daily changes, especially than nighttime-based

LSTs, which is of important to the understand parameter that are sensitive to temperature changes.

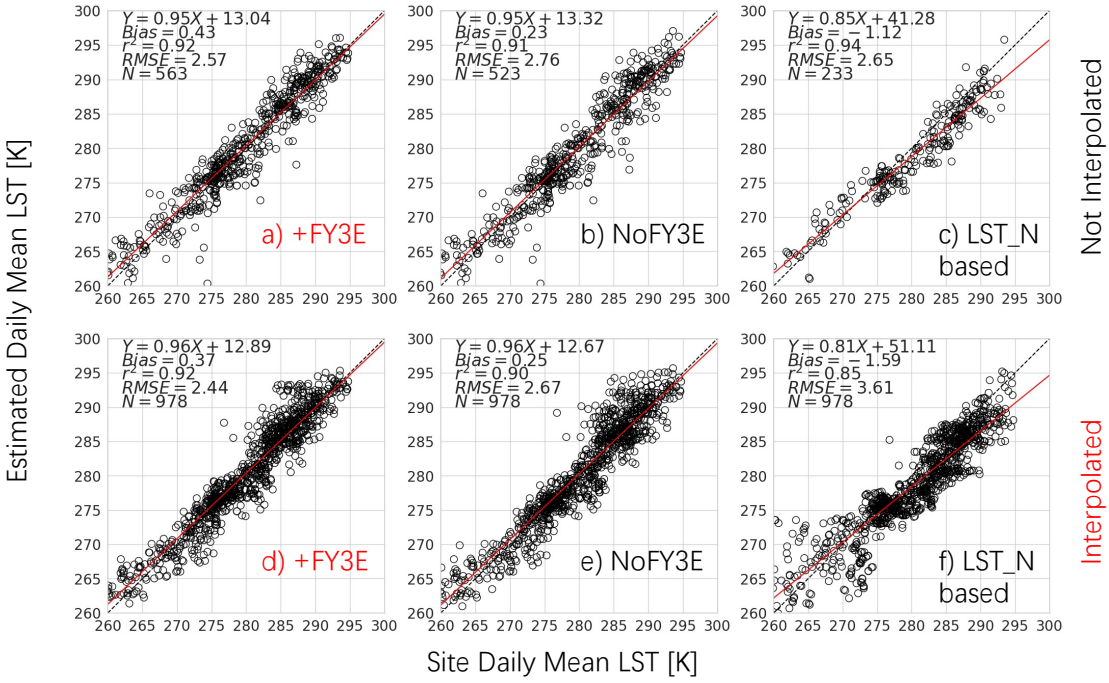

Figure 4.20 Performance of the estimated daily mean LSTs

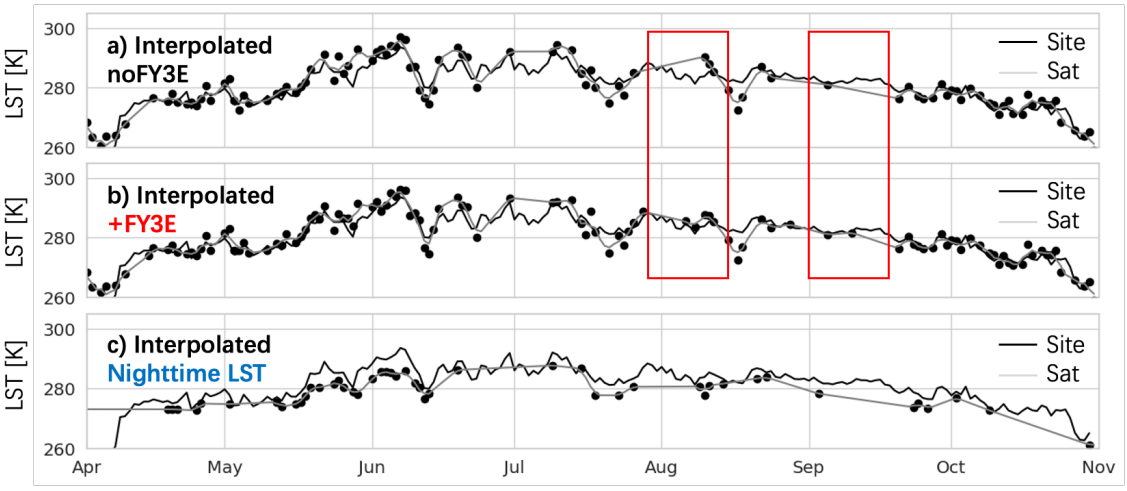

Figure 4.21 Estimated seamless daily mean LST at US-YK1 in 2022.

4.4 Estimation of Ecosystem Respiration

4.4.1 Uncertainty Caused by Temperature

The instantaneous observation of the nighttime LST from MODIS Terra was widely applied to the data-driven method using remote sensing data as input. The original assumption of these studies was based on the conclusion that air temperature showed good consistency to nighttime LST at the specific sites and areas (Figure 4.22). However, as the test in the arctic summer sites, the diurnal LST can change from 25˚C at peak to 5˚C at the minimum (Figure 2.8). Such large change is a challenge for using instantaneous nighttime to represent a mean air temperature given at a day, especially the MODIS Terra observed the nighttime LST when LST was deceasing fast (Figure 2.8). As the test of relationship between nighttime LST and daily mean air temperature or daily mean LST, an increasing bias accompany with the increasing temperatures was found (Figure 4.23). These slope<1 cases, especially at high latitude sites This changing bias on responding to the increasing temperature have as risk to cause the bias in estimation the ecosystem respiration.

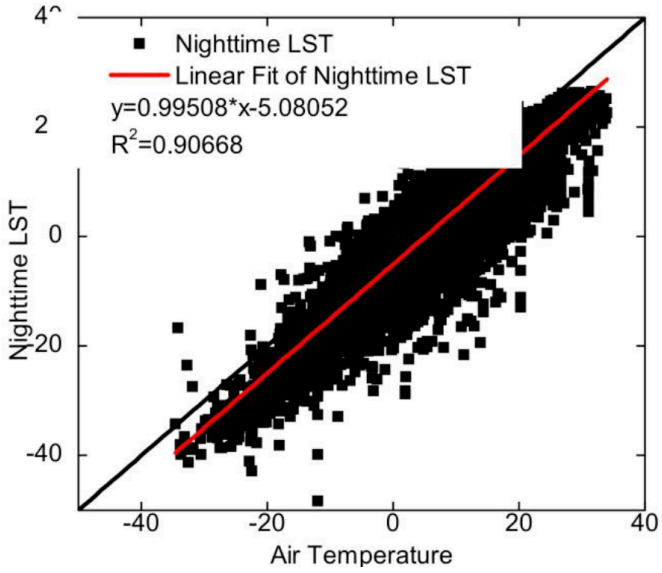

Figure 4.22 Relationship of air temperature and nighttime LST at the observation site in a previous study with more than 200 site-years data (Ai et al., 2018).

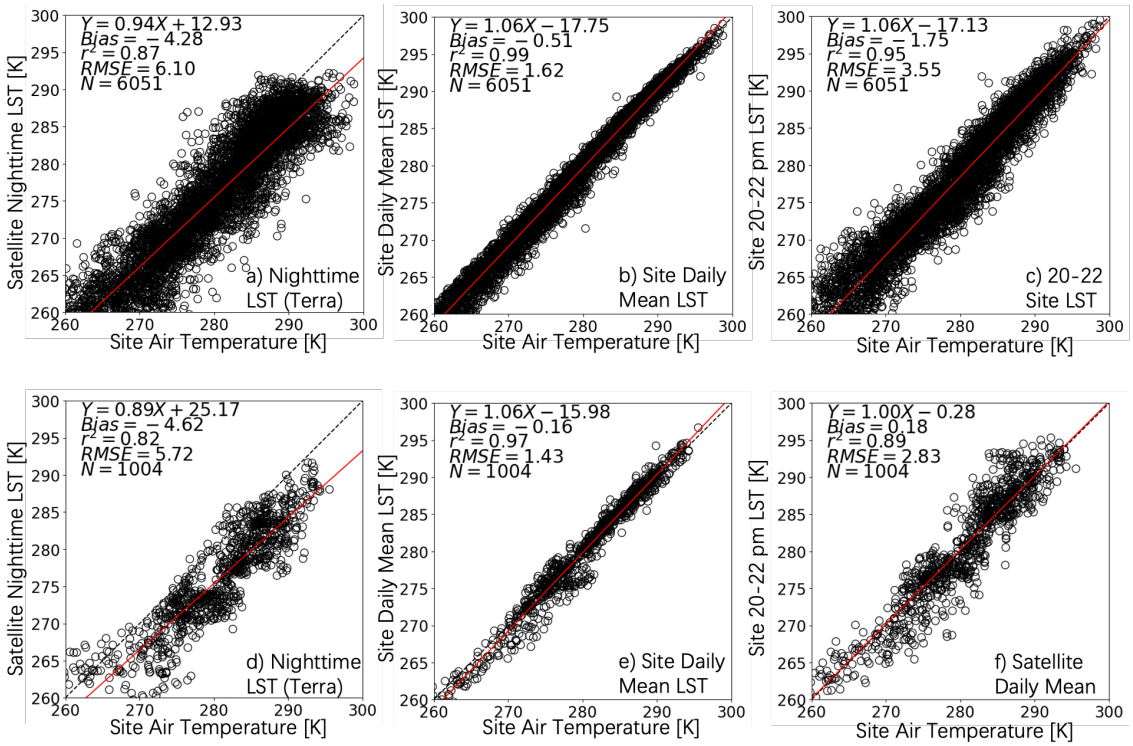

Figure 4.23 The comparison of instantaneous nighttime LST and daily mean air temperature (Ta) or daily mean LST at the sites in this study. (a-c) all sites including traning sites. (d-f) 5 validation sites only with the satellite estimated daily mean. The dotted line is 1:1 line and the red line is the linear regression line of x-axis variable and y-axis variable.

The investigation of error showed the largest sensitivity to the temperature differences between instantaneous nighttime LST and daily mean LST (Figure 4.24). Comparing to other temperature differences including mean-min, max-min, and max-mean, instantaneous nighttime LST-mean showed the largest linear correlation at 0.44 than correlation to DTRs ranging from 0.02 to 0.05 (Figure 4.24). This meant that the error of the ecosystem respiration estimation was less sensitive to various types of DTRs and cannot be explained by just these DTRs but related to the representativeness of the input data. Additionally, it is found that comparing to instantaneous nighttime LST-mean, those differences included instantaneous nighttime LST as input such as instantaneous nighttime LST-min and instantaneous nighttime LST-max also large correlations at approximately 0.24 and 0.29 (Figure 4.24). This suggested the source of error is more related to the ambiguous errors caused by instantaneous nighttime LST itself.

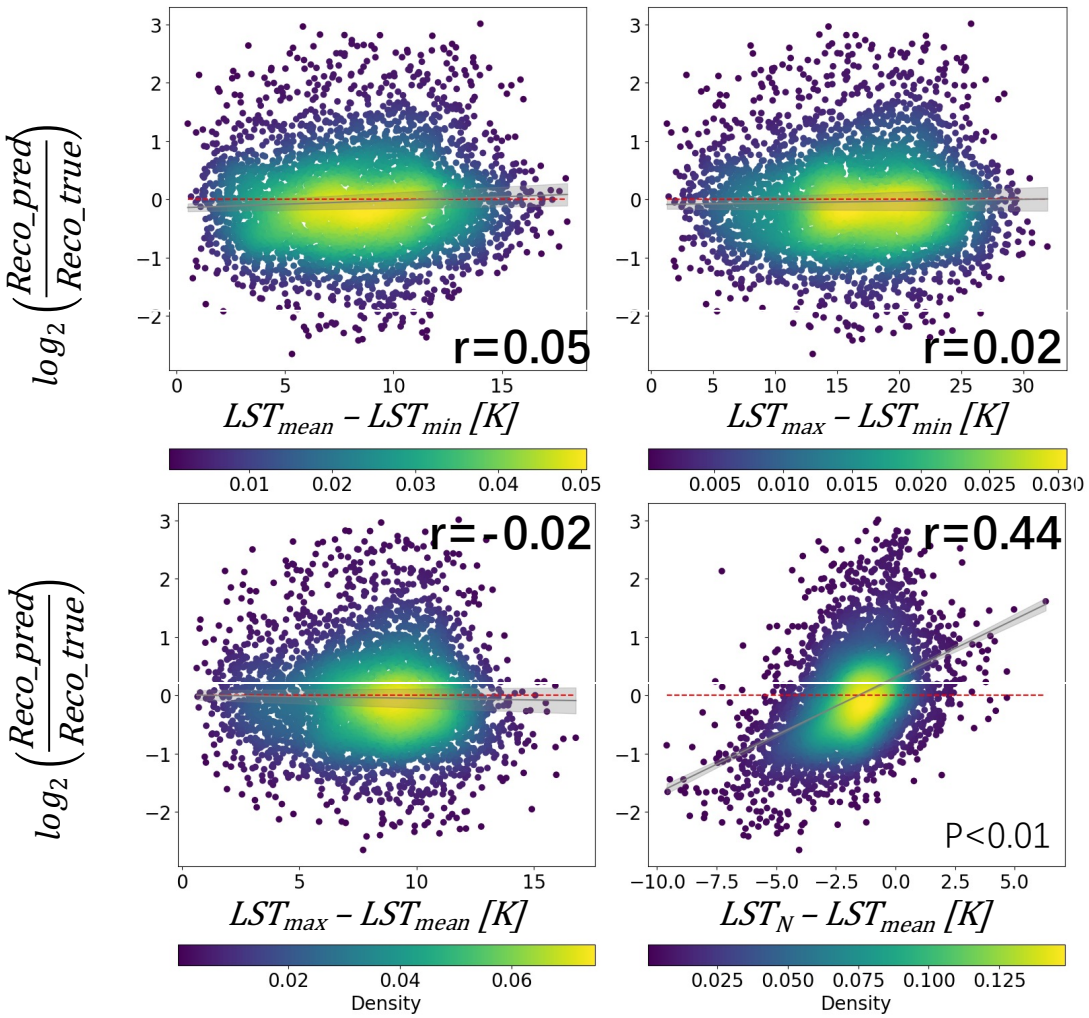

Figure 4.24 Model errors corresponding to the variation of the temperature differences for mean and minimum (mean-min), instantaneous nighttime and minimum (T-min), maximum and instantaneous nighttime (max-T), instantaneous nighttime and mean (T-mean) for sites at different landcovers in June, July and August. The model error is the log2 value of ratio between prediction and true (The Reco estimation was based on Ai et al., 2018.). The red dash line is zero that represent the best estimations. The black lines are the regression lines of x-axis and y-axis variables.

4.4.2 Comparison of Settings in the Estimation Model

To estimate a physical parameter that is addable from sub-hourly inputs to daily outputs, two approaches are possible. One approach is first making aggregation and then making estimation, and another is first making estimation and finally making aggregation. Thus, we can estimate daily Reco using the daily LSTs which was calculated (estimated) from quasi-hourly LSTs or make quasi-hourly Reco estimations and then aggregated to daily means. Both approaches were tested using the site LST and site Reco and showed that first estimating the daily mean LST and then estimating the Reco gives better estimation of daily Reco. This is caused by the difference between hourly LST and hourly Ta, which Ta is key parameter to the Reco output in the site observations (Figure 4.26).

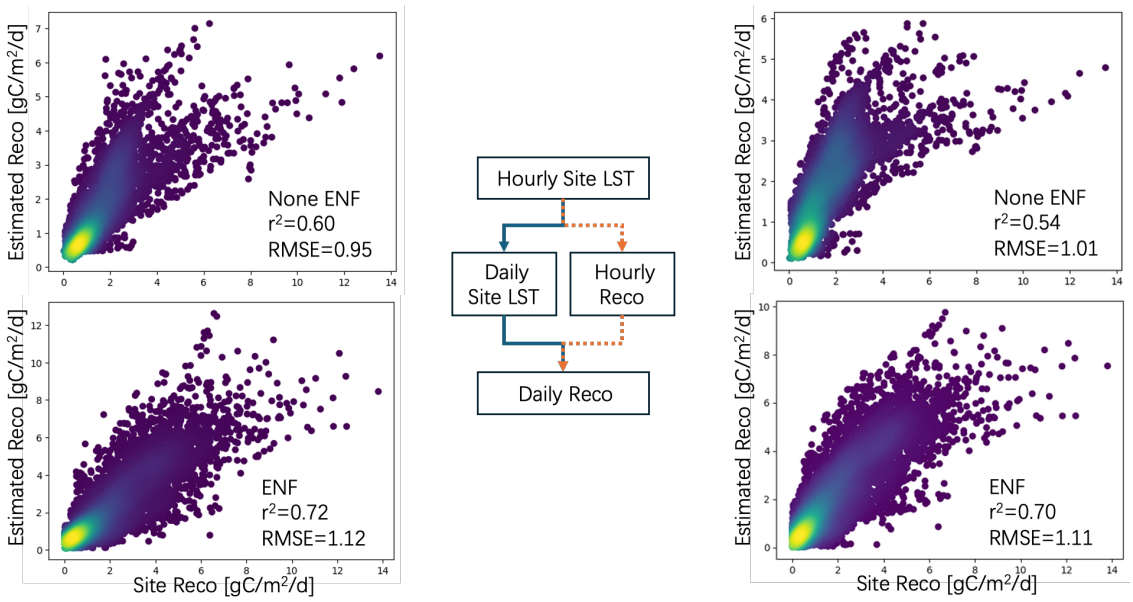

Figure 4.25 The estimated Reco based with two different procedures

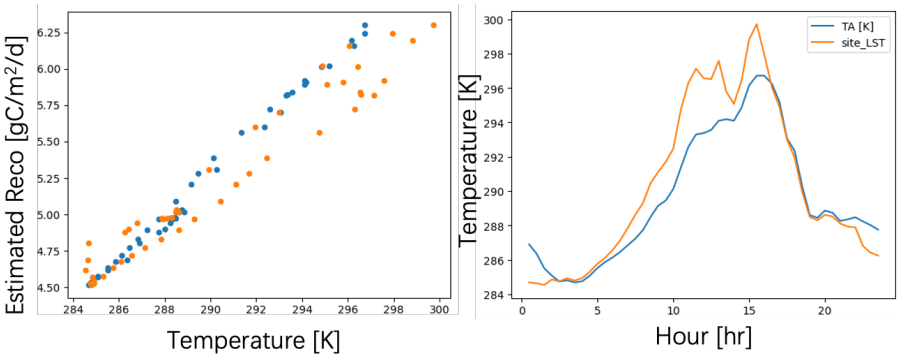

Figure 4.26 Reco response on Ta and LST, and diurnal change of Ta and LST at July,11,2022 in US-Prr

Comparison of the undetermined settings in the model is important before making further estimation. The first is the temperature kernel that determines the temperarture sensitivity of the model. Among 4 candidate temperature kernels, Q10 produced worst RMSE which is much larger than other 3 (Figure 4.27). The difference between ARR, LT and ETA is almost neglectable in each settings. Considering the temperature sensitivity at higher temperature, which represents the ability for extrapolation, the LT kernel was considered the most reasonable since other kernels will produce extremely high Reco when temperature becomes high (Figure 4.28). Also, comparing directly using EVI values, replace it with standarlized EVI produceds better RMSEs among the settings. As for the pattern of the EVI component, adding it with the temperature sensitive component is bettern than fraction pattern. As for the input, as indicated in previous sections, with more candidate and the include of FY3E, the daily mean LST can be better estimated and explained the better performance of Reco estimation, respectively. The determined formular for Reco estimation is given as the following:

$$Reco = Rref \times (e^{LT(T)} + a \times EVI_{std} + b)$$

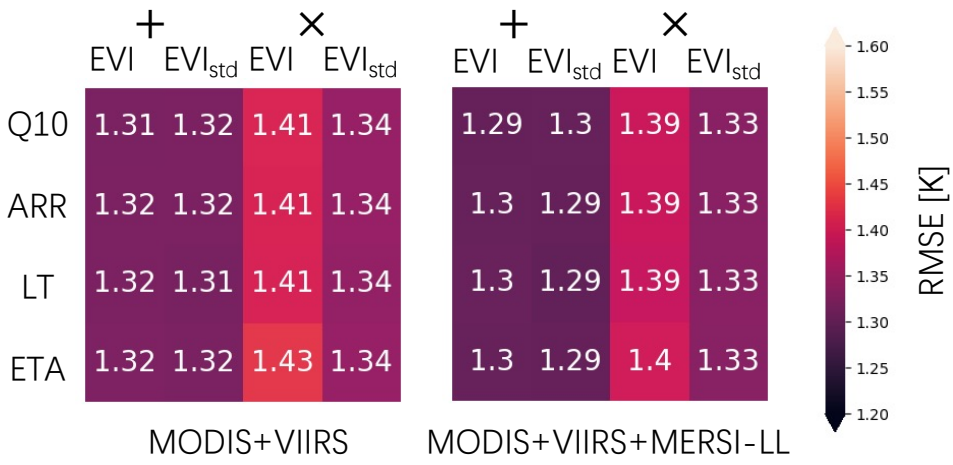

Figure 4.27 Model evaluation with different settings.

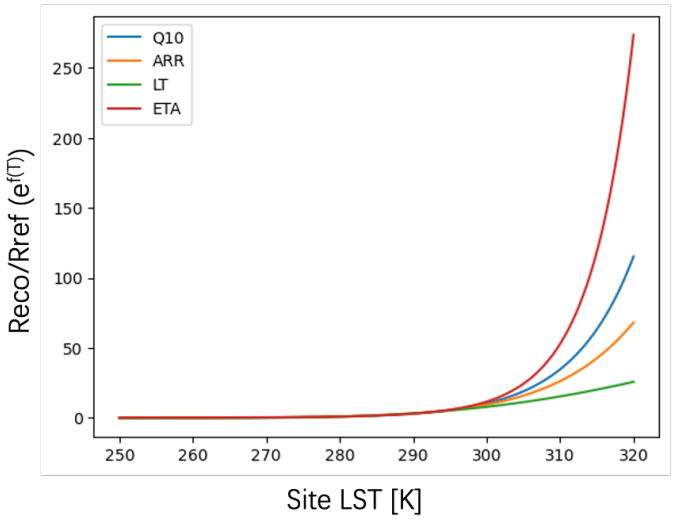

Figure 4.28 Temperature sensitivity of the 4 temperature kernels at the training sites.

4.4.3 Evaluation of the Estimated Ecosystem Respiration

Validation using the test data showed an improvement when the integrating with the daily mean LSTs that was calculated from the hourly LSTs as mentioned in Chapter 2 (Figure 4.29). The validation used the data in 2022 at 5 sites: US-Prr, US-Rpf, US-Uaf, US-YK1, and US-YK2. Among the different combination of the daily mean retrieving models and corresponding LSTs input, FY-3E included hourly LST using the Fit method showed the better estimated Reco than nightime LST based one. The RMSE showed an

improvement from 1.67 gC/m^2/d to 1.29 gC/m^2/d. Meanwhile, the r^2 and bias also showed an improvement. Benefiting from the fit method as well as the utilization of the frequent hour inputs, the Fit method provided good performances regarding the RMSE, Bias and the slope alignment to the 1:1 lines.

Overall, the figure shows that the estimated Reco values are generally close to the observed Reco values, but there are some differences between the different data sources. The estimated Reco values using data from the FY3E satellite show more detail and variation than the estimated Reco values without using this data. Notably, with ultilization of the daily mean LST, although Reco did not catch the correct magnitude and exhibited large sensibility sometimes, the timing of the peak and vally matched better than using nighttime LSTs, and slightly become better when FY3E LSTs were included. This suggests that the FY3E satellite data with LST data from other polar orbiting satellites is providing additional information that is improving the accuracy of the Reco estimates.

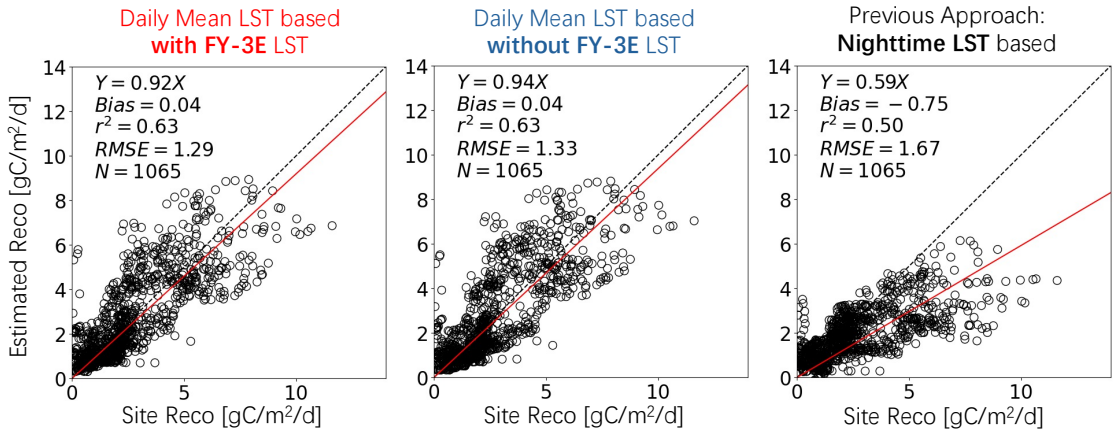

Figure 4.29 Comparison of the daily mean Reco by daily mean LST input and nighttime LST input at the 5 evaluation sites

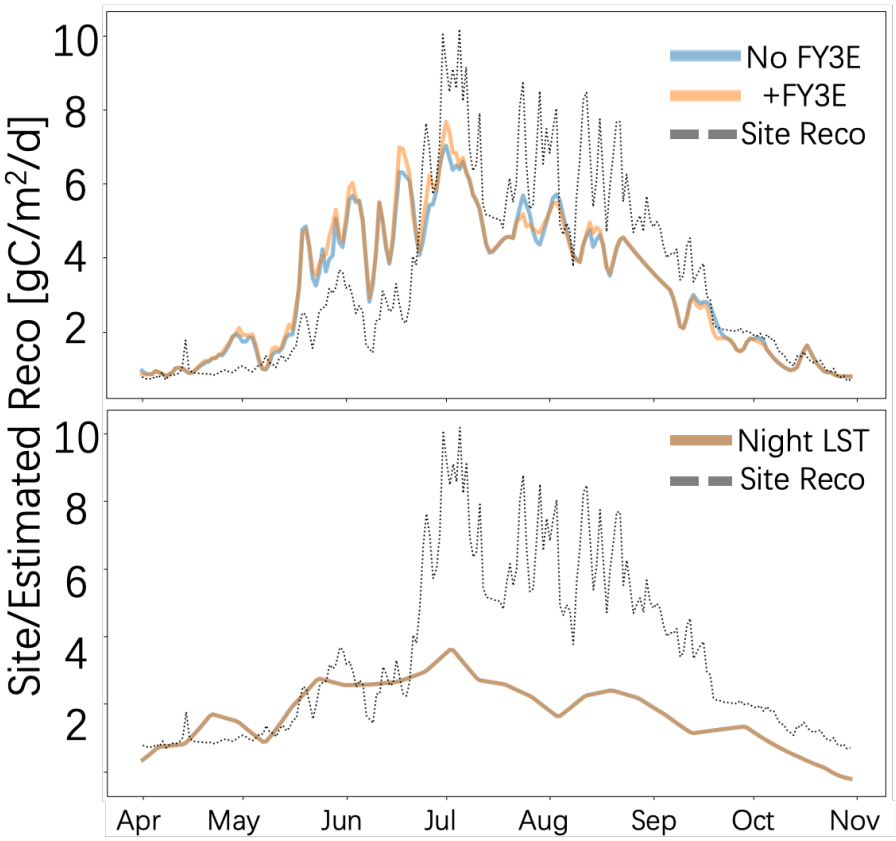

Figure 4.30 Time series comparison of Estimated Reco based on daily mean LST and nighttime LST (Terra nighttime) at US-Rpf

4.5 Discussion

4.5.1 Spatial Upscaling Intercomparison

Ecosystem respiration was upscaled at the region with latitude from 61˚N to 67˚N and longitude from 138˚W to 152˚W, with the vegetation mainly covered by evergreen needleleaf (ENF), mixed forest (MF), open shrublands (OSH), woody savanna (WSA), savanna (SAV), grassland (GRA) and wetlands (WET) (Figure 4.31). The upscaled ecosystem respiration showing the similar spatial pattern as a machine learning based output (Figure 4.32), though at different years (machine learning FLUXCOM ecosystem respiration in 2021, (Jung et al., 2020), this study in 2022). But the daily estimations showed more higher estimated values compared to the nighttime LST based approach or the machine learning based approaches, indicating the potential higher CO_2 emissions. Also, the daily LST based result showed the more spatial variation compared to the

machine learning result at 10km or a process-based model output (LPJ-GUESS) (Figure 4.32, Figure 4.33). Meanwhile, the ecosystem respiration produced from LPJ-GUESS showed very high ecosystem respiration compared to other 3 empirical models. Even with different magnitude, the daily mean LST based ecosystem respiration is showing similar pattern to estimation from different models with different approaches.

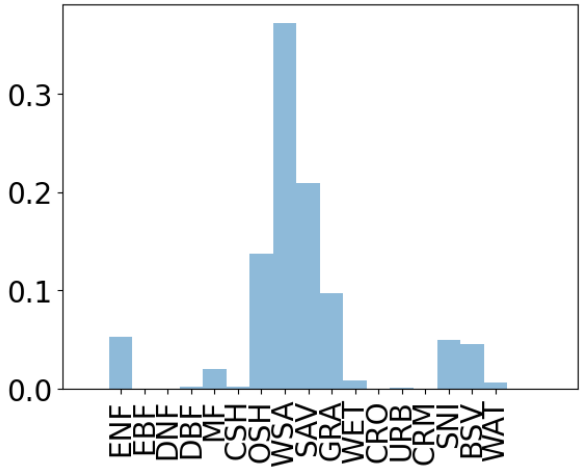

Figure 4.31 The land cover fraction in the upscaling region

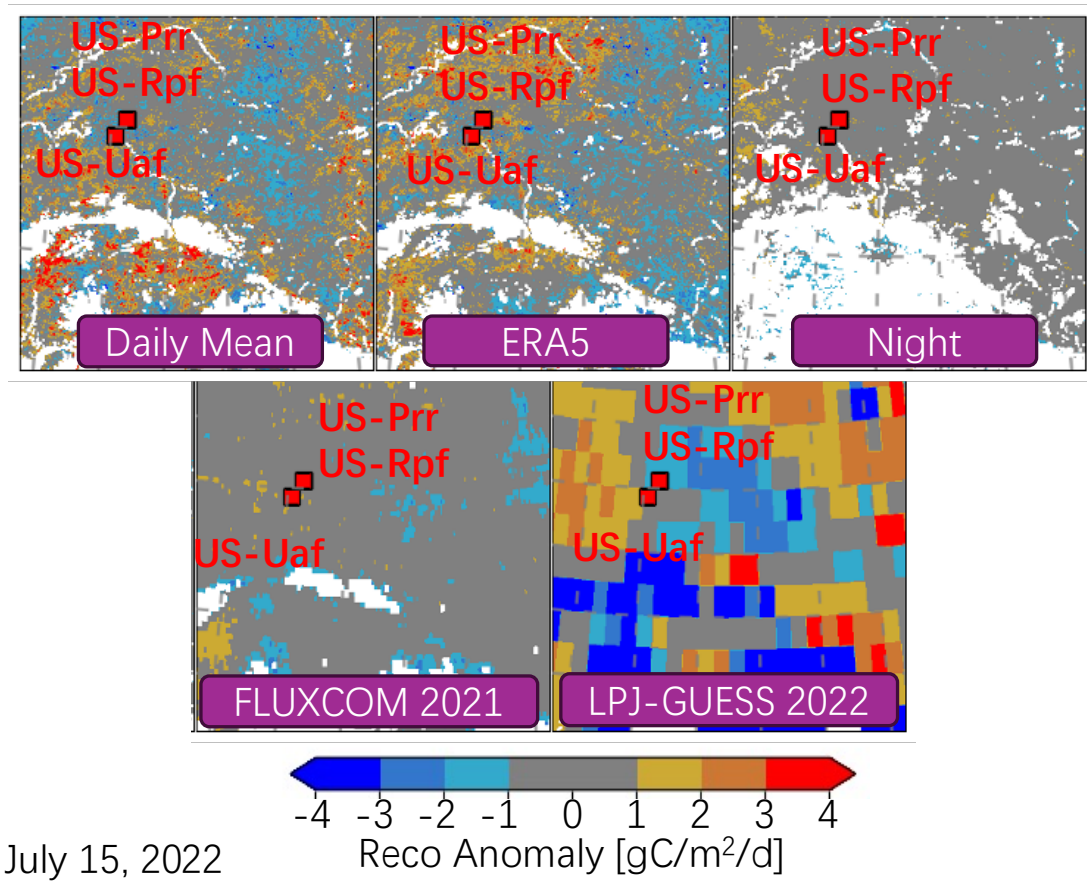

Figure 4.32 Reco anomaly from models on July 15, 2022. a,b) Driven by the estimated daily mean LST (using Terra, Aqua, SNPP and FY3E) and ERA5 daily mean LST with the daily mean model (trained by daily mean LSTs). c) Driven by nighttime LST (Terra Night LST) with nighttime model (trained by nighttime LSTs). d,e) Model output from FLUXCOM (output of 2021) and LPJ-GUESS (output of 2022)

Statistical result showed that ecosystem resiration estimated in this study have similar pattern to FLUXCOM estimations. The most frequent center are almost same between FLUXCOM and ecosystem resipration using daily mean LST as input (Figure 4.33). The nighttime based showed a negative biased center comparing to both FLUXCOM and daily mean LST based estimation, indicating the previous approach may underestimated the ecosystem respiration in this region. Notabaly, the ecosystem respiration at the site ranged from 2 $gC/m^2/d$ to 6 $gC/m^2/d$, but FLUXCOM can only cover 3 of them, which missing the high ecosystem respiration estimation at US-Rpf and US-

Prr. Therefore, the daily mean LST based ecosystem respiration is more likely to reproduce the high ecosystem respiration.

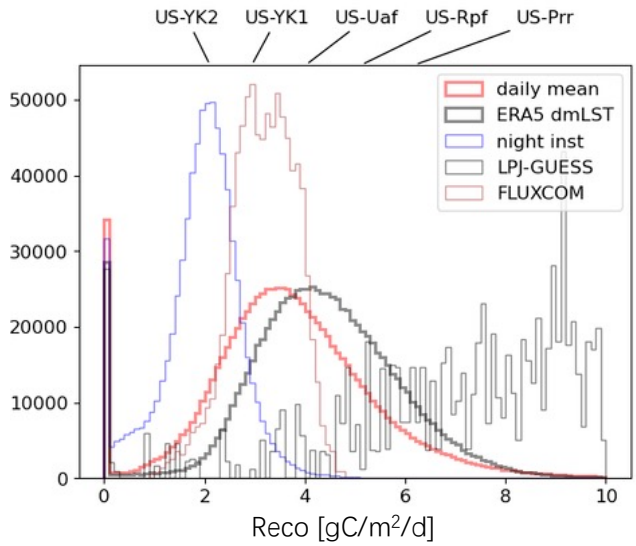

Figure 4.33 Frequency of estimated ecosystem respiration using different approaches. (All the data are aligned with good data and then intercompared)

4.5.2 Model Limitation

Besides the effect of temperature response, ecosystem respiration is also sensitive to soil mositure, soil nutrient condition (organic Carbon content, Nitrogen content) as well as the soil structure (Ai et al., 2023; Maes et al., 2024). However, soil nutrient condition and soil structure usually have a much smaller temporal changes and also challeging for spatial data retrieval, especially through remote sensing technic. Still, there are other parameters that can be analyzed to understand the model limitation because only using the input of EVI and daily mean LST. For example, GPP that was replaced by EVI in this study, soil mositure which was also indicated by EVI, the soil temperature that may be different from daily mean LST or Ta which influence the heterogenity respiration rate more directly, and the shortwave radiation that was used as input for ecosystem respiration estimation using machine learning approaches (Ueyama et al, 2013; Ranjbar et al., 2024).

Among these parameters, ecosystem respiration was underestimated in both ENF or None ENF sites when GPP at high values (Figure 4.34). For example, ecosystem respiration was more likely underestimated at 0–4 gC/m^2/d when GPP larger than 10 gC/m^2/d and was found more frequent at None ENF sites. On the other hand, such underestimation was not found when GPP was at lower values. This Reco error occurred at high GPP cannot be well explained by EVI as shown in Figure 4.34, which showed a saturation curve. Therefore, proxy of GPP can be further developed and considered instead of using reflectance-based vegetation indices such as EVI and NDVI, for example, NIRv and NIRvP (Badgley et al., 2019).

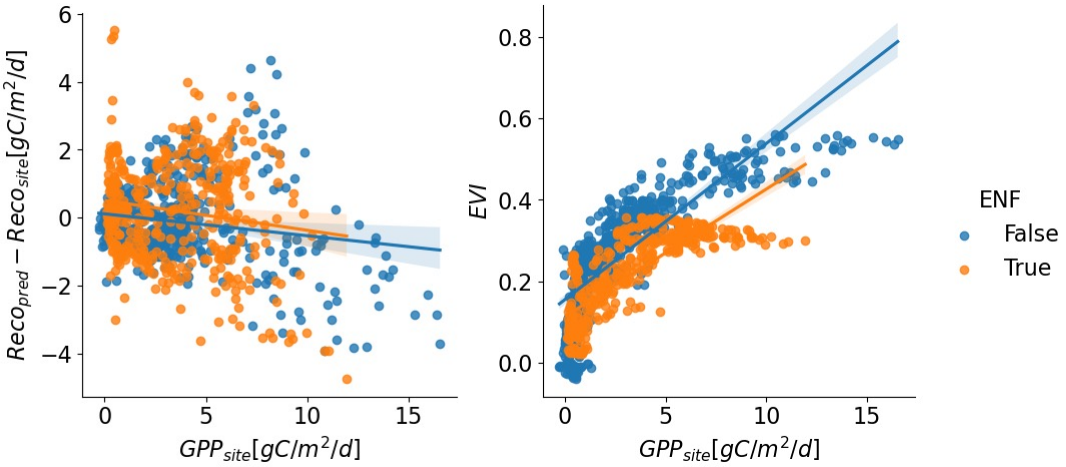

Figure 4.34 The Reco estimation residual against different GPP values and the EVI against GPP values at 5 validation sites.

Shortwave radiation is an extra indicator in ecosystem respiration estimation (Figure 4.35). For sites at both ENF or None ENF land covers, larger incoming shortwave radiation lead to the overestimation of the ecosystem respiration (Figure 4.35). Usually, when shortwave radiation is larger GPP in the ecosystem will become larger. Therefore, should produce a underestimation of ecosystem respiration (Figure 4.34). However, it turns out a opposite relationship and is conflict to the result in Figure 4.35. Therefore, GPP cannot be used to explain this phenomenon and other biotic or abiotic parameters need further discussion.

Shortwave radiation was not included the mechanism of the respiration processes, but is an important role in energy balance and the almost only input energy of the

ecosystem. Energy input do not only increase the organic matter production also heat the surfaces because of the aborsption. Considering the issues related to temperature, as the LST at TIR spectrum usually has low penetration and almost represents the skin temperature, LST is very likely to show gap to the temperature at underlayer. Additionally, the ecosystem was consist of underground respiration (soil respiration) and aboveground respiration while the underground is more related to such underlayer temperatures. If the soil respiration was unnegligible, the difference between LST and soil temperature will increase the uncertainty in soil respiration estimation when LST or TA was used. It was found that in both ENF and None ENF sites, the higher shortwave radiation is causing larger difference between TS (soil temperature) and LST. In our understanding, with more input energy, the surface (canopy) received more energy and has higher temperature, causing such large difference between TS and LST. However, only at None ENF types, the ecosystem respiration can be explained by the gap between TS and LST. This can also explain the increasing trend of observational ecosystem respiration from June to September in 2022 at the None ENF site US-YK1. It was along the increasing trend of the soil temperature but different from the trend of LST or TA, suggesting that the usage of LST or even the most widely used TA has limitation to such cases.

As for estimation error caused by ingorant of soil smoisture, it was found such effect is small in none ENF sites (Figure 4.35). It is quite possible that LST represent the temperatures of the canopy and the canopy block those information that is related to the soil, which can indicate drought information. Such mean value of LST itself correlated to soil mositure condition where dry soils are more likely to produce higher daily mean LSTs as well as high DTRs (Yamamoto et al., 2023). Therefore, the estimation residual of Reco in ENF types can be explained by soil mositure changes.

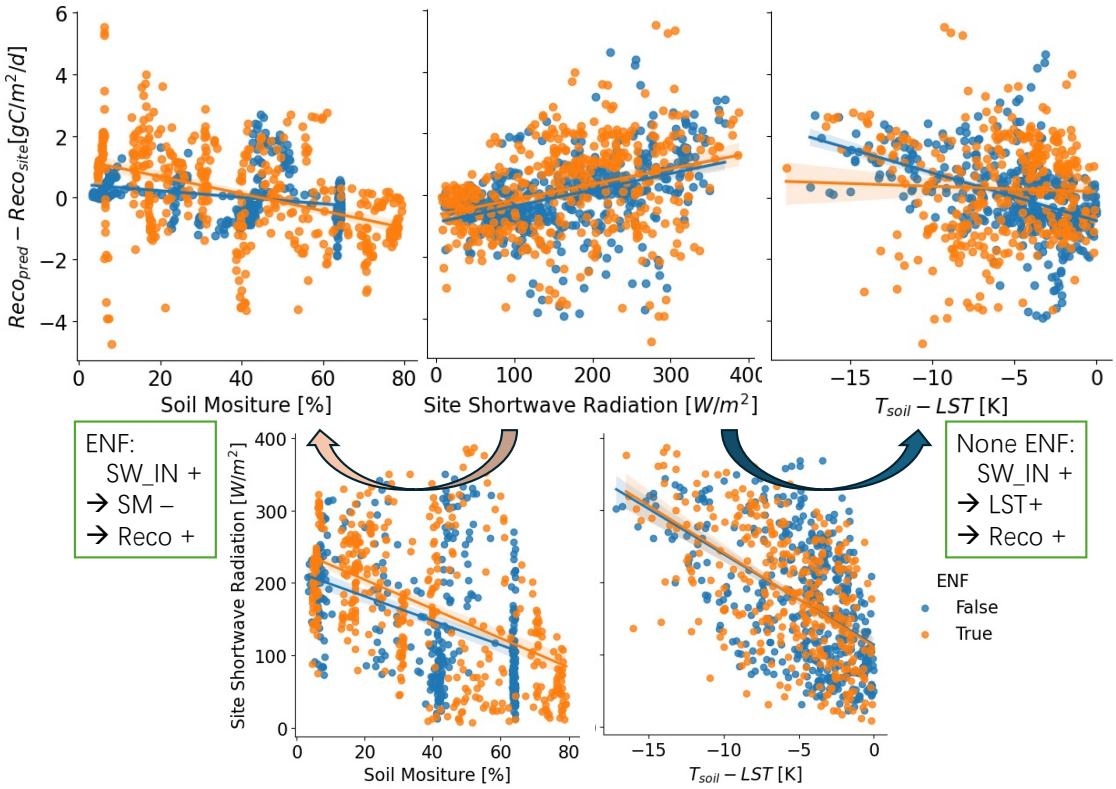

Figure 4.35 Estimation error of the ecosystem respiration (Reco) at different soil water content conditions, GPP values, and income shortwave radiations. Y-axis is the residual between estimated Reco and ground truth Reco. X-axis is the standardized soil water content, which is the value of the ratio between daily soil moisture content and maximum calculated at individual site.

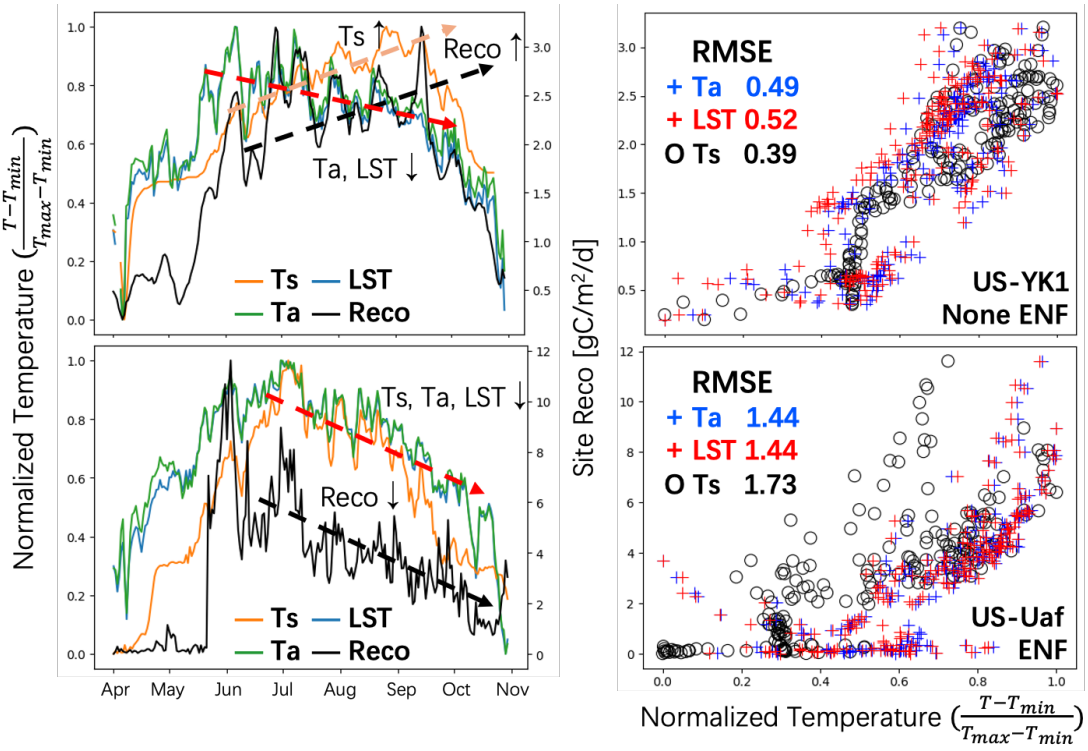

Figure 4.36 Reco, Ta, LST, and Ts daily variation from April to October in 2022 at US-YK1 and US-Uaf. The right figures are the corresponding Reco response to Ta, LST, and Ts. The RMSE values represent the value of Q10 fitted Reco-temperature response curve without considering the EVI component. Ta, LST, and Ts are normalized to 0~1 with each corresponsing minimum and maximum.

The estimated ecosystem respiration in this study produced a comparable RMSE. For example, the RMSE was reported at 1.67 gC/m^2/d for the estimation at summer at the boreal forest (Ai et al., 2018). Thus, the validation result with RMSE at approximately 1.29 gC/m^2/d is considered as an improvememnt. Additinally, the temporal resolution was produced at a daily scale. However, this RMSE is still larger than the ecosystem respiration estimation by other studies, especially, those used a machine leanring method. For example, used about 20 sites with auxiliary remote sensing datraset and meterological dataset that estimated Reco at RMSE ranges from 0.2 to 0.5 gC/m^2/d, smaller than RMSE in this study (Ueyama et al., 2013). Compared to this machine learning approach, the model in this study is rather a simple one that only considered the vegetation productivty indicated by EVI as well the the dynamic changes that response to the temperatures (Figure 4.35) and with the possibility of extrapolation. As the machine leanring model

include the shortwave radiations, that influence the Reco estimation but not well modeled in the current existing models (Figure 4.35). Though it has a easier explainable formular, but cannot address the complex processes that were exceed the asusmption of such approach. For example, due to the foilage that indicated by the decreasing of EVI, the ecosystem respiration was stimulated (Figure 4.37). It indicated the changes in the canopy and consequently influence the energy balance as a result causing the the soil temperature and LST discorded (Figure 4.36). This amplified the ecosystem repiration by stimulating the heterotropical respiration. Additionally, such change of EVI indicated the increase of surface litter which can stiumulate the heterotropheic respiration as the more availibility of the soil organic carbon and disturbe the relasionship between temperature and ecosystem respiration.

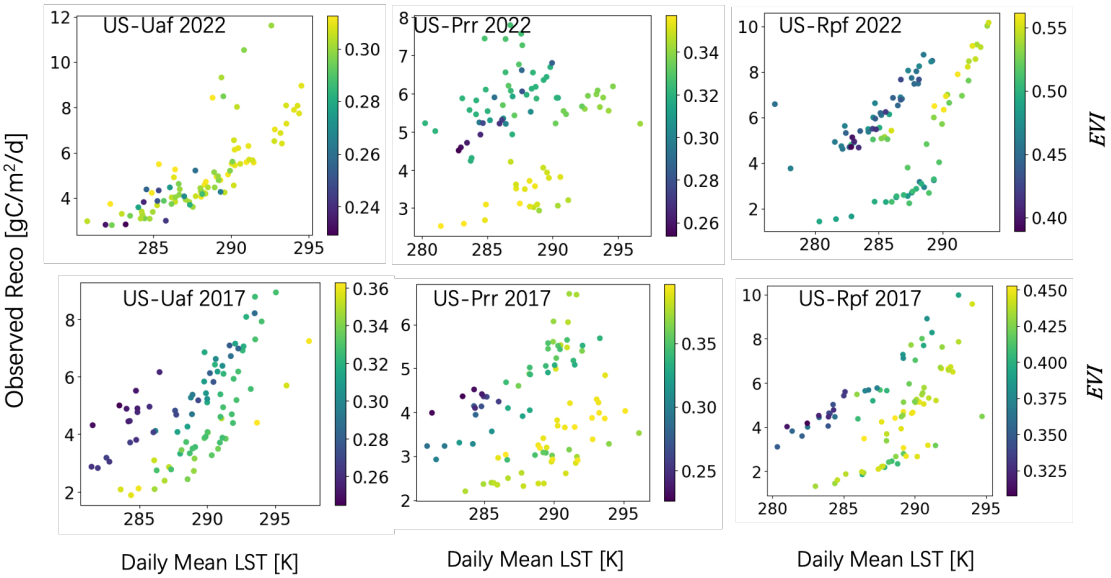

Figure 4.37 Reco Residul against the models and Reco-temperaure responses at three sites corresponding to LST_{MEAN} and EVI in June,July and August of 2017 and 2022.

The LST daily mean in this study strongly relies on clear sky observations. Estimations during cloudy days may suffer from larger errors due to limited observations under clear skies and still causing issues for continuous cloudy days. Various approaches have been developed to address the missing data caused by cloud contamination, including spatiotemporal interpolation and utilization of Surface Energy Balance (SEB) models. Although these methods require more input and under certain assumption, they are beneficial in achieving an all-sky ecosystem respiration product on a daily scale.

Similarly to the high observation frequency LST that achieved in this study, more observations can be captured by geostationary satellites, although at different research regions, but still have potential to benefit from this procedure thus expected to produce a better dynamic of the ecosystem respirations and help us understand the global carbon budget.

The ecosystem respiration in winter is still ongoing and under a risk of increasing accompany with the arctic warming (Sulikowska et al., 2019). In these seasons, the ecosystem respiration that correlated to the EVI/gross primary production is becomning weaker and play as simply carbon source solely. Such relationship cannot be well expressed by the model used in this study. Also, the Thus, in futher studies, the ecosystem respiration should considered with input of other indicator rather than EVI scale factor, especially in winter for deeper understanding of the annual ecosystem respiration and its dynamics.

4.6 Conclusion of the Chapter

In this chapter, the ecosystem respiration in arctic (Alaska) was estiamted using a daily LST as input. The daily mean LST validation result showed the integrating with the FY-3E has the best performances regarding the RMSE, against other approaches and dataset without using FY-3E data. Especially, the boosting observations improved the performances for producing a seamless daily LST with interpolation and smoothing procedures. The consequent using this daily LST to producing daily ecosystem respiration showed more temporal changes and a better estimation results comparing to use nighttime LST as input. This emphasis that synthesisign the LST from polar obiting satellites can provide the daily data with better representtativeness, and in this study qualified for estimating the ecosystem respiration in Arctic regions.

Chapter 5 Discussion and Perspective

5.1 Satellite-based High Frequency Observations

More observation of LSTs within a day is helpful for retrieving accurate daily mean LST and help recover the LSTs that was contaminated by cloud. As indicated by the result (Figure 4.19) as well as the conclusion from a previous study that used the discrete LSTs from MODIS to construct all-weather LSTs (Jia et al., 2022), the availability of the satellite observation can influence the performance of the model outputs and improve the daily mean LST retrieval for Arctic and Pan-arctic regions (Hong et al., 2022).

Satellite technology, especially when observations are made at high frequencies, plays a crucial role in monitoring and retrieving not just LST but also other critical environmental parameters. For instance, terrestrial products such as wildfire activity, sensible heat, and hydrological parameters including cloud fraction and latent heat can be better monitored.

The use of satellites like MODIS Terra, MODIS Aqua, and VIIRS allows for comprehensive coverage throughout the day, enhancing fire detection capabilities across varied time frames. For example, combining MODIS Terra, MODIS Aqua and VIIRS, the fire at 10:00–15:00 and 20:00–5:00 can be captured (Figure 5.1) (Waigl et al., 2017) . But the fire spot out of the time range cannot be captured, as a result will result in delay of the fire alerting. As the MERSI-LL FY-3E has the ability to observe the spectrum around 4.0 μm and 11 μm (Figure 3.2), which indicate its possibility of capture fire events (Waigl et al., 2017), as well as it operates at this invalid time of MODIS and VIIRS, can deal with this issue. If the early morning orbit data from MERSI-LL FY-3E was used with MODIS and VIIRS as a constellation, it will enable the all-time fire monitoring, especially, for the Arctic and Pan-arctic regions, which was under change caused by frequency fire events (Ueyama et al., 2020).

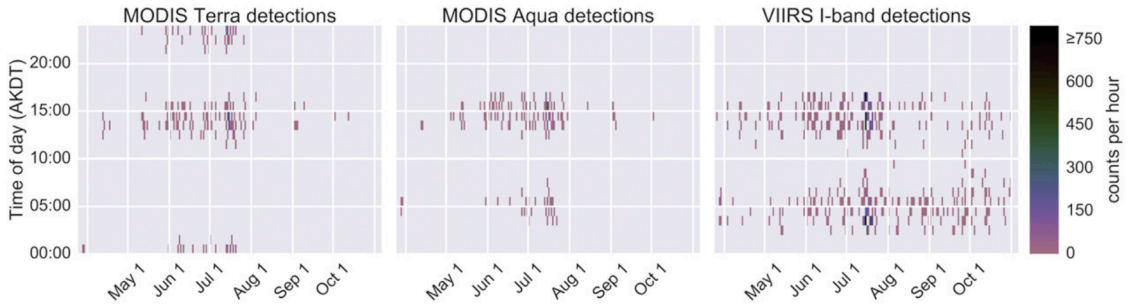

Figure 5.1 Hourly detection counts across the Alaska 2016 fire season for global fire products: MODIS Terra, MODIS Aqua and VIIRS I-band (375 m) detections at the whole Alaska (Waigl et al., 2017).

Satellite-based high frequency observations can be used to retrieve other energy fluxes at an hourly scale, such as latent heat (LE) and sensible heat (H) and solar radiation. The retrieval of LE and H have been achieved using geostationary satellite-based LST (Geng et al., 2022; Rios and Ramamurthy, 2022). The cloud fraction indicated by the high frequency observations align the solar radiation (Figure 2.14) and can be considered into solar radiation retrieval in the further studies. The diurnal change of these parameters can be used for understanding the of Arctic and Pan-arctic.

On the other hand, further improvement can be extended to aspect on spatial resolution and spectral resolution. Current environmental monitoring satellite like MODIS Terra, MODIS Aqua, VIIRS SNPP and MERSI-LL FY-3E can achieve high temporal observation resolution as shown in this study, but still spaces for improvement regarding the spatial resolution. Comparing to high resolution platforms like Landsat and ECOSTRESS which can observe TIR bands at 30 m and 70 m and produce the LST products at the corresponding resolution (Xiao et al., 2021), 1 km spatial resolution loss a lot of heterogeneity detail, which is a typical issue for LST observations (Westermann et al., 2011). Also, studies indicated combinations of certain TIR channels can be used for better retrieving the intermediate parameter Tg,i to various emissivity ranges in the TES method (Zheng et al., 2022, 2019). Advancements in data fusion techniques and the development of new satellite platforms could synthesize the strengths of each system, thereby enhancing environmental monitoring capabilities in the Arctic and Pan-arctic regions, as shown in Figure 2.25.

5.2 Estimation of Ecosystem Respiration

In the further studies, ecosystem respiration estimation can benefit from the diurnal change curve of the LSTs. As indicated in this study, one daily property – daily mean of the LST, can influence the estimation of total ecosystem respiration amount which can be indicated by the bias in the validation result (Figure 4.29). Except from mean values, other parameters such as maximum LST and minimum LST can potentially contribute to soil respiration estimation. For example, the difference of the maximum and minimum LST indicated the water dynamic availability of the ecosystem (Huang et al., 2015; Yamamoto et al., 2023), thereby can be important to ecosystems that are sensitive to soil moistures (Ai et al., 2023; Maes et al., 2024). Alternatively, with the utilization of the early morning LSTs that was induced in the high frequency observation, the calculation of the LST morning trend can be accomplished. This data can be used to modeling the soil moisture better (Z.-L. Li et al., 2021), consequently, helps improving the ecosystem respiration estimation for dry areas in the Arctic and Pan-arctic regions.

Ecosystem respiration in the winter mainly dominated by soil respiration can benefit from the high frequency LST observations. For solving the 1-D heat equation with phase changes, LST at different time will be used with the extra input of the snow depth (Jafarov et al., 2014). Consequently, the LST beneath the snow can be retrieved and used for wintertime respiration estimation for the understanding of the carbon budget accompany with the increasing winter temperatures in the recent decades (Sulikowska et al., 2019).

5.3 Towards a Contribution to Society

Satellite plays an important role in Earth monitoring and providing the basic physical parameters or the input of these parameters. Combined with the high frequency observation indicated in this study, it is possible to fuse the hourly observation network such as GEONEX (Wang et al., 2020) and expand the hourly observations to the whole global area. This global hourly data is expected to improve the output for the Earth system models through data assimilation (Meng et al., 2009). Also, it is possible to provide a fast response of terrestrial change at a high spatial resolution, comparing to a reanalysis data which was generated with 5 days' delay as well as the coarse resolution. In particular towards the frequent wildfire in recent decades, is of important regarding the influence

on economic and ecology (McCarty et al., 2021). On the other hand, the Earth science is on the era that can be synthesized with the trending technic like artifical interlligence (AI). For example, three-dimensional deep networks equipped with Earth-specific priors – Pangu-weather model, showed the success of using historical meteorological data with the AI (Bi et al., 2023). Similarly, the wide observation by satellites especially, the hourly observations can provide the material for these kinds of models and potentially helpful to the numerical prediction models because of the real-time characters of the satellites. Through these services, it is possible to seamlessly integrate hourly observations into the digital twin of the Earth. This integration provides vital information and strategic insights to policymakers. By leveraging this data, decision-makers can better understand environmental changes and implement effective policies tailored to real-time global conditions. This capability enhances our ability to monitor, predict, and respond to environmental challenges with greater precision and efficacy.

Chapter 6 Conclusion

In this thesis, high observation frequency LST at a sub-daily (quasi-hourly) using satellite LST observations was constructed successfully. A consequent validation and evaluation of the LST product of different satellites indicated the possibility to use the product at an acceptable bias. Finally, such high observation frequency LST can be used to calculate a more accurate daily mean. Additionally, integrating with this daily mean LST data, the estimation of ecosystem respiration in arctic regions was improved based on the validation using the site observation data.

This thesis showed its originality at quantifying the observation frequency at the basic data level, also helped the community understanding the latitude and hour character, which is a critical information for the all-sky and all-weather LST development at high-latitude regions. Additionally, the included new platform FY-3E emphasis the development for new platform at orbit other than AM and PM orbit is also necessary for capturing the LST changes in the high latitude regions, in particular, 60-70˚N that were covered by larger terrestrial area, under threaten by the climate changes. And the combination of the LSTs from different platforms were comprehensively validated and proofed it can be used to for deriving a reliable diurnal change of the LSTs, which will broadern the usage of LST among the community. Finally, the hourly LSTs were used to estimate a seamless daily LST, and by using this daily mean LST it showed the possibility of estimating a more reasonable ecosystem repiration at a daily scale. These results showed that the newly proposed approaches are necessary for making better estimation of ecosystem respiration, which is of important to regional or global carbon budget.

Acknowledgements

I would like to give my appreciate for site PIs and organization for maintaining and providing the site observation data and remote sensing data. I would like to give my appreciate to my supervisor Kazuhito Ichii for his supporting to my study. Also, I appreciate the reviewers of my PHD thesis as they provided the insight comments and their expertise. Additionally, I would like to thank the JST SPRING project for provide the funding and living fees for my research and living in Japan. Finally, I would like to thank to my parents and friends, they are supporting me in many aspects, especially encouraging me to challenge the difficulties in my PHD study.

Reference

Ahkinga, O., 2022. Consequences of Rapid Environmental Arctic Change for People. https://doi.org/10.25923/KGM2-9K50

Ai, J., Jia, G., Epstein, H.E., Wang, H., Zhang, A., Hu, Y., 2018. MODIS-Based Estimates of Global Terrestrial Ecosystem Respiration. JGR Biogeosciences 123, 326–352. https://doi.org/10.1002/2017JG004107

Ai, J., Qi, X., Zhang, R., He, M., Li, J., Xu, R., Li, Y., Sarmah, S., Wang, H., Zhao, J., 2023. A novel approach for ecosystem respiration simulation in drylands. Front. Ecol. Evol. 11, 1186272. https://doi.org/10.3389/fevo.2023.1186272

Augustine, J.A., DeLuisi, J.J., Long, C.N., 2000. SURFRAD—A National Surface Radiation Budget Network for Atmospheric Research. Bull. Amer. Meteor. Soc. 81, 2341–2357. https://doi.org/10.1175/1520-0477(2000)081<2341:SANSRB>2.3.CO;2

Azevedo, O., Parker, T.C., Siewert, M.B., Subke, J.-A., 2021. Predicting Soil Respiration from Plant Productivity (NDVI) in a Sub-Arctic Tundra Ecosystem. Remote Sensing 13, 2571. https://doi.org/10.3390/rs13132571

Badgley, G., Anderegg, L.D.L., Berry, J.A., Field, C.B., 2019. Terrestrial gross primary production: Using NIRV to scale from site to globe. Global Change Biology 25, 3731–3740. https://doi.org/10.1111/gcb.14729

Bahn, M., Rodeghiero, M., Anderson-Dunn, M., Dore, S., Gimeno, C., Drösler, M., Williams, M., Ammann, C., Berninger, F., Flechard, C., Jones, S., Balzarolo, M., Kumar, S., Newesely, C., Priwitzer, T., Raschi, A., Siegwolf, R., Susiluoto, S., Tenhunen, J., Wohlfahrt, G., Cernusca, A., 2008. Soil Respiration in European Grasslands in Relation to Climate and Assimilate Supply. Ecosystems 11, 1352–1367. https://doi.org/10.1007/s10021-008-9198-0

Baldridge, A.M., Hook, S.J., Grove, C.I., Rivera, G., 2009. The ASTER spectral library version 2.0. Remote Sensing of Environment 113, 711–715. https://doi.org/10.1016/j.rse.2008.11.007

Barba, J., Cueva, A., Bahn, M., Barron-Gafford, G.A., Bond-Lamberty, B., Hanson, P.J., Jaimes, A., Kulmala, L., Pumpanen, J., Scott, R.L., Wohlfahrt, G., Vargas, R., 2018. Comparing ecosystem and soil respiration: Review and key challenges of tower-based and soil measurements. Agricultural and Forest Meteorology 249, 434–443. https://doi.org/10.1016/j.agrformet.2017.10.028

Bastos, A., Ciais, P., Friedlingstein, P., Sitch, S., Pongratz, J., Fan, L., Wigneron, J.P., Weber, U., Reichstein, M., Fu, Z., Anthoni, P., Arneth, A., Haverd, V., Jain, A.K., Joetzjer, E., Knauer, J., Lienert, S., Loughran, T., McGuire, P.C., Tian, H., Viovy, N., Zaehle, S., 2020. Direct and seasonal legacy effects of the 2018 heat wave and drought on European ecosystem productivity. Sci. Adv. 6, eaba2724. https://doi.org/10.1126/sciadv.aba2724

Beale, C., Norouzi, H., Sharifnezhadazizi, Z., Bah, A.R., Yu, P., Yu, Y., Blake, R., Vaculik, A., Gonzalez-Cruz, J., 2020. Comparison of Diurnal Variation of Land Surface Temperature From GOES-16 ABI and MODIS Instruments. IEEE Geoscience and Remote Sensing Letters 17, 572–576. https://doi.org/10.1109/LGRS.2019.2930174

Bengtsson, L., Semenov, V.A., Johannessen, O.M., 2004. The Early Twentieth-Century Warming in the Arctic—A Possible Mechanism. Journal of Climate 17, 4045–4057. https://doi.org/10.1175/1520-0442(2004)017<4045:TETWIT>2.0.CO;2

Berk, A., Conforti, P., Kennett, R., Perkins, T., Hawes, F., Van Den Bosch, J., 2014. MODTRAN6: a major upgrade of the MODTRAN radiative transfer code, in: Velez-Reyes, M., Kruse, F.A. (Eds.), . Presented at the SPIE Defense + Security, Baltimore, Maryland, USA, p. 90880H. https://doi.org/10.1117/12.2050433

Bi, K., Xie, L., Zhang, H., Chen, X., Gu, X., Tian, Q., 2023. Accurate medium-range global weather forecasting with 3D neural networks. Nature 619, 533–538. https://doi.org/10.1038/s41586-023-06185-3

Biskaborn, B.K., Smith, S.L., Noetzli, J., Matthes, H., Vieira, G., Streletskiy, D.A., Schoeneich, P., Romanovsky, V.E., Lewkowicz, A.G., Abramov, A., Allard, M., Boike, J., Cable, W.L., Christiansen, H.H., Delaloye, R., Diekmann, B., Drozdov, D., Etzelmüller, B., Grosse, G., Guglielmin, M., Ingeman-Nielsen, T., Isaksen, K., Ishikawa, M., Johansson, M., Johannsson, H., Joo, A., Kaverin, D., Kholodov, A., Konstantinov, P., Kröger, T., Lambiel, C., Lanckman, J.-P., Luo, D., Malkova, G., Meiklejohn, I., Moskalenko, N., Oliva, M., Phillips, M., Ramos, M., Sannel, A.B.K., Sergeev, D., Seybold, C., Skryabin, P., Vasiliev, A., Wu, Q., Yoshikawa, K., Zheleznyak, M., Lantuit, H., 2019. Permafrost is warming at a global scale. Nat Commun 10, 264. https://doi.org/10.1038/s41467-018-08240-4

Bodesheim, P., Jung, M., Gans, F., Mahecha, M.D., Reichstein, M., 2018. Upscaled diurnal cycles of land–atmosphere fluxes: a new global half-hourly data product. Earth System Science Data 10, 1327–1365. https://doi.org/10.5194/essd-10-1327-2018

Borbas, E. E., Suzanne Wetzel Seemann, Hung-Lung Huang, Jun Li, W. Paul Menzel, 2005. Global profile training database for satellite regression retrievals with estimates of skin temperature and emissivity. Proceedings of the XIV. International ATOVS Study Conference, Beijing, China 763–770.

Bounoua, L., Collatz, G.J., Los, S.O., Sellers, P.J., Dazlich, D.A., Tucker, C.J., Randall, D.A., 2000. Sensitivity of Climate to Changes in NDVI. J. Climate 13, 2277–2292. https://doi.org/10.1175/1520-0442(2000)013<2277:SOCTCI>2.0.CO;2

Box, J.E., Colgan, W.T., Christensen, T.R., Schmidt, N.M., Lund, M., Parmentier, F.-J.W., Brown, R., Bhatt, U.S., Euskirchen, E.S., Romanovsky, V.E., Walsh, J.E., Overland, J.E., Wang, M., Corell, R.W., Meier, W.N., Wouters, B., Mernild, S., Mård, J., Pawlak, J., Olsen, M.S., 2019. Key indicators of Arctic climate change: 1971–2017. Environ. Res. Lett. 14, 045010. https://doi.org/10.1088/1748-9326/aafc1b

Brown, C.F., Brumby, S.P., Guzder-Williams, B., Birch, T., Hyde, S.B., Mazzariello, J., Czerwinski, W., Pasquarella, V.J., Haertel, R., Ilyushchenko, S., Schwehr, K., Weisse, M., Stolle, F., Hanson, C., Guinan, O., Moore, R., Tait, A.M., 2022. Dynamic World, Near real-time global 10 m land use land cover mapping. Sci Data 9, 251. https://doi.org/10.1038/s41597-022-01307-4

Buch, E., Madsen, M.S., She, J., Stendel, M., Leth, O.K., Fj, A.M., 2019. ARCTIC IN SITU DATA AVAILABILITY.

Chandrasekar, K., Sai, M.V.R.S., Roy, P.S., Dwevedi, R.S., 2010. Land Surface Water Index (LSWI) response to rainfall and NDVI using the MODIS Vegetation Index product. International Journal of Remote Sensing 31, 3987–4005. https://doi.org/10.1080/01431160802575653

Chang, Y., Xiao, J., Li, Xuxiang, Frolking, S., Zhou, D., Schneider, A., Weng, Q., Yu, P., Wang, X., Li, Xing, Liu, S., Wu, Y., 2021. Exploring diurnal cycles of surface urban heat island intensity in Boston with land surface temperature data derived from GOES-R geostationary satellites. Science of The Total Environment 763, 144224. https://doi.org/10.1016/j.scitotenv.2020.144224

Chaudhary, N., Zhang, W., Lamba, S., Westermann, S., 2022. Modeling Pan-Arctic Peatland Carbon Dynamics Under Alternative Warming Scenarios. Geophysical Research Letters 49, e2021GL095276. https://doi.org/10.1029/2021GL095276

Chen, J., He, T., Jiang, B., Liang, S., 2020. Estimation of all-sky all-wave daily net radiation at high latitudes from MODIS data. Remote Sensing of Environment 245, 111842. https://doi.org/10.1016/j.rse.2020.111842

Chen, Y., Romps, D.M., Seeley, J.T., Veraverbeke, S., Riley, W.J., Mekonnen, Z.A., Randerson, J.T., 2021. Future increases in Arctic lightning and fire risk for

permafrost carbon. Nat. Clim. Chang. 11, 404–410. https://doi.org/10.1038/s41558-021-01011-y

Cheng, J., Liang, S., Yao, Y., Zhang, X., 2013. Estimating the Optimal Broadband Emissivity Spectral Range for Calculating Surface Longwave Net Radiation. IEEE Geoscience and Remote Sensing Letters 10, 401–405. https://doi.org/10.1109/LGRS.2012.2206367

Cheng, Y., Ni, L., Li, X., Feng, R., Wu, H., 2023. Retrieval and validation of the dawn-dusk land surface temperature from FY-3E MERSI-LL. International Journal of Remote Sensing 1–18. https://doi.org/10.1080/01431161.2023.2221804

Chiang, L.H., Pell, R.J., Seasholtz, M.B., 2003. Exploring process data with the use of robust outlier detection algorithms. Journal of Process Control 13, 437–449. https://doi.org/10.1016/S0959-1524(02)00068-9

Chu, H., Luo, X., Ouyang, Z., Chan, W.S., Dengel, S., Biraud, S.C., Torn, M.S., Metzger, S., Kumar, J., Arain, M.A., Arkebauer, T.J., Baldocchi, D., Bernacchi, C., Billesbach, D., Black, T.A., Blanken, P.D., Bohrer, G., Bracho, R., Brown, S., Brunsell, N.A., Chen, J., Chen, X., Clark, K., Desai, A.R., Duman, T., Durden, D., Fares, S., Forbrich, I., Gamon, J.A., Gough, C.M., Griffis, T., Helbig, M., Hollinger, D., Humphreys, E., Ikawa, H., Iwata, H., Ju, Y., Knowles, J.F., Knox, S.H., Kobayashi, H., Kolb, T., Law, B., Lee, X., Litvak, M., Liu, H., Munger, J.W., Noormets, A., Novick, K., Oberbauer, S.F., Oechel, W., Oikawa, P., Papuga, S.A., Pendall, E., Prajapati, P., Prueger, J., Quinton, W.L., Richardson, A.D., Russell, E.S., Scott, R.L., Starr, G., Staebler, R., Stoy, P.C., Stuart-Haëntjens, E., Sonnentag, O., Sullivan, R.C., Suyker, A., Ueyama, M., Vargas, R., Wood, J.D., Zona, D., 2021. Representativeness of Eddy-Covariance flux footprints for areas surrounding AmeriFlux sites. Agricultural and Forest Meteorology 301–302, 108350. https://doi.org/10.1016/j.agrformet.2021.108350

Ciappa, A., Pietranera, L., Budillon, G., 2012. Observations of the Terra Nova Bay (Antarctica) polynya by MODIS ice surface temperature imagery from 2005 to 2010. Remote Sensing of Environment 119, 158–172. https://doi.org/10.1016/j.rse.2011.12.017

Ciavarella, A., Cotterill, D., Stott, P., Kew, S., Philip, S., van Oldenborgh, G.J., Skålevåg, A., Lorenz, P., Robin, Y., Otto, F., Hauser, M., Seneviratne, S.I., Lehner, F., Zolina, O., 2021. Prolonged Siberian heat of 2020 almost impossible without human influence. Climatic Change 166, 9. https://doi.org/10.1007/s10584-021-03052-w

Coll, C., Caselles, V., Galve, J.M., Valor, E., Niclòs, R., Sánchez, J.M., Rivas, R., 2005. Ground measurements for the validation of land surface temperatures derived from AATSR and MODIS data. Remote Sensing of Environment 97, 288–300. https://doi.org/10.1016/j.rse.2005.05.007

Cramer, W., Bondeau, A., Woodward, F.I., Prentice, I.C., Betts, R.A., Brovkin, V., Cox, P.M., Fisher, V., Foley, J.A., Friend, A.D., Kucharik, C., Lomas, M.R., Ramankutty, N., Sitch, S., Smith, B., White, A., Young-Molling, C., 2001. Global response of terrestrial ecosystem structure and function to CO_2 and climate change: results from six dynamic global vegetation models. Global Change Biology 7, 357–373. https://doi.org/10.1046/j.1365-2486.2001.00383.x

De Frenne, P., Zellweger, F., Rodríguez-Sánchez, F., Scheffers, B.R., Hylander, K., Luoto, M., Vellend, M., Verheyen, K., Lenoir, J., 2019. Global buffering of temperatures under forest canopies. Nat Ecol Evol 3, 744–749. https://doi.org/10.1038/s41559-019-0842-1

Dobricic, S., Russo, S., Pozzoli, L., Wilson, J., Vignati, E., 2020. Increasing occurrence of heat waves in the terrestrial Arctic. Environ. Res. Lett. 15, 024022. https://doi.org/10.1088/1748-9326/ab6398

Duan, S.-B., Li, Z.-L., 2015. Intercomparison of Operational Land Surface Temperature Products Derived From MSG-SEVIRI and Terra/Aqua-MODIS Data. IEEE

Journal of Selected Topics in Applied Earth Observations and Remote Sensing 8, 4163–4170. https://doi.org/10.1109/JSTARS.2015.2441096
Duan, S.-B., Li, Z.-L., Li, H., Göttsche, F.-M., Wu, H., Zhao, W., Leng, P., Zhang, X., Coll, C., 2019. Validation of Collection 6 MODIS land surface temperature product using in situ measurements. Remote Sensing of Environment 225, 16–29. https://doi.org/10.1016/j.rse.2019.02.020
Freitas, S.C., Trigo, I.F., Macedo, J., Barroso, C., Silva, R., Perdigão, R., 2013. Land surface temperature from multiple geostationary satellites. International Journal of Remote Sensing 34, 3051–3068. https://doi.org/10.1080/01431161.2012.716925
Frey, R.A., Ackerman, S.A., Holz, R.E., Dutcher, S., Griffith, Z., 2020. The Continuity MODIS-VIIRS Cloud Mask. Remote Sensing 12, 3334. https://doi.org/10.3390/rs12203334
Frolova, E.A., Nesterov, E.S., Salagina, A.A., 2022. Using Arktika-M No. 1 Satellite MSU-GS Data for Monitoring and Analyzing Mesoscale Cyclones in the Arctic Region. Cosmic Res 60, S69–S79. https://doi.org/10.1134/S0010952522700083
Geng, X., Li, B., Pan, X., Wei, Z., Yang, X., Liao, K., Cui, Y., 2022. Generating Hourly Continuous Evapotranspiration Using Fengyun-2F Geostationary Satellite Data. Earth and Space Science 9, e2021EA002090. https://doi.org/10.1029/2021EA002090
Gillespie, A., Rokugawa, S., Matsunaga, T., Cothern, J.S., Hook, S., Kahle, A.B., 1998. A temperature and emissivity separation algorithm for Advanced Spaceborne Thermal Emission and Reflection Radiometer (ASTER) images. IEEE Transactions on Geoscience and Remote Sensing 36, 1113–1126. https://doi.org/10.1109/36.700995
Gitelson, A.A., Peng, Y., Masek, J.G., Rundquist, D.C., Verma, S., Suyker, A., Baker, J.M., Hatfield, J.L., Meyers, T., 2012a. Remote estimation of crop gross primary production with Landsat data. Remote Sensing of Environment 121, 404–414. https://doi.org/10.1016/j.rse.2012.02.017
Gitelson, A.A., Peng, Y., Masek, J.G., Rundquist, D.C., Verma, S., Suyker, A., Baker, J.M., Hatfield, J.L., Meyers, T., 2012b. Remote estimation of crop gross primary production with Landsat data. Remote Sensing of Environment 121, 404–414. https://doi.org/10.1016/j.rse.2012.02.017
Global Modeling And Assimilation Office, Pawson, Steven, 2015a. MERRA-2 inst3_3d_asm_Nv: 3d,3-Hourly,Instantaneous,Model-Level,Assimilation,Assimilated Meteorological Fields V5.12.4. https://doi.org/10.5067/WWQSXQ8IVFW8
Global Modeling And Assimilation Office, Pawson, Steven, 2015b. MERRA-2 tavg1_2d_slv_Nx: 2d,1-Hourly,Time-Averaged,Single-Level,Assimilation,Single-Level Diagnostics V5.12.4. https://doi.org/10.5067/VJAFPLI1CSIV
Glover, P.W.J., Blouin, M., 2022. Increased Radon Exposure From Thawing of Permafrost Due To Climate Change. Earth's Future 10, e2021EF002598. https://doi.org/10.1029/2021EF002598
Göttsche, F.-M., Olesen, F.-S., Bork-Unkelbach, A., 2013. Validation of land surface temperature derived from MSG/SEVIRI with *in situ* measurements at Gobabeb, Namibia. International Journal of Remote Sensing 34, 3069–3083. https://doi.org/10.1080/01431161.2012.716539
Grigorieva, E.A., 2024. Climate Change and Human Health in the Arctic: A Review. Climate 12, 89. https://doi.org/10.3390/cli12070089
Grosse, G., Jones, B., Arp, C., 2013. 8.21 Thermokarst Lakes, Drainage, and Drained Basins, in: Treatise on Geomorphology. Elsevier, pp. 325–353. https://doi.org/10.1016/B978-0-12-374739-6.00216-5
Guillevic, P.C., Biard, J.C., Hulley, G.C., Privette, J.L., Hook, S.J., Olioso, A., Göttsche, F.M., Radocinski, R., Román, M.O., Yu, Y., Csiszar, I., 2014.

Validation of Land Surface Temperature products derived from the Visible Infrared Imaging Radiometer Suite (VIIRS) using ground-based and heritage satellite measurements. Remote Sensing of Environment 154, 19–37. https://doi.org/10.1016/j.rse.2014.08.013

Hassol, S.J., 2004. Impacts of a warming Arctic: Arctic Climate Impact Assessment. Cambridge University Press, Cambridge, U.K. ; New York, N.Y.

Haylock, M.R., Hofstra, N., Klein Tank, A.M.G., Klok, E.J., Jones, P.D., New, M., 2008. A European daily high-resolution gridded data set of surface temperature and precipitation for 1950–2006. J. Geophys. Res. 113, 2008JD010201. https://doi.org/10.1029/2008JD010201

Hijmans, R.J., Cameron, S.E., Parra, J.L., Jones, P.G., Jarvis, A., 2005. Very high resolution interpolated climate surfaces for global land areas. Int. J. Climatol. 25, 1965–1978. https://doi.org/10.1002/joc.1276

Hill, D.J., Haywood, A.M., Lunt, D.J., Hunter, S.J., Bragg, F.J., Contoux, C., Stepanek, C., Sohl, L., Rosenbloom, N.A., Chan, W.-L., Kamae, Y., Zhang, Z., Abe-Ouchi, A., Chandler, M.A., Jost, A., Lohmann, G., Otto-Bliesner, B.L., Ramstein, G., Ueda, H., 2014. Evaluating the dominant components of warming in Pliocene climate simulations. Clim. Past 10, 79–90. https://doi.org/10.5194/cp-10-79-2014

Hiyama, T., Ueyama, M., Kotani, A., Iwata, H., Nakai, T., Okamura, M., Ohta, T., Harazono, Y., Petrov, R.E., Maximov, T.C., 2021. Lessons learned from more than a decade of greenhouse gas flux measurements at boreal forests in eastern Siberia and interior Alaska. Polar Science 27, 100607. https://doi.org/10.1016/j.polar.2020.100607

Hjort, J., Karjalainen, O., Aalto, J., Westermann, S., Romanovsky, V.E., Nelson, F.E., Etzelmüller, B., Luoto, M., 2018. Degrading permafrost puts Arctic infrastructure at risk by mid-century. Nat Commun 9, 5147. https://doi.org/10.1038/s41467-018-07557-4

Hoffert, M.I., Covey, C., 1992. Deriving global climate sensitivity from palaeoclimate reconstructions. Nature 360, 573–576. https://doi.org/10.1038/360573a0

Hofstra, N., New, M., McSweeney, C., 2010. The influence of interpolation and station network density on the distributions and trends of climate variables in gridded daily data. Clim Dyn 35, 841–858. https://doi.org/10.1007/s00382-009-0698-1

Hong, F., Zhan, W., Göttsche, F.-M., Liu, Z., Dong, P., Fu, H., Huang, F., Zhang, X., 2022. A global dataset of spatiotemporally seamless daily mean land surface temperatures: generation, validation, and analysis. Earth Syst. Sci. Data 14, 3091–3113. https://doi.org/10.5194/essd-14-3091-2022

Hotaling, S., Lutz, S., Dial, R.J., Anesio, A.M., Benning, L.G., Fountain, A.G., Kelley, J.L., McCutcheon, J., Skiles, S.M., Takeuchi, N., Hamilton, T.L., 2021. Biological albedo reduction on ice sheets, glaciers, and snowfields. Earth-Science Reviews 220, 103728. https://doi.org/10.1016/j.earscirev.2021.103728

Hu, F.S., Higuera, P.E., Duffy, P., Chipman, M.L., Rocha, A.V., Young, A.M., Kelly, R., Dietze, M.C., 2015. Arctic tundra fires: natural variability and responses to climate change. Frontiers in Ecol & Environ 13, 369–377. https://doi.org/10.1890/150063

Huang, J., Zhang, X., Zhang, Q., Lin, Y., Hao, M., Luo, Y., Zhao, Z., Yao, Y., Chen, X., Wang, L., Nie, S., Yin, Y., Xu, Y., Zhang, J., 2017. Recently amplified arctic warming has contributed to a continual global warming trend. Nature Clim Change 7, 875–879. https://doi.org/10.1038/s41558-017-0009-5

Huang, N., Gu, L., Black, T.A., Wang, L., Niu, Z., 2015. Remote sensing-based estimation of annual soil respiration at two contrasting forest sites: ESTIMATING ANNUAL SOIL RESPIRATION. J. Geophys. Res. Biogeosci. 120, 2306–2325. https://doi.org/10.1002/2015JG003060

Huang, S., Tang, L., Hupy, J.P., Wang, Y., Shao, G., 2021. A commentary review on the use of normalized difference vegetation index (NDVI) in the era of popular

remote sensing. J. For. Res. 32, 1–6. https://doi.org/10.1007/s11676-020-01155-1

Hudson, S.R., 2011. Estimating the global radiative impact of the sea ice–albedo feedback in the Arctic. J. Geophys. Res. 116, D16102. https://doi.org/10.1029/2011JD015804

Hulley, G.C., Hook, S.J., Abbott, E., Malakar, N., Islam, T., Abrams, M., 2015. The ASTER Global Emissivity Dataset (ASTER GED): Mapping Earth's emissivity at 100 meter spatial scale. Geophysical Research Letters 42, 7966–7976. https://doi.org/10.1002/2015GL065564

Hulley, G.C., Hughes, C.G., Hook, S.J., 2012. Quantifying uncertainties in land surface temperature and emissivity retrievals from ASTER and MODIS thermal infrared data. Journal of Geophysical Research: Atmospheres 117. https://doi.org/10.1029/2012JD018506

Hulley, G.C., Malakar, N.K., Islam, T., Freepartner, R.J., 2018. NASA's MODIS and VIIRS Land Surface Temperature and Emissivity Products: A Long-Term and Consistent Earth System Data Record. IEEE Journal of Selected Topics in Applied Earth Observations and Remote Sensing 11, 522–535. https://doi.org/10.1109/JSTARS.2017.2779330

Huntzinger, D.N., Schaefer, K., Schwalm, C., Fisher, J.B., Hayes, D., Stofferahn, E., Carey, J., Michalak, A.M., Wei, Y., Jain, A.K., Kolus, H., Mao, J., Poulter, B., Shi, X., Tang, J., Tian, H., 2020. Evaluation of simulated soil carbon dynamics in Arctic-Boreal ecosystems. Environ. Res. Lett. 15, 025005. https://doi.org/10.1088/1748-9326/ab6784

Ikawa, H., Nakai, T., Busey, R.C., Kim, Y., Kobayashi, H., Nagai, S., Ueyama, M., Saito, K., Nagano, H., Suzuki, R., Hinzman, L., 2015. Understory CO2, sensible heat, and latent heat fluxes in a black spruce forest in interior Alaska. Agricultural and Forest Meteorology 214–215, 80–90. https://doi.org/10.1016/j.agrformet.2015.08.247

IPCC, 2022. The Ocean and Cryosphere in a Changing Climate: Special Report of the Intergovernmental Panel on Climate Change, 1st ed. Cambridge University Press. https://doi.org/10.1017/9781009157964

Irvine, D.J., Briggs, M.A., Lautz, L.K., Gordon, R.P., McKenzie, J.M., Cartwright, I., 2017. Using Diurnal Temperature Signals to Infer Vertical Groundwater-Surface Water Exchange. Groundwater 55, 10–26. https://doi.org/10.1111/gwat.12459

Islam, T., Hulley, G.C., Malakar, N.K., Radocinski, R.G., Guillevic, P.C., Hook, S.J., 2017. A Physics-Based Algorithm for the Simultaneous Retrieval of Land Surface Temperature and Emissivity From VIIRS Thermal Infrared Data. IEEE Transactions on Geoscience and Remote Sensing 55, 563–576. https://doi.org/10.1109/TGRS.2016.2611566

Jacob, F., Lesaignoux, A., Olioso, A., Weiss, M., Caillault, K., Jacquemoud, S., Nerry, F., French, A., Schmugge, T., Briottet, X., Lagouarde, J.-P., 2017. Reassessment of the temperature-emissivity separation from multispectral thermal infrared data: Introducing the impact of vegetation canopy by simulating the cavity effect with the SAIL-Thermique model. Remote Sensing of Environment 198, 160–172. https://doi.org/10.1016/j.rse.2017.06.006

Jafarov, E.E., Nicolsky, D.J., Romanovsky, V.E., Walsh, J.E., Panda, S.K., Serreze, M.C., 2014. The effect of snow: How to better model ground surface temperatures. Cold Regions Science and Technology 102, 63–77. https://doi.org/10.1016/j.coldregions.2014.02.007

Jägermeyr, J., Gerten, D., Lucht, W., Hostert, P., Migliavacca, M., Nemani, R., 2014. A high-resolution approach to estimating ecosystem respiration at continental scales using operational satellite data. Global Change Biology 20, 1191–1210. https://doi.org/10.1111/gcb.12443

Jeong, S.-J., Bloom, A.A., Schimel, D., Sweeney, C., Parazoo, N.C., Medvigy, D., Schaepman-Strub, G., Zheng, C., Schwalm, C.R., Huntzinger, D.N., Michalak,

A.M., Miller, C.E., 2018. Accelerating rates of Arctic carbon cycling revealed by long-term atmospheric CO_2 measurements. Sci. Adv. 4, eaao1167. https://doi.org/10.1126/sciadv.aao1167

Jia, A., Liang, S., Wang, D., 2022. Generating a 2-km, all-sky, hourly land surface temperature product from Advanced Baseline Imager data. Remote Sensing of Environment 278, 113105. https://doi.org/10.1016/j.rse.2022.113105

Jiao, W., Wang, L., McCabe, M.F., 2021. Multi-sensor remote sensing for drought characterization: current status, opportunities and a roadmap for the future. Remote Sensing of Environment 256, 112313. https://doi.org/10.1016/j.rse.2021.112313

Johannessen, O.M., Bengtsson, L., Miles, M.W., Kuzmina, S.I., Semenov, V.A., Alekseev, G.V., Nagurnyi, A.P., Zakharov, V.F., Bobylev, L.P., Pettersson, L.H., Hasselmann, K., Cattle, H.P., 2004. Arctic climate change: observed and modelled temperature and sea-ice variability. Tellus A: Dynamic Meteorology and Oceanography 56, 328. https://doi.org/10.3402/tellusa.v56i4.14418

Jung, M., Schwalm, C., Migliavacca, M., Walther, S., Camps-Valls, G., Koirala, S., Anthoni, P., Besnard, S., Bodesheim, P., Carvalhais, N., Chevallier, F., Gans, F., Goll, D.S., Haverd, V., Köhler, P., Ichii, K., Jain, A.K., Liu, J., Lombardozzi, D., Nabel, J.E.M.S., Nelson, J.A., O'Sullivan, M., Pallandt, M., Papale, D., Peters, W., Pongratz, J., Rödenbeck, C., Sitch, S., Tramontana, G., Walker, A., Weber, U., Reichstein, M., 2020. Scaling carbon fluxes from eddy covariance sites to globe: synthesis and evaluation of the FLUXCOM approach. Biogeosciences 17, 1343–1365. https://doi.org/10.5194/bg-17-1343-2020

Ke, G., Meng, Q., Finley, T., Wang, T., Chen, W., Ma, W., Ye, Q., Liu, T.-Y., 2017. Lightgbm: A highly efficient gradient boosting decision tree. Advances in neural information processing systems 30.

Kharuk, V.I., Dvinskaya, M.L., Im, S.T., Golyukov, A.S., Smith, K.T., 2022. Wildfires in the Siberian Arctic. Fire 5, 106. https://doi.org/10.3390/fire5040106

Kilibarda, M., Hengl, T., Heuvelink, G.B.M., Gräler, B., Pebesma, E., Perčec Tadić, M., Bajat, B., 2014. Spatio-temporal interpolation of daily temperatures for global land areas at 1 km resolution. JGR Atmospheres 119, 2294–2313. https://doi.org/10.1002/2013JD020803

Koutroumanou-Kontosi, K., Cartalis, C., Philippopoulos, K., Agathangelidis, I., Polydoros, A., 2022. A Methodology for Bridging the Gap between Regional- and City-Scale Climate Simulations for the Urban Thermal Environment. Climate 10, 106. https://doi.org/10.3390/cli10070106

Kruse, J., Adams, M.A., 2008. Three parameters comprehensively describe the temperature response of respiratory oxygen reduction. Plant Cell & Environment 31, 954–967. https://doi.org/10.1111/j.1365-3040.2008.01809.x

Kuhry, P., Grosse, G., Harden, J.W., Hugelius, G., Koven, C.D., Ping, C., Schirrmeister, L., Tarnocai, C., 2013. Characterisation of the Permafrost Carbon Pool. Permafrost & Periglacial 24, 146–155. https://doi.org/10.1002/ppp.1782

Lalbakhsh, A., Pitcairn, A., Mandal, K., Alibakhshikenari, M., Esselle, K.P., Reisenfeld, S., 2022. Darkening Low-Earth Orbit Satellite Constellations: A Review. IEEE Access 10, 24383–24394. https://doi.org/10.1109/ACCESS.2022.3155193

Lasslop, G., Reichstein, M., Papale, D., Richardson, A.D., Arneth, A., Barr, A., Stoy, P., Wohlfahrt, G., 2010. Separation of net ecosystem exchange into assimilation and respiration using a light response curve approach: critical issues and global evaluation. Global Change Biology 16, 187–208. https://doi.org/10.1111/j.1365-2486.2009.02041.x

Lawrence, D.M., Koven, C.D., Swenson, S.C., Riley, W.J., Slater, A.G., 2015. Permafrost thaw and resulting soil moisture changes regulate projected high-latitude CO_2 and CH_4 emissions. Environ. Res. Lett. 10, 094011. https://doi.org/10.1088/1748-9326/10/9/094011

Lee, J.-Y., Chae, N., Kim, Y., Yun, J., Jeong, S., Choi, T., Kim, S.-J., Lee, B.-Y., Park, S.-J., 2024. Differential responses of respiration and photosynthesis to air temperature over a moist tundra ecosystem of Alaska and its impact on changing carbon cycle. Environ. Res. Commun. 6, 041003. https://doi.org/10.1088/2515-7620/ad3c17

Li, H., Li, R., Yang, Y., Cao, B., Bian, Z., Hu, T., Du, Y., Sun, L., Liu, Q., 2021. Temperature-Based and Radiance-Based Validation of the Collection 6 MYD11 and MYD21 Land Surface Temperature Products Over Barren Surfaces in Northwestern China. IEEE Transactions on Geoscience and Remote Sensing 59, 1794–1807. https://doi.org/10.1109/TGRS.2020.2998945

Li, X., Ryu, Y., Xiao, J., Dechant, B., Liu, J., Li, B., Jeong, S., Gentine, P., 2023. New-generation geostationary satellite reveals widespread midday depression in dryland photosynthesis during 2020 western U.S. heatwave. Sci. Adv. 9, eadi0775. https://doi.org/10.1126/sciadv.adi0775

Li, X., Xiao, J., Fisher, J.B., Baldocchi, D.D., 2021. ECOSTRESS estimates gross primary production with fine spatial resolution for different times of day from the International Space Station. Remote Sensing of Environment 258, 112360. https://doi.org/10.1016/j.rse.2021.112360

Li, Z., Wu, H., Duan, S., Zhao, W., Ren, H., Liu, X., Leng, P., Tang, R., Ye, X., Zhu, J., Sun, Y., Si, M., Liu, M., Li, J., Zhang, X., Shang, G., Tang, B., Yan, G., Zhou, C., 2023. Satellite Remote Sensing of Global Land Surface Temperature: Definition, Methods, Products, and Applications. Reviews of Geophysics 61. https://doi.org/10.1029/2022RG000777

Li, Z.-L., Leng, P., Zhou, C., Chen, K.-S., Zhou, F.-C., Shang, G.-F., 2021. Soil moisture retrieval from remote sensing measurements: Current knowledge and directions for the future. Earth-Science Reviews 218, 103673. https://doi.org/10.1016/j.earscirev.2021.103673

Li, Z.-L., Tang, B.-H., Wu, H., Ren, H., Yan, G., Wan, Z., Trigo, I.F., Sobrino, J.A., 2013. Satellite-derived land surface temperature: Current status and perspectives. Remote Sensing of Environment 131, 14–37. https://doi.org/10.1016/j.rse.2012.12.008

Linke, O., Feldl, N., Quaas, J., 2023. Current-climate sea ice amount and seasonality as constraints for future Arctic amplification. Environ. Res.: Climate 2, 045003. https://doi.org/10.1088/2752-5295/acf4b7

Liu, Z., Kimball, J.S., Parazoo, N.C., Ballantyne, A.P., Wang, W.J., Madani, N., Pan, C.G., Watts, J.D., Reichle, R.H., Sonnentag, O., Marsh, P., Hurkuck, M., Helbig, M., Quinton, W.L., Zona, D., Ueyama, M., Kobayashi, H., Euskirchen, E.S., 2020. Increased high-latitude photosynthetic carbon gain offset by respiration carbon loss during an anomalous warm winter to spring transition. Global Change Biology 26, 682–696. https://doi.org/10.1111/gcb.14863

Ma, J., Zhou, J., Göttsche, F.-M., Liang, S., Wang, S., Li, M., 2020. A global long-term (1981–2000) land surface temperature product for NOAA AVHRR. Earth Syst. Sci. Data 12, 3247–3268. https://doi.org/10.5194/essd-12-3247-2020

Mack, M.C., Bret-Harte, M.S., Hollingsworth, T.N., Jandt, R.R., Schuur, E.A.G., Shaver, G.R., Verbyla, D.L., 2011. Carbon loss from an unprecedented Arctic tundra wildfire. Nature 475, 489–492. https://doi.org/10.1038/nature10283

Maes, S.L., Dietrich, J., Midolo, G., Schwieger, S., Kummu, M., Vandvik, V., Aerts, R., Althuizen, I.H.J., Biasi, C., Björk, R.G., Böhner, H., Carbognani, M., Chiari, G., Christiansen, C.T., Clemmensen, K.E., Cooper, E.J., Cornelissen, J.H.C., Elberling, B., Faubert, P., Fetcher, N., Forte, T.G.W., Gaudard, J., Gavazov, K., Guan, Z., Guðmundsson, J., Gya, R., Hallin, S., Hansen, B.B., Haugum, S.V., He, J.-S., Hicks Pries, C., Hovenden, M.J., Jalava, M., Jónsdóttir, I.S., Juhanson, J., Jung, J.Y., Kaarlejärvi, E., Kwon, M.J., Lamprecht, R.E., Le Moullec, M., Lee, H., Marushchak, M.E., Michelsen, A., Munir, T.M., Myrsky, E.M., Nielsen, C.S., Nyberg, M., Olofsson, J., Óskarsson, H., Parker, T.C., Pedersen,

E.P., Petit Bon, M., Petraglia, A., Raundrup, K., Ravn, N.M.R., Rinnan, R., Rodenhizer, H., Ryde, I., Schmidt, N.M., Schuur, E.A.G., Sjögersten, S., Stark, S., Strack, M., Tang, J., Tolvanen, A., Töpper, J.P., Väisänen, M.K., Van Logtestijn, R.S.P., Voigt, C., Walz, J., Weedon, J.T., Yang, Y., Ylänne, H., Björkman, M.P., Sarneel, J.M., Dorrepaal, E., 2024. Environmental drivers of increased ecosystem respiration in a warming tundra. Nature 629, 105–113. https://doi.org/10.1038/s41586-024-07274-7

Mahadevan, P., Wofsy, S.C., Matross, D.M., Xiao, X., Dunn, A.L., Lin, J.C., Gerbig, C., Munger, J.W., Chow, V.Y., Gottlieb, E.W., 2008. A satellite-based biosphere parameterization for net ecosystem CO2 exchange: Vegetation Photosynthesis and Respiration Model (VPRM). Global Biogeochemical Cycles 22. https://doi.org/10.1029/2006GB002735

Malakar, N.K., Hulley, G.C., 2016. A water vapor scaling model for improved land surface temperature and emissivity separation of MODIS thermal infrared data. Remote Sensing of Environment 182, 252–264. https://doi.org/10.1016/j.rse.2016.04.023

Malbéteau, Y., Parkes, S., Aragon, B., Rosas, J., McCabe, M., 2018. Capturing the Diurnal Cycle of Land Surface Temperature Using an Unmanned Aerial Vehicle. Remote Sensing 10, 1407. https://doi.org/10.3390/rs10091407

Matricardi, M., Chevallier, F., Kelly, G., Thépaut, J.-N., 2004. An improved general fast radiative transfer model for the assimilation of radiance observations: AN IMPROVED RADIATIVE TRANSFER MODEL. Q.J.R. Meteorol. Soc. 130, 153–173. https://doi.org/10.1256/qj.02.181

Matt Davies, G., 2013. Understanding Fire Regimes and the Ecological Effects of Fire, in: Belcher, C.M. (Ed.), Fire Phenomena and the Earth System. Wiley, pp. 95–124. https://doi.org/10.1002/9781118529539.ch6

McCarty, J.L., Aalto, J., Paunu, V.-V., Arnold, S.R., Eckhardt, S., Klimont, Z., Fain, J.J., Evangeliou, N., Venäläinen, A., Tchebakova, N.M., Parfenova, E.I., Kupiainen, K., Soja, A.J., Huang, L., Wilson, S., 2021. Reviews and syntheses: Arctic fire regimes and emissions in the 21st century. Biogeosciences 18, 5053–5083. https://doi.org/10.5194/bg-18-5053-2021

McGuire, A.D., Anderson, L.G., Christensen, T.R., Dallimore, S., Guo, L., Hayes, D.J., Heimann, M., Lorenson, T.D., Macdonald, R.W., Roulet, N., 2009. Sensitivity of the carbon cycle in the Arctic to climate change. Ecological Monographs 79, 523–555. https://doi.org/10.1890/08-2025.1

Meerdink, S.K., Hook, S.J., Roberts, D.A., Abbott, E.A., 2019. The ECOSTRESS spectral library version 1.0. Remote Sensing of Environment 230, 111196. https://doi.org/10.1016/j.rse.2019.05.015

Meng, C.L., Li, Z.-L., Zhan, X., Shi, J.C., Liu, C.Y., 2009. Land surface temperature data assimilation and its impact on evapotranspiration estimates from the Common Land Model. Water Resources Research 45. https://doi.org/10.1029/2008WR006971

Miller, G.H., Alley, R.B., Brigham-Grette, J., Fitzpatrick, J.J., Polyak, L., Serreze, M.C., White, J.W.C., 2010. Arctic amplification: can the past constrain the future? Quaternary Science Reviews 29, 1779–1790. https://doi.org/10.1016/j.quascirev.2010.02.008

Miller, P.A., Smith, B., 2012. Modelling Tundra Vegetation Response to Recent Arctic Warming. AMBIO 41, 281–291. https://doi.org/10.1007/s13280-012-0306-1

Musacchio, C., Coppa, G., Begeš, G., Hofstätter-Mohler, C., Massano, L., Nigrelli, G., Sanna, F., Merlone, A., 2021. Effect of snow-covered ground albedo on the accuracy of air temperature measurements. Atmos. Meas. Tech. 14, 6195–6212. https://doi.org/10.5194/amt-14-6195-2021

Muster, S., Langer, M., Abnizova, A., Young, K.L., Boike, J., 2015. Spatio-temporal sensitivity of MODIS land surface temperature anomalies indicates high potential for large-scale land cover change detection in Arctic permafrost

landscapes. Remote Sensing of Environment 168, 1–12. https://doi.org/10.1016/j.rse.2015.06.017
Nakai, T., Kim, Y., Busey, R.C., Suzuki, R., Nagai, S., Kobayashi, H., Park, H., Sugiura, K., Ito, A., 2013. Characteristics of evapotranspiration from a permafrost black spruce forest in interior Alaska. Polar Science 7, 136–148. https://doi.org/10.1016/j.polar.2013.03.003
Nanni, U., DeRepentigny, P., Lundén, A., Popovaitė, V., Shen, Y., Basaran, I.K., Duarte Neubern, N., Mascorda-Cabre, L., Bennett, A., Vold Hansen, T., Holmes, F.A., Kavvatha, E., Meyer, A., Prakash, A., Wołoszyn, A., 2024. Redefining Arctic boundaries in a changing climate: interdisciplinary perspectives on governance strategies. Polar Geography 47, 127–155. https://doi.org/10.1080/1088937X.2024.2359926
Nemani, R.R., Keeling, C.D., Hashimoto, H., Jolly, W.M., Piper, S.C., Tucker, C.J., Myneni, R.B., Running, S.W., 2003a. Climate-Driven Increases in Global Terrestrial Net Primary Production from 1982 to 1999. Science 300, 1560–1563. https://doi.org/10.1126/science.1082750
Nemani, R.R., Keeling, C.D., Hashimoto, H., Jolly, W.M., Piper, S.C., Tucker, C.J., Myneni, R.B., Running, S.W., 2003b. Climate-Driven Increases in Global Terrestrial Net Primary Production from 1982 to 1999. Science 300, 1560–1563. https://doi.org/10.1126/science.1082750
Nielsen, D.M., Pieper, P., Barkhordarian, A., Overduin, P., Ilyina, T., Brovkin, V., Baehr, J., Dobrynin, M., 2022. Increase in Arctic coastal erosion and its sensitivity to warming in the twenty-first century. Nat. Clim. Chang. 12, 263–270. https://doi.org/10.1038/s41558-022-01281-0
Nill, L., Ullmann, T., Kneisel, C., Sobiech-Wolf, J., Baumhauer, R., 2019. Assessing Spatiotemporal Variations of Landsat Land Surface Temperature and Multispectral Indices in the Arctic Mackenzie Delta Region between 1985 and 2018. Remote Sensing 11, 2329. https://doi.org/10.3390/rs11192329
Njoku, E.A., Akpan, P.E., Effiong, A.E., Babatunde, I.O., 2023. The effects of station density in geostatistical prediction of air temperatures in Sweden: A comparison of two interpolation techniques. Resources, Environment and Sustainability 11, 100092. https://doi.org/10.1016/j.resenv.2022.100092
Obu, J., Westermann, S., Bartsch, A., Berdnikov, N., Christiansen, H.H., Dashtseren, A., Delaloye, R., Elberling, B., Etzelmüller, B., Kholodov, A., Khomutov, A., Kääb, A., Leibman, M.O., Lewkowicz, A.G., Panda, S.K., Romanovsky, V., Way, R.G., Westergaard-Nielsen, A., Wu, T., Yamkhin, J., Zou, D., 2019. Northern Hemisphere permafrost map based on TTOP modelling for 2000–2016 at 1 km2 scale. Earth-Science Reviews 193, 299–316. https://doi.org/10.1016/j.earscirev.2019.04.023
Østby, T.I., Schuler, T.V., Westermann, S., 2014. Severe cloud contamination of MODIS Land Surface Temperatures over an Arctic ice cap, Svalbard. Remote Sensing of Environment 142, 95–102. https://doi.org/10.1016/j.rse.2013.11.005
Paek, S.W., Kim, S., Kronig, L., Weck, O. de, 2020. Sun-synchronous repeat ground tracks and other useful orbits for future space missions. The Aeronautical Journal 124, 917–939. https://doi.org/10.1017/aer.2020.21
Pearson, R.K., 2002. Outliers in process modeling and identification. IEEE Trans. Contr. Syst. Technol. 10, 55–63. https://doi.org/10.1109/87.974338
Perovich, D.K., Light, B., Eicken, H., Jones, K.F., Runciman, K., Nghiem, S.V., 2007. Increasing solar heating of the Arctic Ocean and adjacent seas, 1979–2005: Attribution and role in the ice-albedo feedback. Geophysical Research Letters 34, 2007GL031480. https://doi.org/10.1029/2007GL031480
Przybylak, R., 1999. Influence of cloudiness on extreme air temperatures and diurnal temperature range in the Arctic in 1951-1990. POLISH POLAR RESEARCH 20, 149–173.

Pumpanen, J., Kulmala, L., Lindén, A., Kolari, P., Nikinmaa, E., Hari, P., 2015. Seasonal dynamics of autotrophic respiration in boreal forest soil estimated by continuous chamber measurements 20.

Rahman, A.F., Sims, D.A., Cordova, V.D., El-Masri, B.Z., 2005. Potential of MODIS EVI and surface temperature for directly estimating per-pixel ecosystem C fluxes. Geophysical Research Letters 32, 2005GL024127. https://doi.org/10.1029/2005GL024127

Rawlins, M.A., Willmott, C.J., 2003. Winter Air Temperature Change over the Terrestrial Arctic, 1961–1990. Arctic, Antarctic, and Alpine Research 35, 530–537. https://doi.org/10.1657/1523-0430(2003)035[0530:WATCOT]2.0.CO;2

Rebmann, C., Aubinet, M., Schmid, H., Arriga, N., Aurela, M., Burba, G., Clement, R., De Ligne, A., Fratini, G., Gielen, B., Grace, J., Graf, A., Gross, P., Haapanala, S., Herbst, M., Hörtnagl, L., Ibrom, A., Joly, L., Kljun, N., Kolle, O., Kowalski, A., Lindroth, A., Loustau, D., Mammarella, I., Mauder, M., Merbold, L., Metzger, S., Mölder, M., Montagnani, L., Papale, D., Pavelka, M., Peichl, M., Roland, M., Serrano-Ortiz, P., Siebicke, L., Steinbrecher, R., Tuovinen, J.-P., Vesala, T., Wohlfahrt, G., Franz, D., 2018. ICOS eddy covariance flux-station site setup: a review. International Agrophysics 32, 471–494. https://doi.org/10.1515/intag-2017-0044

Reiners, P., Asam, S., Frey, C., Holzwarth, S., Bachmann, M., Sobrino, J., Göttsche, F.-M., Bendix, J., Kuenzer, C., 2021. Validation of AVHRR Land Surface Temperature with MODIS and In Situ LST—A TIMELINE Thematic Processor. Remote Sensing 13, 3473. https://doi.org/10.3390/rs13173473

Richardson, A.D., Braswell, B.H., Hollinger, D.Y., Burman, P., Davidson, E.A., Evans, R.S., Flanagan, L.B., Munger, J.W., Savage, K., Urbanski, S.P., Wofsy, S.C., 2006. Comparing simple respiration models for eddy flux and dynamic chamber data. Agricultural and Forest Meteorology 141, 219–234. https://doi.org/10.1016/j.agrformet.2006.10.010

Rios, G., Ramamurthy, P., 2022. A novel model to estimate sensible heat fluxes in urban areas using satellite-derived data. Remote Sensing of Environment 270, 112880. https://doi.org/10.1016/j.rse.2021.112880

Rocha, A.V., Shaver, G.R., 2011. Postfire energy exchange in arctic tundra: the importance and climatic implications of burn severity. Global Change Biology 17, 2831–2841. https://doi.org/10.1111/j.1365-2486.2011.02441.x

Romanovsky, V.E., Smith, S.L., Christiansen, H.H., 2010. Permafrost thermal state in the polar Northern Hemisphere during the international polar year 2007–2009: a synthesis. Permafrost & Periglacial 21, 106–116. https://doi.org/10.1002/ppp.689

Rousi, E., Kornhuber, K., Beobide-Arsuaga, G., Luo, F., Coumou, D., 2022. Accelerated western European heatwave trends linked to more-persistent double jets over Eurasia. Nat Commun 13, 3851. https://doi.org/10.1038/s41467-022-31432-y

Saunders, R., Hocking, J., Turner, E., Rayer, P., Rundle, D., Brunel, P., Vidot, J., Roquet, P., Matricardi, M., Geer, A., Bormann, N., Lupu, C., 2018. An update on the RTTOV fast radiative transfer model (currently at version 12). Geosci. Model Dev. 11, 2717–2737. https://doi.org/10.5194/gmd-11-2717-2018

Schuppenhauer, M., Biraud, S., 2022. AmeriFlux AmeriFlux US-RGB Butte County Rice Farm. https://doi.org/10.17190/AMF/1870591

Schuur, E.A.G., McGuire, A.D., Schädel, C., Grosse, G., Harden, J.W., Hayes, D.J., Hugelius, G., Koven, C.D., Kuhry, P., Lawrence, D.M., Natali, S.M., Olefeldt, D., Romanovsky, V.E., Schaefer, K., Turetsky, M.R., Treat, C.C., Vonk, J.E., 2015. Climate change and the permafrost carbon feedback. Nature 520, 171–179. https://doi.org/10.1038/nature14338

Serreze, M.C., Barrett, A.P., Stroeve, J.C., Kindig, D.N., Holland, M.M., 2009. The emergence of surface-based Arctic amplification. The Cryosphere 3, 11–19. https://doi.org/10.5194/tc-3-11-2009

Serreze, M.C., Francis, J.A., 2006. The Arctic on the fast track of change. Weather 61, 65–69. https://doi.org/10.1256/wea.197.05

Shupe, M.D., Intrieri, J.M., 2004. Cloud Radiative Forcing of the Arctic Surface: The Influence of Cloud Properties, Surface Albedo, and Solar Zenith Angle. J. Climate 17, 616–628. https://doi.org/10.1175/1520-0442(2004)017<0616:CRFOTA>2.0.CO;2

Sims, D.A., Rahman, A.F., Cordova, V.D., El-Masri, B.Z., Baldocchi, D.D., Flanagan, L.B., Goldstein, A.H., Hollinger, D.Y., Misson, L., Monson, R.K., Oechel, W.C., Schmid, H.P., Wofsy, S.C., Xu, L., 2006. On the use of MODIS EVI to assess gross primary productivity of North American ecosystems. Journal of Geophysical Research: Biogeosciences 111. https://doi.org/10.1029/2006JG000162

Sobrino, J.A., Zhao-Liang Li, Stoll, M.P., 1993. Impact of the atmospheric transmittance and total water vapor content in the algorithms for estimating satellite sea surface temperatures. IEEE Trans. Geosci. Remote Sensing 31, 946–952. https://doi.org/10.1109/36.263765

Stroeve, J., Notz, D., 2018. Changing state of Arctic sea ice across all seasons. Environ. Res. Lett. 13, 103001. https://doi.org/10.1088/1748-9326/aade56

Sulikowska, A., Walawender, J.P., Walawender, E., 2019. Temperature extremes in Alaska: temporal variability and circulation background. Theor Appl Climatol 136, 955–970. https://doi.org/10.1007/s00704-018-2528-z

Sullivan, R., Billesbach, D., Keeler, E., Ermold, B., Pal, S., 1997. Eddy Correlation Flux Measurement System. https://doi.org/10.5439/1025039

Sun, D., 2003. Estimation of land surface temperature from a Geostationary Operational Environmental Satellite (GOES-8). J. Geophys. Res. 108, 4326. https://doi.org/10.1029/2002JD002422

Teichmann, F., Pichlhöfer, A., Sulejmanovski, A., Korjenic, A., 2024. Measurement Errors When Measuring Temperature in the Sun. Sensors 24, 1564. https://doi.org/10.3390/s24051564

Thunberg, S.M., Walsh, J.E., Euskirchen, E.S., Redilla, K., Rocha, A.V., 2021. Surface moisture budget of tundra and boreal ecosystems in Alaska: Variations and drivers. Polar Science, Special Issue on “The Sixth International Symposium on Arctic Research (ISAR-6)” 29, 100685. https://doi.org/10.1016/j.polar.2021.100685

Tonooka, H., 2005. Accurate atmospheric correction of ASTER thermal infrared imagery using the WVS method. IEEE Trans. Geosci. Remote Sensing 43, 2778–2792. https://doi.org/10.1109/TGRS.2005.857886

Tonooka, H., 2001. An atmospheric correction algorithm for thermal infrared multispectral data over land-a water-vapor scaling method. IEEE Trans. Geosci. Remote Sensing 39, 682–692. https://doi.org/10.1109/36.911125

Tonooka, H., 2000. Introduction of Water Vapor Dependent Coefficients to Multichannel Algorithms. Journal of the Remote Sensing Society of Japan 20, 137–148. https://doi.org/10.11440/rssj1981.20.137

Torre Jorgenson, M., Harden, J., Kanevskiy, M., O’Donnell, J., Wickland, K., Ewing, S., Manies, K., Zhuang, Q., Shur, Y., Striegl, R., Koch, J., 2013. Reorganization of vegetation, hydrology and soil carbon after permafrost degradation across heterogeneous boreal landscapes. Environ. Res. Lett. 8, 035017. https://doi.org/10.1088/1748-9326/8/3/035017

Ueyama, M., Ichii, K., Iwata, H., Euskirchen, E.S., Zona, D., Rocha, A.V., Harazono, Y., Iwama, C., Nakai, T., Oechel, W.C., 2013. Upscaling terrestrial carbon dioxide fluxes in Alaska with satellite remote sensing and support vector

regression. Journal of Geophysical Research: Biogeosciences 118, 1266–1281. https://doi.org/10.1002/jgrg.20095

Ueyama, M., Iwata, H., Harazono, Y., 2014. Autumn warming reduces the CO_2 sink of a black spruce forest in interior Alaska based on a nine-year eddy covariance measurement. Glob Change Biol 20, 1161–1173. https://doi.org/10.1111/gcb.12434

Ueyama, M., Iwata, H., Nagano, H., Tahara, N., Iwama, C., Harazono, Y., 2019. Carbon dioxide balance in early-successional forests after forest fires in interior Alaska. Agricultural and Forest Meteorology 275, 196–207. https://doi.org/10.1016/j.agrformet.2019.05.020

Ueyama, M., Yamamori, T., Iwata, H., Harazono, Y., 2020. Cooling and Moistening of the Planetary Boundary Layer in Interior Alaska Due to a Postfire Change in Surface Energy Exchange. Journal of Geophysical Research: Atmospheres 125, e2020JD032968. https://doi.org/10.1029/2020JD032968

Waigl, C.F., Stuefer, M., Prakash, A., Ichoku, C., 2017. Detecting high and low-intensity fires in Alaska using VIIRS I-band data: An improved operational approach for high latitudes. Remote Sensing of Environment 199, 389–400. https://doi.org/10.1016/j.rse.2017.07.003

Wan, Z., 2014. New refinements and validation of the collection-6 MODIS land-surface temperature/emissivity product. Remote Sensing of Environment 140, 36–45. https://doi.org/10.1016/j.rse.2013.08.027

Wang, K., Wan, Z., Wang, P., Sparrow, M., Liu, J., Zhou, X., Haginoya, S., 2005. Estimation of surface long wave radiation and broadband emissivity using Moderate Resolution Imaging Spectroradiometer (MODIS) land surface temperature/emissivity products. Journal of Geophysical Research: Atmospheres 110. https://doi.org/10.1029/2004JD005566

Wang, Q., Imasu, R., Arai, Y., Ito, S., Mizoguchi, Y., Kondo, H., Xiao, J., 2021. Sub-Daily Natural CO2 Flux Simulation Based on Satellite Data: Diurnal and Seasonal Pattern Comparisons to Anthropogenic CO2 Emissions in the Greater Tokyo Area. Remote Sensing 13, 2037. https://doi.org/10.3390/rs13112037

Wang, W., Li, S., Hashimoto, H., Takenaka, H., Higuchi, A., Kalluri, S., Nemani, R., 2020. An Introduction to the Geostationary-NASA Earth Exchange (GeoNEX) Products: 1. Top-of-Atmosphere Reflectance and Brightness Temperature. Remote Sensing 12, 1267. https://doi.org/10.3390/rs12081267

Wang, X., Liu, J., Yang, B., Bao, Y., Petropoulos, G.P., Liu, H., Hu, B., 2021. Seasonal Trends in Clouds and Radiation over the Arctic Seas from Satellite Observations during 1982 to 2019. Remote Sensing 13, 3201. https://doi.org/10.3390/rs13163201

Wang, Z., Schaaf, C.B., Sun, Q., Shuai, Y., Román, M.O., 2018. Capturing rapid land surface dynamics with Collection V006 MODIS BRDF/NBAR/Albedo (MCD43) products. Remote Sensing of Environment 207, 50–64. https://doi.org/10.1016/j.rse.2018.02.001

Watts, J.D., Natali, S.M., Minions, C., Risk, D., Arndt, K., Zona, D., Euskirchen, E.S., Rocha, A.V., Sonnentag, O., Helbig, M., Kalhori, A., Oechel, W., Ikawa, H., Ueyama, M., Suzuki, R., Kobayashi, H., Celis, G., Schuur, E.A.G., Humphreys, E., Kim, Y., Lee, B.-Y., Goetz, S., Madani, N., Schiferl, L.D., Commane, R., Kimball, J.S., Liu, Z., Torn, M.S., Potter, S., Wang, J.A., Jorgenson, M.T., Xiao, J., Li, X., Edgar, C., 2021. Soil respiration strongly offsets carbon uptake in Alaska and Northwest Canada. Environ. Res. Lett. 16, 084051. https://doi.org/10.1088/1748-9326/ac1222

Westermann, S., Langer, M., Boike, J., 2011. Spatial and temporal variations of summer surface temperatures of high-arctic tundra on Svalbard — Implications for MODIS LST based permafrost monitoring. Remote Sensing of Environment 115, 908–922. https://doi.org/10.1016/j.rse.2010.11.018

Williamson, S., Hik, D., Gamon, J., Kavanaugh, J., Flowers, G., 2014. Estimating Temperature Fields from MODIS Land Surface Temperature and Air Temperature Observations in a Sub-Arctic Alpine Environment. Remote Sensing 6, 946–963. https://doi.org/10.3390/rs6020946

Wolken, J.M., Hollingsworth, T.N., Rupp, T.S., Chapin, F.S., Trainor, S.F., Barrett, T.M., Sullivan, P.F., McGuire, A.D., Euskirchen, E.S., Hennon, P.E., Beever, E.A., Conn, J.S., Crone, L.K., D'Amore, D.V., Fresco, N., Hanley, T.A., Kielland, K., Kruse, J.J., Patterson, T., Schuur, E.A.G., Verbyla, D.L., Yarie, J., 2011. Evidence and implications of recent and projected climate change in Alaska's forest ecosystems. Ecosphere 2, art124. https://doi.org/10.1890/ES11-00288.1

Wongsai, N., Wongsai, S., Huete, A., 2017. Annual Seasonality Extraction Using the Cubic Spline Function and Decadal Trend in Temporal Daytime MODIS LST Data. Remote Sensing 9, 1254. https://doi.org/10.3390/rs9121254

Xia, L., Zhao, F., Chen, L., Zhang, R., Mao, K., Kylling, A., Ma, Y., 2018. Performance comparison of the MODIS and the VIIRS 1.38 μm cirrus cloud channels using libRadtran and CALIOP data. Remote Sensing of Environment 206, 363–374. https://doi.org/10.1016/j.rse.2017.12.040

Xiao, J., Fisher, J.B., Hashimoto, H., Ichii, K., Parazoo, N.C., 2021. Emerging satellite observations for diurnal cycling of ecosystem processes. Nat. Plants 1–11. https://doi.org/10.1038/s41477-021-00952-8

Xin, Q., Olofsson, P., Zhu, Z., Tan, B., Woodcock, C.E., 2013. Toward near real-time monitoring of forest disturbance by fusion of MODIS and Landsat data. Remote Sensing of Environment 135, 234–247. https://doi.org/10.1016/j.rse.2013.04.002

Xing, Z., Li, Z.-L., Duan, S.-B., Liu, X., Zheng, X., Leng, P., Gao, M., Zhang, X., Shang, G., 2021. Estimation of daily mean land surface temperature at global scale using pairs of daytime and nighttime MODIS instantaneous observations. ISPRS Journal of Photogrammetry and Remote Sensing 178, 51–67. https://doi.org/10.1016/j.isprsjprs.2021.05.017

Xiong, X., Butler, J.J., 2020. MODIS and VIIRS Calibration History and Future Outlook. Remote Sensing 12, 2523. https://doi.org/10.3390/rs12162523

Yamamoto, Y., Ichii, K., Ryu, Y., Kang, M., Murayama, S., 2022. Uncertainty quantification in land surface temperature retrieved from Himawari-8/AHI data by operational algorithms. ISPRS Journal of Photogrammetry and Remote Sensing 191, 171–187. https://doi.org/10.1016/j.isprsjprs.2022.07.008

Yamamoto, Y., Ichii, K., Ryu, Y., Kang, M., Murayama, S., Kim, S.-J., Cleverly, J.R., 2023. Detection of vegetation drying signals using diurnal variation of land surface temperature: Application to the 2018 East Asia heatwave. Remote Sensing of Environment 291, 113572. https://doi.org/10.1016/j.rse.2023.113572

Yamamoto, Y., Ishikawa, H., 2018. Spatiotemporal Variability Characteristics of Clear-Sky Land Surface Temperature in Urban Areas of Japan Observed by Himawari-8. Sola 14, 179–184. https://doi.org/10.2151/sola.2018-032

Yang, J., Zhou, J., Göttsche, F.-M., Long, Z., Ma, J., Luo, R., 2020. Investigation and validation of algorithms for estimating land surface temperature from Sentinel-3 SLSTR data. International Journal of Applied Earth Observation and Geoinformation 91, 102136. https://doi.org/10.1016/j.jag.2020.102136

Young-Robertson, J.M., Raz-Yaseef, N., Cohen, L.R., Newman, B., Rahn, T., Sloan, V., Wilson, C., Wullschleger, S.D., 2018. Evaporation dominates evapotranspiration on Alaska's Arctic Coastal Plain. Arctic, Antarctic, and Alpine Research 50, e1435931. https://doi.org/10.1080/15230430.2018.1435931

Zanaga, D., Ruben, V.D.K., De Keersmaecker, Wanda, Souverijns, Niels, Brockmann, Carsten, Quast, Ralf, Wevers, Jan, Grosu, Alex, Paccini, Audrey, Vergnaud, Sylvain, Cartus, Oliver, Santoro, Maurizio, Fritz, Steffen, Georgieva, Ivelina, Lesiv, Myroslava, Carter, Sarah, Herold, Martin, Li, Linlin, Tsendbazar,

Nandin-Erdene, Ramoino, Fabrizio, Arino, Olivier, 2021. ESA WorldCover 10 m 2020 v100. https://doi.org/10.5281/ZENODO.5571936

Zeng, H., Ren, H., Nie, J., Zhu, J., Ye, X., Jiang, C., 2021. Land Surface Temperature and Emissivity Retrieval from Nighttime Middle and Thermal Infrared Images of Chinese Fengyun-3D MERSI-II. IEEE J. Sel. Top. Appl. Earth Observations Remote Sensing 14, 7724–7733. https://doi.org/10.1109/JSTARS.2021.3098579

Zhan, W., Zhou, J., Ju, W., Li, M., Sandholt, I., Voogt, J., Yu, C., 2014. Remotely sensed soil temperatures beneath snow-free skin-surface using thermal observations from tandem polar-orbiting satellites: An analytical three-time-scale model. Remote Sensing of Environment 143, 1–14. https://doi.org/10.1016/j.rse.2013.12.004

Zhang, P., Hu, X., Lu, Q., Zhu, A., Lin, M., Sun, L., Chen, L., Xu, N., 2022. FY-3E: The First Operational Meteorological Satellite Mission in an Early Morning Orbit. Adv. Atmos. Sci. 39, 1–8. https://doi.org/10.1007/s00376-021-1304-7

Zhang, Ruonan, Sun, C., Zhu, J., Zhang, Renhe, Li, W., 2020. Increased European heat waves in recent decades in response to shrinking Arctic sea ice and Eurasian snow cover. npj Clim Atmos Sci 3, 1–9. https://doi.org/10.1038/s41612-020-0110-8

Zhang, T., Zhou, Y., Zhu, Z., Li, X., Asrar, G.R., 2022. A global seamless 1 km resolution daily land surface temperature dataset (2003–2020). Earth Syst. Sci. Data 14, 651–664. https://doi.org/10.5194/essd-14-651-2022

Zhang, Y., Msangi, S., Edmonds, J., Waldhoff, S., 2024. Limited increases in Arctic offshore oil and gas production with climate change and the implications for energy markets. Sci Rep 14, 6699. https://doi.org/10.1038/s41598-024-54007-x

Zheng, X., Li, Z.-L., Nerry, F., Zhang, X., 2019. A new thermal infrared channel configuration for accurate land surface temperature retrieval from satellite data. Remote Sensing of Environment 231, 111216. https://doi.org/10.1016/j.rse.2019.111216

Zheng, X., Li, Z.-L., Wang, T., Huang, H., Nerry, F., 2022. Determination of global land surface temperature using data from only five selected thermal infrared channels: Method extension and accuracy assessment. Remote Sensing of Environment 268, 112774. https://doi.org/10.1016/j.rse.2021.112774

Zhou, S., Cheng, J., 2020. An Improved Temperature and Emissivity Separation Algorithm for the Advanced Himawari Imager. IEEE Trans. Geosci. Remote Sensing 58, 7105–7124. https://doi.org/10.1109/TGRS.2020.2979846

Zimov, S.A., Davydov, S.P., Zimova, G.M., Davydova, A.I., Schuur, E.A.G., Dutta, K., Chapin, F.S., 2006. Permafrost carbon: Stock and decomposability of a globally significant carbon pool. Geophysical Research Letters 33, 2006GL027484. https://doi.org/10.1029/2006GL027484

Zou, X., 2021. Studies of FY-3 Observations over the Past 10 Years: A Review. Remote Sensing 13, 673. https://doi.org/10.3390/rs13040673